University of Naples Federico II

Dynamic simulation of polygeneration systems for buildings

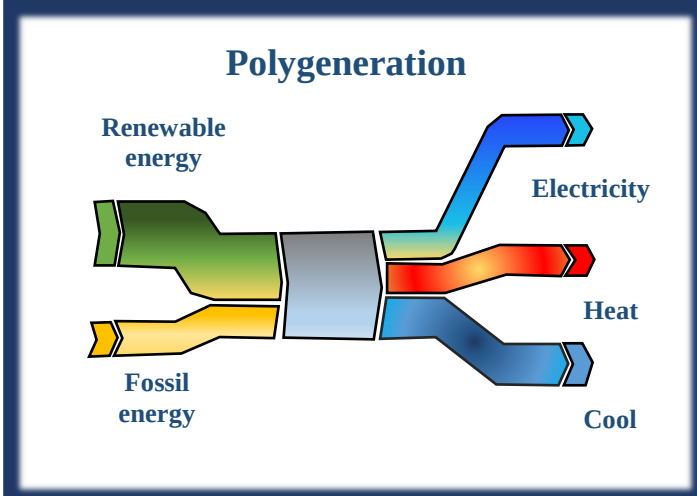

Maria Vicidomini

TUTORS
PROF. FRANCESCO CALISE
PROF. MASSIMO DENTICE D'ACCADIA
PROF. ADOLFO PALOMBO

DOCTORATE THESIS

RESEARCH DOCTORATE IN INDUSTRIAL ENGINEERING

XXX CYCLE

UNIVERSITY OF NAPLES FEDERICO II

SCHOOL OF DOCTORATE IN INDUSTRIAL ENGINEERING

RESEARCH DOCTORATE IN INDUSTRIAL ENGINEERING

XXX CYCLE

DOCTORATE THESIS

Dynamic simulation of polygeneration systems for buildings

TUTORS

PROF. FRANCESCO CALISE

PROF. MASSIMO DENTICE D'ACCADIA

PROF. ADOLFO PALOMBO

CANDIDATE

MARIA VICIDOMINI

DOCTORATE COORDINATOR

PROF. MICHELE GRASSI

2018

To my daughter Dèsirèe

I am proud of many things in my life,

but nothing beats being your mother

CONTENTS

Aim of the thesis

This thesis aims at investigating the polygeneration systems for buildings by dynamic simulation models. In particular, different polygeneration systems, supplied both by the solar renewable energy source and by natural gas, were examined.

Solar polygeneration systems were investigated by considering a new configuration of solar technology with respect to traditional one, based on the Building Integrated Solar Technologies (BISTSs), that today in EU Countries is often recommended or mandatory for new buildings. In particular, BISTSs (e.g. BI Solar Thermal Collectors BISTC, BI PhotoVoltaic panels BIPV, BI PV Thermal collectors BIPVT, etc.) replace partly or totally the building envelope elements (opaque roof and façades and transparent/semi-transparent elements, sunshades and sunscreens, balcony, etc.), by addressing both the functional and aesthetic aspects.

In more detail, the thesis aims to:

- investigate the thermal and electric performance of BIPVT collectors with water as working fluid, since very few works are available in literature concerning this technology respect the more diffused systems based on BIPV or air BIPVT;
- assess the active and passive effects of different BIPVT system layouts on the building energy demand and consumption, avoiding focusing only on the BIPVT system itself, and analysing the whole building-plant system;
- analyse the BIPVT collectors electricity production when they are coupled to electricity storage batteries, in order to obtain a grid-independent system;
- analyse the heat production of BIPVT collectors when they are coupled to low temperature heat-driven chillers, as adsorption chillers;
- find out the set of building/plants design and operating parameters which maximize the system energy, exergy, environmental and economic performance, by comprehensive parametric analysis;
- outline design guidelines related to the system layouts and building envelope features as a function of weather conditions.

The general purpose is to fill some knowledge gaps found in literature regarding BISTSs, from both numerical and/or experimental points of view, providing a contribution to their diffusion.

Natural gas polygeneration systems were investigated by adopting an innovative approach based on detailed dynamic simulations, able to predict the real time-dependent operation of the polygeneration systems preceding their installation, to optimize the configurations and to enhance their energetic, economic and environmental performance. The application of this methodology to polygeneration systems based on fossil fuels, in this case natural gas, is very attractive in order to overcome the main drawbacks of this technology due to the scarce reliability of the feasibility analyses. In fact, a number of profitable polygeneration systems are discarded in a preliminary design phase, whereas several apparently profitable systems are realized, revealing a poor energy and economic performance over their operating lifetime. This is mainly due to the dramatic simplifications used in the prediction of the performance of the systems to be evaluated. By

considering this aspect and the knowledge gaps emerged from the literature review, in this thesis the following points were investigated:

- the coupling of polygeneration plants and buildings, as a unique system, analysed through a detailed model of the hydronic system strictly related to a building dynamic simulation model;
- a detailed thermo-economic comparison among the different conventional, innovative /optimized control strategies, considering the real-time operation of the controllers and of the whole system, and taking into account the temperature fluctuations in every component, as well as the effects of varying set-point temperatures and/or activation periods;
- investigating high capacity polygeneration systems (for industrial and hospital applications) that with respect to the micro-polygeneration systems don't suffer for the low operating hours and for the high capital costs typical of residential application.

Outline of the thesis

The thesis is outlined as follows:

Chapter 1: This chapter provides information about the energy and environmental issues in the worldwide framework, mainly focusing on the energy consumption of the buildings sector. The most recent international regulations adopted to reduce the energy consumption and to increase building energy performance are also reported.

Chapter 2: In this chapter, the description and classification of Building Integrated Solar Thermal Systems (BISTSs) is reported. These systems are integrated into building envelope and can be used in both the construction of new buildings and the refurbishment of existing buildings, enhancing their energy performance. The real applications and simulation works concerning the several technologies and configurations of such innovative collectors are reported, mainly focusing on the BI PhotoVoltaic Thermal (BIPVT) collectors.

Chapter 3: In this chapter, the work concerning the simulation of polygeneration systems is presented. By reading this chapter, the reader will understand that the possible layouts of polygeneration systems are virtually infinite, since the polygeneration can use different inputs (fossil and renewable), conversion technologies and can produce several outputs: energy (power, heating and cooling) and / or other products (hydrogen, syngas, biodiesel, fertilizers, drinking water, etc.).

Chapter 4: In this chapter, the performances of BIPVT collectors and natural gas polygeneration plants are analysed in specific cases in which they are coupled to buildings with different uses. In particular, in this chapter suitable dynamic simulation models, developed in TRNSYS 17 environment, are presented and adapted for different cases studies, calculating the energy, exergy, economic and environmental performance of the investigated systems for various time basis.

Chapter 1 Introduction

1.1 International energy framework

In the last year as in next future, the total primary energy supply (TPES) is growing, fact highlighted by several factors: the global economy growth at an average rate of 3.4%/year; expansion of population that from 7.4 billion today will be more than 9 billion in 2040; the urbanization process. To face this demand the production estimated at 2015 was 13790 Mtoe (Figure 1).

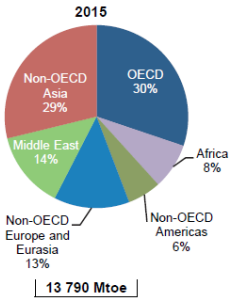

Figure 1. Total production by region [1].

At a regional level, the OECD economies produced 4 160 Mtoe, 30% of global energy, with a share of the US and Canada for almost 2500 Mtoe. Non-OECD Asia accounted for 29%, around 3980 Mtoe. This value is mainly supported by India and China. Only China produces about 2500 Mtoe, achieved by an increase of crude oil, natural gas, hydro, nuclear and power renewables productions: +1.5%, +3.4%, +6.0%, +28.9% and +14.8% respectively, respect 2014. China produces almost half of the world coal, and 29% of hydro. Instead, other biggest energy producers in this region, Indonesia and Thailand, driven by coal and natural gas, respectively, reduce their total production. Third is the Middle East with 1880 Mtoe, supported instead by an increase of crude oil production. With 1830 Mtoe, 1120 Mtoe and 816 Mtoe in 2015, respectively for non-OECD Europe and Eurasia, Africa and non-OECD Americas, they produce the similar levels of energy of 2014. Between 1971 and 2015, world TPES multiplied up to 2.5 times and also changed structure (Figure 2):

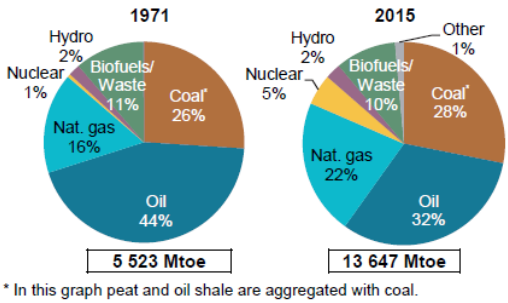

Figure 2. Total primary energy supply by fuel [1].

- *oil* fell from 44% to 32% of TPES. Of the world crude oil production Saudi Arabia, The Russian Federation and the US contributed about 40%;
- *coal* after a significant increase operated by China started to decline at 28%;

- *natural gas* grew from 16% to 22% with the Russian Federation and the US accounting for 40% of the world natural gas;
- *nuclear* from 1% to 5%, with US and France accounting a combined production of 50% of the global one.

In 2016, production growth of fossil fuels significantly decreased, -1.3% compared to 2015 – Figure 3, although the increase of natural gas production with +0.7%, except in OECD where it was stable at 1 080 Mtoe, and of crude oil with +0.1%. This is mainly due to coal reduction -4.5%, strong in OECD countries (-95 Mtoe) and China (-110 Mtoe).

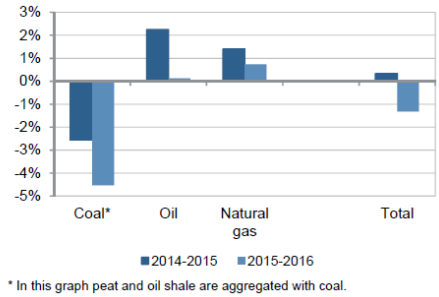

Figure 3. Annual average change in fossil fuels production by fuel [1].

In fact, power generation from coal decreases for the three last years, reaching 39.3% of the electricity produced globally in 2015 (Figure 4). Although its share of over 40% in 2016., it will be replaced by renewable energy.

Generation from gas grew slowly to reach 22.9% in 2015. The recovery from the declines of the previous two years is due to natural gas-fired power generation in OECD countries (+7.1%) and in US. Conversely in Europe, where the gas generation remains well below its peak in 2008, despite strong growth in 2015 and 2016. Reductions in Japanese and Korean gas-fired power generation led a 5.7% decline in 2015. Outside the OECD, gas generation is estimated to remain strong in 2015 and 2016.

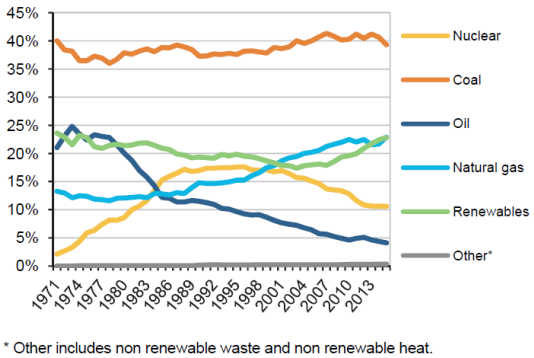

Figure 4. World electricity generation mix 1971-2015 [1].

The share of renewables is about 22.8% in 2016, which initially was dominated by hydropower with around 70%, but recent growth is due to the development of wind, bioenergy and solar PV, with 16%, 9% and 5%. In 2016, a global increase up to 24% of global power output was estimated. Hydropower additions are estimated to have decreased for the third consecutive year since 2013, with fewer projects becoming operational in China (12.5 GW) and in Brazil (5 GW). In 2016, onshore wind capacity grew by 50 GW, about 15% less versus 2015. This decline was mainly due

to China, which connected 19 GW of new onshore wind capacity, significantly less than 32 GW in 2015. The European Union added over 11 GW, led by Germany and France, followed by the US (8.2 GW), India (3.6 GW) and Brazil (2.5 GW). Annual grid-connected solar PV capacity in China more than doubled in 2016 versus 2015, with 34.5 GW becoming operational. In the US, solar PV annual additions doubled, with over 14 GW coming on line in 2016, followed by Japan (7.5 GW). The European Union's annual solar PV market contracted by a third to 5.5 GW in 2016 as growth slowed in the United Kingdom. India's annual solar PV additions doubled, with 4 GW.

Nuclear production steadily increased in the 1970s and 1980s, before plateauing at around 17% of world electricity. A decline saw since the 2000s. 2016 brought only 3 GW of new construction, sign of a reduction of the future growth in this sector.

Power production from oil has peaked at almost 25% of power production in 1973, just before the oil crisis, then it reduces less than 5%, becoming the least used.

In Figure 5, the top ten energy consumers at 2015 in terms of TPES are reported. China accounted for 22% of global TPES with 19% of the world's population while the US accounted for 16%, with 4% of the world's population. India (18% of population) and the Russian Federation ranked third and fourth, respectively. Japan, the second largest OECD consuming country, was in fifth position. Together, these five countries accounted for more than half the global TPES in 2015. In 2015, the top five countries in terms of TPES accounted for less than half of world population (47% and 45% respectively) but consumed 52% of total world energy.

Between 1971 and 2015, total final consumption (TFC) more than doubled (Figure 6).

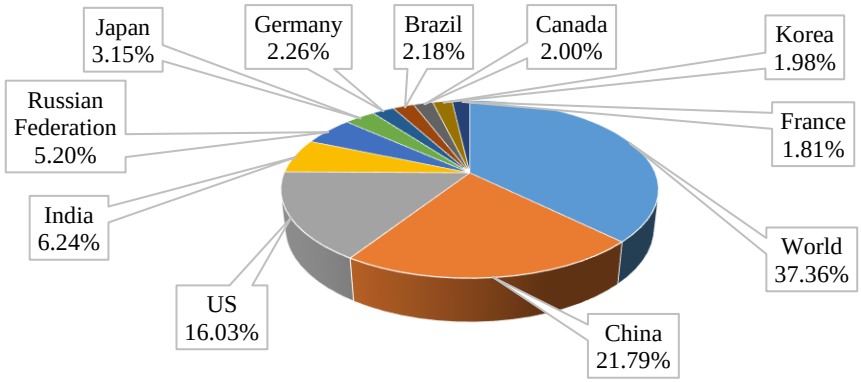

Figure 5. TPES-top ten countries in 2015.

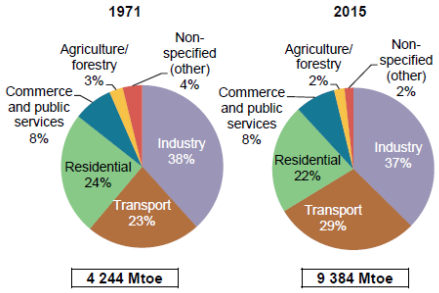

Figure 6. TFC from 1971 to 2015 [1].

Energy use in transport significantly increased, from 23% of TFC in 1971 to 29% in 2016. Nevertheless, in industry remained the largest consuming sector, with 37%, followed by the residential sector, 22%.

Future scenario

For the prevision of 2040, growing energy needs will be satisfied mainly by i) natural gas (up to 45%), ii) the energy efficiency improvements (key factor because without them, the projected rise in final energy use would more than double), iii) use of renewables sources (up to 40%).

In fact, in the New Policies Scenario by 2040, *natural gas* generation will become the second-largest fuel in the global mix after oil. This will happen in resource-rich regions, such as Middle East by substituting the oil, and in the US, also without national policies limiting the use of coal. 80% of the projected growth takes place in developing economies, led by China, India and other countries in Asia. The competition of natural gas is not just with coal but also to renewables, which in some countries become a cheaper form of new power generation, than gas by the mid-2020s, pushing gas-fired plants towards a balancing rather than a baseload role. Efficiency policies also play a part in constraining gas use: while the electricity generated from gas grows by more than half to 2040, related gas use rises by only one-third, due to high efficiency of these plants. A new gas type is emerging, the US liquefied natural gas (LNG), helping to accelerate a shift towards a more flexible, liquid, global market. Ensuring that gas remains affordable and secure, beyond the current period of ample supply and lower prices, is critical for its long-term prospects. LNG accounts for almost 90% of the projected growth in long-distance gas trade to 2040. The amount of liquefaction sites worldwide doubles to 2040, with the main additions coming from the US and Australia, followed by Russia, Qatar, Mozambique and Canada.

In next future *renewable energies* will be the least-cost source for power production, covering two-thirds of global investment in power plants to 2040. Rapid deployment of solar PV, led by China and India, helps solar become the largest source of low-carbon capacity by 2040. In the European Union, renewables account for 80% of new capacity and wind power becomes the leading source of electricity soon after 2030, due to strong growth both onshore and offshore. Policies continue to support renewable electricity worldwide, increasingly through competitive auctions rather than feed-in tariffs, and the transformation of the power sector is amplified by millions of households, communities and businesses investing directly in distributed solar PV. Growth in renewables is not only due to the power sector, but also to provide heat and mobility. In Brazil, the share of direct and indirect renewable use in final energy consumption rises from 39% today to 45% in 2040.

Although *nuclear* production reduction, in this sector, China continues to lead a gradual rise in output, overtaking the US by 2030 to become the largest producer of nuclear-based electricity.

Oil demand continues to grow to 2040, but with a steadily decreasing trend.

The reduction of *coal* use in power mix is mainly observed in India, by dropping from three-quarters in 2016 to less than half in 2040. Without large-scale carbon capture and storage, global coal consumption unavoidably will stop.

The growing *electrification* of energy also changes the global energy system, making up 40% of the rise in final consumption to 2040. Such rising is due to several factors: many millions of households add electric appliances (with an increasing of “smart” devices) and install cooling systems; adoption of electric device in supplying heat and mobility; the decarbonising of power supply; the increase of global investments in electricity sectors which overtook that of oil and gas for the first time in 2016. The electrification also explains the reason of industrial initiatives and the policy support, pushing to the global spreading of the electric vehicles (EVs) fleet. (up to 280 million at 2040 from 2 million in 2016.

A significant changing in the energy system, in order to reach a worldwide low-carbon reality, is pursued by China, with emphasis in energy policy on electricity, natural gas and cleaner, high-efficiency technologies. Energy efficiency regulation explains also the slowdown of energy demand growth, from less than 2% per year since 2012, to an average of 1% per year to 2040. Without new efficiency measures, end-use consumption in 2040 would be 40% higher. In order to pursue this changing, one-third of the world's new wind power and solar PV will is installed in China. China also accounts for more than 40% of global investment in EVs and provides a quarter of the projected rise in global gas demand and its projected imports of 280 billion cubic metres (bcm) in 2040 making China one of main country of global gas trade. China overtakes the US as the largest oil consumer around 2030, and its net imports reach 13 million barrels per day (mb/d) in 2040. But stringent fuel-efficiency measures for vehicles (both car and trucks), and a shift which sees one-in-four cars being electric by 2040, means that China is no longer the main driving force of global oil use, growth that instead will be larger in India post-2025. China remains a significant presence in coal markets, but projections suggest a reduction.

The US reach a level 50% of combined production of oil and gas; already a net exporter of gas, the US becomes a net exporter of oil in the late 2020s. The 8 mb/d rise in US oil output from 2010 to 2025 (Figure 7) would match the highest sustained period of oil output growth by a single country in the history of oil markets. Expansion on this scale is having wide-ranging impacts within North America, fuelling major investments in petrochemicals and other energy-intensive industries. By the mid-2020s, the US become the world's largest LNG exporter.

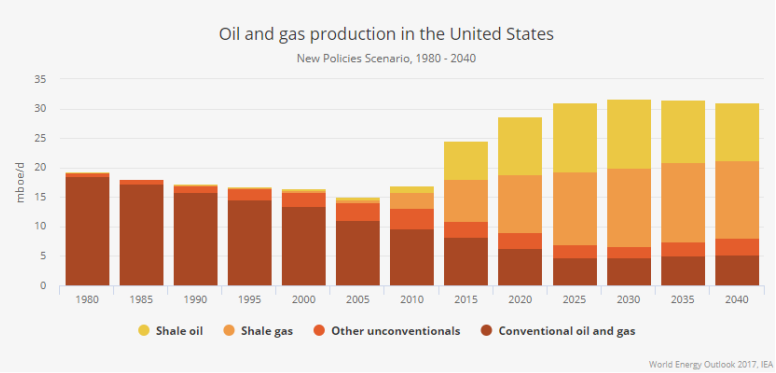

Figure 7. Oil and gas production in the US [2].

Up until the mid-2020s, oil demand growth remains robust, but then slows markedly, as greater efficiency and fuel switching reduce oil use for passenger vehicles (although, the global car fleet doubles from today to reach 2 billion by 2040). A significant influence from other sectors, as petrochemicals, aviation and shipping, supports the oil demand up to 105 mb/d by 2040. In the late 2020s, the switch to electric cars could lower oil prices lower. Energy policy support a rapid expansion in the global electric car fleet, approaching almost 300 million cars by 2040 (Figure 8). Although the growing electrification of energy in India and Indonesia, with over 100 million people/year have gained access to electricity since 2012, around 675 million people – 90% of them in sub-Saharan Africa – remain without access to electricity in 2030 and 2.3 billion continue to use biomass, coal or kerosene for cooking. Household air pollution from these sources is currently linked to 2.8 million premature deaths per year, and several billion hours are spent collecting firewood for cooking.

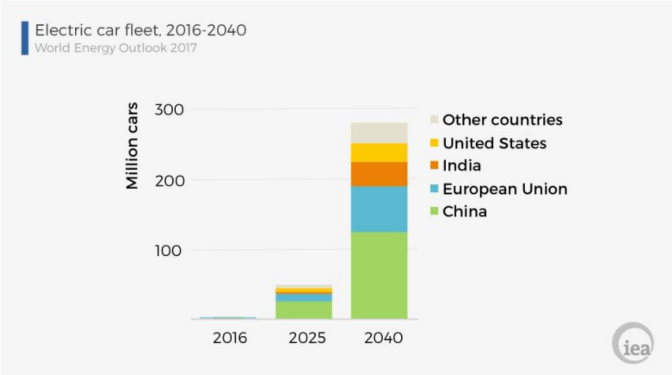

Figure 8. Electric car fleet, 2016-2040 [2].

Policy attention to air quality is rising and global emissions of all the major pollutants reduce in 2040 (Figure 9, left), but their health impacts remain severe. Premature deaths worldwide from outdoor air pollution rise from 3 million today to more than 4 million in 2040 in the New Policies Scenario, even though pollution control technologies are applied more widely and other emissions are avoided, because energy services are provided more efficiently or (as with wind and solar) without fuel combustion.

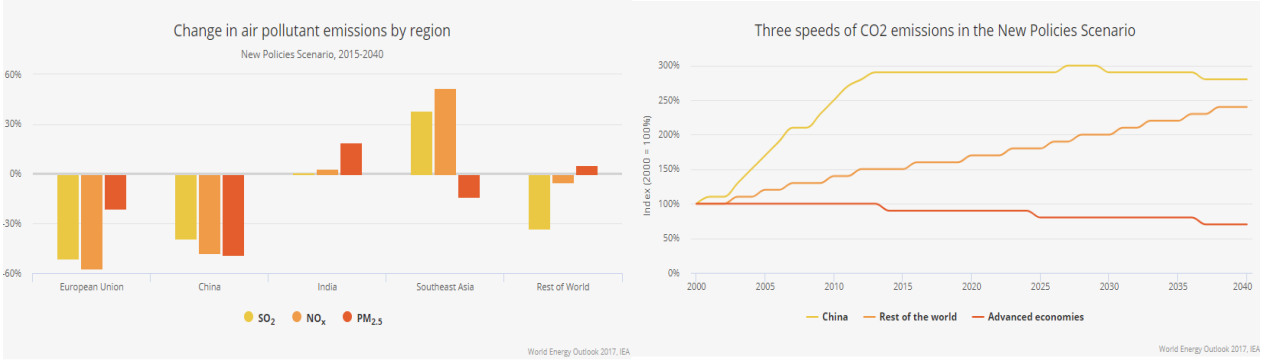

Figure 9. Change in air pollution emissions by region (left), three speeds of CO_2 emissions in the New Policies Scenario (right) [2].

Global CO_2 emissions increase slightly to 2040 in the New Policies Scenario. This outcome is far from enough to avoid severe impacts of climate change, but there are a few positive signs. Projected 2040 emissions in the New Policies Scenario are lower by 600 million tonnes than the last year ones (35.7 Gt versus 36.3 Gt). In China, CO_2 emissions are projected to plateau at 9.2 Gt by 2030 before starting to reduce (Figure 9, right). Worldwide emissions from the power sector are limited to a 5% increase between now and 2040, also if electricity demand grows by 60%.

Sustainable energy development

Key elements to achieve a sustainable economic-energy development are the climate stabilisation, cleaner air, universal access to modern energy and also the reducing energy security risks. Fundamental to these elements is i) the maintaining of the world average temperature rise well below 2°C as a long-term goal; ii) the limitation of the increase to 1.5°C, since this would significantly reduce the risks and impacts of climate change; iii) the achievement of a peak in global CO_2 emissions as soon as possible, for then proceeding to a rapid reductions in accordance with the

most advanced scientific solutions available (actions consistent with the Paris Agreement (December 2015)).

To pursued the decline in CO_2 emissions and limit climate risks further, in the Sustainable Development Scenario, low-carbon sources double their share in the energy mix to 40% in 2040, all avenues to improve efficiency are pursued, coal demand goes into an immediate decline and oil consumption peaks soon thereafter. Power generation is all decarbonised, based by 2040 on generation from renewables (over 60%), nuclear power (15%) as well as a contribution from carbon capture and storage (6%) – a technology that plays an equally significant role in cutting emissions from the industry sector. EVs are more and more significant at this aim, but decarbonising of transport sector also requires much more stringent efficiency measures, particularly for road transport. In this scenario, renewables and efficiency are the key mechanisms to drive forward the low-carbon transition and reduce pollutant emissions. The provision of highly efficient appliances, combined with decentralised renewables, also play a major role in extending full access to electricity and clean cooking, especially in rural communities and isolated settlements that are hard to reach with the grid.

As oil and coal use reduces, and renewables strongly increase, natural gas becomes the largest single fuel in the global mix in the Sustainable Development Scenario. Anyway, securing clear climate benefits from use of natural gas depends on carried out action to minimise the losses of methane – a potent greenhouse gas – to the atmosphere. Consumption of natural gas rises by nearly 20% to 2030 in the Sustainable Development Scenario and remains close at this level to 2040. The contribution of gas varies widely across regions, between sectors and over time in this scenario. In energy systems heavily depending on coal (as in China and India), where renewable alternatives are less readily available (particularly in some industrial sectors), or where seasonal flexibility is required to integrate high shares of variable renewables, gas plays an important role. Reducing the methane losses is essential to support the environmental case for gas: these emissions are not the only anthropogenic emissions of methane, but they are probably among the cheapest ones to abate. The cost analysis of abating of methane, suggest that 40-50% of the yearly total methane emissions (76 million tonnes/year) in oil and gas operations, can be mitigated at no net cost, because the value of the captured methane could cover the abatement measures. Implementing these measurements could have the same impact on reducing the average global surface temperature rise in 2100, as closing all existing coal-fired power plants in China.

1.2 Energy consumption in buildings

During the past decades, several countries focused on improve building energy performance, but average energy consumption per person in the global buildings sector still remains practically unchanged since 1990 at just less than 5 MWh/year per person [3], with a total energy consumption representing almost one-third of global final energy consumption. As a result of increasing floor area growth, buildings final energy consumption grew steadily from 33055 TWh in 2010 to 34444 TWh in 2016. The global equivalent CO_2 emissions related at this consumption accounts for nearly 20%. Building sector reached in 2013 a peak of 9.5 $GtCO_2$-eq decreased to 9.0 Gt in 2016, therefore, building consumption reduction will play a critical role in achieving the goal stated by the Paris Agreement to remain well below 2°C. Anyway, the growing population, as well as rapid growth in purchasing power in emerging economies and many developing countries, suggest that energy demand in buildings could increase by 50% by 2050 [4].

In OECD countries, average energy consumption per person started to fall from a peak of 12 MWh in 2010, but this decline may be partly explained by warmer winters in recent years, as space heating accounts for 45% of OECD building final energy use. A significant impact to the energy consumption increase is also due to the global use of electricity in buildings, grew on average by 2.5% per year since 2010, and in non-OECD countries increased by nearly 6% per year.

The energy consumption is subdivided as reported in Figure 10, corresponding to 11.8 petawatt-hours [P[1]Wh] for heating (56%), 5 PWh for hot water (23%), 2.6 PWh for lighting (12%) and 1.8 PWh for cooling (9%) [5].

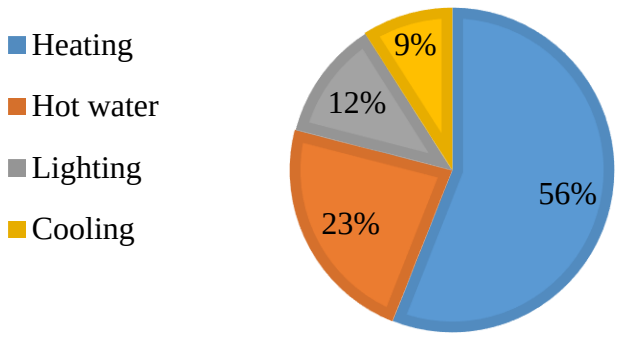

Figure 10. Building energy consumptions.

Energy demand for lighting and space cooling in buildings grew considerably over the last decade, particularly due to improved access to electricity, increasing of families wealth and demand of thermal comfort, resulting in greater energy demand in developing countries. Globally, cooling and lighting demand both grew by roughly 2% per year since 2005, while in non-OECD countries the average annual growth rate was more than 5% [6]. Globally growing is of 50% between 1990 and 2016. Space heating and hot water energy demand grew at a slower rate, about 0.5% per year since 2010. This lesser rate is due in part to shifts away from traditional use of biomass in non-OECD countries, while energy efficiency progress (e.g. condensing boiler and heat pump adoption in many OECD countries) also helped to improve energy demand in those end uses. One major change expected is a shift from heating to cooling demand. In fact, whereas there are important challenges and actions to improving building heat demand in most developed economies, space cooling demand will rise steadily nearly in all regions, and in particular in rapidly emerging economies with warmer climates Figure 11. Decisive policy action aiming at reducing the overall primary energy consumption in buildings is needed, in order to improve global average energy use per person by at least 10% by 2025 using energy-efficient and low-carbon building technologies. In this sector, some progress has been seen since the Paris Agreement in 2015, with nearly 90 countries, 3 000 city-level and 500 private sector building commitments, industry and professional bodies have mobilised to support high-performance buildings, including initiatives to implement net-zero/carbon-neutral building programmes. Therefore, thanks to continued adoption and enforcement of building energy codes and efficiency standards, global buildings sector energy intensity (measured by final energy per square metre) is reduced by 1.3% per year between 2010 and 2014.

[1] 1 PWh = 1 million of GWh or 1 000 TWh

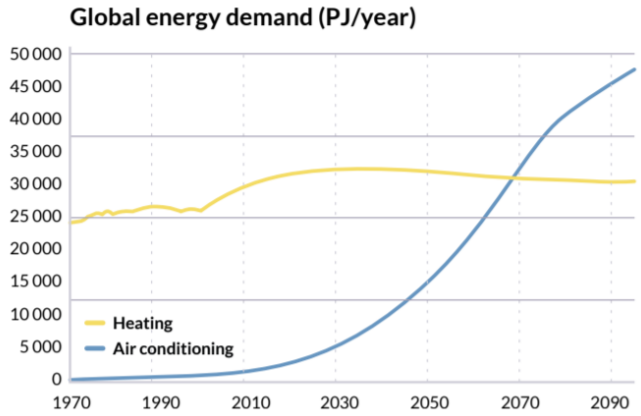

Figure 11. Projected global energy demand for heating vs cooling [5].

Progress on energy efficiency policies for buildings continues to increase, though the share of progress on building envelopes and heating, ventilation and air conditioning (HVAC) equipment. For example, in some countries, such as Denmark and Germany, building envelope policy has been the key driver for policy progress, while in other countries, such as Japan and Korea, HVAC equipment has been a key driver (Figure 12).

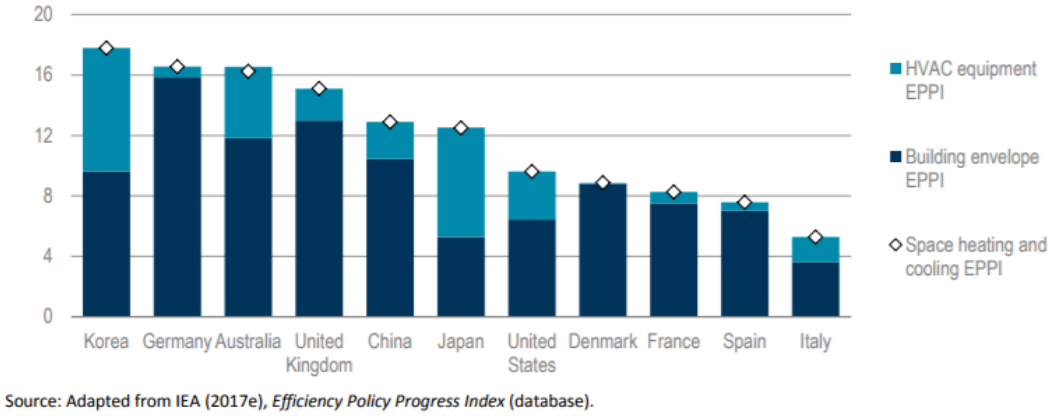

Source: Adapted from IEA (2017e), *Efficiency Policy Progress Index* (database).

Figure 12. Share of space heating and cooling efficiency policy progress since 2000 from building envelopes vs. HVAC equipment [7].

A combination of both envelope and equipment policies is critical for the transition to sustainable buildings. Highly efficient building envelopes enable the use of higher-efficiency equipment and energy sources, such as low temperature waste heat, heat pumps and renewable energy.

Energy efficiency in buildings is reached through the development of new policy codes for efficient buildings in several parts of the world. Mexico took two major steps in the last year, including publishing the first national building energy efficiency code in collaboration with the International Code Council, and launching a building energy code roadmap that provides national targets in three-year increments to 2050. California is leading the way in the US, with the latest 2016 Building Energy Efficiency Standards. On 19 June 2017, India released a national model code that can be adopted and enforced by state and local governments to improve the efficiency of non-residential buildings.

Further efficiency improvements of 10-20% are available in most countries from products already being sold in the market, including energy savings of over 75% by switching from halogen lighting to LED lighting. The market for efficient lighting will continue to grow and 90% of all

indoor lighting will be efficient by 2022, due to a combination of improved policy and decreasing cost of efficient lighting.

More energy can be saved by switching between types of water heater, by increasing the efficiency of each equipment type; heat pumps enable energy savings of 60% to 85% compared with typical instantaneous and storage heaters. Japan's Top Runner programme and Australia's white certificate schemes have enabled the water heating markets in both countries to have increasing sales of highly efficient heat pumps, with over 500 000 heat pump water heaters sold in Japan alone each year. Heat pumps are increasingly recognised as a solution for many building energy needs. For years, less sophisticated heat pumps did not efficiently operate in cold climates. Conversely, today heat pumps can operate much more efficiently with a heating capacity output higher than 70% in temperatures of -25°C. Cold climate heat pumps could shift significant portions of global heating energy use away from less efficient electric and fuel heating systems in mixed and cold climates. In district energy systems, large-scale heat pumps are improving the efficiency of space heating, water heating, cooling and refrigeration. Heat pumps are an increasingly cost-effective way to meet both energy efficiency targets and countries' emissions reductions targets.

Two key international agreements – the Paris climate change agreement and the Montreal Protocol on ozone depletion – are targeting energy efficiency in buildings as a means to achieve broader goals. The result could be a significant boost for energy efficiency efforts worldwide. The launch of the Global Alliance for Buildings and Construction (GABC) at the COP21 climate summit in 2015 and the Kigali Amendment to the Montreal Protocol in 2016 have motivated funders and other interested parties to support efforts to increase energy efficiency [7].

Energy efficiency efforts are being added to the existing Montreal Protocol network due to the Kigali Amendment to reduce the use of ozone depleting hydrofluorocarbons for cooling, the fastest growing end-use in buildings, To follow the efficiency target, the rate of annual building energy renovations also needs to improve considerably, from rates of 1% to 2% of existing stock per year today to more than 2% to 3% per year by 2025 [8].

Chapter 2 Building Integrated Solar Thermal Systems

In UE, the building sector accounts for approximately 40% of the total end use of energy and it is responsible for more than 30% of greenhouse gas emissions in OECD Countries [9]. At the same time, residential and commercial buildings show a high potential of energy savings, which may contribute to a wide reduction of global energy consumptions. To this scope, developed Countries are promoting building energy efficiency policies and their implementation through efficient, affordable, and high impact technologies. As a consequence of the recent global agreements regarding the reduction of climate changes, new and more challenging goals for pollutant emission and energy consumptions are being established [9]. In Europe, such targets mainly regard the greenhouse gas emissions reduction, the energy efficiency improvement and the renewables share (20% by 2020 and 27% by 2030).

In this framework, the European Directive 2010/31/EU for building energy efficiency promoted the development of building effective energy options based also on renewable energy applications [10]. Among the available renewable technologies, those based on solar energy are considered among the most promising for energy saving and carbon emissions reduction. The solar source can be suitably exploited through suitable Solar Thermal Collectors (STC) and PhotoVoltaic (PV) panels, which today are the most practical options for the building applications of renewable energy sources. Anyway, such devices are usually installed on building roofs without to be architectonically integrated into the building envelope (standalone configuration). In order to increase the application of solar energy in buildings, as required by Energy Performance of Buildings Directive (EPBD), aiming at obtaining buildings with a nearly zero energy consumption (for public buildings by 2018, and for commercial and residential buildings by the year 2020), the architectonic integration of solar systems into building elements (roofs, façades, windows, tiles, balcony railings, sunshades and sunscreens, etc.) is more and more diffused. In fact, in EU Countries, the Building Integration of Solar Thermal Systems (BISTSs) is often recommended or mandatory for new buildings in order to address both the functional and aesthetic aspects [11]. In the next future, building envelop elements will be required to be partly or totally replaced by the solar energy system components (integrated in building opaque and transparent / semi-transparent façades, double skin façades, sunshades and sunscreens, balcony, etc.).

BISTSs (e.g. BISTC, BIPV panels, BIPVT collectors, etc.) represent a valuable and effective measure to help and achieve the energy efficiency goal, by cutting energy consumption in buildings while boosting the share of renewables, also required by the nearly zero energy building target [12]. These are a valid option for increasing the energy performance of the building, by satisfying the building heating, cooling and domestic hot water requirements and by also having an aesthetic and functional role. In this contest, the functionality is in the thermal and acoustic insulation, shading, construction stability, and means that a BISTS is not just an added element, but it replaces the building element (for example the roof) and its dismounting expects that the building element will be totally or partly replaced by conventional building component. In addition, a building integration of a solar system consists also of a design improvement by giving to the building a more elegant look by achieving an aesthetic harmony with the building architecture [13]. Therefore, size, shape,

colour of BISTS are significant elements which must be taken into account. In addition, integration leads also to reduce the need of land and the related costs as well as for solar collectors support structures or of several building elements, such as tiles and cladding elements.

Aim of this chapter is to briefly present the state of the art of BISTSs, which include BISTCs for heat production, BIPV panels for electricity production, and BIPVT collectors for combined production of heat and electricity.

In particular, special attention in this work thesis was paid to BIPVT collectors, technology investigation. In addition, in this chapter, literature works concerning the simulation and experimentation of such systems, are also reported.

Therefore, by reading this chapter it is possible to understand how this integration occurs and which are the consequences on the building-plant performance.

A very significant issue of the BISTSs, in the framework of the evaluation of the building-plant performances, concerns the *passive effects* of such systems on the energy demand of the building for space heating and cooling.

In particular, as for the conventional stand-alone solar systems (no integrated in the building), the useful outputs of the BISTSs (electricity and/ or heat) are used to satisfy the energy demand of the building by reducing the energy demanded to the conventional systems. These are simply the *active effects* of their function, certainly useful and positive, on the building energy demand. But, the evaluation and the analysis of their passive effects are equally important and can be observed only performing a global evaluation of the whole building-plant system.

The passive effects come from the contact of the back surface of the collector (PV panel, PVT collector or STC collector) with the external surface of the roof and/or façade of the building. In particular, this contact leads to a useful passive effect during the winter season, and to an unwanted passive effect during the summer season, due to the fact that the back surface temperature of the collector is averagely higher than the outdoor air temperature where the building is located. The higher temperature of the external surface of the building results in a higher mean radiant temperature of the internal surface, which, in turn, decreases the space heating demand and increases the cooling one. About how much the unwanted summer overheating effects are higher / lower than the useful winter ones, depends on the considered weather location, thermal features of the building, heat transfer fluid, etc. Note that the unwanted summer effect is practically certain in the case of water as heat transfer fluid. In case of air systems, the summer effect could be also useful in term of reduction of the cooling energy. This depends on the flux of the air flowing through the cavity. In fact, for systems adopting the forced convection (ventilated façades) a cooling positive passive effect of the building is obtained.

In this thesis the evaluation of the passive effects of BISTSs was deeply investigated, by evaluating also how the magnitude of these passive effects is affected by some design parameters of the building envelope, in order to obtain interesting guidelines for the design of such innovative systems.

2.1 Classification, description and application of BISTSs

BISTSs can be classified across a range of operating and system features and layout details. Anyway, the main classification criterion of all solar thermal systems, and therefore, also of the BISTSs, is based on the type of the adopted heat transfer fluid (air, water, water-glycol, oil, etc.) and the final use of the collected energy (Domestic Hot Water, DHW, production and/or space heating & cooling, electricity and/or process heat production, etc.). In Figure 13 a simple BISTSs classification scheme is reported.

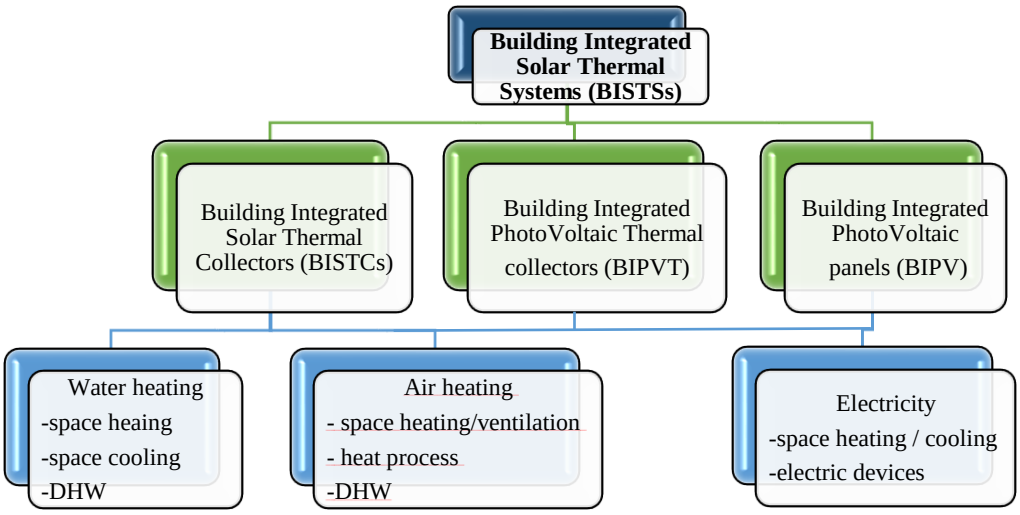

Figure 13: Building Integrated Solar Thermal Systems classification

2.1.1 Domestic hot water production

A popular application of BISTC and BIPVT collectors is the production of DHW, typically at 50-60°C. The key element for this application is classically a flat plate or a vacuum tube collector with water as the Heat Transfer Fluid (HTF). Often as HTF is adopted air, by using an air-to-water heat exchanger. A suitable thermal storage tank (typically, 150 to 400 l for a single-family), installed between the solar collector system and the user is often implemented. An auxiliary heating system is always used to guarantee the DHW production in case of scarce (or absence of) solar radiation.

HTFs are transported either naturally (passive systems) or by forced circulation (active systems). Natural water circulation occurs by natural convection in thermosiphon systems or in Integrated Collector Storage (ICS) system. In thermosiphon system, the hot water naturally rises to the top of the water storage tank and returns from the tank bottom to the solar collector as inlet fluid. In the ICS, the water storage (50-100 l/m^2) is included into the collectors, by obtaining an optimal configuration in case of façade or roof integration. In case of forced circulation systems, pumps or fans are used. Forced circulation can be open or closed. The first possibility allows one to use water as HTF without the problem of freezing of cold climate operation, since during night time the collectors are drained of the water which is stored into a suitable vessel.

In the close circulation, the fluid of collector loop is normally pressurized, so that to increase its boiling temperature, and therefore, the system operating temperatures. Anyway, the fluid is always in the collector, and therefore, a freezing protection is necessary. One option is the use of water-glycol mixtures as HTF (passive freezing protection). Note that such mixture has a lower freezing point (depending on the glycol concentration).

Another option is an active freezing protection, where circulating water in the collector field in winter time is heated by an auxiliary heating system or by the hot water from the storage tank. A further important issue to be considered for the health of the users is due to the legionellae problem occurring when water temperatures are around 30-35°C. This is avoided by a regularly heating of the stored water for a short period of time (about 30 mins) above a critical temperature (about 50-70°C for legionellae), by preventing excessive bacteria population growth.

2.1.2 Space heating and ventilation

BISTSs offer a wide range of system configurations for space heating applications. This technology results to be useful to reduce the energy demand of the building for space heating (*active effect*), but also to reduce the peak load of the conventional heating system. This last function is due to the useful *passive effect* of the integration of the solar system into building element. Note that this positive contribution to the reduction of the energy consumption for space heating is obtained although the seasonal mismatch between the heating season and the maximum heat production from the solar system (occurring during the summer season)

Between the several configurations, for example, BIPVT or BISTC collectors may be used as *active* solar systems for space heating production by using water or air as HTF.

In case of water as HTF, the basic configuration consists of BIPVT or BISTC collectors coupled to a water heat storage which supplies HVAC systems (fan coil unit, radiant floor system, air handling units, etc.)

In case of air as HTF, BIPVT or BISTC, coupled to an auxiliary heated air system, can be used to preheat the fresh air or (Figure 14), in case of air production at high temperature, directly used to provide space air heating and/or ventilation to the building.

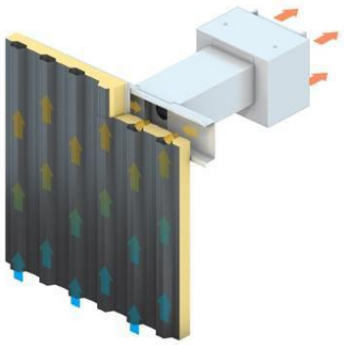

Figure 14: Solar air heating façade BISTS with auxiliary heating system.

The collector outlet air can be used to provide heat to other traditional building heating systems (e.g. heat pumps), by increasing their operational energy efficiency.

Another potential solution to reduce the space heating load of the building is represented by *passive* solar systems, like solar collector-storage walls, direct-gain windows or sunspaces [14], where solar gains are captured directly by the building structural elements.

Collector-storage walls consists of a single glazing layer covering the external walls of buildings. The efficiency of such technology is limited by the high thermal losses, therefore, to avoid them, Transparent Insulation Materials (TIMs) were developed (since ´80). With a transparent insulating element covering the outside of a massive wall, this portion of the building can be converted to a large solar wall heating area. Solar energy is converted to heat at the absorber and conducted with a time delay of some hours - depending on thickness and type of building material - through the massive wall to the indoor space. Windows and solar walls with transparent insulation operate differently with respect to the solar radiation, as the direct solar gain through the window can be of use immediately, whilst the indirect gains from the solar wall reaches the space to be heated a number of hours later, thereby extending the passive solar heating period considerably.

The most cost effective and widely deployed passive system is the direct-gain window. Solar radiation enters a room and is converted to useful heat by being absorbed by the building structure.

Most traditional buildings use windows, but the aim for which they are designed and included into external façades is only for obtaining the daylight and visual contact with the external environment, by neglecting their significant function with respect to the solar gain. These solar gains are, therefore, normally neglected in statistics relating to renewable energy contributions.

Often the needs of the space heating are well suited to the ventilation needs. In fact, as it is well-known, in order to provide fresh air for the occupants and guarantee acceptable indoor air parameters (oxygen, CO_2 and moisture), the building needs to be ventilated by exchanging indoor air with the outdoor one. In many climates, it is necessary to heat this ventilating air prior to its supply into the building. This air may be preheated by a solar thermal system in order to reduce the building heating load. Unglazed façade collectors are an interesting option and many examples especially for commercial and industrial buildings exist. The systems may be combined with heat recovery heat exchangers to provide additional heat to the fresh air supply stream from the building exhaust air stream. The Solar Wall® is a perforated wall used as a solar absorber. Air flowing through the wall is heated during the solar collection mode and can be used in conjunction with the building ventilation system. The same systems operating at night can be used for building cooling.

2.1.3 Cooling

In cooling dominated climates buildings, BISTSs are very promising, since they can also extract heat from buildings. However, this depends on the kind of BISTS technology, the adopted HTF, the operating temperatures, but undoubtedly on the weather location where the building is located.

Generally, as above-mentioned, a passive effect of the BISTSs on the energy demand for space cooling is the overheating of the indoor space, caused by the higher temperature of the internal surface where the STSs is integrated. This is an unwanted negative passive effect occurring in summer season.

Anyway, BISTS are implemented also for the purpose of cooling the building by applying several methods, which are both passive, as shading elements, ventilation, night-time radiation cooling, or active, supplying heat directly to ‘sorption’ equipment. This last application can be a promising solution for space cooling purposes, since during the summer season cooling energy demands are typically simultaneous to the solar radiation. This is based on the technology of Solar Cooling using absorption [15], adsorption [16] or desiccant evaporative [17] cooling (DEC) systems, according to the level of the obtained solar collector outlet temperature.

Absorption chillers are commonly used in combination with high temperature solar collectors [18] (evacuated tube or concentrating solar collectors), capable to provide relatively low (80-95°C) [19] or high (> 130°C) [20] driving temperatures. In this last case, it is possible to use double effect absorption chillers, with Coefficient Of Performance (COP) higher than 1. Low temperatures (45-65°C) can be obtained by flat-plate PhotoVoltaic - Thermal (PVT) collectors [21], which can drive adsorption chillers [22], increasing the range of applications of SC systems [23]. Anyway, lower temperatures influence the chiller COP. Typically, the COP of an adsorption chiller with heat supplied from flat plate solar collectors is around 0.5-0.6.

In case of DEC systems, the solar energy is used to regenerate a desiccant material that dehumidifies moist air by vapour adsorption; the resulting dry and warm air is cooled in a sensible heat exchanger and then in a direct evaporative cooler. A disadvantage of DEC systems is the high consumption of the water that occurs in system. However, the required heat temperature in such systems is low and can be easily supplied by flat plate solar collectors.

2.2 BIPVT (Building Integrated PhotoVoltaic and Thermal collectors)

Among the available solar technologies, nowadays the combination of STCs and PV panels (i.e. BIPVT system) represents the most interesting application for the building integration. Their integration occurs into different traditional building envelope components (tilted roof, flat roof, skylight, façade cladding, façade glazing) which have constructive and functional capacity. Therefore, these systems are not simply added to the building (BAPVT - Building Added PVT systems), but they are designed to displace traditional building components totally or partially, assuring a cross-functional role. For example, a BIPVT skylight is considered to be part of the building envelope, a solar generator of heat and electricity, and a daylighting element. The advantages of BIPVT systems are numerous:

1. BIPVT systems are capable to simultaneously produce useful low temperature thermal energy and electricity [24] used to balance the building demand of the related electric devices (heat pumps, electric heaters, lights, etc.);
2. BIPVT systems can be used as complimentary exterior building material and component solutions; with respect to stand-alone applications,
3. BIPVT systems potentially reduces the building construction capital cost, including land costs for ground-installations;
4. BIPVT systems are able to solve the issue regards the competition for suitable roof or façade area between STCs and PV panels.

However, the BIPVT systems have certain disadvantages that must be taken into account:

1. The orientation of the BIPVT systems is not always the optimal one (conversely, selected for the stand-alone PVT collectors). The selected orientation depends on the orientation of the available free surface where the PVT systems are integrated.
2. The tilt of the BIPVT systems is not always the optimal one. For example, in case of vertically aligned BIPVT collectors (integration into the building façade), the solar incident angle is not optimal, especially during the summer season when the sun is relatively high in the sky
3. The area of the BIPVT systems depends on the free surfaces available on roofs and façades.

Regarding the 4th point, the solution of the BIPVT collectors can offer an alternative option for the production of solar thermal heat at levels similar to conventional STC and generate electricity similar to standard PV panels. Anyway, careful design is necessary as the thermal applications often require higher operating temperatures, whereas the PV module efficiency drops with increasing temperature. In residential applications (where low-temperature heat is required), the thermal energy obtained by a BIPVT system is delivered to users through a suitable working fluid and it usually exploited in different ways, as for example: i) for supplying Solar Heating (SH) [25], Solar Cooling (SC) [26] and Solar Heating and Cooling (SHC) systems [27]; ii) for preheating heat pumps water-sources [28]; iii) for DHW preparation [29].

BIPVT collectors can be divided into air or water types, according to the thermal fluid used to remove the heat from the BIPV panel. The choice depends upon the mounting location and its application, varying according with the building demands (space heating, DHW) and/or with strategies for enhancing the module efficiency (cooling, ventilation). For residential applications, the most used BIPVT system is the water cooled one, due to the possibility to utilize the obtained thermal energy for DHW preparation, instead for space heating application, the most commonly used BIPVT is the air cooled on. In this application, the air directly cools the PV cells by flowing

through the cavity behind the PV panel with a twofold benefit: the air preheating by heat recovery and the PVT collector cooling. With this last aspect in mind, the common approaches to mitigate/reduce the BIPVT temperature fall in two categories: natural ventilation and active heat recovery [30] or forced/mechanical ventilation. This positive cooling effect of BIPVT collectors leads also to higher electric efficiencies compared to those reached by BIPV panels (because of lower operating temperatures of the PVT cells) [31] and the simultaneous production of low-temperature heat and electricity . In fact, it is well known that the PV electric efficiency decreases in case of high PV operating temperatures. In case of BIPV, the PV operating temperature may significantly increase with respect to a stand-alone one [32]. The heating effect is determined by the reduction of the back losses due to the PV installation within building envelope. Note that the passive effect of the integration on the indoor spaces is different by comparing both the systems, BIPV panels and BIPVT collectors, in summer and winter seasons. In fact, for the first system, without any air cavity between the PV panels and the external surface of the building, all the heat is transferred to the building with the consequential increase of the indoor air temperature. This effect is positive/useful during the winter season and negative/undesired during the summer one. The undesired effect may be mitigated using a BIPVT collector, in order to extract the heat from the whole building-plant system with air or water.

Although BIPVT collectors, as well as all the BISTSs, have been used since decades, they are still far from a massive commercialization, due to their technological and economic issues (e.g. perceived low reliability, lack of pre-packaged fully-integrated for plug-and-play installation, lack of well-validated design tools with multiple capabilities) [33]. Therefore, the development of new techniques for their building integration, emphasizing their active and passive effects on the overall building energy demand, is crucial in order to promote the utilization of such technology [11].

2.3 BIPVT system experimental and simulation studies

In the last decades, both from numerical and/or experimental point of view, a number of studies focused on different aspects of BIPVT collectors. A detailed discussion of such applications is reported in several review papers, such as [34, 35]. From the experimental point of view, several analyses on BIPVT systems were completed with the twofold aim to aid the design of prototypes and to validate the developed simulation models, also useful for assessing the BIPVT systems performance [36]. Instead, from the numerical point of view, the majority of simulation papers available in literature (carried out through several commercial and suitably developed dynamic energy performance simulation models) is focused on several thermal and electric aspects of roof and façades integration of PVT collectors (i.e. the most common applications of this technology [33]), by analysing the active effect of the building integration on the building energy consumptions and on the electricity and heat production of these collectors.

This section aims at presenting the current literature works concerning the study of BIPVT collectors, by focusing on both experimental works and simulation ones. After this detailed review (subsections 2.3.1 and 2.3.2) concerning the state of the art of the BIPVT collectors, the main lack of the knowledge about this topic will be highlighted and listed (subsection 2.3.3), from a positive and critical perspective, also in order to clarify the aims of this thesis.

2.3.1 BIPVT experimental works

The available experimental studies are related to both small scale indoor [37] and large outdoor [38, 39] applications, and real scale experimental buildings [40].

In reference [37], the tests performed on a module of a double-skin PVT façade (Figure 15) by transient indoor and outdoor measurements is discussed. This consists of a vertically placed monocrystalline PV panel (1.50 m × 0.99 m), with an air–gap in-between. The external heating of the panel is achieved by means of four 500 W halogen lamps. Although the aim of this work is to study a BIPV system, any building wall part is taken into account. Instead, the attention is focused on air flow and heat transfer coefficients calculation in the cavity, and its modelling in ANSYS CFX environment. Three characteristic modes of operation have been dealt with: Mode 1 with cooling by natural convection and Mode 2 and 3 with fan cooling with forced convention, flow rate 110 m^3/h and 190 m^3/h fans were tested, respectively. The results achieved by Computational Fluid Dynamics (CFD) computation are summarised in Table 1. In natural convection case for the indoor test with heated PV panel, an average value of h = 3.7 W/m^2K is obtained, which amounts to a Nu = 21. The same computation for the respective outdoor test (different panel temperatures and air inlet conditions) gives h = 4.1 W/m^2 K. Significantly higher convection coefficients are predicted for outdoor tests with the low or the high capacity fan (10.4 and 10.6 W/m^2 K, respectively).

Figure 15. Experimental layout [37].

Table 1. Comparison of average values of wall heat transfer coefficients computed by CFD.

Test conditions	**Wall Heat transfer coefficient (W/m^2K)**
Natural convection INDOORS	3.7
Natural convection OUTDOORS	4.1
110 m^3/h fan OUTDOORS	10.4
190 m^3/h fan OUTDOORS	10.6

Koyunbaba et al. [38] validated their simulation model with the experimental results of a model BIPV Trombe wall built in Izmir, Turkey. The system consists of 4 semi-transparent PV modules (each one 0.50 m wide, 2.56 m high and 1.00 m) having nominal power of 27 W each, with an air gap of 0.50 m. The system has two opened vents when the air temperature in the inter-space is higher than the indoor air temperature. The cold indoor air leaves the room from the bottom air vent while the hot air in the cavity is transferred to the room from the top air vent. The air flow in the

inter-space is driven based on thermosyphon effect which helps removing heat from the PV module and the thermal mass. The vents are closed when the indoor air temperature is higher than the inter-space temperature to prevent reverse air flow at night. They performed an energy transient analysis aiming at determining the BIPV Trombe wall performance, integrated to the façade of a room. CFD was applied to predict the temperature and velocity distribution in the test room model. The simulation results and the measured values (in days of February 4–7, 2008) of surface temperatures of PV module and outlet air temperatures (Figure 16), as well as the thermal wall/ indoor/ inter-space/ inlet temperature, were compared and it was observed that they are in good agreement. The experimental results also show that 10% of solar radiation transmittance was supplied by using a semi-transparent amorphous (a-Si) solar cell. Thus, an increased thermal energy input to the system is obtained compared to other BIPV systems. Meanwhile, the experimental daily average electric and thermal efficiency of this system can reach 4.52% and 27.2%, respectively. In addition, as well known, it is resulted that as the surface temperature of the PV module decreases, the electric efficiency increases.

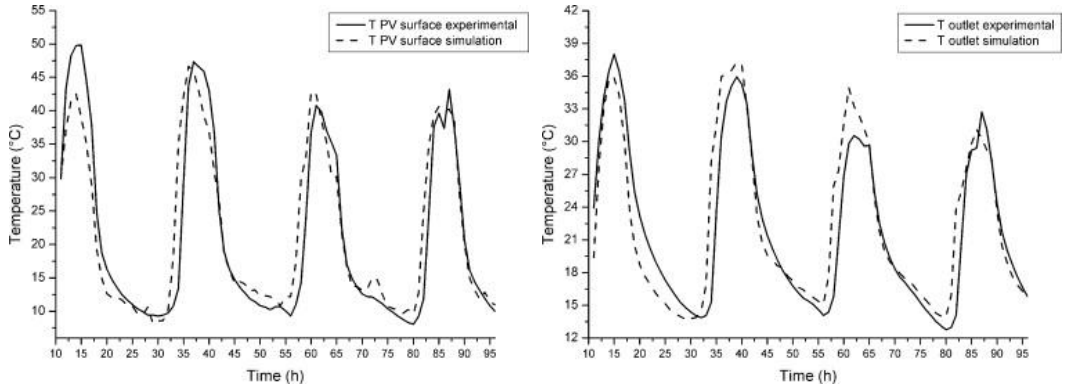

Figure 16. Experimental and simulation results of PV module and outlet air temperatures [38].

Natural convection inside the air gap of BIPV-PCM device was experimentally and numerically investigated by Aelenei et al. [41]. A suitable prototype (0.73 m×1.75 m, Figure 17), was installed on the main façade of SolarXXI office building in Lisbon in January 2013.

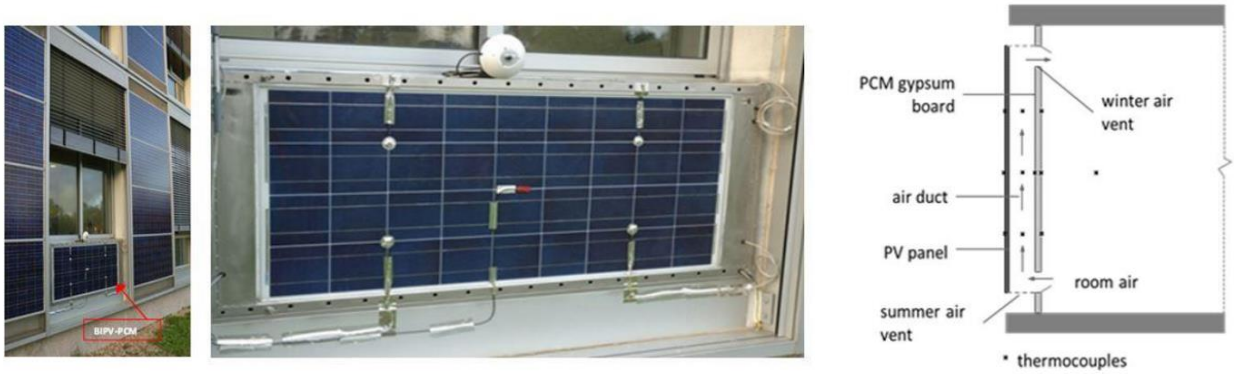

Figure 17. Prototype (left) system configuration (right).

It consists of a PV panel and an inner gypsum layer (incorporating PCM). When prototype is exposed to sunlight, PV panels absorb solar radiation and generate heat, which is then stored by the PCM gypsum layer. During the night, the melted PCM solidifies and delivers the heat back keeping the system warm for a longer period of time. The system is designed to be integrated within the

building envelope and store the thermal energy directly into the building wall structure. The external and internal frame of the prototype is equipped with a ventilation system that can provide, if necessary, indoor or outdoor ambient air into the gap. Calculated thermal and overall (electric and thermal) efficiencies are about 10 and 20%, respectively.

The combination of BIPVT and Unglazed Transpired Collector (UTC) systems for building façades is investigated in reference [40]. The basic concept of this system and the demonstration project located on the roof of a full-scale office building in Montreal (Canada), are depicted in Figure 18. Here, polycrystalline PV panels are attached on 70% of top surface of a UTC (black galvanized steel with horizontal corrugations) by achieving a BIPVT system. The horizontal corrugation of UTC was chosen to facilitate the closing of a gap between the upper frame of the PV panel (Figure 18 b) and the UTC, in order to reduce heat losses by natural convection, while inducing turbulence behind the panels and increasing the mixing vs. vertically oriented corrugations.

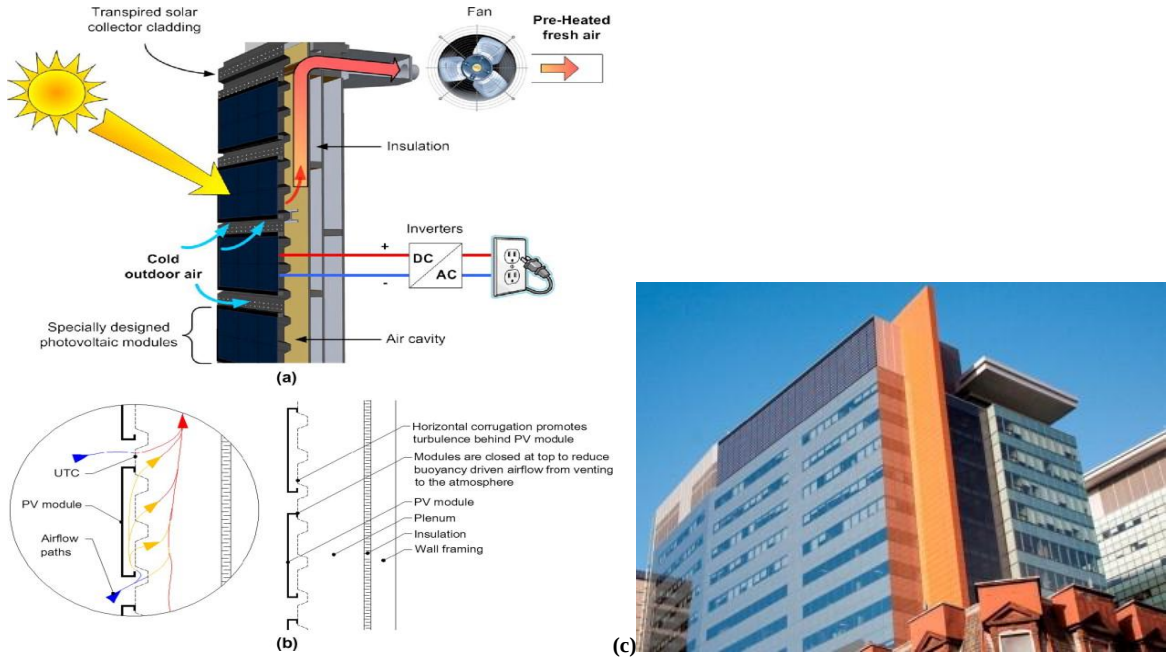

Figure 18. a) BIPVT system and (b) detail showing attachment of PV modules and airflow paths around the bottom frame of a PV module and into the transpired collector (c) BIPVT demonstration project [40].

The heat extract by BIPVT system may be utilized for space heating or possibly to heat water through a heat pump or air-to-water heat exchanger. The experiment carried out in this work aims at comparing the performance of: i) UTC and ii) innovative BIPVT system. In Figure 19, the experimental results obtained regarding the UTC thermal efficiency, combined BIPVT efficiency (thermal plus electric) and equivalent thermal BIPVT efficiency (thermal plus electric multiplied by heat pump COP equal to 4) as a function of mass flow rate, are reported. Note that the reported results are the average among the 30 min data collected for each flow rate between 1130 h and 1330 h, local time. BIPVT system equivalent thermal efficiency varies from about 50 to 63% and it is about 17% and 7% higher than that of the UTC at the low and high flow rate, respectively. This is because the electricity produced at all flow rates is relatively constant, and in turn, when converted into an equivalent thermal energy, represents a more significant portion with respect to the actual

thermal energy at low flow rates. Authors state that an annual energy analysis is required, taking into account that the produced heat is useful throughout the year or in the heating season only.

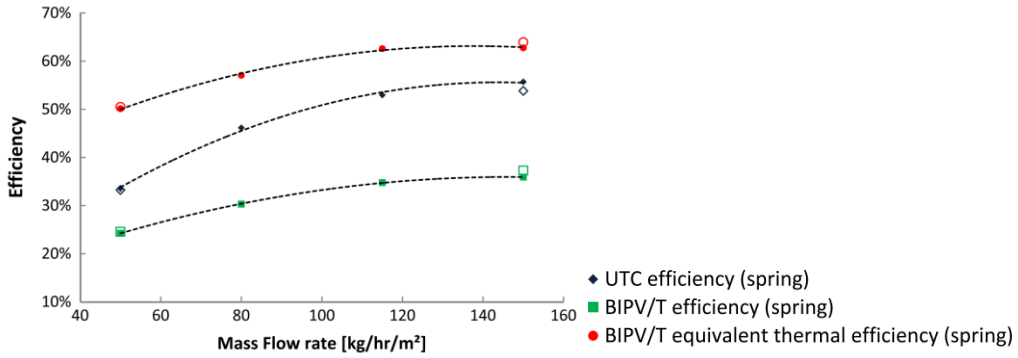

Figure 19. UTC thermal efficiency, combined BIPVT efficiency (thermal plus electric) and equivalent thermal BIPVT efficiency as a function of mass flow rate [40].

On real scale experimental buildings, influences of BIPVT system configurations on the thermal and electric performances were also experimentally assessed for different roof integration layouts [42] and air gap heights [43]. For example, in reference [42] a full scale test of a new solar collector (flat heat pipe) was carried out in Cardiff, UK. Three identical systems, were simultaneously compared: i) a solar/thermal; ii) uncooled PV and iii) PVT system. The novel flat heat pipe collector, named “heat mat” (Figure 20), was designed and built to be integrated into roof buildings and to become an energy-active system, by producing electricity and heat for the building. The tests showed that the thermal efficiency of i) and iii) configurations are around 64% and 50%, respectively. This is due to the higher reflection by the glass cover of the PV layer. The effect of cooling in configuration iii) leads to an increase of 15% of the electric efficiency with respect to the one of configuration ii), as well as a reduction of the temperature, varying between 28 and 33°C vs. 40 and 58°C of configuration ii.

Figure 20. The heat mats' based solar roof installation [42].

D’Orazio et al. [43] analysed the performance of three mono-crystalline silicon cells PV modules installed in a real scale experimental building over a traditional clay tile pitched roof in Italy. The analysed configurations (Figure 21, above) are the following: Type A, fully integrated PV module installed at the same level of the roof covering with an air gap of 0.04 m between panel and insulation; Type B, partly integrated PV module installed over the roof with an air gap of 0.2 m

between the panel and the tile covering; Type C, fully integrated PV module mounted directly in contact with roof insulation.

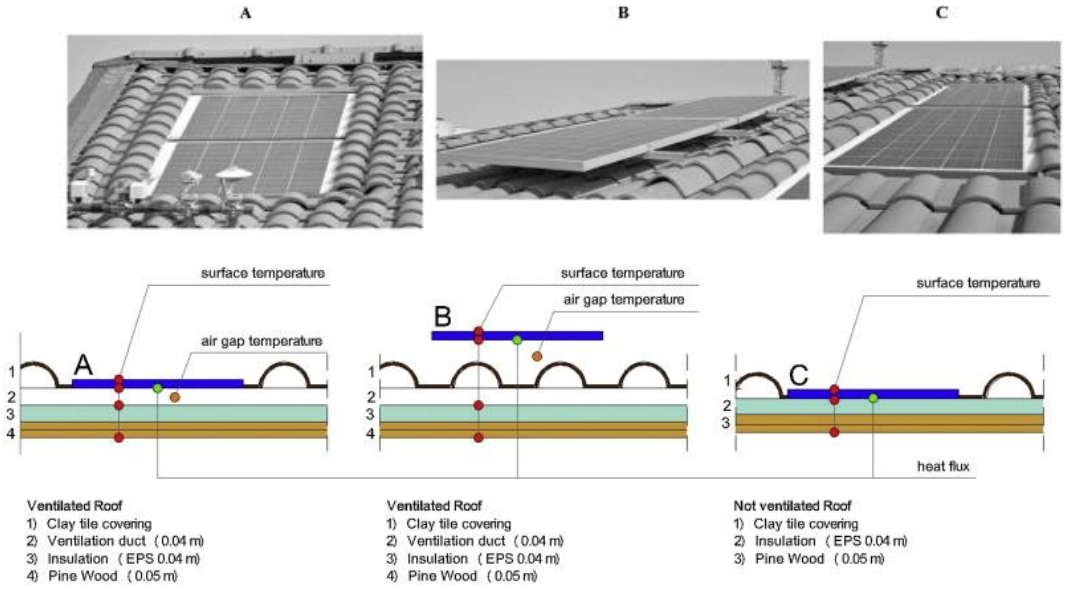

Figure 21. PV modules (above) and stratigraphy of the roofs with the measurements probes (below) [43].

Aim of this work is the comparison between different air gap heights on the performance of the analysed PV modules. Anyway, it is worth to note that: i) the roofs are different from each other due to the presence of a ventilation duct between the traditional clay tile covering and insulation (A and B roofs are ventilated, while C is not ventilated, Figure 21); ii) the three modules were formed by a different number of PV cells, and therefore, by different peak powers (for Type B, 60 cells and 0.21 kW, while for the Types A and C, 50 cells and 0.185 kW). Three summer day were analysed: a sunny day without wind, a cloudy day and a sunny day with wind. On a sunny and non-windy day, the peak cell temperature of Type B is lower than that of Type A and C (65.5°C vs. 77.3°C and 78.8°C, respectively). When fully integrated PV modules are considered with the structure of the panel remaining in contact with roof insulation, an overheating of module is obtained. On a sunny day with wind (4.15 m/s) a general reduction in cell temperature (54.3°C, 47.5°C and 64.6°C) of Types A, B and C was observed. In this day, the module A and B have a substantial reduction in air gap temperature (less than 40°C and 30°C, respectively), while in Type C the air temperature is close to the back temperature of the panel (60.9°C). On a day with poor solar irradiance, the difference in the performance between the three systems are negligible. Finally, experimental results demonstrate that although the PV module temperature of Type B is lower than other full-building integrated modules, the difference in the electricity produced by the BIPV modules, estimated for the entire monitoring period, is less than 4%.

All such studies mainly aim at investigating possible passive and active strategies necessary to lower the cells temperature, and therefore, to maximize the heat recovery, as well as the electric performance. This is obtained through different novel and modified operation strategies, such as: increase of the flow velocity inside the absorber channel [44], optimization of forced air cooled channels [45], development of suitable water cooled devices [46].

In reference [44], an experimental rig was used to validate a dynamic numerical model of a water BIPVT system, consisting of PVT collectors located on a vertical building wall of an air-conditioned building at the City University of Hong Kong. The constituent layers of the BIPVT from the front glazing to the structural wall are depicted in Figure 22. The PV encapsulation includes the TPT (Tedlar–Polyester–Tedlar) and the EVA (Ethylene-Vinyl Acetate) layers. The building consists of a brick with thickness of 0.15 m and a thermal conductivity 1.9 W/mK. The flow of the water inside the BIPVT collector was evaluated both in natural circulation mode (thermosyphon mode) and pump-operated mode. Results achieved by the model in terms of thermal performance, as well as the inside surface temperature where the BIPVT is located, agree with the simulative results, both summer and winter conditions (deviation is only about 1%). The same result was not obtained from electric point of view. In fact, the measured output power was found less than the prediction from the simulation model, because the partial shadowing of the PV modules by the neighbouring structures. This is evident in Figure 22, where the experimental and simulation electricity production in thermosyphon mode are depicted. A comparison between the two modes is also performed in terms of reached electric efficiency: in the same summer day the experimental value of the electric efficiency was 7.0% in thermosyphon mode vs. 9.1% in pump-operated mode.

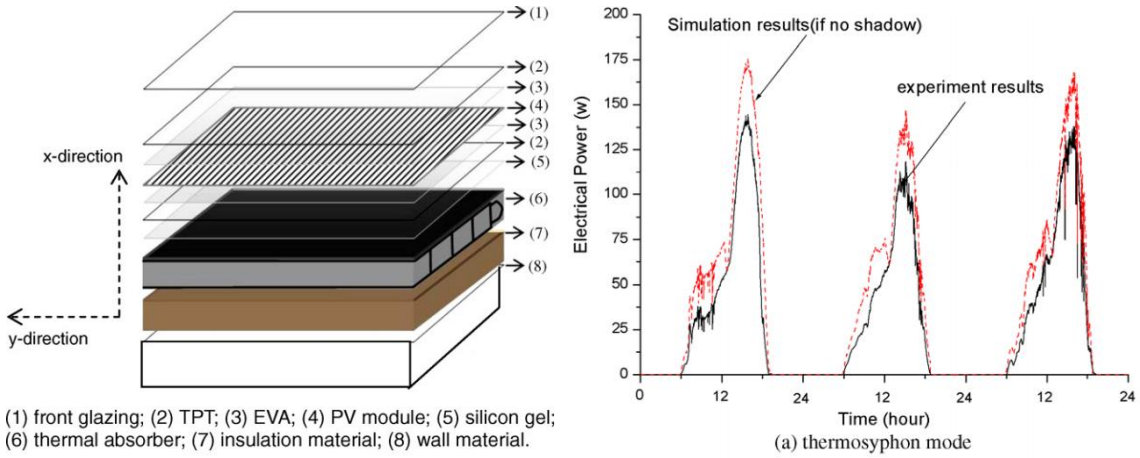

Figure 22. Constituent layers of the BIPVT (left), simulation and experimental electric power (right) [44].

A water roof BIPVT system for enhancing the heat utilization and increasing the PV efficiency, was designed in reference [47]. Mono-crystalline PV modules are embedded between a transparent protective layer and a Functionally Graded Material (FGM) layer (a mixture of heat conducting aluminium and insulating high density polyethylene), with water tubes within, supported by a thermal resistive structural substrate Figure 23. Due to the high thermal insulation of the FGM lower part and heat collection by water flow, excellent indoor thermal comfort can be achieved, by reducing the cooling needs of the building. The produced warm water can be used for a radiant floor or for a PCM storage unit. This system is multifunctional because it fulfils the basic functions of the building envelope (waterproofing, insulation, and structural strength and durability) and it simultaneously produces energy and reduces the building energy demand. Such BIPVT collectors were tested in a solar room equipped with a metal-halide lamp. Experiment tests show that before the water flow started, the solar panel surface temperatures increased quickly around 50°C and 55 C, for the irradiation of 850 W/m^2 and 1100 W/m^2, respectively. With the introduced water flow, the solar panel surface temperatures sharply dropped and then stabilized at 32°C–38°C (by following

the water flow direction). The outlet water temperature was around 32°C–34°C. These results show that water tubes integrated with FGM layers can effectively cool the PV cells.

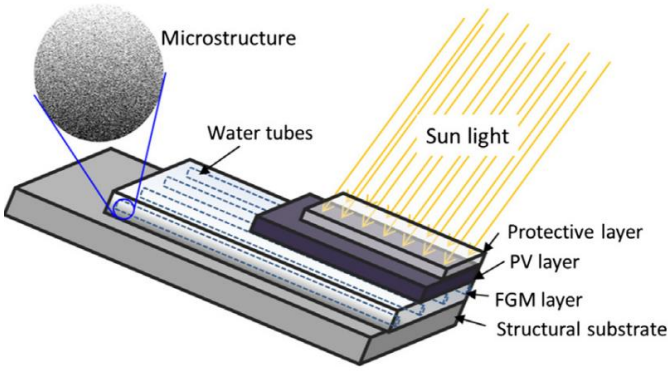

Figure 23. Schematic illustration of the water roof BIPVT [47].

An experimental setup for studying the influence of the air gap size and the forced convection on the cooling BIPV modules (and consequently on the electric efficiency of a PV module) is presented in reference [45]. They state that the PV cell temperature reduction by forced ventilation is a valid option to also reduce the building energy consumption, by preheating the outdoor incoming air to the building, necessary for a sufficient ventilation level, through the BIPV duct. The experimental setup consists of two PV panels, one of them is cooled by a fan. The main achieved results regards: i) the critical channel aspect ratio (duct depth/duct length) of 0.11, in order to minimize overheating of PV cells, in case of natural convection (V = 0.5 m/s); ii) an increase in the power output over 19% from the natural ventilation case to the case of forced convection (V = 6 m/s); the lower values of the aspect ratio which may be used for obtaining the same cooling in the PV module.

Four different configurations of 68 W multicrystalline PV façades, namely: 1) a conventional passively cooled PV façade, with a variable air duct placed between the façade and the wall; 2) an actively cooled PV façade by forced convection of 2 m/s; 3) similar to configuration 1 but with 12.5 cm layer of mineral wool (k = 0.32 W/mK) attached directly to the back of the PV-façade; 4) a thermal insulating PV façade along with an integrated cooling system (Figure 24), were investigated by Krauter et al. [46]. The “artificial wall” to whom the PV modules were connected was made of smoothened pressboard. The experiments carried out at Laboratorio Fotovoltaico of the Universidade Federal do Rio de Janeiro, were performed through a solar simulator.

By the experimental results it was obtained that with respect to the configuration 1 (the conventional PV-façade):

- configuration 2 reduces the operating cell temperatures of 18°C. This leads to an electric power increase of 8%;
- configuration 3 leads to a temperature increase of 20.7°C, which causes a 9.3% loss of electric yield. Anyway, it may become an attractive option, for the possible savings of installation costs by considering the substitution of the insulation layer of the building wall;
- configuration 4 allows an electric yield that is 9% higher and an additional cooling effect of about 20°C.

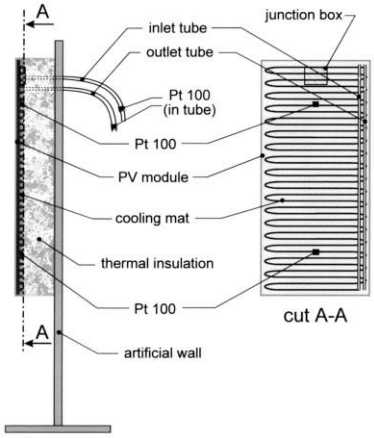

Figure 24. Side and rear view of the hybrid thermal insulating PV façade element [46].

The available literature also highlights the research effort on the design of prototypal BIPVT devices and novel systems [35]. Regarding the novel devices, recent interesting prototypes were developed and analysed.

For example, in reference [48], the experimental comparison between a two-inlet and an one-inlet air BIPVT system, incorporating opaque or semi-transparent monocrystalline silicon PV panels was carried out. As depicted in Figure 25, the second inlet is halfway along the air path and this is an important design element affecting the system performance. The comparison was performed by using a full-scale solar simulator, which simulates a more realistic sky temperature and allows a more accurate, repeatable and controlled experimentation, with respect to the outdoor environment test method.

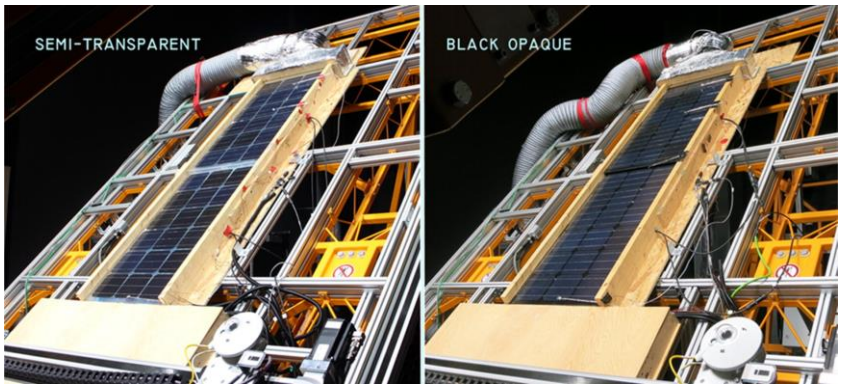

Figure 25. Semi-transparent (left) and black opaque (right) BIPVT prototype with two inlets [48].

In addition, a ventilation unit was installed above the top surface of the PV panel to generate an artificial wind along the length of the BIPVT collector. Some important experimental results are reported in Figure 26. In particular, it resulted that: i) the two-inlet system can increase the thermal efficiency by 5% compared to a conventional one-inlet system; ii) thermal efficiency decreases with increasing wind speed from 3.1 to 2.1 m/s, since a bigger portion of the PV panel heat is lost to outside; iii) BIPVT system with semi-transparent PV panels achieves 7.6% higher thermal efficiency due to the absorption of some solar radiation at the bottom surface in the BIPVT system cavity. In addition, in two-inlets BIPVT, the cool ambient air entering the second inlet tends to

descend due to higher density and to mix with the warm air entering the first inlet, tending, instead, to rise in the BIPVT channel. This leads to a good mixing between two flows and a greater temperature difference between air and the PV than in the conventional system with 1 inlet. Such temperature difference also leads to greater heat extraction from the PV modules.

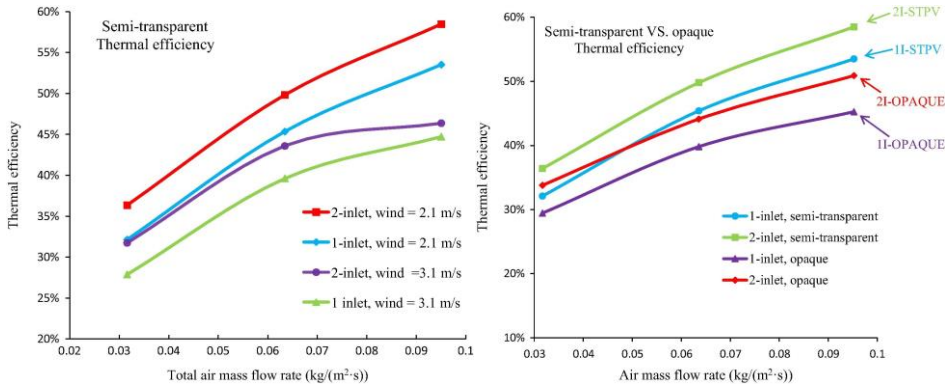

Figure 26. Thermal efficiency of one-inlet and two-inlet semi-transparent (left and right) and opaque BIPVT systems (right) [48].

An innovative spiral flow absorber for a water cooled BIPVT system (Figure 27) was constructed and investigated by Ibrahim et al. [49]. The innovative absorber, with one inlet and one outlet, was designed as a continuous stainless steel tube with dimension of 12.7×12.7 mm, attached underneath the flat plate single glazing sheet of polycrystalline silicon 80 W PV module.

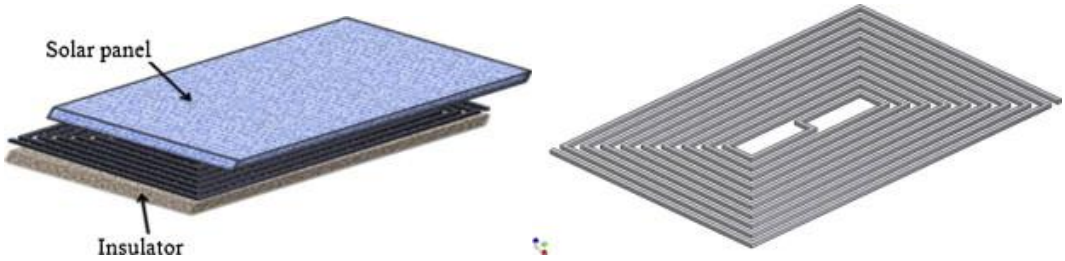

Figure 27. Assembly view of spiral flow absorber.

Water with low temperature enters the tube, flows toward the collector centre and then again to the collector edge, and by covering the entire PV panel, the fluid leaves the tube as hot water. Thermal insulator was also packed underneath the absorber. Experimental energy and exergy analysis was performed in Malaysia. From energy analysis at a mass flow rate of 0.027 kg/s and average solar radiation of 690 W/m^2, the average PV, thermal and PVT energy efficiencies were 10.8%, 48% and 59%, respectively. Moreover, from exergy analysis, the PVT exergy efficiency was 13.1%.

Another example concerning a pilot scale experimental set-up consisting of novel roof BIPVT water collectors combined to a liquid desiccant enhanced indirect evaporative cooling system was investigated in reference [26]. The novel BIPVT system (Figure 28), located in Nottingham, consists of a polyethylene heat exchanger underneath mono-crystalline PV modules to form a PVT roof collector. The complete roof structure has several layers, an outer cover; a layer of photovoltaic cells beneath the cover; EVA plastic layer at the back of PV adjacent to the PV cells layer, polyethylene heat exchanger and roof support. The system acts as a roof that properly blends into surroundings thus avoiding ‘add-on’ appearance and it represents an adaptable solution as heat extraction component, not affecting the original structure of already mounted PV modules. Exposed roof area

and tilt angle are 140 m^2 and 10°, respectively, whereas the south facing active area of PV arrays with heat exchanger is 40 m^2. Authors couple such innovative collectors with a liquid desiccant cooling system (i.e. the regeneration heat to regenerate the dilute desiccant solution is supplied by BIPVT water collectors) to provide air conditioning through dehumidification of humid air and indirect evaporative cooling. Such experimental set-up was designed to boost thermal and electric efficiency of the system and recovery useful heat supplying the cooling system. Experimental results showed that the system is capable to provide 3 and 5.2 kW of heating and cooling power, respectively, and to supply 10.3 MWh/year of electricity.

Figure 28. Integration of polyethylene loop underneath PV modules [26].

Shukla et al. [50] presented the performance analysis through energy and exergy efficiencies and evaluation of electric and thermal energy output of an experimental setup consisting of Semi-transparent BIPV (BISPV) system for roof and façade of buildings. The performance analysis of the systems, two BISPV modules each of 75 W rating, was conducted for a clear sky day at the roof and façade of the Energy Centre building, MANIT Bhopal, India. Experimental setup for façade integration is represented in Figure 29.

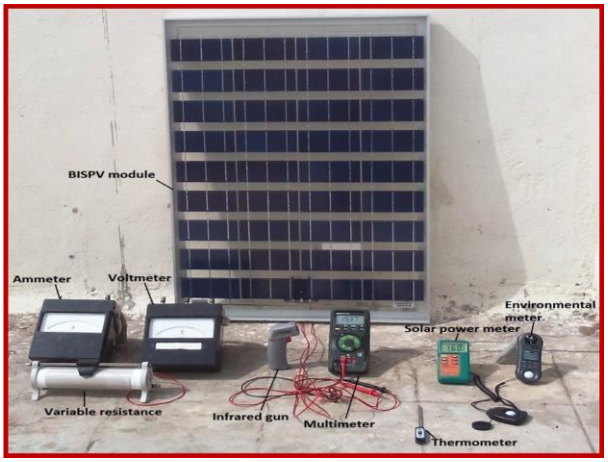

Figure 29. Experimental setup [50].

They show that the exergy efficiency of the BISPV module growths with the increase in solar intensity and decreases up to 40% when the ambient temperature increases due to the higher module temperature. The low exergy efficiency is due to the irreversibility of the PV conversion process. The energy and exergy performance of BISPV module resulted higher in case of façade with respect to the rooftop of building. The results are true in terms of electric energy (135 vs. 92.7 kWh/year), thermal energy (96.9 kWh/year vs. 45 kWh/year) and thermal exergy (157.2 kWh/year vs. 103.86

kWh/year). It is observed that the total energy efficiency varies between 11 and 18% at roof and 13 and 18% at façade throughout the day. The maximum value of electrical efficiency of BISPV module is 85% for the roof and 72% for the façade.

2.3.2 BIPVT simulation studies

The adoption of simulation tools, particularly of the dynamic ones, is useful since by such approach it is possible to design and adapt an optimal and efficient control strategy as a function of the features of the investigated system. By the development of a simulation model is also possible to simulate as much realistic as possible the system operation to be simulated and, as consequence, to predict its real time performance. In the last years, several literature works based on dynamic and stationary simulations of BIPVT collectors were performed in order to find energy solutions, for the improvement and optimization of the system energy performance. In particular, the works implementing the dynamic analysis approach presents a multiplicity of positive effects, regarding the possibility to expect the real time-dependent system operation. This allows one to also enhance the systems performance and, as a consequence, to optimize its design. Therefore, the application of this approach is very attractive.

In the following several numerical simulation studies, investigating passive or active strategies to low cell temperatures, enhance the natural ventilation or use BIPVT collectors for preheating HVAC supply air/water, are reported.

Corbin and Zhai [30] explore, numerically by a CFD model, and also experimentally, the effect of active heat recovery by a water cooled heat absorber on the performance of BIPVT collectors. In this study, authors also develop a new correlation between PV efficiency and collector inlet water temperature, ambient air temperature and insolation incident on the collectors. It resulted that new correlation reveals two important features of BIPVT collectors: i) as insolation increases from 250 W/m^2 to 1000 W/m^2, cell efficiency decreases due to higher cell temperatures; ii) the difference between fluid inlet temperature and ambient air temperature has a declining effect on efficiency as insolation decreases. The thermal and combined (thermal plus electric) calculated efficiencies reach 19 and 34.9%, respectively.

A dynamic simulation program by FORTRAN was developed for analysing and comparing the annual thermal performance of mono-Si PV modules on a normal multi-layer façade with a normal wall, supposed to be located in Hong Kong [51]. The normal wall consists of: a mosaic tiles layer exposed to the solar irradiation, a cement/sand screed layer, a concrete layer and a gypsum plaster layer exposed to the indoor environment. A ventilation air duct between PV modules and wall is expected, in order to enhance the PV efficiency, and also to reduce the heat absorbed by the building wall (Figure 30). It was found that the PV module temperature in October is higher than 65°C, and it is lower in summer; this because the beam solar radiation on the south-facing wall reduces dramatically in summer. The summer average inside and outside surface temperatures of the façade of PV wall were about 23.9 and 24.9°C, lower than those of the normal wall by 1.9 and 2.9°C, respectively. Therefore, PV wall could reduce heat gain through the envelope by 51% in summer. Instead, the winter outside wall temperature was sometimes lower or higher than that of inside surface, which indicated that the PV wall may not only have heat loss but also have heat gain under Hong Kong weather conditions. Yearly, the heat gain and heat loss through the PV wall in winter were reduced by 69 and 32%, respectively, compared with a normal wall. Totally, a thermal energy

consumption reduction of 52.1 kWh/year was achieved by replacing each m^2 of a south-facing normal wall by a PV wall, which is equivalent to a saving of 18.6 kWh of electric energy for the air conditioning system in a building. It resulted that 0.06 m is the optimal thickness of air gap in terms of PV wall thermal performance; exceeding this value, the annual heat transfer through the PV wall increases.

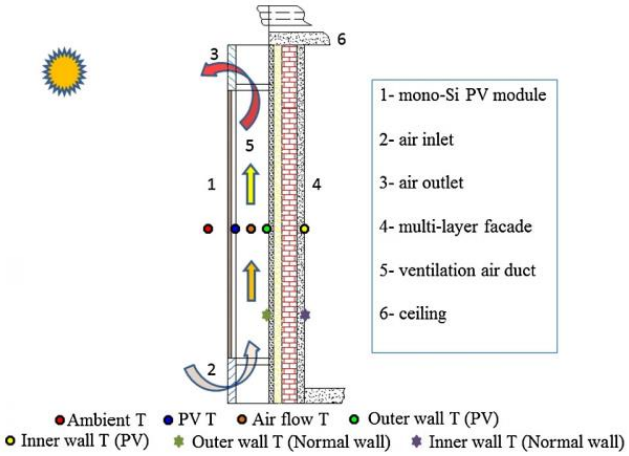

Figure 30. Layout of PV wall [51].

Analytical expressions (valid for different climatic conditions and different design parameters of the building) for the assessment of the electric efficiency of thin film PV modules coupled to BI Opaque PVT (BIOPVT) systems, with and without air duct, were obtained in reference [52]. Authors state that the recovery of thermal energy of such system, in both cases with and without air duct, is useful for reducing the PV module temperature, and therefore, for increasing its electric efficiency. In addition, the thermal energy, in both the cases, is used for space heating. In particular, in case of BIOPVT without air duct, the incident radiation is transmitted through the solar cells and is absorbed by the back sheet of the module; such absorbed heat enters the room through convection. Instead, in case of BIOPVT system with air duct, the cooler air entering through bottom inlet takes the heat of PV module and by exiting hotter enters the room.

A computer program 'MathCad 8' was used to solve such analytical expressions, which are applied to amorphous Silicon (a-Si), Cadmium Telluride (CdTe) and Copper Indium Gallium diSelenide (CIGS) thin film solar modules, for a typical winter day of Srinagar, India. The module temperature T_m, air room temperature T_r and electric efficiency of a-Si based BIOPVT system, with and without air duct are reported in Figure 31. The air circulation through the duct causes more heat dissipation of module by causing lower T_m and T_r with respect to the case without duct. Since the efficiency is a function of temperature, the lower T_m with duct case implies its higher efficiency. Without duct the average daily efficiency and average T_r were found to be 7.25% and 18.7°C respectively, whereas with duct they were found to be 7.57% and 15.2°C respectively.

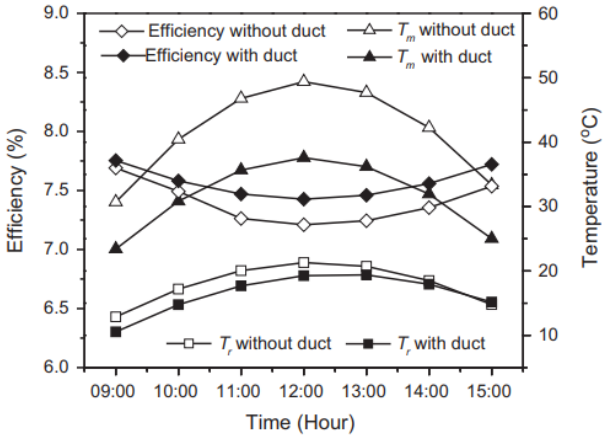

Figure 31. Hourly variation in T_r,T_m and electric efficiency for a-Si thin film BIOPVT system with and without air duct [52].

The influence of the six different PV modules ((1) monocrystalline Silicon (m-Si), (2) polycrystalline Silicon (p-Si), (3) a-Si, (4) CdTe, (5) CIGS, and (6) a heterojunction comprised of a thin a-Si PV cell on top of a crystalline Si cell (also known as HIT)) on the energy and exergy performance of novel air BI Semi-transparent PVT (BISPVT) was investigated by Vats and Tiwari [53]. In this study, a room, with dimensions of 3 m × 1.81 m x 4 m and a roof with area of 5.44 m^2 for BISPVT collectors at angle of 34°, insulated by the layer of sand, cement, polystyrene and straw fibre was considered. The system was assumed to be located at cold climatic conditions of Srinagar city (India). Matlab 7.1 software was used for evaluating the hourly BISPVT energy and exergy performance. It is observed that yearly, the maximum electric energy is 810 kWh/year, for HIT module; the maximum thermal energy is 464 kWh/year for a-Si, and therefore, suitable for space heating applications. The maximum overall thermal energy, sum of thermal energy and equivalent thermal energy (electric energy and conversion factor ratio) is obtained for HIT PV module (2497 kWh/year), as well as its exergy (834 kWh/year). The maximum module efficiency of 16.0% in case of HIT is obtained for a minimum cell temperature of 42°C; whereas in case of a-Si, the minimum efficiency of 6.0% is obtained for a maximum cell temperature of 49°C, which corresponds to a higher indoor air room temperature.

Vats and Tiwari [54] carried out a comparative study by analytical analysis between BISPVT and BIOPVT each integrated within façade and roof of a room, with (Figure 32) and without air duct. Aim of their analysis is to derive analytical expressions of room air temperature, where PVT collectors are integrated, by Matlab software. Again, as in previous reference, Srinagar city and the same room and tilt angle of the collectors were considered. By their analysis, the hourly variation of room air temperature (T_r) and solar cell temperature (T_c) for both SPVT and OPVT systems each integrated to façade and roof of a room, with air duct and air mass flow rate of 0.85 kg/s and without air duct, for an ambient air temperature of 4.4°C are obtained in Table 2. From the study it can be concluded that the BISPVT system for roof integration without air duct is more suitable for the cold climatic conditions, as the highest room air temperature equal to 22.0°C vs. the lowest one of BIOPVT system for façade integration equal to 6.7°C, is reached.

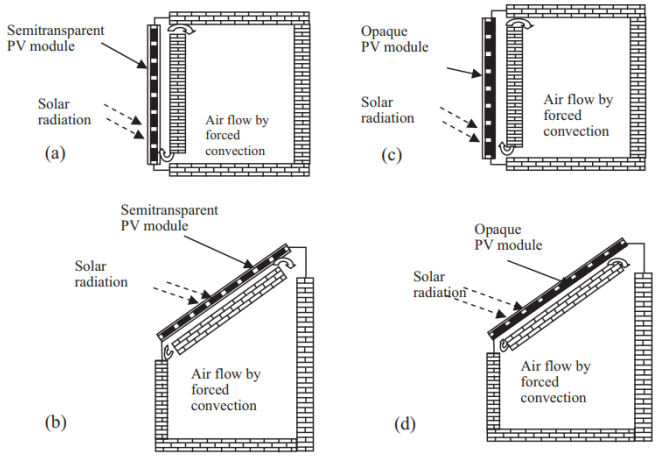

Figure 32. Cross-section view of BISPVT and BIOPVT collectors for roof and façade integration with air duct [54].

Table 2. Comparison between room air and solar cell temperature of BISPVT and BIOPVT system.

	With air duct at air mass flow rate of 0.85 kg/s				**Without air duct**			
	SPVT (Façade)	SPVT (Roof)	OPVT (Façade)	OPVT (Roof)	SPVT (Façade)	SPVT (Roof)	OPVT (Façade)	OPVT (Roof)
T_r(°C)	8.2	9.4	6.7	8.3	20.3	22.0	10.6	12.3
T_c(°C)	35.5	53.4	38.3	58.0	33.0	48.0	33.1	48.0

The performance analysis of a roof air opaque BIPVT system evaluated by one-dimensional transient model for different parallel and series combinations under the cold climatic conditions of India, was performed in reference [55]. The modelled system (Figure 33) is similar to that installed on the roof of the Centre for Sustainable Technology, Indian Institute of Science Bangalore, covering an area 65 m^2, producing a total of 7.2 kW_p and having an air duct at a constant flow rate of 1.2 kg/s. The results show that:

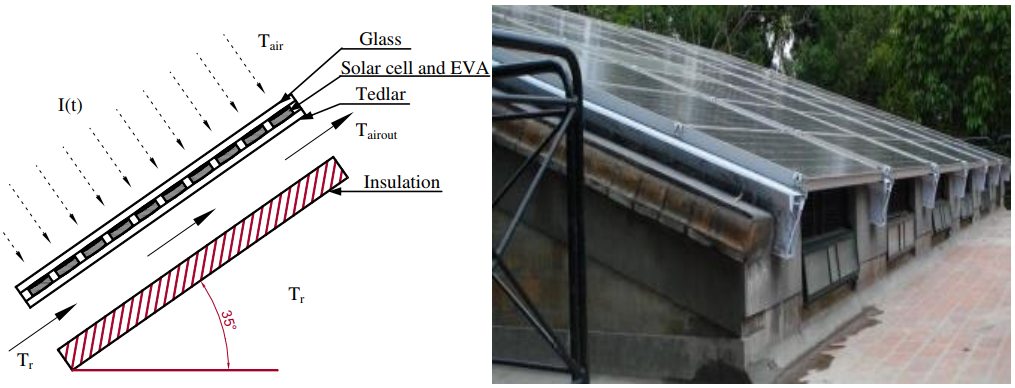

Figure 33. Cross-section of a roof BIPVT system (left) roof BIPVT at Sustainable Technology, Indian Institute of Science Bangalore, India (right) [55].

- for a constant mass flow rate of air, the system connected in series gives a better performance. In particular, BIPVT system provides a higher air room and outlet temperature, up to 8°C than the other combinations. This corresponds to a lower solar cells temperature, since the air flowing in the

duct has a higher velocity, by collecting a higher amount of heat. Therefore, the electric efficiency is higher in this case (up to 15.5%), by producing yearly an electric energy of 16,209 kWh, 371 kWh higher than the parallel combination and 1182 kWh higher than a similar BIPV system. The overall thermal efficiency is 53.7%, relatively higher than other combinations. The net thermal gain is 18,062 kWh, 4112 kWh higher than the parallel combination.

- for a constant velocity of air, the system connected in parallel gives a better performance. In particular, the higher air flow rate obtained, provides lower air outlet temperature as well as lower solar cells temperature, therefore, the electric efficiency is higher. The yearly electric production is 15,942 kWh, 170 kWh higher than the series combination and 916 kWh higher than a similar BIPV system. The overall thermal efficiency is 50%, relatively higher than the other combinations. The net thermal gain is 15,285 kW h, 3300 kWh higher than the series combination.

A study including a detailed dynamic Model Predictive Control (MPC), developed in TRNSYS, of 65 m^2 façade BIPVT collectors, was performed by Li et al. [56]. An open plan office space at Purdue's Living Laboratory is used as test-bed, in which the integrated system preheats ventilation air, while also, it is coupled to the building through an air-to-water heat pump and a Thermal Energy Storage (TES) tank that serves as the heat source for the Radiant Floor Heating (RFH). Energy saving potential evaluation of the innovative system, by considering a corrugated Unglazed Transpired Collector (UTC) with and without PV panels, is carried out (Figure 34). The PC is compared with baseline operation strategies, by using weather data of West Lafayette, In, during the heating period. The results show that predictive control for the optimal set-point temperature of the TES tank can reduce the electric energy consumption of the heat pump by 34.5%. Utilizing the configuration of UTCs with PV panels can result in 45.4% total energy saving compared to the baseline RFH, due to the electricity generation by the PV panels. Adding the TES tank and PC strategy to the regular RFH system can result in 10.8% energy saving of the heat pump electric energy cost, and when integrating the UTC plates to the system, the total energy saving is 17.4% comparing to regular RFH system.

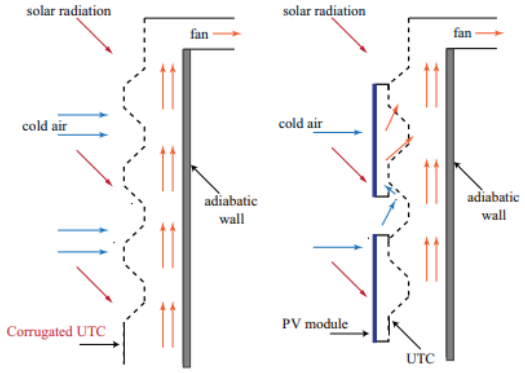

Figure 34. UTC without (left) and with (right) PV panels [56].

A simulation study aims to evaluate the building energy performance, as well as the electric and thermal performance of air façades BIPVT collectors was carried out by Kim et al. [57]. For this study, building models with BIPV (without ventilation channel) and BIPVT (with 10 cm ventilation channel, Figure 35) were compared through TRNSYS simulation results.

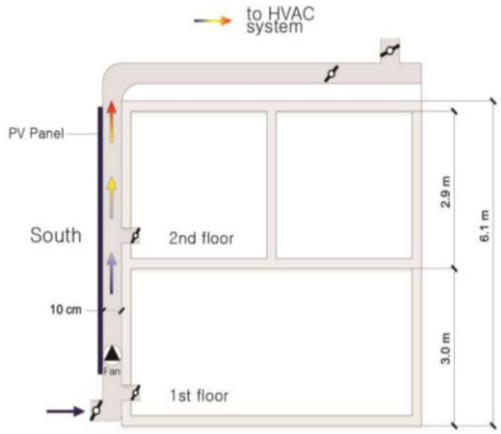

Figure 35. Building with air channel BIPVT system for simulation [57].

Systems are assumed to be located in Daejon, Republic of Korea and covering the south-facing façades of a two-storey office building with 129 m^2 of collectors. They concluded BIPVT system with outdoor ventilation is more advantageous from electricity production point of view (+6%), by avoiding the efficiency decrease, caused by the PV module temperature rise, observed in BIPV system without ventilation. Anyway, in this case the heating load is slightly increased (+1%) due to the external wall cooling, by forced inflow of cold outdoor air. Whereas, BIPV system can slightly reduce the heating load compared to the conventional building.

Shahsavar et al. [58] present a simulation work concerning the performance analysis of roof BIPVT collectors used for ventilation and electricity production in Kerman, Iran. BIPVT collectors operate in two different modes depending on the season. In summer, ambient air temperature is higher than indoor one, therefore, the exhausted air from the ventilation system goes outside through the air channels below the PV panels, thus cooling them down. This leads to an increase of the electricity production by 10.1% and electric performance by 7.2%. In the winter the incoming ventilation air temperature which is lower than indoor temperature, flows in the air channels of BIPVT collectors to be preheated before it enters the building. In this way, BIPVT collectors provide 10.2% of the ventilation air heating load.

The performance of an innovative multifunctional PVT Solar Window is analysed in reference [59]. Simulations results were calibrated against measurements on prototype solar windows placed in Lund University and into a single family-house in Sweden. Solar Window is on the inside of an anti-reflective (insulated) window with concentrating mobile reflector screens and provides electricity and heated water, besides passive space heating and daylighting. Simultaneously, the reflector screens act as sunshades and added internal insulation for the window. Simulation results shows that Solar Window annually produces about 35% more electric energy per unit area of PV cells compared to a flat PV module placed on a wall at a 90° tilt.

In the framework of simulation works, the combination of BIPVT collectors with solar driven cooling technologies has also gained an increasing attention in literature.

For example, a study concerning the evaluation of energy performance of façade BIPVT and BISTC, installed on “Pompeu Fabra” Library located in a Spanish warm and temperate weather zone (Mataro), is presented by Eicker et al [11]. Here, BIPVT collectors are used to preheat winter

cold air for heating purposes, whereas the heat obtained by the integrated solar thermal collectors is exploited to feed an adsorption chiller, balancing 93% of the building cooling demand, with an average COP equal to 0.5.

Results of a numerical investigation based on façades BIPVT collectors coupled to a DC-driven vapour compression refrigeration system and façades BI flat-plate STC for driving an absorption chiller, are compared with the results obtained by a system equipped by stand-alone solar collectors, conventionally installed on the roof of an office building located in Hong Kong [60]. TRNSYS simulation software is used for the analysis. They investigate the use of BISTSs as way to reduce the heat transfer across the external façades, thus lowering the peak cooling load requirement. Façades BISTSs resulted in a smaller solar fraction and a higher primary energy consumption. The solar primary energy gains decreased severely between 47 to 79% (Figure 36). BISTSs orientation was the major cause. With vertically aligned BISTSs, the solar incident angle was not optimal, especially during the midday when the sun was vertically above the building zone and that the solar radiation was normally the highest. The zone loads dropped by around 9% with the adoption of BISTSs due to their shading effects. This led to a reduction in the driving energy requirement. These benefits don't balance the negative effects of outputs reduction of BISTSs, therefore the total primary energy consumptions consequently increased by more than 7%.

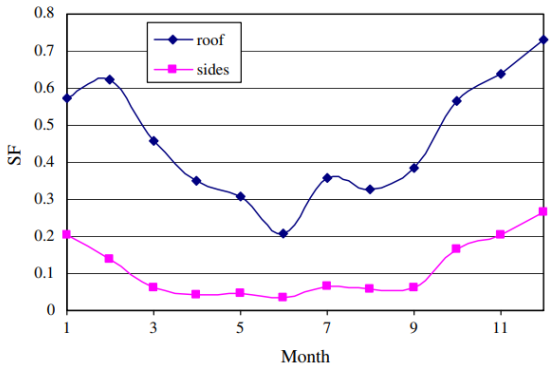

Figure 36. Variation of monthly-averaged SF of conventional system (on roof) and proposed system (façades BISTSs) [60].

A computational fluid dynamics model, experimentally validated, of a BIPVT collector was developed by Corbin and Zhai [61], to evaluate the effect of active heat recovery on cell efficiency and to determine the effectiveness of the device as a solar hot water heater. In particular, the model of a collector employing a liquid-cooled tube-fin absorber into the cavity, was simulated. The single row (7.3 m wide, 0.8 m deep, 20° tilted) of the collectors simulated in the model is shown in Figure 37. By this model, important correlations, useful for predicting the electrical efficiency of the collector under different operating conditions, between cell efficiency and absorber inlet temperatures at various insolation levels are created. Investigation of these correlations (Figure 38) reveals that i) an increase in insolation results in higher cell temperatures, so cell efficiency decreases; ii) the difference between fluid inlet temperature and ambient air temperature has a declining effect on efficiency as insolation decreases.

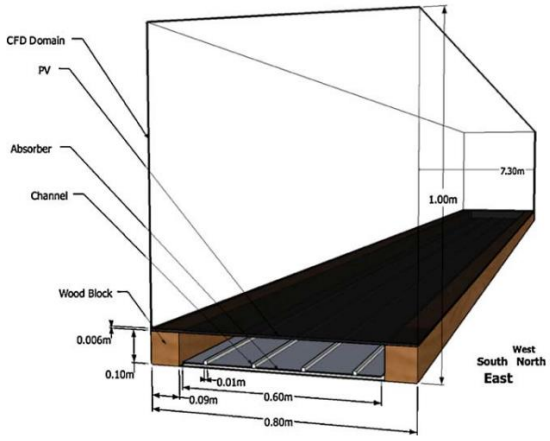

Figure 37. CFD simulation domain, objects and dimensions [61].

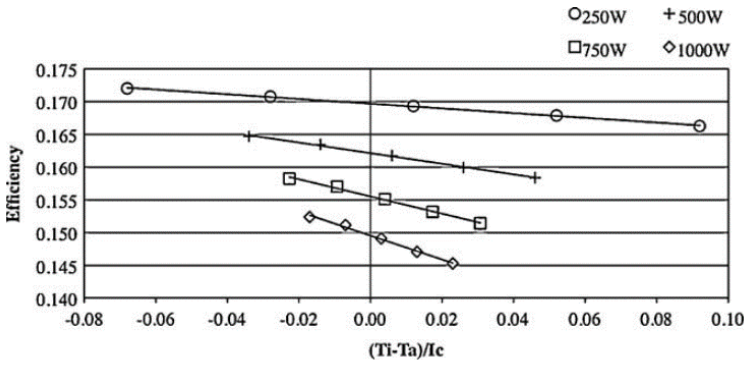

Figure 38. Electrical efficiency at varying inlet temperatures and insolation [61].

The carried out analysis indicates that the active heat recovery of the BIPVT collectors reaches electric efficiency up to 5.3% over a naturally ventilated BIPV roof, reducing the negative effects of integration into the building façade. The produced water temperatures are about 51.1°C and 57.4°C, depending on the ambient temperature, suitable for domestic hot water use and hydronic heating systems. Thermal and combined (thermal plus electrical) efficiencies reach 19% and 34.9%, respectively.

Several simulation works are available in literature regarding energy and exergy analyses of water PVT collectors [62-64] of BIPV systems [65, 66] and air BIPVT systems [67], whilst only a few studies deal with water BIPVT systems up to now. Exergy analysis is a useful tool, able to calculate the magnitude of the irreversibilities into a system, in order to propose a possible enhancement. This well-known methodology is used to determine a more efficient use of energy resources using the conservation of mass and of energy principles together with the second law of thermodynamics, for the design and analysis of energy systems [68]. In the following the recent works presenting energy and exergy analyses of air and water BIPVT collectors, are reported.

Vats and Tiwari [67] carried out an electric and thermal energy and exergy analysis of a BI Semi-transparent PVT system (BISPVT) for six types of PV modules (m-Si, p-Si, a-Si, CdTe, CIGS, and HIT). Climatic data for solar radiation, ambient temperature and number of clear days for weather zone of Srinagar (India) were adopted. The BISPVT system is located outside the room (3 m×1.81

m×4 m) and sealed from all the sides. Inlet and outlet vents are provided on the roof for the air flow (0.85 kg/s). When solar radiation falls on the PV module, it gets heated. The room air enters through inlet vent, takes the heat of PV module (5.44 m^2) and escapes through outlet vent. The hot air at outlet enters into the room and replaces the cooler room air. In this work, different packing factors (ratio of total area of PV cells to total area of PV module) like 0.42, 0.62 and 0.83 were considered. Their results show that the difference in building room hourly temperature, calculated for all six PV modules is marginal and that the PV module with 0.42 packing factor produces low amount of electric energy as compared to 0.62 and 0.83. For this last result, the exergy analysis was carried out only for 0.62 and 0.83 packing factors, by achieving that the annual overall exergy is maximum for HIT, 834 kWh, and minimum for a-Si, 334 kWh, for packing factor equal to 0.62, Figure 39.

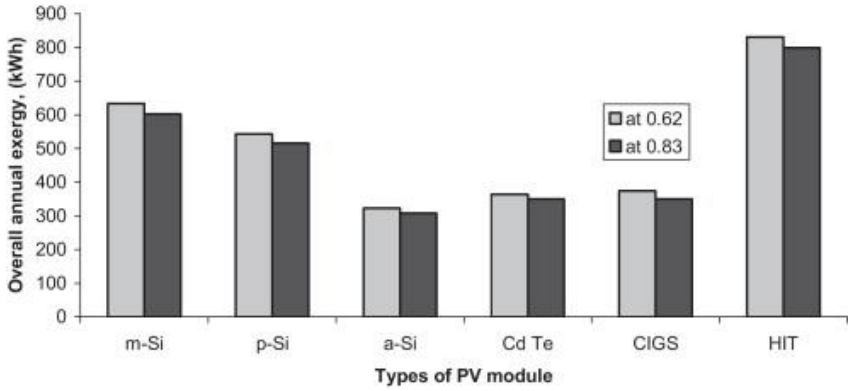

Figure 39. Overall annual exergy for different PV modules for 0.62 and 0.83 packing factor [67].

Dubey et al. [69] analysed energy and exergy of PVT air collectors connected in series and integrated within the south façade of a room, by a thermal model using the weather data of solar radiation for five different cities (New Delhi, Bangalore, Mumbai, Srinagar, and Jodhpur) of India. The analysis was performed for air circulated in forced mode by considering the two different cases with, namely, Case I (collector fully covered by PV module (glass to glass) and air flows above the absorber plate) and Case II (collector fully covered by PV module (glass to glass) and air flows below the absorber plate), Figure 40. It is found that the air flows below the absorber plate of collectors, fully covered by PV module (Case II), give better results in terms of hot air production and electricity generation simultaneously. Therefore, the exergy analysis, as well as the energy one, by comparing the five different cities, was carried out for this case and for four collectors connected in series at constant air velocity of 0.5 m/s. The detailed analysis shows that the maximum annual exergy gain, higher than 800 kWh/year, is obtained for the Jodhpur city, the best place for installation of such type of system.

Agrawal and Tiwari [70] developed a thermodynamic model of air roof integrated PVT collectors to calculate energy, exergy and life cycle cost of system in order to compared it with a similar model of BIPV panels. The hourly climatic conditions of New Delhi are used. Different PV technologies are compared: (i) monocrystalline Silicon (m-Si), (ii) polycrystalline Silicon (p-Si), (iii) edge-defined film-fed growth ribbon crystalline Silicon (r-Si), (iv) amorphous Silicon (a-Si), (v) Cadmium Telluride (CdTe) and (vi) Copper Indium Gallium diSelenide (CIGS). The m-Si

silicon BIPVT systems show higher energy and exergy efficiencies (17–20% and 1.5-2%, respectively) than BIPV system, due to the cooling of BIPVT solar cells, which helps in producing higher electric energy. On the other hand, the amorphous silicon BIPVT system is found to be more economical and its energy and exergy efficiencies are found to be 33.54% and 7.13%, respectively.

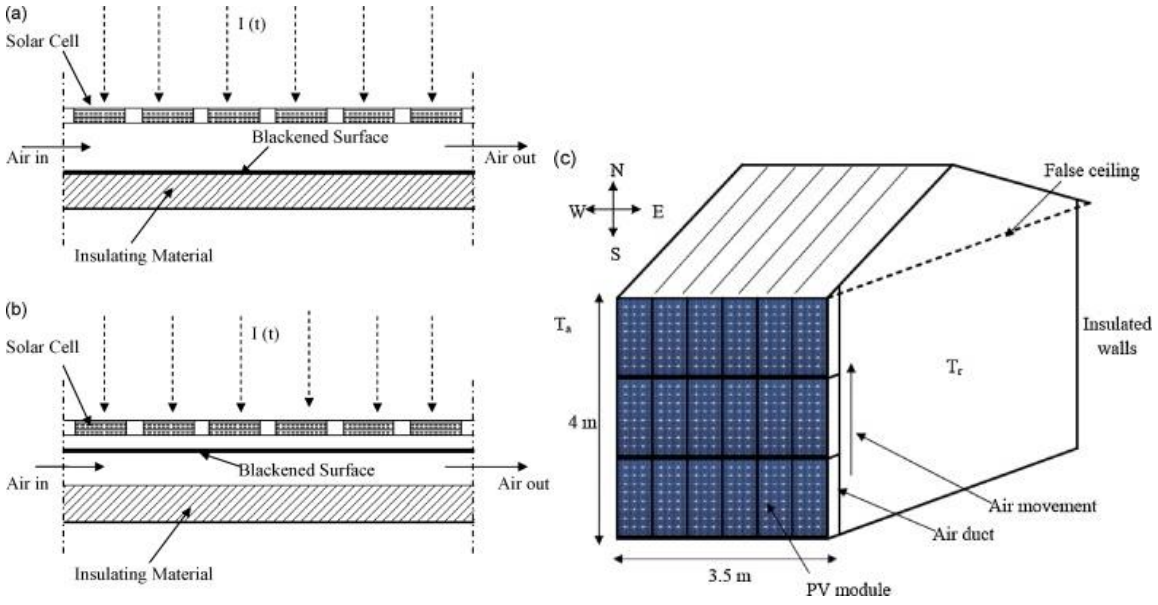

Figure 40. (a) (Case I), (b) (Case II), (c) Schematic diagram of PV integrated room [69].

Agrawal and Tiwari [71] compared four different parallel and series system configurations (Figure 41), by developing an one-dimensional transient model, of air roof integrated PVT collectors for cold climatic conditions.

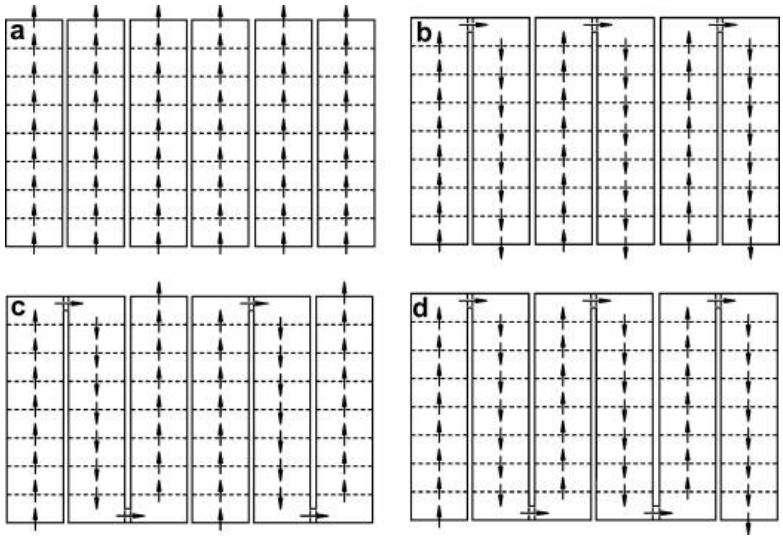

Figure 41. (a) Case 1 – all rows of BIPVT system are connected in parallel. (b) Case 2 – three rows of BIPVT system are connected in parallel each having two rows in series. (c) Case 3 – two rows of BIPVT systems are connected in parallel each having three rows in series. (d) Case 4 – all the rows of BIPVT systems are connected in series [71].

The solar radiation and climatic condition data of Srinagar city was considered. PV performances, net energy gain and exergy of the building are determined. They concluded that for

a constant mass flow rate of air, the series combination produces the maximum air outlet temperature and in turn it provides a higher room temperature. In this case, annual electric and thermal exergies of 16209 kWh and 1531 kWh, with an average overall thermal efficiency of 53.7% are obtained. The net exergy output is up to 975 kWh higher than any other combination of the BIPVT systems and up to 2713 kW h higher than a BIPV system.

Wu et al. [72] proposed and described a BI heat pipe PVT collector isothermally absorbing the excess heat from solar PV cells. The system was analysed by a theoretical model in terms of heat transfer process analysis in PV module panel and introducing the effectiveness–Number of Transfer Unit (ε–NTU) method in heat exchanger design. The scheme of this collector is reported in Figure 42. Solar PV modules absorb solar energy and transform it into electricity, but simultaneously PV panel is also heated and most of the energy is transferred by conduction to the high thermal conductivity material between PV panel and wick heat pipe evaporator section. Inside the wick heat pipe, the liquid medium is vaporized and the generated vapor moves toward the wick heat pipe condenser section, where it gives out the evaporation latent heat. The resulting liquid is returned to the evaporator passively by gravity and/or capillary forces in distributed wick and re-absorbs heat for repeating evaporation. In the meantime, the cooling (heated) fluid flows into the cooling (heated) fluid channel through cooling (heated) fluid inlet header and pipe, absorbing the heat released from the wick heat pipe condenser section by forced convection, and finally flows out through the cooling (heated) fluid outlet header and pipe when the outflow reaches a certain temperature. By the developed model, they evaluated the overall thermal, electric and exergy efficiencies of heat pipe PVT system, equal to 63.65, 8.45 and 10.26%, respectively. The varying range of operating temperature for solar cell on the solar PV panel is less than 2.5°C

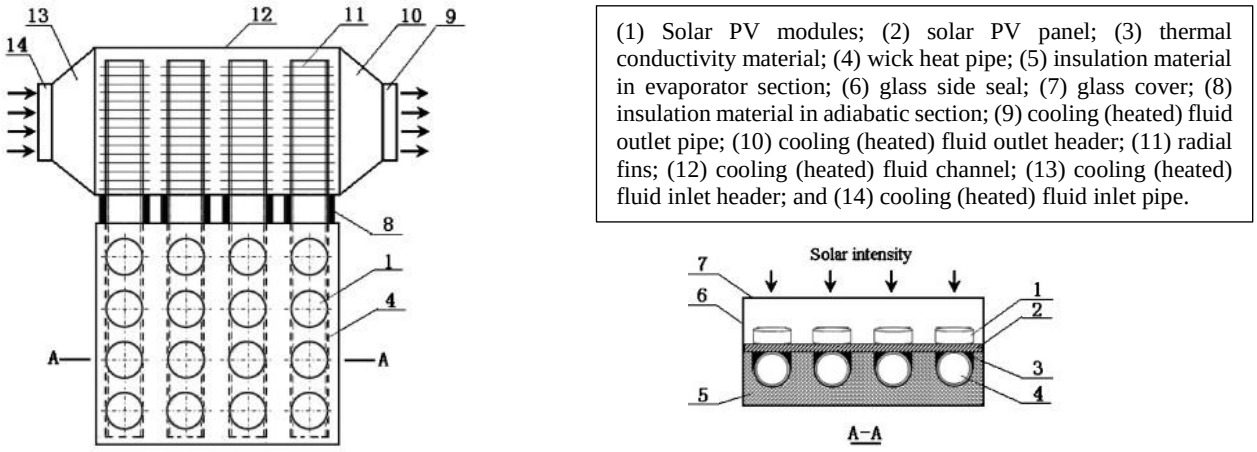

Figure 42. Scheme of wick heat pipe PVT hybrid system

The setup experimental of novel BIPVT system presented in reference [26] was analysed by numerical model allowing one to perform the energy, economic and exergy evaluation in reference [73] by Buker et al. The main result obtained from exergy point of view is that the polyethylene heat exchanger underneath PV modules enhances PV cell efficiency by increasing also the system exergy efficiency (Figure 43), with respect to the system without the polyethylene heat exchanger.

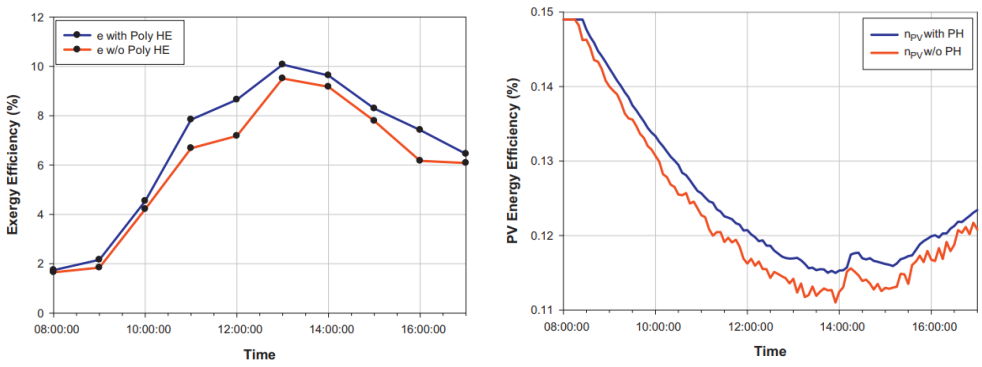

Figure 43. Effect of poly HE on PV exergy and PV energy efficiency (right) [73].

Sohel et al. [74] developed a dynamic model for simulating real operating conditions of air-based PVT systems, validated by using the operational data of BIPVT systems installed in two unique buildings (the net-zero energy Solar Decathlon (SD) house and the net-zero energy office building at the University of Wollongong, Australia). The energy and exergy performance are evaluated. They show that as the ambient temperature increases from −20 to 50°C, the heat loss to the ambient reduces and consequently both thermal and 1st law efficiencies increase (Figure 44). However, as the ambient temperature increases the usefulness of available heat decreases. Consequently, the second law efficiency decreases, as well as PVT electric efficiency. This is an expected result, also considering the additional heat generated from the PVT during the summer.

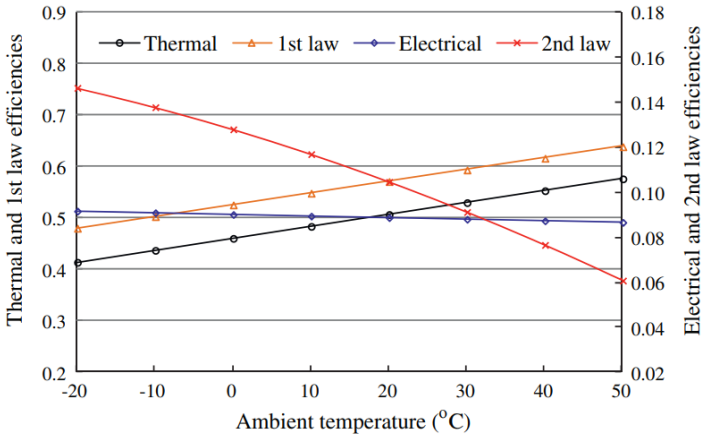

Figure 44. Efficiency vs. ambient temperature [74].

This analysis demonstrates the effectiveness of the second law analysis. In fact, the first law efficiency shows that, during the summer, more heat is available, and the second law efficiency provides the information on the usefulness of the heat: although more heat generated from the PVT during the summer, this heat is less useful.

2.3.3 The state of the art of the BIPVT collectors: analysis

Although the large number of BIPVT experimental prototypes focused on experimental studies, the available literature highlights a lack of knowledge regarding the assessment of the passive effects (summer unwanted overheating and winter useful heating) on the building energy demands due to the building integration of such devices. In particular, the majority of such studies is only focused

on several thermal and electrical aspects of the BIPVT collector without analysing the whole building-BIPVT collector system, and therefore, without considering the heat transfer between both systems (building and PVT collectors).

Because in this thesis a detailed approach based on the dynamic simulations was developed, a comprehensive critical analysis of the literature studies regarding the state of the art presented at subsection 2.3.2, will be better provided.

It resulted, from a numerical point of view, that simulations, carried out through several commercial and suitably developed dynamic simulation models, were widely adopted in many literature studies concerning building integrated solar systems, but few studies are focused on BIPVT collectors and these:

- evaluate the thermal and electric features of the BIPVT collector, as single unit, by disregarding the whole building-plant system
- often specified and quantified the thermal and electric outputs of the BIPVT collector as occurs for the stand-alone conventional configurations of the PVT collectors, without taking into account how these could be affected (positively or negatively) by a building integrated configuration;
- analyse only the active effects of the BIPVT collectors, (i.e. production of heat and electricity) neglecting the passive ones;
- neglect the effects of the integrated configuration on the exergy of the BIPVT collectors and their exergy efficiency;
- do not take into account the electricity grid conditions of the building-BIPVT- system and neither include the use of storage energy systems in the form of conventional batteries;
- do not take into account the solar heating and cooling systems coupled to the BIPVT collectors, including suitable management strategies;
- are not always focused on BIPVT collectors with water as heat transfer fluid, although for residential applications, the most common application of BIPVT collector could be the water cooled one, due to the possibility to utilize the obtained thermal energy for DHW preparation [61];
- do not always evaluate the energy, exergy, economic and environmental performances of the whole building-plant system;
- do not emphasize the function of the BIPVT collectors as polygeneration systems;
- do not adopt the approach based on the dynamic simulations for the performances evaluation of the whole building-plant system.

Thus, as highlighted for the experimental studies, very few numerical studies assessed the passive effects and the performances of BIPVT collectors, by considering the heat transfer mechanism for the whole building-plant system. About this significant issue, examples are the works reported in references [47, 56]. In order to fill the above-mentioned lack of literature, in this thesis these aspects are investigated and the results of these analyses, coupled to interesting design guidelines and swift feasible considerations, will be presented in the subsection 4.1.

Chapter 3 Polygeneration

In the last years, the international energy consumption is considerably increased, principally due to the economic growth of developing countries. A significant issue regards the environmental impact and availability of the fossil or non-renewable fuels, which today satisfy the mostly of the worldwide energy demand. At the same time, the demand, as well as the consumption of potable water is also significantly increasing. Therefore, some noteworthy actions were taken in order to head towards a sustainable development, as enhancing the systems energetic performance, using renewable energy sources, by reducing the consumption and the environmental impact of energy-related technologies [75]. In this framework, polygeneration systems represent one of the most attractive and innovative concepts for the multi-generation of various energy vectors (power, heat, cooling) and other products (hydrogen, syngas, biodiesel, fertilizers, drinking water, etc.), by converting one or multiple energy sources. These systems became particularly interesting if coupled to the renewable energy sources (geothermal, solar, biomass, wind, hydro), by obtaining high energy efficiency and environmental compatibility. Although these positive aspects, the concept of polygeneration is still scarcely used. In fact, averagely, the global power generation is only obtained for 10% by means polygeneration systems. Exceptions are the countries as The Netherlands, Finland and Denmark, where this ration is also up to 30%–50%. Presently, many European Union countries are encouraging the development of sustainable and efficient systems based on polygeneration, since it is recognised as a strategic technology able to reduce the greenhouse gas emission at the target values. The same strategy is adopted also by USA with the aim at cutting down the costs of energy production, mainly in the industrial sector.

In order to pursue the integration of polygeneration, industries and academic institutions are presently carrying out a noteworthy research effort, for developing and designing plants based on the use of both renewable and fossil energy sources. In addition, it is also important observing that polygeneration plants are more and more interesting mainly when they are involved to coproduce potable water along with power, heat and cool. This is a very attractive arrangement, particularly for remote and inaccessible communities where a sole optimized plant can be adopted to provide, at the same time, all the energy vectors and fresh water [76]. An example of this application are the islands, where the fossil fuels availability and potable water is particularly limited, whereas they are frequently featured by a high presence of renewable sources (geothermal, solar, biomass and wind) and, obviously, very close to the sea [77].

This section aims at presenting the current works concerning the polygeneration systems simulation, by specially focusing on the potential integration of different technologies into a single system. The number of possible polygeneration layouts is virtually infinite since it is possible to combine all the available fossil and renewable conversion technologies. This concept is clearly depicted in Figure 45.

In particular, the presented review regards the simulation of polygeneration systems analysed in literature and was developed by considering:

i) the several energy inputs to the polygeneration systems, by including both fossil and renewable energy;

ii) the conversion technologies in polygeneration systems (gas turbine, steam turbine, combined cycle, ORC, internal combustion engine, FC);
iii) the energy (power, heating, cooling, etc.) and material outputs (liquid and gaseous fuels, desalinated water, etc.) of polygeneration systems.

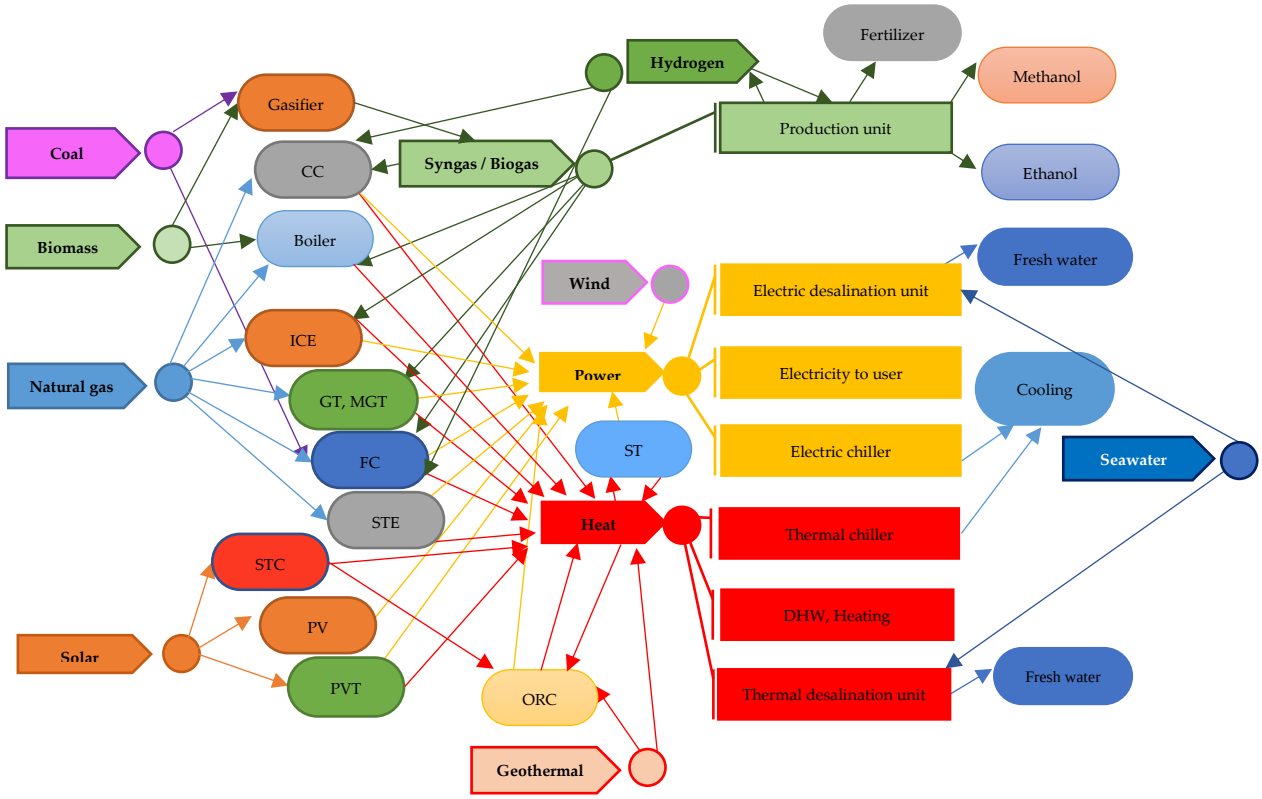

Figure 45. Possible combinations of fossil and renewable technologies in polygeneration.

In the below presented review concerns the simulation of polygeneration systems, dozens of works carried out studies based on dynamic simulations [16, 25, 77-79] and others on steady simulations [80-86]. In particular, the works implementing the dynamic approach investigated several topologies of polygeneration systems, supplied both from fossil fuels and by renewable energy sources for the coproduction of desalinated water, heating, cooling, electricity, H_2, syngas or others. The methodology based on dynamic simulations, presents a multiplicity of positive effects, regarding to the possibility to expect the real time-dependent system operation. This allows one to also enhance the polygeneration systems performance and, therefore, to optimize its design. Therefore, the application of this approach to polygeneration systems is very attractive for the potential enhancement of its energetic and economic performance indexes.

3.1 Inputs to polygeneration systems

Polygeneration systems are fuelled by fossil and renewable energy sources but in many cases, these are also fuelled by a mix of different sources. The selection of the determined input depends on mainly the conversion technology, the source availability, its localization, the cost and on the outputs to be produced. In the next subsections, some of the literature works concerning the simulation of polygeneration systems fuelled by fossil fuels, renewable energy sources and by hybrid energy inputs are reported.

3.1.1 Fossil energy inputs

Several works investigating the simulation of polygeneration plants driven by fossil energy fuels (H_2, coal, natural gas, etc.) are performed in literature [87-90] and, therefore, numerous possible configurations of polygeneration systems can be developed. Coal and natural gas, along with oil fuels represent the 80% of global energy demand due to their affordability and availability [91]. In the followings, some of the most relevant works available in literature, concerning their application in polygeneration systems, are summarised.

Coal

The clean and efficient use of coal is one of the most significant aims of the worldwide research. In the last years, in order to maximize energy utilization efficiency and achieve a near-zero level pollutant emission, several advanced coal gasification technologies were developed. An example is the coal partial gasification technology analysed in the work presented by Li et al. [92], where the thermodynamic analysis of this process in a polygeneration system for the methanol and power generation, is carried out. The commercial software Aspen Plus was used to perform the system simulation. In contrast to traditional coal gasification technologies featured by total gasification of coal through simple or rough oxidization, partial gasification technology, based on pressurized circulating fluidized bed controls the quantities of oxygen agent and detention time during gasification, by achieving, relatively higher cold gas efficiency (up to 65.5%). The investigated system layout is reported in Figure 46. Here, the syngas from the partial gasifier is synthesized to methanol, whereas the unreacted gas enters gas turbine combined cycle to produce power. The system shows an energy and exergy efficiency equal to 51.16% and 50.58%.

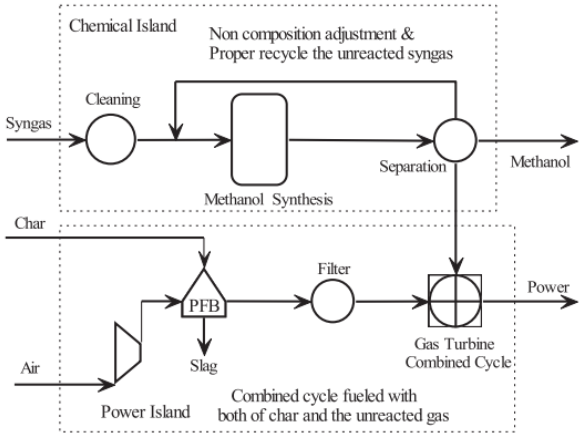

Figure 46. Schematic of a polygeneration system based on partial gasification [92].

Another novel coal gasification technology, aiming at separating CO_2 emissions during combustion process without extra or with few energies required, is based on the concept of chemical looping combustion. This process is simulated in the polygeneration system investigated by Fan et al. [93]. In this system, the combustion flue gases from both air reactor and fuel reactor are sequentially fed into gas turbines for electricity production; here a heat recovery vapour generator unit for further electricity generation with driving an absorption chiller (ACH) in summer and a heat exchanger for daily heat water production is also simulated. This novel system maintains a

maximum energy efficiency of 60.34%, whereas the fossil energy saving ratio of this process of 27.20%.

Utilizing captured CO_2 for utility outputs in coal-based polygeneration has twofold advantages: eliminating the subsequent cost of CO_2 sequestration and earning additional revenue from utility products using. In the work developed by Bose et al. [94], the performance assessment of a coal-based polygeneration for power with CO_2 capture and subsequent use of this captured CO_2 for production of a common fertilizer, i.e., urea is proposed. In particular, the syngas produced by gasification, is treated with steam in a water gas shift reactor, after that CO_2 is captured. Produced hydrogen is partially utilized for power generation in a combined cycle gas turbine and for urea production. A detailed ASPEN Plus model is developed for this plant. It resulted that, the higher the percentage of captured CO_2 used, the higher the production of urea, but a simultaneous decrease of net power output is achieved as both depend on amount of hydrogen of syngas used for these processes.

The majority of polygeneration energy systems analysed in literature involving coal gasification, use a single gas source and produce only a unique type of chemical product. Conversely, in the study reported by Li et al. [95] a dual-gas source polygeneration process which uses, besides syngas from coal gasification, coke oven gas as gas sources and co-produces dimethyl ether, methanol and dimethyl carbonate via an integrated catalytic synthesis procedure. The system performance is calculated by numerical simulations, based on detailed chemical kinetics which shows the system feasibility, whereas the carried out exergoeconomic analysis, reported the exergy loss and the production cost of product in each functional block of the process.

Natural gas

Over the past few years, combined cooling heating and power (CCHP) system fuelled by natural gas has been receiving increasing attention [96]. In particular, liquefied natural gas (LNG) is recognized as preferred fuel in many countries [91], mainly because LNG is the cleanest form of natural gas. Therefore, LNG CCHP systems were recognized as a potential energy system option for sustainable development and low-carbon society.

An example of this system was investigated by Li et al. [97], for hotels, offices and residential buildings by an energetic, economic and environmental analysis. In the proposed polygeneration system, two prime movers are taken into account: a gas turbine and a gas engine. The produced heat is recovered to meet the thermal demands through the thermal exchanger and the cooling load through the ACH. Such system was compared to a reference system, where the space heating and cooling are produced by a boiler and electric chiller. The resulted biggest economic merits are received in offices, 39.21%, driven by gas turbine and 52.83% driven by gas engine. The biggest reduction of emissions and energy consumption are received in hotels, with a maximum value equal to 60.65% and 42.28%, respectively.

The concept of chemical looping combustion and gasification investigated in [93], is also included in a new polygeneration system simulated by Salkuyeh and Adams [80]. The simplified layout of the chemical looping gasification is reported in Figure 47. With respect to the previous work using coal, here natural gas and petroleum coke are used as input fuels and different products

such as chemicals, olefins, electricity and transportation fuels are coproduced. All process unit operation models were simulated in Aspen Plus 2006.5 simulation software, except for the gas turbines for which a custom model in VBA (Visual Basic for Applications) was linked into the Aspen simulation model instead. The system is not only able to capture 100% of CO_2 emissions, but also can be an incentive for those producers to convert stockpiled petroleum coke to more valuable products.

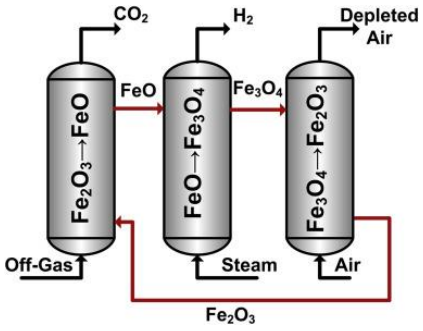

Figure 47. Simplified schematic of the chemical looping gasification system [80].

An innovative polygeneration system fuelled by natural gas for the production of methanol and electricity is investigated by Gao et al. [98]. The novelty regards the integration of partial-reforming and partial-recycle scheme (Figure 48) in methanol synthesis which contribute to enhance the system performance (energetic and exergy) with respect to the one of full reforming and without recycle, assumed as reference system. In particular, in this new layout, only a part of natural gas entering the reformer will be converted into syngas, which will be cooled by heat recovery unit, and before will be sent to the methanol synthesis process. Here a partial-recycling operation is adopted, which expects that the unreacted syngas is recycled back to the synthesis reactor, and a part will be fed to the power generation subsystem as fuel, and the rest part will be burnt with the GT exhaust gas to cover the heat demand for the reforming process.

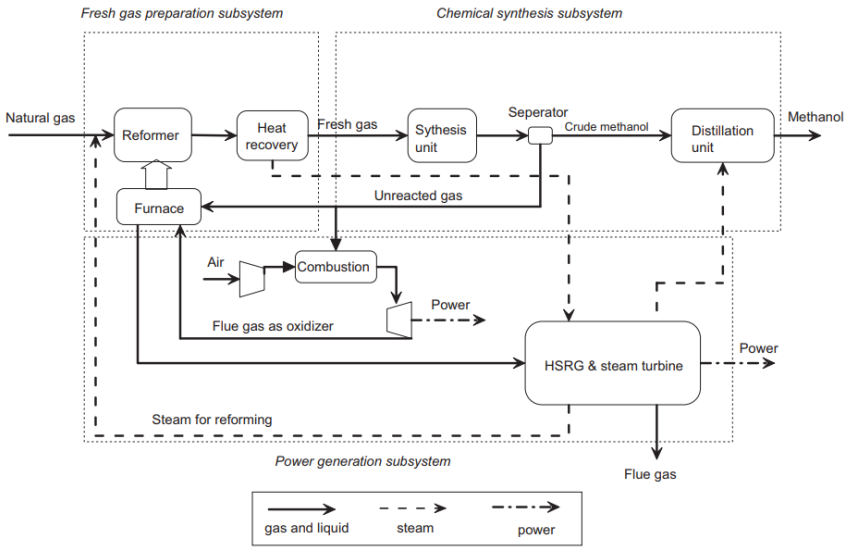

Figure 48. Flow sheet of part reforming and part cycling (PR/PC) system [98].

The system simulations were carried out by using ASPEN PLUS steady state simulation software. In this work, the energy saving ratio is used to assess the polygeneration system energy and exergy performance. The energetic results are summarised in Table 3. The reference system has rather bad performance with respect to the innovative one which also able to reduce about 6% of energy consumption compared with the single product systems.

Table 3. Performance comparison between systems

System	Reference	Innovative
Fuel consumption (LHV, kW)	315951	
Net work (kW)	69753	81350
Methanol production, M (kg/h)	21211	21034
Relative energy saving ratio (%)	-0.2	5.8
Exergy efficiency	61.02	64.14

In the work of Calise et al. [88], a trigeneration system consisted of a natural gas fired reciprocating engine and an ACH, producing DHW, space heating / cooling and electricity for a real hospital building was simulated and modelled in TRSNSYS environment. Three different operating strategies were compared in order to reduce the capital cost and maximize the performance of whole plant. The investigated operating strategies were: the Thermal Load Tracking strategy (TLT) - the engine partializes to follow the thermal demand, by adopting a proportional controller; the Maximum Power Thermal Load Tracking strategy (MPTLT) - the engine does not partialize and it works always at maximum power, by adopting an On/Off hysteresis controller; the Electricity Load Tracking strategy (ELT) - the engine partializes to follow the electric request. From the carried out simulations, it resulted that the best strategy from the energetic point of view is the ELT one with the higher electric production equal to 1203 MWh/year, but the worst value of the thermal efficiency (equal to 38.9%) and global efficiency (equal to 75.6% vs 89.9% for TLT strategy and 90.3% for MPTLT strategy). The PES values for the TLT, MPTLT and ELT strategies were respectively: 23, 24 and 14%. ELT strategy is the best also for the achieved economic results being the SPB values for the ELT, MPTLT and TLT strategies respectively 4, 4.2 and 4.4 years. After the comparison of three strategies, in this work, an optimization, by the TRNEdit tool of TRSNSYS and computer Design of Experiment (DoE), selecting as objective functions the SPB and PES, for the ELT strategy (the best one) was also carried out. From the optimization results it was found out that the lowest SPB value is equal to 3.9 years and the highest PES value is 20.6%.

3.1.2 Renewable energy inputs

During the past few years, renewable energy sources represented an attractive alternative with respect to the conventional systems fuelled by fossil fuels, since their application allows one to prevent the well-known undesirable effects such as global warming, emissions of pollutants, fossil fuel depletion, etc. [99] and to promote a "sustainable" development considering the limited availability of natural resources [100]. Dozens of papers available in the open literature investigated polygeneration systems supplied by renewable energy sources (biomass, geothermal, solar, wind, hydro etc.) and, therefore, also in this case, a wide number of different system layouts can be designed. The present section provides an overview of those systems classified on the basis of the used renewable energy inputs.

Biomass

In many cases, biomass-based polygeneration systems use cheap biomass as fuels. Biomass is especially promising in such systems by allowing one to produce a plurality of by-products, along with the conventional energy vectors (electricity, cool and heat). In addition, the possibility to fuel such polygeneration systems by agricultural wastes is extremely promising, since many of these have good potential to be energy resource [101].

An example of this configuration is presented by Jana and De [81, 102]. They used rice straw, sugarcane bagasse and coconut fibre dust. The polygeneration system (Figure 49) is designed as follows: in a fluidized bed gasifier, the agricultural waste is gasified in syngas, which cleaned, cooled and compressed is utilized for power generation in a combined cycle. An ACH is supplied by the heat generated in syngas cooler, whereas an ethanol production unit is supplied by a fraction of the whole generated syngas.

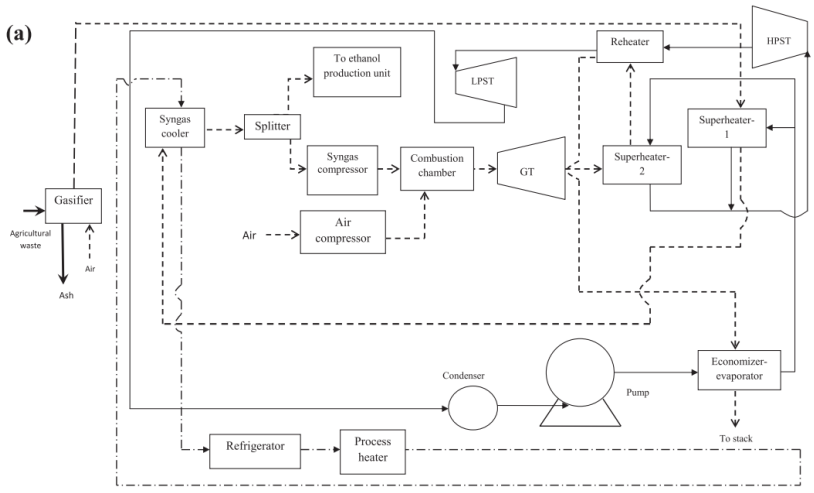

Figure 49. Schematic of the polygeneration process [81].

The whole system was modelled in Aspen and a detailed economic analysis was also developed. In Figure 50, a comparison of net power produced for three different agricultural wastes are shown.

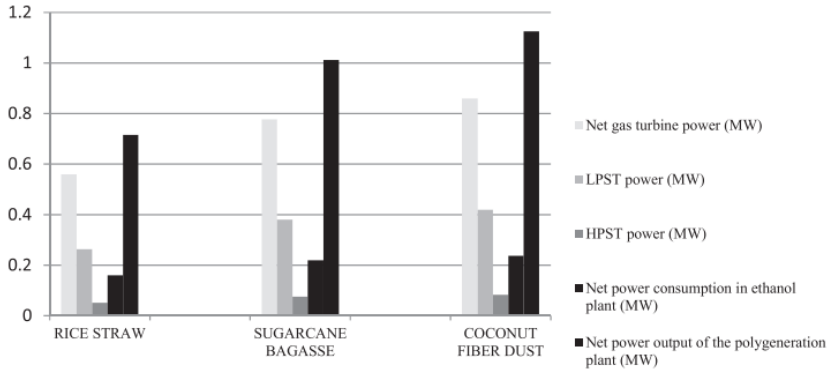

Figure 50. Power outputs for different agricultural wastes per t/year [81].

Power output is contributed mostly by the gas turbine plant, then, by the low pressure steam turbine and the rest by the high pressure steam turbine. It is noted that net power output for coconut

fibre dust is the maximum, and then for sugarcane bagasse followed by that for rice straw. The results of the economic analysis showed that the proposed system is very interesting, specifically for rural communities, by achieving a payback period just above 5 years, when the rice straw biomass is taken into account. The same system layout displayed in Figure 49 was again proposed by the authors to evaluate the system performance from the techno-economic point of view, by focusing only on rice straw energy source [103]. Here, the carried out analysis is specific for a district in the state of West Bengal of India. Results show that the polygeneration plant using rice straw as energy resource is a feasible option in energy services for developing countries like India. In fact, the estimated payback period of the plant is 4.76 years. The return on investment (ROI) is 15.5% and the net present value is 97 million USD.

Based on the results of the carried out simulations in the previous work, a Life cycle analysis (LCA) was developed in reference [104], where the environmental impact of this polygeneration plant is discussed. Here, the polygeneration system is compared with stand-alone conventional plants with same utilities. This study helps to estimate the life cycle emission, specifically greenhouse gas emission of this plant. Exergy based allocation method is used for this analysis. Results indicate that global warming potential of the standalone generations of same utilities in conventional ways is 100 times more than corresponding straw based polygeneration. Logistics of biomass cause maximum environmental impacts out of the unit processes of the polygeneration. It shares almost 50% of the global warming potential and the acidification potential of this polygeneration.

A technoeconomic model of biofuel fired trigeneration systems equipped with electric and thermal energy storages for remote households was simulated by Huang et al. [105]. In particular, in this study wood pellets and willow chips are chosen to supply a Stirling engine and to evaluate the internal combustion engine (ICE) performance, biodiesel is also selected (Figure 51).

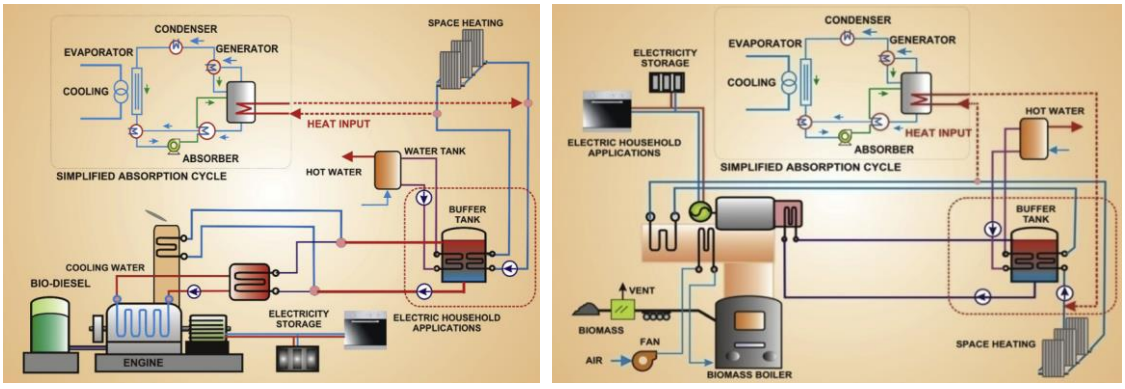

Figure 51. Schematic diagram of trigeneration system, ICE (left) and Stirling engine (right) [105].

In addition to the power and heat production, a thermally-driven chiller which produces cooling energy is also included. The ECLIPSE process simulation package, successfully used to analyse a wide range of energy conversion systems, such as coal fired power plants and biomass energy systems, was adopted to perform the simulations. In Table 4, some of the main energy results of simulations are reported. From the economic point of view, calculations showed that the economic feasibility of this type of plant, evaluated by the breakeven electricity selling price (BESP) is affected on the renewable energy incentive schemes (Renewable Heat Incentive (RHI), for 7 years

at a rate of 12.2 p/kWh. and Feed-In Tariffs (FITs) for 10 years at a rate of 13.2 p/kWh.). If the plant obtains both incentives, the BESP for wood pellets, willow chips and biodiesel are 216, 169 and 310 £/MWh, respectively.

Table 4. Technical results.

Feedstock	Wood pellets	Willow chips	Bio-diesel
Electric output, kW_e (Net)	3.2	3.2	5.2
Overall electricity efficiency, %	19.3	18.8	30
Heat output, kW_{th} (maximum)	10.9	11.1	7.6
Cooling output, kW_{th}	4.4	4.5	2.2
Overall CHP efficiency, %	84.3	82.4	74.6
Overall trigeneration efficiency, %	66.9	65.4	64.1
CO_2 emissions, g/kWh (CHP)	409	413	433
Reduction in CO_2 emissions, t/year	8.7	8.9	6.1

Technoeconomic performances of biomass (sawdust) direct chemical looping conversion for hydrogen and power coproduction are evaluated in [106]. For the rated sizes of components included into analysed polygeneration plant, a net power output of about 400–50 MW and a flexible hydrogen output in the range of 0 to 200 MW_{th} were taken into account. CC is adopted as prime mover. ChemCAD software is used to model and simulate the several investigated plant configurations, including layouts with biomass and/or coal gasification, with and without carbon capture and biomass direct chemical looping. Authors state that the reason to use coal and biomass is due to the fact that currently there are no industrial size gasifiers able to process only biomass. For these gasifiers, biomass ratio can be up to 30% from total fuel input. Results regarding power and hydrogen production reached for biomass direct chemical looping case are summarised in Table 5.

Table 5. Energy results of biomass chemical looping case.

Main plant data	Units	Power only	Hydrogen and power co-generation	
Sawdust flow rate	t/h		268.6	
Gross electric power output	MW_e	558.19	500.31	441.52
Hydrogen output — LHV	MW_{th}	0	100	200
Gross electric efficiency	%	46.59	41.76	36.85
Hydrogen efficiency	%	0	8.34	16.69
Carbon capture rate	%	99.6	99.6	99.6

From the economic point of view, it resulted that the biomass direct chemical looping has a reduced carbon capture capital cost penalty than the gas–liquid absorption carbon capture case (7% points lower specific investment cost).

A further sector where the concept of polygeneration was often adopted concerns the coproduction of power and fuels via bioorganic wastes. An example of this application is the work reported in reference [107]. Here the multi-generation of different fuels such as DME, methanol, ethanol, FT fuels, fertilizers and biogas from biomass wastes is investigated. The layout of this production process is depicted in Figure 52 and it is based on anaerobic digestion and dry reforming processes. In particular, accurate models for production of biogas are written in order to compute the optimal mixture of biomass wastes between cattle and pig slurry, cattle and pig manure, sludge, urban food waste and urban green waste to be digested to obtain the required biogas. The models

are written in GAMS® and in order to identify the optimal solution, corresponding to the optimal mixture which maximize the amount of methane, CONOPT tool was used. It resulted that for a syngas optimal production, achieved by biogas dry reforming, a mixture of biogas consisting of 50% CH_4, and 48% CO_2 is the most appropriate.

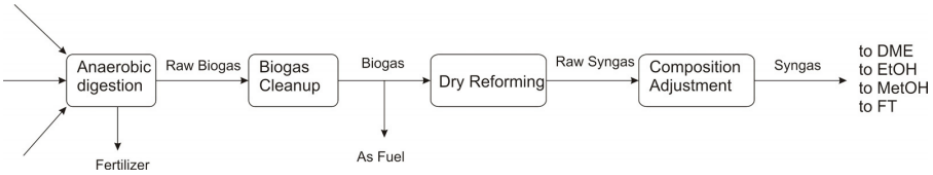

Figure 52. Scheme of biomass waste processing to fuels and chemicals [107].

When the biogas is intended as fuel, a 70% methane content is targeted. In addition, they state that if the aim is obtaining the most typical fertilizer composition, 65% of cattle slurry and 35% urban food waste is the optimal blend.

Solar

Several papers also investigated the integration of polygeneration systems with solar thermal collectors and PV panels. In fact, in polygeneration plants fuelled by solar energy, solar technologies can convert the solar incident irradiation in thermal energy used for solar power plant in case of medium or high temperature heat production or, conversely, for space heating or DHW (by STC), in electricity (by PV) and in cooling energy, by thermally driven chillers or electric vapour compression chillers.

In this framework, an interesting work is reported in reference [78], where a solar trigeneration system, based on sheet and tube PVT solar collectors, a single-stage LiBr/H_2O ACH, storage tanks and auxiliary heaters (Figure 53), is dynamically simulated by means of a dynamic simulation model, developed with TRNSYS.

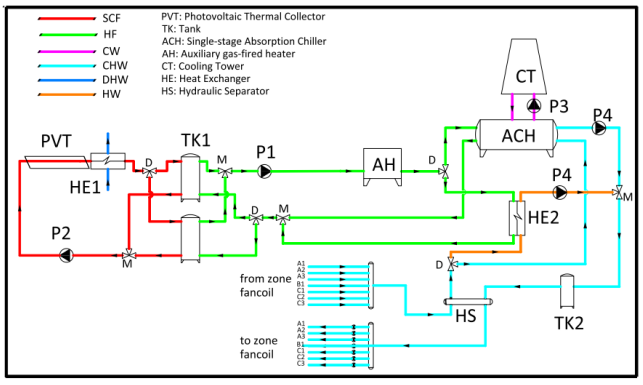

Figure 53. System layout [78].

In this work [78], an example of integration of solar heating and cooling system with low temperature PVT collectors is reported. System producing electricity, space heating and cooling and domestic hot water for a university building located in Naples (Italy). The system performance is analysed from both energetic and economic points of view. It resulted that the polygeneration system performance is mainly affected on PVT performance that is excellent during the summer,

decreasing significantly in winter. The amount of PVT heat used for DHW is 60.7%; the electric solar fraction is satisfactory since the PVT can cover about 65% of the overall electricity demand. The PVT average electric efficiency is slightly lower than 10%. This value is not so bad, considering that the nominal efficiency at 25°C was 16% and taking into account that PVT operates at 50°C and 80°C respectively in winter and in summer. The overall primary energy saving (PES) achieved by the whole system is slightly higher than 70%. The best resulted pay-back period, by the carried out economic analysis, is 3.6 years, when a proper feed-in tariff is considered.

An example of application of low temperature PVT collectors coupled to a solar-assisted heat pump and an adsorption chiller in a novel polygeneration system based is reported in reference [16]. Here, the dynamic simulation model and a thermo-economic analysis is carried out. The plant produces electricity, space heating and cooling and DHW for a small residential building. During the winter, thermal energy of PVT collectors primarily supplies the heat pump evaporator, whereas in summer, supplies the adsorption chiller (usually activated for lower hot fluid temperatures) providing the required space cooling (Figure 54). The results showed a total energy efficiency of the PVT of 49%, a heat pump yearly COP for heating mode above 4 and a COP of adsorption chiller of 0.55.

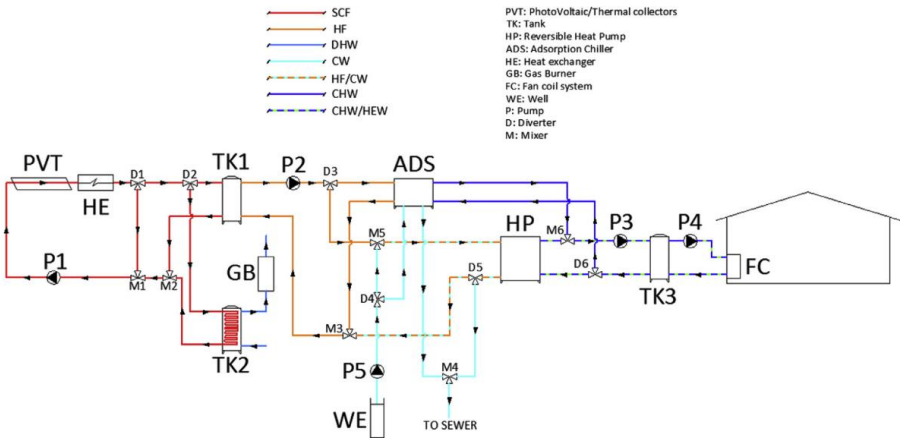

Figure 54. Layout of the proposed system including the main components and loops [16].

In reference [108] the exergy modelling of a new solar driven trigeneration system was performed. With respect to the previous systems, here high temperature PTC collectors are coupled to a high critical temperature efficient ORC, with the n-octane as working fluid. A single-effect ACH from production of cooling energy is also included (Figure 55). Both heating (steam water) and cooling production are achieved by the thermal recovery from the ORC. Different operating conditions, namely power generation, power-heating and power-cooling cogeneration and trigeneration were analysed. In particular, by an appropriate integration of heat exchangers and thermal storages, three different modes of operation were taken into account depending on low or high availability of solar radiation and operation during the night time. The exergy analysis was carried out by varying the temperature difference at the pinch point of the ORC evaporator, the inlet temperature of the ORC pump and the turbine inlet pressure. The maximum electric-exergy efficiency ranged between 7.00% and 3.00% depending the operating condition. In case of trigeneration, global exergy efficiency ranged between 20.0% and 7.00%. Finally, most of the exergy destruction rate occurred in the solar collectors and ORC evaporators.

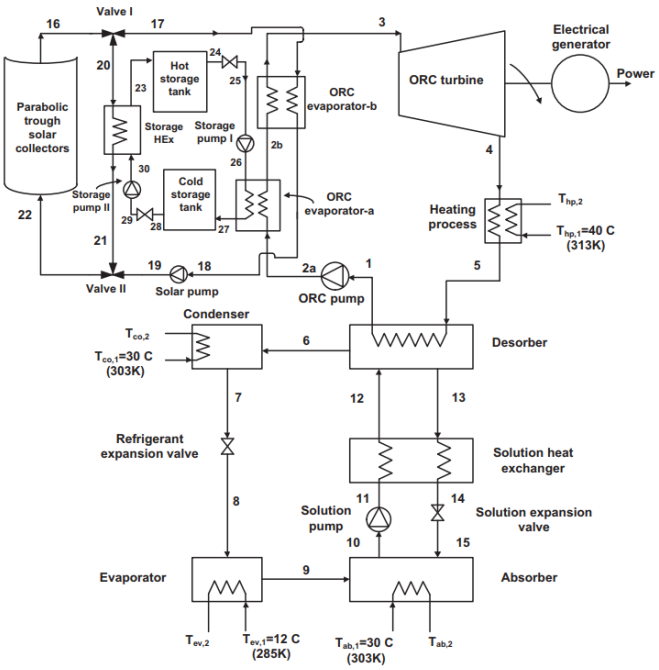

Figure 55. Schematic of the solar-trigeneration system [108].

Biomass and solar

Several studies examined different configurations of polygeneration plants consisted of both solar (STC, PV and PVT) and biomass technologies. An efficient approach to simultaneously use biomass and solar sources is investigated by Calise et al. [109]. Here, a reciprocating engine, fed by rapeseed oil, was coupled to concentrating parabolic trough solar collectors (PTC) to produce thermal energy and a double-stage LiBr/H_2O ACH to produce cooling energy. In the framework of polygeneration systems, this type of plant that integrates reciprocating engines with solar thermal collectors is scarcely investigated [109]. In particular, the solar and biomass source are linked because exhaust gases produced by biomass fuelled reciprocating engine are used to provide additional heat to the fluid heated by PTC. In this study, the whole trigeneration system was modelled and dynamically simulated in transient system simulation tool (TRNSYS).

The economic results show that the system under investigation is profitable, especially if properly funded and from the energy point of view the rapeseed oil reciprocating engine is suitable for integration in polygeneration systems based on high temperature solar heating and cooling systems, achieving a PES higher than 93%.

PTC are coupled to a willow pellets boiler in a tri/co-generation plant, consisted of an ORC–Vapour Compression Cycle (VCC) systems in the energy–exergy analysis and economic investigation performed by Karellas and Braimakis [110]. Here, ORC produces power consumed partially by VCC compressor, activated only in summer, whereas the heat generated in the condenser is used to meet hot water demand. With respect to the previous work, here PTC and boiler are used to provide the request heat of ORC (Figure 56), and the cooling energy is produced by VCC system. The resulted net electric efficiency is 2.38%; maximized thermal efficiency of the ORC is equal to 5.5% when the evaporation temperature is equal to 90°, while the exergy efficiency is 7% when the biomass boiler operates at full load operation. Findings suggested that superheating

process and the adoption of a recuperator lead to higher capacities of the heat exchanger areas and of the solar field extensions, without returning any significant increase of the system efficiency. By considering a typical apartment block on a Greek Island, assuming PTC area of 50 m^2 a payback period of 7 years is achieved. A sensitivity analysis was carried out by varying the investment cost and the biomass price, analysing their impact on the IRR and SPB.

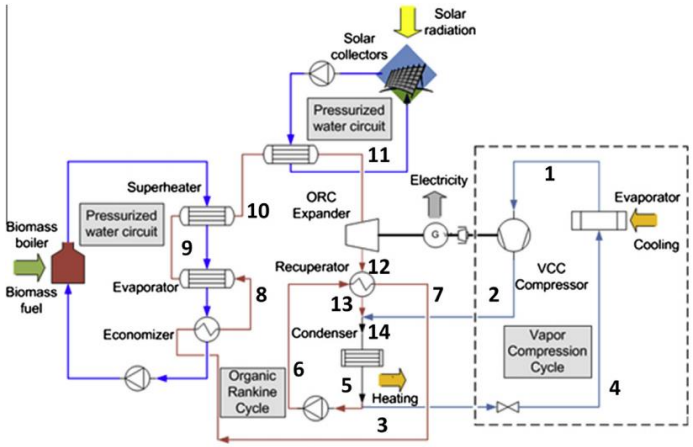

Figure 56. Combined ORC–VCC cycle and biomass boiler and PTC heating water circuits [110].

A wood chips gasification system and solar evacuated collectors are coupled in the simulation work carried out by Wang and Yang [111]. Here, an ICE supplied by the produced gas by gasifier and a dual-source powered mixed-effect ACH are also included. Waste heat of ICE and produced heat of solar field are utilized to produce cooling and heating energy. The plant is simulated by using the EES software package, and a comparison of the simulated linear curve of the instantaneous efficiency of the evacuated tube collectors between the simulation data and the experimental one, achieved by the solar energy research institute of Beijing is performed. The results indicate that the primary energy ratio and the exergy efficiency are 57.9% and 16.1%, respectively, and the carbon emission reduction ratio is about 95.7%, at the design condition.

A polygeneration system of generating methanol and power with the solar thermal gasification of the cotton stalk is proposed in reference [82]. A field of heliostats concentrates the solar radiation on the solar tower where the biomass gasification occurs.

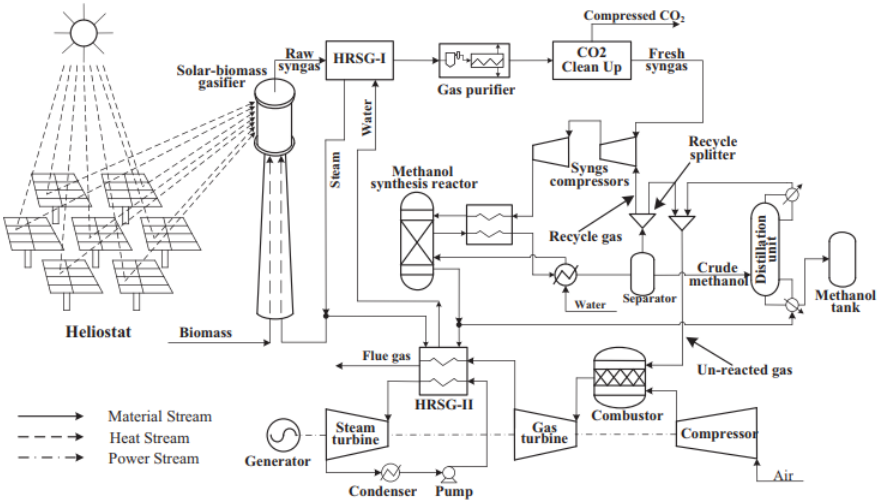

Figure 57. Schematic diagram of the proposed polygeneration system [82].

Here, the high-temperature solar source is directly employed in the gasification process and, therefore, is considered a promising option for the supply of the process heat (Figure 57). The syngas from the biomass gasification is used to produce the methanol via a synthesis reactor. The un-reacted gas is used for the power generation via a CC power plant. The solar assisted polygeneration system is located in Yanqi (China) and is numerically simulated by the Aspen Plus software to estimate the polygeneration system thermal performances. The highest energy efficiency and the exergy efficiency of the polygeneration system approximately are 56.09% and 54.86%, respectively.

A hybrid solar-biomass polygeneration system, based on PTC, for the simultaneous production of power, cooling by vapour absorption refrigeration (VAR) and fresh water by a multi-effect humidification and dehumidification (MEHD) desalination unit is investigated by Sahoo et al. [112]. The VAR cooling system operates using the extracted heat taken from steam turbine and condenser heat of the VAR cooling system is used in desalination system for production of drinking water. The system PES is 50.5% and the energy output is increased to 78.12% from this system as compared to simple power plant.

Geothermal and solar

Integration of geothermal and solar energy is one of the most investigated configuration in the framework of the polygeneration systems. In fact, low-medium enthalpy renewables energies, as solar and geothermal sources, represent an interesting solution to activate, by thermal energy, the Thermally Activated Technologies (TAT, or Thermally Driven Technology, TDT) as multi effect distillation (MED) technology, as well as the ORC and ACH machines [88]. Therefore, numerous studies can be found in literature about the investigation of different layout schemes, and subsequently some of them are reported.

A novel trigeneration system obtained by new prototypal flat-plate evacuated solar collectors coupled to a geothermal well is dynamically simulated in the work of Buonomano et al. [25].

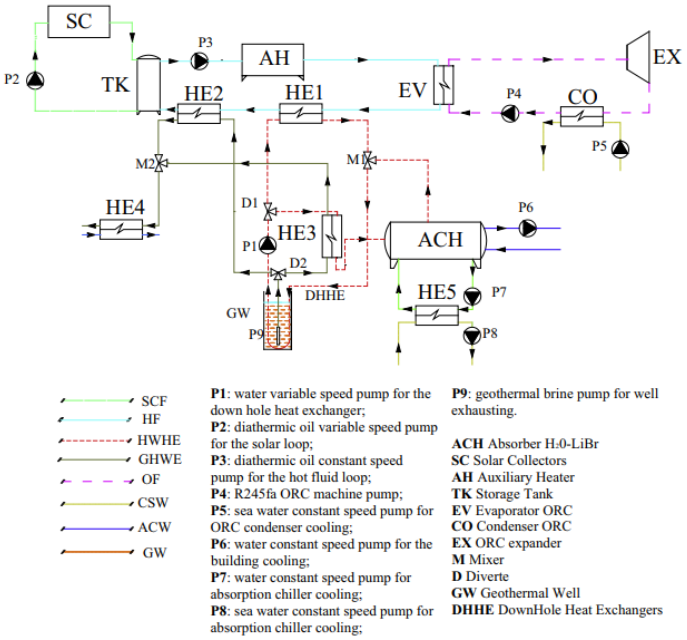

Figure 58. Sketch of the system layout [25].

The whole system, designed for a hotel building in Ischia Island (Mediterranean Sea), includes a new simulation model for ORC, and produces power, DHW and cooling by a single stage LiBr/H_2O ACH driven by geothermal energy only (Figure 58). The ORC is supplied by heat obtained by a geothermal well in which geothermal brine is about at 95°C, but in order to improve system performance, additional heat is provided by solar energy obtained through a 25 m^2 solar field. In fact, it resulted that most of the thermal energy supplied to the ORC is due to the contributions of geothermal source which is dominant over the solar one. The efficiency of solar collectors, ORC and ACH are 59.2%, 6.4% and 0.68, respectively. Here, a sensitivity analysis in order to investigate the effects of the variation of groundwater temperature, from 90 to 100°C is performed (Figure 59): the higher the well geothermal brine temperature, the higher the ORC inlet temperature.

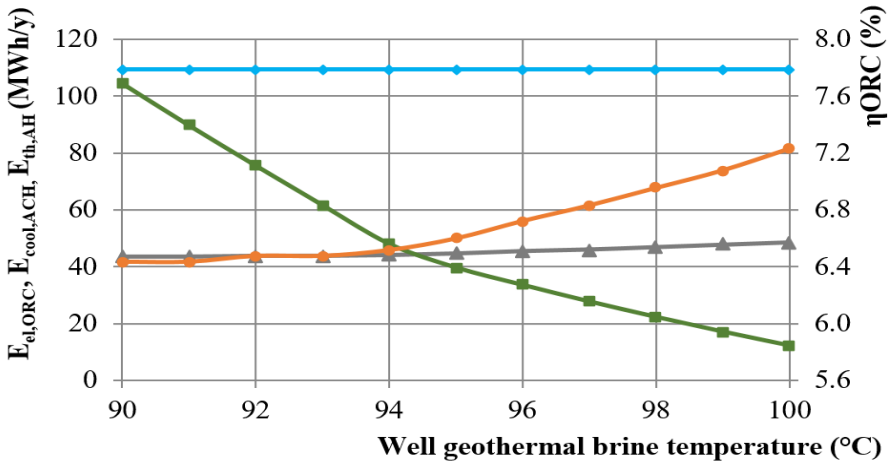

Figure 59. Sensitivity analysis: energy, efficiency vs. well geothermal brine temperature [25].

This leads to an increase in the ORC output electricity $E_{el,ORC}$, due to the improvement of ORC efficiency, η_{ORC}, from 6.4% to 7.2% and to a decrease of the energy supplied by the auxiliary heater, $E_{th,AH,}$ since the geothermal source is able to achieve the ORC minimum inlet temperature. Conversely, the produced cooling energy, $E_{cool,ACH,}$ is not significantly affected by the variation of well temperature.

A hybrid solar and geothermal polygeneration system combining CPVT field, a single-stage LiBr/H_2O ACH and a MED unit was studied through dynamic simulations in reference [77]. The plant provides electric, thermal and cooling energy, DHW and a quantity of desalinated water able to cover the whole request of the Pantelleria Island, assumed as case study. In particular, as depicted in Figure 60, solar thermal energy, at a maximum temperature of about 100°C, in combination with the thermal energy produced by low-enthalpy (about 80°C) geothermal wells (GW), is used to supply the MED system. Geothermal energy is also used to produce DHW at 45°C. The performance predicted through dynamic simulations, supported by appropriate economic models, was excellent. This work is particularly interesting because it presents a comprehensive assessment on combination of different kinds of technologies (SHC, CPVT, GW and MED).

Several additional islands in the Italian Mediterranean Sea, Ischia and Aeolian Islands, show a similar potential in terms of availability of geothermal and solar energy are also investigated. For

all the investigated locations, a parametric analysis aiming at evaluating the variation of Profit Index as a function of the ratio of DHW produced by the system (Q_{HE4}) and demanded by the user is performed. It resulted that Profit Index dramatically decreases in case of scarce DHW demand.

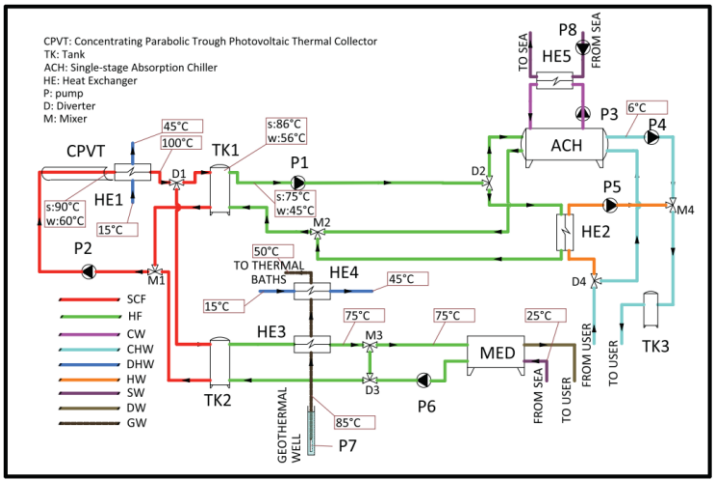

Figure 60. System layout [77].

Other studies concerning the dynamic simulation of a novel hybrid solar and geothermal polygeneration system capable to produce electric energy, fresh water and space heating and cooling, for the Pantelleria Island was presented and discussed in references [113] and [114]. Here, with respect to the previous layout, an ORC supplied geothermal and solar energy is considered. In particular, in reference [77], a low-temperature geothermal well (85°C) is used, mainly for the desalinization process, whereas here a medium-enthalpy geothermal source (160°C) is considered. In addition, in this work, the CPVT collectors are replaced by PTC field coupled to a thermal storage tank (Figure 61). The MED unit and ORC were developed in Engineering Equation Solver (EES). From the energetic analysis resulted that the solar energy input is much lower than the geothermal one, as highlighted by the low value found for the solar fraction, 9.60%; the ORC efficiency is about 11.6%. During the year the MED unit is able to produce fresh water, equal to 54% of the total seawater flowrate. Using an accurate energetic, economic, exergy and exergoeconomic analysis of the system, it was found out that the global exergy efficiency varies from 40% to 50% during the thermal mode and from 16% to 20% during the cooling one [114]; besides, the exergoeconomic costs of electricity, cooling water, chilled water and desalinated water resulted very interesting, respectively in the ranges 0.1475–0.1722 €/kWh, 0.01612–0.01702 €/kWhex, 0.1863–0.1888 €/kWhex and 0.5695–0.6023 €/kWhex. The previous works [113, 114] are developed by considering that all the useful products are consumed by the user. Instead, in a further study [88], based almost on the same plant configuration, the system is supposed to be connected to a district electric, heating and cooling network. In this case, system energy production must match the real time-dependent demands of electricity and space heating and cooling of typical buildings of Pantelleria Island (assumed as a case study). The system achieved a SPB equal to 8.50, with a potential primary source saving of 3039 tons and a potential CO_2 avoided emission of 9451 tons. It resulted capable to cover the energy demands of 800 examined buildings. Moreover, the plant produces 1006 10^3 m^3 of desalinated water and it is capable to cover the fresh water global demand. Average ORC efficiency amounts to 15.30%; the system is mainly powered by geothermal energy in fact, the average solar fraction is only 14.6%.

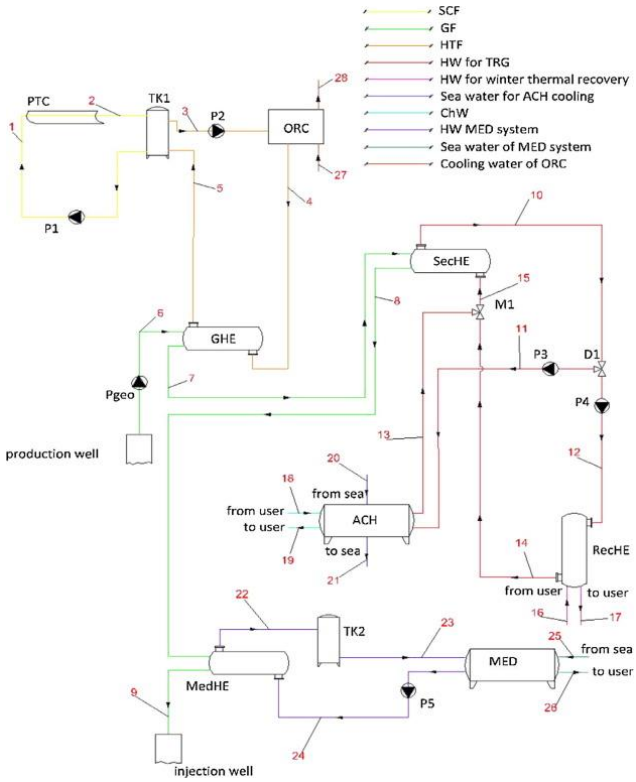

Figure 61. System layout [113, 114].

In reference [115] authors propose an interesting renewable multi-generation system, which integrates geothermal energy and solar air PVT system, produces electricity, hot water, drying air and capable to perform space heating and cooling. In particular, in this multi-generation system, solar PVT and geothermal energy are two independent sources. Power production is achieved by the PVT system and by the ORC, powered only by medium–high geothermal source. Cooling production is provided by a LiBr/H_2O ACH, whose thermal input at the generator is represented by the ORC turbine output. The cooling effect provided by ACH is used to cool the products of a dairy farm, which is heated by a heat pump. Ambient hot air coming from the solar PVT system is conditioned for the food drying process in the farm. The overall energy and exergy efficiencies of the multi-generation system are calculated to be 11% and 28%, respectively. Exergy efficiency of the solar system is around 12%. The energetic and exergy COPs of ACH are found to be 0.73 and 0.21, respectively. Energetic and exergy COP of heat pump system are 4.1 and 0.03, respectively. In addition, the energy and exergy efficiencies respectively are calculated to be 9% and 42% for ORC.

In reference [116] two novel ORC-based CHP systems powered by solar and low-temperature geothermal (90°C) sources are presented and compared. Both the configurations are designed to provide 50 kW_{el}, 400 kW_{th} and in both cases three working fluids (e.g. R134a, R236fa, and R245fa) were considered. In particular, one configuration is based on evacuated tube collectors and the power is produced by a single turbine, while the second one is based on a double stage system, in which a field of evacuated solar collectors heats the working fluid up to an intermediate temperature. After this first stage, only a part of the working fluid flow rate is heated in a second solar field, composed of direct-steam PTCs, up to the maximum temperature of the cycle. The mechanical work is then produced in two turbo-expanders arranged in series. In both configurations, the best

performance in terms of first law and exergy efficiency was obtained with R245fa (Table 6); while the best performance in terms of heat recovered was obtained with R134a. Moreover, findings suggested that single pressure configuration showed better performances, considering design conditions, heat source and lower system complexity.

Table 6. Results: efficiencies first and second configuration for three working fluids.

Fluid	**R245fa**		**R245fa**		**R245fa**	
Configuration	**First**	**Second**	**First**	**Second**	**First**	**Second**
System efficiency (%)	9.1	6.9	9.78	7.4	13.0	10.0
Cycle efficiency (%)	10.5	8.9	11.3	9.5	15.1	12.7
Exergetic efficiency (%)	22.7	17.5	23.3	18.4	25.0	20.0

3.1.3 Hybrid energy inputs

One of the most promising peculiarities of the polygeneration system lies in the possibility of hybridizing existing technologies, based on fossil fuels, with renewable energy sources. Several works available in literature on polygeneration systems, present the integration of renewable technologies (solar, geothermal, wind, etc.) into different conventional systems (trigeneration, DHC, gas-fired boiler, electric heat pump) or are based on the coupling of CCHP and renewable energy systems in a plurality of several applications [117]. The main potential applications of hybrid polygeneration systems featured by high energy and economic feasibility are hospitals, which have large and constant cooling and thermal loads, but also hotels, residential districts, schools, commercial buildings and so forth [118].

In this framework, a theoretical analysis focused on the feasibility of a hybrid plant applied to a real hospital located in Ferrara, Italy, is presented in reference [119]. Several hybrid schemes were investigated and compared: i) the conventional system consisting of electric grid, gas-fired boilers and compression chiller; ii) PAFCs (phosphoric acid fuel cells) integrated with ACHs and gas-fired boilers; iii) solar thermal collectors coupled to Rankine power cycle and ACHs; iv) PV panels coupled to conventional systems.

Basrawi et al. [120] investigated a hybrid energy system based on a polycrystalline PV and MGT (Figure 62) system able to produce power, heating and cooling of a group of residential buildings under a tropical region. Some of the electricity produced can be stored to the battery. Exhaust heat of the MGT is recovered by the heat exchanger, and it is used to cover water heating demand of the houses, and the rest is supplied to the ACH. This hybrid polygeneration system was compared with a system without PV.

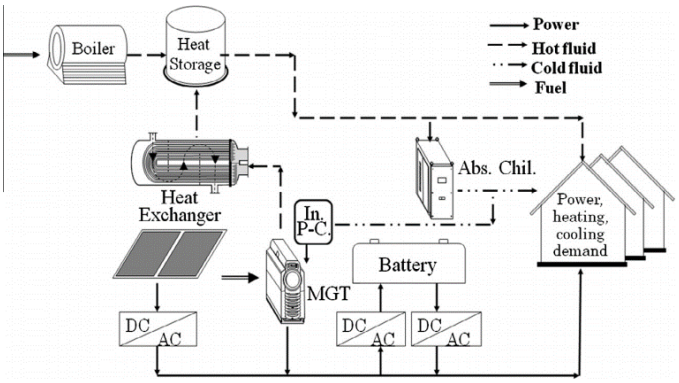

Figure 62. Configuration of the overall hybrid energy system for all cases [120].

It resulted that, when the proposed system operates with power-match operation strategy, the highest Net Profit is obtained. This circumstance occurs mainly because in this case no battery system is needed and the related high cost can be saved. However, this system presents low environmental performance especially if compared to a combined cycle gas turbine, because larger MGTs in this system operated frequently under partial load. Operation strategy that had smaller MGT that operated under full load can still generate Net Profit but at lower degree because it needs larger PV and battery.

In reference [121], an existing trigeneration system was hybridized with a solar field equipped with concentrating photovoltaic thermal (CPVT) collectors. The system includes a gas turbine, CPVT collectors, ACHs, tanks and balance of the plant (BOP) devices. The system supplies electricity, heat and cooling and was designed and dynamically simulated to be installed at the District Hospital of Naples, (South of Italy). The system energy and economical parameters were also evaluated. The system profitability was found to be acceptable (pay-back period equal to 15 years), even in the case of no public funding. However, if a feed-in tariff of 0.30 €/kWh (similar to the one adopted in Italy for PV systems), the SPB period becomes 6.1 years. Considering also a possible feed-in tariff of 0.10 €per kWh of thermal energy produced by the CPVT, the SPB becomes 4.1 years.

A polygeneration system investigating more renewable energy sources and a natural gas engine, for residential and tertiary buildings is developed in the work of Soutullo et al. [79]. Here, the developed system, modelled in TRNSYS, includes: PV panels, flat plate STC, biomass boilers, wind turbines, polymer electrolyte membrane fuel cells (PEMFCs), and ORC (Figure 63). A natural gas engine is used as a backup when both renewable technologies cannot supply the thermal district loads. Single effect ACH to supply the cooling demand is also simulated. These renewable systems were analysed statistically using the methodology of “design of experiments” applied to dynamic simulation models of polygeneration plants. The carried out dynamic simulations were used by analysing the performance of centralized polygeneration system for three representative Spanish buildings, located in different cities (Oviedo, Seville and Zamora). In the thermal model two cases were evaluated, namely Case 1 and Case 2 with renewable fractions 90% and 50%, respectively. In both cases Seville obtained the lowest solar contribution due to the highest cooling district demand. In the electric model, three configurations were evaluated: PV + PEM, wind + PEM and PV + Wind + PEM. The last configuration achieved the best results.

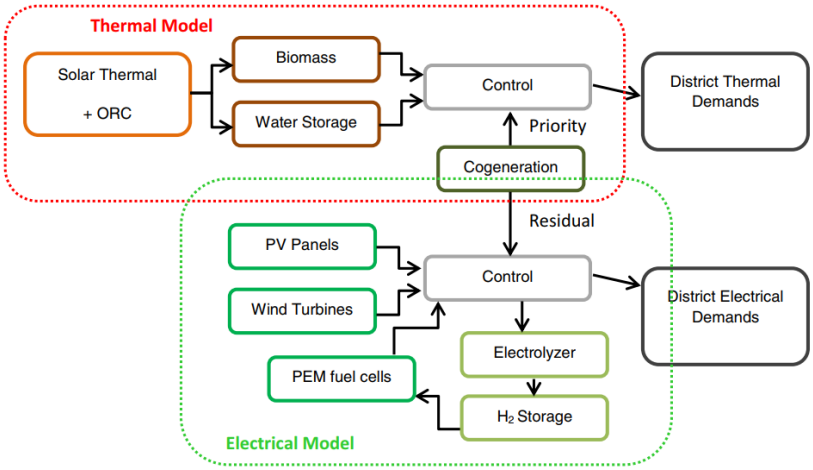

Figure 63. Blocks diagram of the polygeneration plant [79].

An interesting work is presented by Arsalis et al. [122], showing a thermoeconomic analysis of a PV-assisted 1 MW CCHP system driven by liquefied natural gas (LNG). The system includes a gas turbine cycle, ACHs, heat exchangers, LNG storage, PV solar field and BOP components (pumps, valves, etc.) and is designed to a complex of households in Nicosia, Cyprus. The system was modelled in EES and simulated both at part-load and full-load. The simulations results, performed on an annual basis, showed that the primary energy ratio is almost constant at all load condition and that the CCHP can completely fulfil the load profile of 436 households. In addition, without PV integration, the system must generate an additional 1959 MWh/year of electricity by LNG conversion. The economic analysis shows a minimum of the life cycle cost (LCC) around a PV capacity of 300 kW.

The energetic and economic feasibility of a solar-assisted heating and cooling system and DHW production for a school building in different Italian climates is assessed by Calise [123]. Here, evacuated solar collectors, a single-stage LiBr/H_2O ACH, and a conventional electric-driven reversible heat pump are simulated by using the software TRNSYS. From the energetic point of view, results are encouraging, for the potential of energy saving: 64.7%, 52.4% and 61.4% for Naples, Milan and Trapani, respectively. On the contrary, the economic profitability can be achieved only in case of public funding policies (e.g. feed-in tariffs), as always happens for the great majority of renewable energy systems, since the results SPB are 12.1, 15.7 and 12 years for Naples, Milan and Trapani, respectively.

3.2 Conversion technologies

Energy conversion technologies or prime movers are defined as the devices that by converting the input fuel, produce power and heat. Therefore, an energy conversion technology represents the main component of a polygeneration plant. These are selected according to input fuels, capacity, economy, availability, etc. [124]. In the followings, the research works regarding the simulation of various types of energy conversion technology in polygeneration plants are summarised.

3.2.1 Gas turbine (GT)

The integration of gas turbines in well-known CCHP systems is investigated in several research works [125-127]. Usually, in such systems, the high-temperature flue gases are used to generate power by the turbine expansion, heating, through heat exchangers by exploiting residual thermal energy in the turbine outlet flue gas and cooling, by an ACH.

An example of this configuration is reported in the work of Ziher and Poredos [125], which evaluated from the economic point of view a trigeneration system in the Slovenian biggest hospital building (Figure 64).

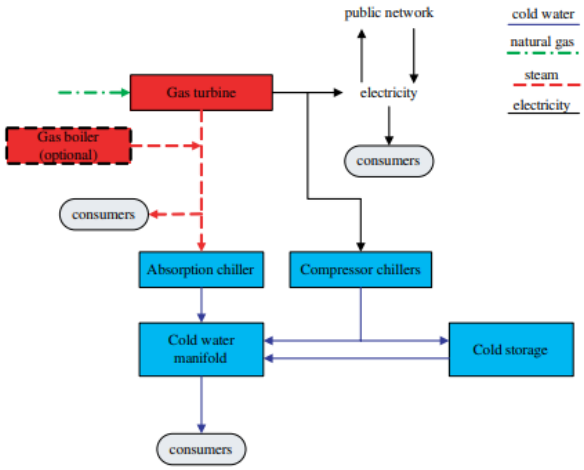

Figure 64. The concept of energy supply with a trigeneration system [125].

Here, a gas turbine is used as a driving unit because of high needs for electric and heating energy of hospital. Gas-fuelled reciprocating engines are used to 3 MW of power. The generated steam will be used to drive the two-stage steam-ACH and delivered to individual consumers of heat. An additional peak-time hot-water gas boiler will cover the need for additional heat during the winter period. In order to produce cooling energy one ACHs with a cooling power of 2 MW and two compressor chillers, one with a cooling power of 2 MW and one with 1.5 MW are included. By considering the needs for electric and heating energy the cogeneration module is designed on the basis of the peak electric power (4.2 MW). In this work, author focused mainly on the: i) economic aspect, by evaluating the payback period (static method), and net present value and profitability index (dynamic method); ii) optimization of the cooling production (with and without cold storage). The main results are summarised in Table 7.

Table 7. Economic evaluation of the trigeneration system.

	Static method	**Dynamic method**	
	Payback period (years)	Net present value (Mill. Euro)	Profitability index (–)
Trigeneration without cold storage	6.71	2.02	1.07
Trigeneration with cold storage	5.86	2.72	1.09

Ghaebi et al. [126] performed the energy, exergy and thermoeconomic analysis of a CCHP system with gas turbine as prime mover. Again, in such CCHP system the hot gases of GT are used in a dual pressure HRSG to generate low and high pressure steam; low pressure steam is supplied

to generator of ACH. From energetic results, this CCHP system produces 6.96 MW, 24.65 MW and 19.23 MW of cooling, heating and power; the first and second law efficiency of CCHP are 84.01% and 43.92%, respectively.

A similar configuration is reported in reference [127]: a gas turbine trigeneration system for combined heat cold and power production. Here, expanded gas is utilized in the heat recovery steam generator to generate process heat sent to the generator of the vapour absorption system. Thermodynamic performances of such system were studied on the basis of first law as well as second law analysis. In order to perform such analysis, the most relevant parameters able to characterize an energy generating facility were the fuel-utilization efficiency, the electric to thermal energy ratio, and the exergy efficiency. In their results, they conclude that maximum exergy is destroyed during the combustion and steam generation process, which represents over 80% of the total exergy destruction in the overall system.

In case of small power applications, the only commercially mature technology is represented by micro gas turbine (MGT) [128]. In particular, the MGT are preferred among small-scale distributed generators, mainly due to high fuel flexibility, high overall efficiency, environmental benefits, and low maintenance requirement [129]. In this framework, the combination of MGT and ACHs in CCHP systems is often investigated. An example of this configuration is reported in reference [130] (Figure 65), where this system was investigated for a supermarket user from both experimental and numerical points of view. In particular, the MGT is an 80 kW_e recuperated MGT generation package (MTG 80RC-G) with a built-in hot water heat exchanger.

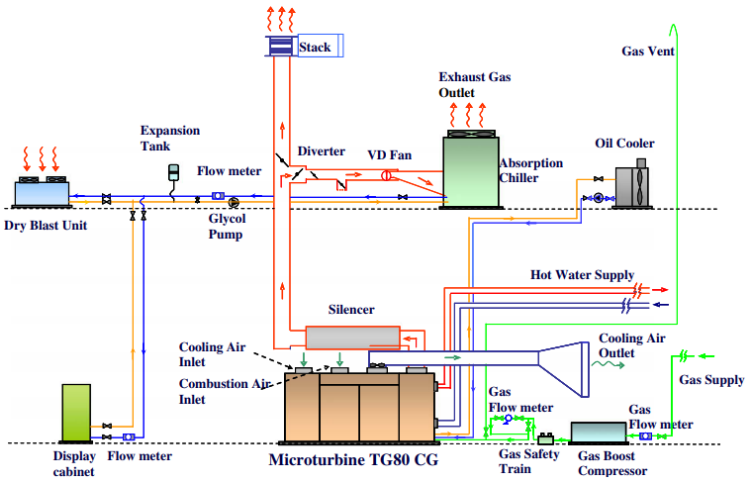

Figure 65. Schematic diagram of the tri-generation test facility [130].

For the energy needs of users, three MTG system and several ACHs are included. The system model was developed in TRNSYS simulation environment and was validated with the test results and consequently used to predict the system performance at different operating and design conditions, such as varied ambient temperature, fuel flow rate and pressure ratio etc. In particular, the simulation model includes in detail the models of the following components: compressor, recuperator, combustion chamber, gas turbine, electric generator, gas pipes, generator (desorber), rectifier, absorbers, condenser and evaporator etc. The energy parameter used to evaluate such system is the Primary Energy Rate (PER), defined as the ratio of the primary energy demand to the

required output. The system with the lowest value of PER is considered the best with respect to energy consumption. The results show an interesting trend of PER as a function of ambient air temperature: since both the power generation and cooling capacity decrease in case of a higher ambient air temperature, the PER value, as a result, increases with the rise in ambient air temperature.

Medrano et al. [131] developed a thermodynamic model of an integrated energy system formed by a MGT and an exhaust fired single-double effect ACH. The overall exergy efficiency of the studied system resulted equal to 0.285, higher than the ones resulting from the same MTG and exhaust gas fired single or double effect chillers.

In reference [132] energy and exergy performance of a CCHP, consisting of a small scale GT for a building cluster, were evaluated by the dynamic simulation under the rated and part-load conditions. With respect to the previous configurations, a double-effect ACH is coupled to a 1748 W MGT. For the thermodynamic analysis of the CCHP system, the Fuel Energy Saving Ratio (FESR), defined as the ratio of the energy saving of CCHP system in comparison with the conventional separation system to the energy consumption by the separation system, is taken into account. The variation of the FESR under different load levels indicates that for the design point, the FESR has a value as high as 26.6%. The lower the load level is, the smaller the FESR value becomes. When the load level decreases to approximately 30% of the full load level, the FESR is zero, which means that the energy saving performance of the CCHP system is identical to the SP system. As for the load level of 19%, the performance of the CCHP system has deteriorated considerably with the FESR value of −7.4%. The CCHP system allows one to achieve energy saving when the power output of the gas turbine exceeds 30% of the full load. Concerning the CO_2 emission, it is also found that these are reduced by 66.7%–70.5%, compared with conventional separation system, when the power output of gas turbine increased from about 30% to 100%.

A thermodynamic simulation of a trigeneration system consisting of a 28 kW_e MGT coupled to a double effect ACH and a heat exchanger to produce hot water is performed in reference [133]. In particular, a certain amount of the energy of the exhaust gases at high temperature of the MT are used to supply heat to the generator of the double effect ACH and the remaining percentage, featured by high enough temperature, is used to generate hot water by the heat exchanger.

The trigeneration system was evaluated for different operating conditions: i) MGT fuel mass flow rate; ii) ambient temperature, the higher the ambient temperature, the lower the MGT power; iii) generation temperatures, showing the sensitivity of the ACH performance to the variation of the temperatures of the MT exhaust gases (Figure 66). If the ambient temperature is higher, for instance at 36°C, the cooling system cannot operate at generation temperatures lower than 146°C and it is necessary to reach temperatures close to 166°C to obtain the highest COP of 1.289, at ambient temperature.

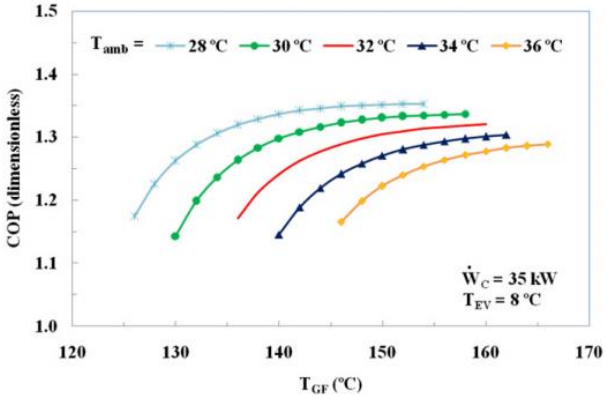

Figure 66. COP against generator temperature at five different ambient temperatures [133].

The possibility of integration of an externally fired micro-gas turbine (EFMGT) with membrane distillation plant in a standalone application for the production of electricity, heat and drinking water is investigated by Rahman and Malmsquit [134] through a computational simulation model. Here, the components models included in polygeneration system (MGT, electric and thermal loads, membrane distillation unit, and electric and thermal storage) are developed. The modelling of the entire polygeneration system is simulated in Matlab/Simulink environment. The resulted overall efficiency is 72% at rated electric output (2 kW). Authors declare that to maximize the overall efficiency, it is required to maximize the thermal energy flow rate utilization by increasing thermal energy use. However, maximizing the overall efficiency subsequently leads to a lower temperature level at the demand side, and thus, the efficiency of the pure water production decreases. Therefore, such a polygeneration system can perform more efficiently in colder regions. Another important conclusion of this work is that the fuel consumption for an EFMGT does not vary significantly with no-load to full-load condition. As a result, to obtain highest fuel utilization it is recommended to operate such EFMGT system close to the rated electric load.

3.2.2 Steam turbine (ST)

Worldwide electricity production is mainly based on the use of steam turbines converting heat from warm sources into useful energy. Therefore, several research works available in literature [135, 136] are focused on the way to improve the total efficiency of such system [137], often also by including such technology in polygeneration systems and exploiting it for producing different outputs. In this subparagraph some works are reported.

The operation of the three different configurations, respectively, based on a backpressure steam cycle (configuration #1, Figure 67 b), a condensing steam cycle (configuration #2, Figure 67 c), and a combined cycle (configuration #3, Figure 67 d), for the production of sugar and energy in a sugarcane factory was simulated with the EES software in reference [138]. In this system, the bagasse produced in the extraction system of sugar cane is delivered to the cogeneration system, where it is used as fuel, to produce the electricity and steam consumed by the process. The most relevant results are given in Table 8. In particular, it resulted that the global energy efficiency of polygeneration system decreases from configuration #1 to #3, but it is very important to highlight that the economic and the quality value of the total product increases, due to the share of electricity production which also increases.

Table 8. Plants performance [138].

Configuration	Energy efficiency overall (%)	Bagasse (+) excess (−) shortage (t/year)	Electricity excess (MWh/year)
#1	84.2	(+) 316,400	119,300
#2	65.2	0	306,100
#3	56.9	(−) 301,600	503,100

Configuration #2 produces a considerably higher amount of electricity (186,800 MWh/year) than #1 one. This increase of electricity production is obtained by consuming 316,400 t/year of bagasse, which represents a virtual electric efficiency of 28%. In the case of configuration #3, the surplus electricity production is 503,100 MWh/year higher than #1 one; but for this configuration it requires buying more bagasse.

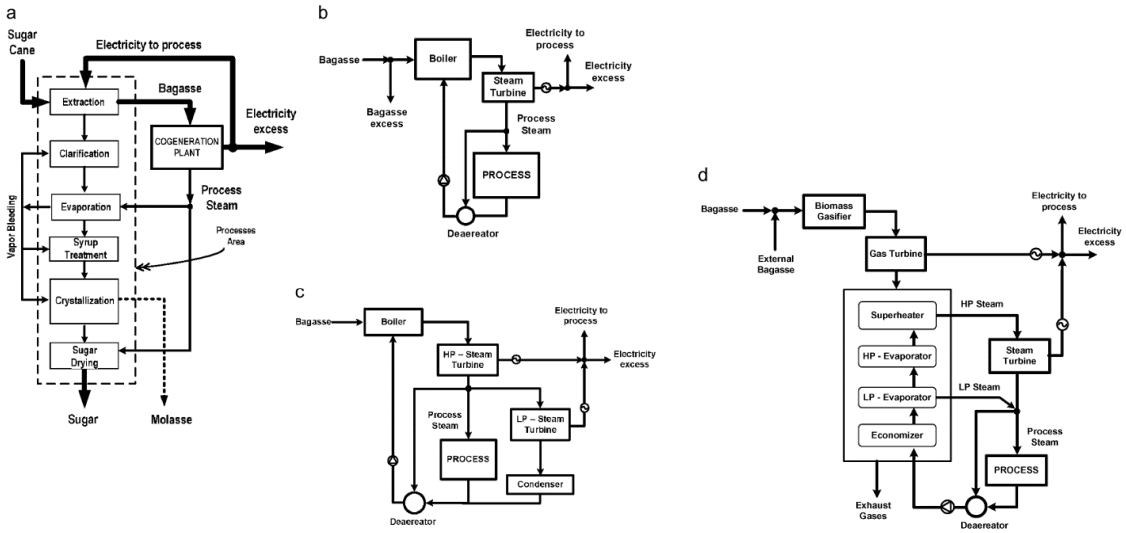

Figure 67. Scheme of sugarcane production and different configurations of cogeneration systems integrated with the sugarcane factory: (a) diagram of integrated production of electricity, sugar and molasses; (b) configuration #1: backpressure steam cycle; (c) configuration #2: condensing steam cycle and (d) configuration #3: combined cycle [138].

With respect to the previous work, in reference [139] a steam turbine plant is integrated in a lignocellulosic wood-to-ethanol process. The simulation study here carried out by software IPSEpro™, is based on an existing CHP plant and on the pilot scale plant for the ethanol production. In particular, measured data from operation of the Enköping (Sweden) CHP plant were used for modelling and validating the CHP plant model, whereas the configuration of the pilot scale plant, owned by two universities of Örnsköldsvik (Sweden), was used for modelling the ethanol production. The resulted system total efficiency was 50%, meeting the heating load in the district heating system. The authors concluded that with respect to the stand-alone production plants, the ethanol production from wood is more efficient when integrated into a CHP plant. The total biomass consumption is reduced by 13.9% while producing the same amounts of heat, electricity and ethanol fuel as in the stand-alone configurations. The results showed that another feature of the integrated polygeneration system is the longer annual operating period compared to existing cogeneration. Thus, the renewable electricity production is increased by 2.7% per year. The system is suitable for the retrofit or extension of an existing cogeneration plant to a polygeneration system.

Cormos [140] developed a combined polygeneration process for power, hydrogen and carbon dioxide production, consisting of a steam turbine, a bio-methanol steam reformer and carbon capture technologies. In particular, the author is focused on the hydrogen production from bioethanol at industrial scale by investigating three carbon capture designs: one based on pre-combustion capture using chemical gas–liquid absorption, Case1, and two based on chemical looping (one based on syngas, Case 2, and one using direct bioethanol looping, Case 3, Figure 68). In all the cases, the heating duties needed for various processes (e.g. reformer, carbon capture by gas–liquid absorption or chemical looping) are recovered from available hot streams within the plant, therefore, the only energy input of the plant is the bioethanol feedstock. Cormos modelled and simulated the different carbon capture designs by the ChemCAD software.

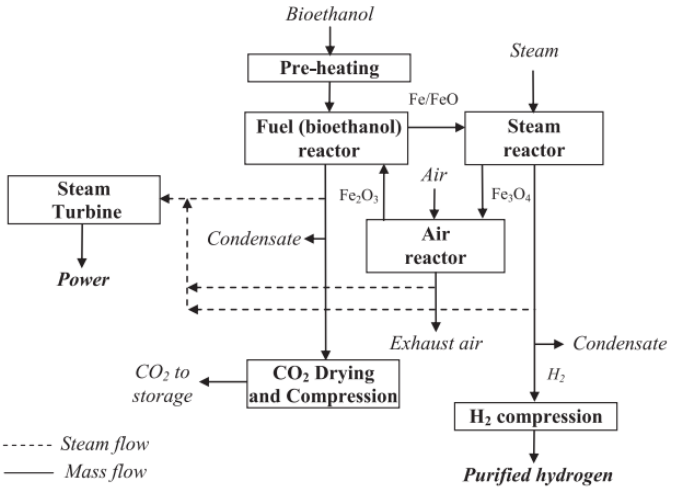

Figure 68. Bioethanol conversion for H_2 production with direct bioethanol chemical looping (Case 3) [140].

From the obtained results, it is noticed that the chemical looping cases (Cases 2 and 3) reach higher energy efficiency (59–63% vs. 53–58%) and almost total decarbonisation of the fuel (>99% vs. 80–92%). Case 3 resulted the most promising mainly for the feature to capture almost total carbon of the feedstock and to have a lower plant complexity. In particular, the operation of this configuration expects that the bioethanol is vaporised and then it is introduced in the fuel reactor together with the oxygen carrier. The bioethanol is totally oxidised to CO_2 and water. The Case 3 energy efficiency resulted equal to 63.66% vs. 59–62% of bioethanol reforming technologies without carbon capture,

A new power and refrigeration cycle is simulated in reference [141], where a Rankine cycle and the ejector refrigeration cycle are combined to produce both power and refrigeration simultaneously with only one heat source. This system can be driven by the flue gas of gas turbine or engine, solar energy, geothermal energy and industrial waste heats, assumed at constant temperature equal to 150°C. In this work, an exergy and parametric analysis and a parameter optimization are adequately performed. In particular, the parameter optimization is achieved by means of genetic algorithm to reach the maximum exergy efficiency. The results show that the biggest exergy loss due to the irreversibility occurs in heat addition processes, and the ejector causes the next largest exergy loss. The thermal efficiency, evaluated as the ratio between the product net power plus the refrigeration output and the total heat added to the cycle from the heat source, is equal to 13.72%, whereas the optimized exergy efficiency is 27.10%.

3.2.3 Combined Cycles plants (CC)

The CC plants stand for the most efficient technology for energy conversion, and the most-wanted option selected to satisfy the increased demand for electric energy in the world [142].

In combined cycles (CC), gas turbine cycle is used as topping cycle and steam turbine cycle may be used as bottoming cycle to increase the overall thermodynamic efficiency [102]. In the polygeneration plants, the CC plants are often analysed in order to obtain the generation of several useful products. An example of integration of CC as prime mover in a trigeneration plant is reported in reference [143]. Here, the thermodynamic modelling and both exergy and environmental analyses of a trigeneration system based on gas turbine, a steam turbine and a single-effect ACH for heating, cooling and electricity generation is carried out. The schematic of this trigeneration system is depicted in Figure 69.

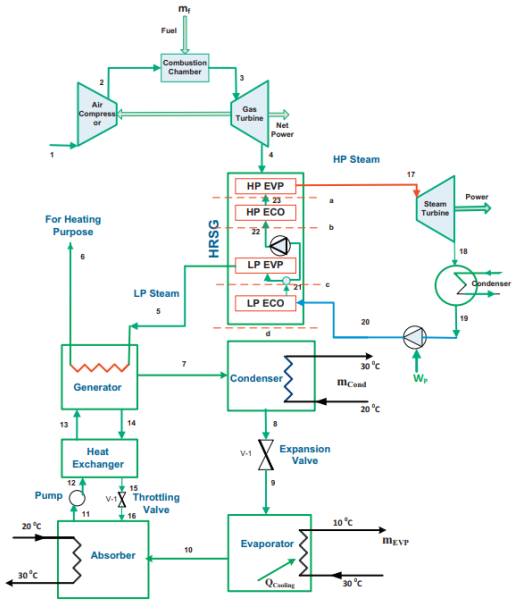

Figure 69. The schematic of the trigeneration system [143].

The hot gases of GT are utilized in the dual-pressure HRSG with two economizers and two evaporators to generate low-pressure (LP) and high-pressure (HP) steam. The LP steam is used to drive the ACH and the HP steam to generate electricity. The results obtained from energy and exergy analyses are reported in Table 9.

Table 9. Parameter values resulting from energy and exergy analyses.

Parameter	Value
$Q_{heating}$ (MW)	46.60
$Q_{cooling}$ (MW)	3.50
W_{net} (MW)	35.15
$\eta_{I,Tri}$ (%)	75.50
$Ex_{D,Tot}$ (MW)	65.80
$\eta_{ex,Tri}$ (%)	47.50
Normalized CO_2 emission (kg/MWh)	158

Authors declare that the CO_2 emissions and system exergy efficiency for the CCHP system are lower and higher, respectively, than those for typical CHP systems or GT cycles.

A similar layout is investigated also by Wang et al. [83], assessing a new CCHP system integrating gas turbine and heat-driven cooling/power cogeneration system, by Aspen Plus software. In particular, the developed layout in this work with respect to the previous one consists of an ammonia-water Rankine cycle, a single-double $LiBr/H_2O$ ACH, which better matches the temperature variation of ammonia-water condensation, and the Bryton cycle and a hot water exchanger. The novel system was compared to a reference CCHP system including a gas turbine, a double effect ACH and a heat exchanger. Two evaluation criteria are adopted to evaluate the CCHP performance, the exergy efficiency (η_{ex}) and the fuel energy saving ratio (FESR). It resulted that with the same amount of exergy input (7477.78 kW), the exergy output of the proposed system is 2833.58 kW, and that of the reference system is 2265.09 kW. η_{ex} of the proposed system reaches 37.89%, which is 7.60% higher than that of the reference system. Because of the high-temperature heat cascade utilization in the CCHP subsystem, the FESR reaches 31.70%, which is 5.19% higher than that of the reference system.

Several works are also focused on polygeneration systems coupling CC systems to a gasification technology (coal gasification or biomass gasification).

In fact, where coal is used, to reduce its greenhouse gas emission, the integrated gasification combined cycle (IGCC) results a power generation technology, with the potential to capture carbon dioxide with low energy efficiency penalty and costs. In an IGCC scheme, the solid feedstock is partially oxidized by oxygen and steam to produce syngas (mainly a mixture of carbon monoxide and hydrogen). An example of this configuration is reported in reference [144], where the modelling and simulation of a novel polygeneration technology, for the coproduction of hydrogen and power based on coal gasification integrated to a CC with a dual chemical processes (with carbon capture and storage and with calcium-based chemical looping) is performed.

Other simulation study regards the coal gasification-based polygeneration systems coupling methanol synthesis and CC for power production with CO_2 recovery. This topic is analysed in the work of Lin et al. [87]. Here, the proposed system was analysed with and without CO_2 recovery from the techno-economic viewpoint. In particular, the proposed polygeneration system is based on the concept of CO_2 generation, reaction, transportation, and conversion in energy, with the production of excellent clean fuel such as methanol (Figure 70).

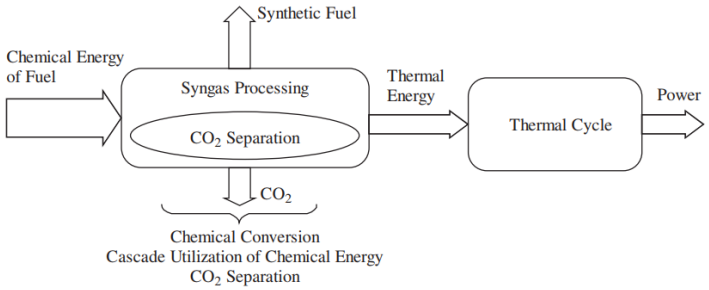

Figure 70. Sketch map of the integration of cascading utilization of chemical energy and CO_2 capture [87].

In this way, the polygeneration system can recover CO_2 with reduced (or even without) energy penalty. From the most important results of this work, it resulted that the polygeneration system without CO_2 recovery consumes less energy on methanol production, which is about 76% of that of

the traditional methanol production, and achieves higher power generation efficiency, which is 15% points higher than that of the traditional power generation technology. And with CO_2 recovery, the energy consumption of methanol production of polygeneration system is much less than those of the Fischer–Tropsch fuel and conventional methanol production.

As above mentioned, the biomass gasification represents a further technology which can be used to generate both process heat and significant amounts of electricity. An example where this technology in a combined cycle plant is investigated, is reported in reference [84]. Here, the produced electricity is used to march the needs of dry-grind ethanol facilities by utilizing the ethanol process co-products and other biomass sources (corn cobs). The model of the dry-grind ethanol process is simulated by Aspen Plus process simulation software and, then, used as basis for a subsequent gasification system model. The authors declare that this technology is able to reduce fuel costs for ethanol plants and that the renewable energy ratio of ethanol production could be improved from a typical value of 1.7 up to 5.1, and that a dry-grind ethanol facility with a capacity of 190 million litres per year, could produce 30.4 MW_e of power while supplying all its process heat needs using ethanol co-products and corn cobs.

3.2.4 Organic Rankine Cycles (ORC)

Organic Rankine cycle (ORC) is a very attractive and suitable technology [85], in applications where the available heat is at relatively low-medium temperature. In fact, when the temperature of the heat source is low, water as working fluid may be unfeasible, due to the trend of its saturation curve. Instead, organic fluids show a significantly better performance thanks to the higher molecular weight, the lower evaporation heat, the positive slope of the saturated vapour curve in the T–s diagram and the lower critical and boiling temperatures [145]. Anyway, to obtain high efficiency the selection of appropriate working fluid is the very first step to optimise an ORC plant [146]. Several works deal with the simulation of polygeneration plants coupled to ORC systems supplied by low-medium temperature sources (geothermal heat [25], solar thermal heat [145, 147], waste heat [148], biomass products [149], etc.). In the work reported in reference [150], where an ORC-based trigeneration system is supplied by the waste heat recovery from a micro GT, the modelling (by Matlab software) and the exergo-environmental analysis of this system is performed. The system layout mainly consists of a GT cycle, an ORC, a single-effect ACH and a DHW heater (Figure 71) and it produces heating, cooling, hot water and electricity. The selected organic fluid, featured by its high critical temperature is the n-octane, whose thermodynamic properties were obtained from the EES software. From the carried out exergy-environmental analysis, it resulted that the highest exergy destruction occurs in the combustion chamber and heat exchanger (Figure 72) mainly due to the irreversibilities associated with the large temperature difference occurring in these components. The absorption cycle does not exhibit significant exergy destructions, mainly because it does not directly utilize fuel energy but instead uses steam produced by the ORC. It resulted that the trigeneration cycle has less CO_2 emissions and higher exergy efficiency than the GT and CHP cycles, providing a significant motivation for the use of trigeneration cycles.

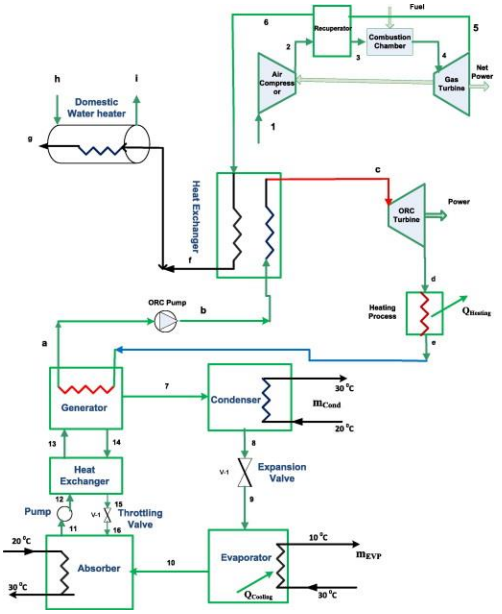

Label	Specification
1	Inlet air entering compressor
2	Outlet air from compressor
3	Outlet air from recuperator
4	Combustion gases exiting combustion chamber
5	Outlet hot gases exiting gas turbine
6	Hot combustion gases entering the heat exchanger
7	Water vapor entering condenser
8	Liquid water exiting condenser
9	Water vapor entering evaporator
10	Saturated water entering absorber
11	Low pressure LiBr water mixture
12	High pressure LiBr water mixture
13	Weak solution mixture
14	Strong solution mixture
15	LiBr solution exiting heat exchanger
16	LiBr solution entering absorber
a	Saturated ORC liquid leaving the generator
b	ORC fluid leaving the ORC pump
c	ORC vapor entering the ORC turbine
d	ORC saturated fluid entering the heating process
e	ORC fluid entering the generator
f	Combustion gases entering the domestic water heater
g	Combustion gases leaving the heat exchanger
h	Cool water entering the domestic water heater
i	Hot water leaving the domestic water heater

Figure 71. Schematic of the trigeneration system [150].

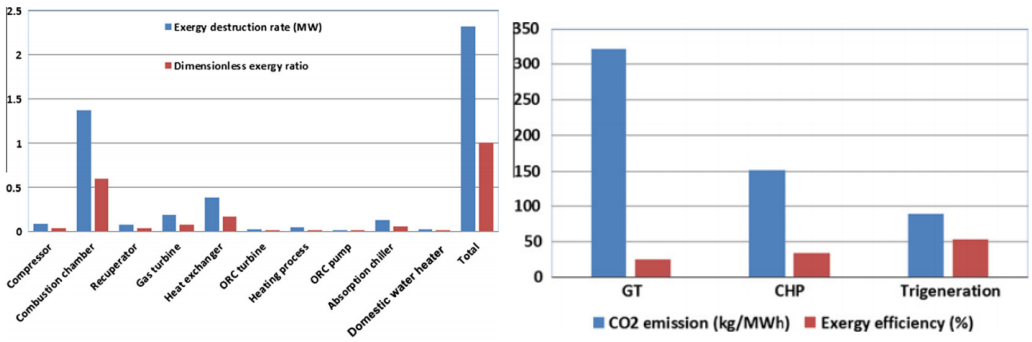

Figure 72. Exergy-environmental results [150].

The simulation of an ORC system, driven by the waste heat recovered from a diesel engine generator is studied in reference [151]. In particular, the aim and the novelty of this work is to investigate the system performance and efficiency of a small scale trigeneration system integrating an ORC system into a diesel engine generator, used as primary mover. The ORC model is developed in Matlab and the diesel engine generator of the laboratory at Newcastle University is used as the case study. R245fa is used as the working fluid. In addition, in order to expand the system supply capacity, the trigeneration system is also coupled to a smart energy storage system. Based on the simulation results, with the energy storage system, the capacity of the electric cycle increased by 47%. The ORC system may generate 0.737 kW electric power, by contributing around 8.91% of the total electricity production, with 9.25% efficiency at the generator full-load operation point. The waste heat recovered from the engine is 35.3% of total energy. Regarding the heating and cooling energy demand, for the selected household, it is demonstrated that the ratio of the recovered heat by ORC satisfies the 41% of the heating energy demand and that part of waste heat used by ACH produce 9.36% of the cooling energy demand.

Solar thermal collectors can be adapted to collect solar energy at low temperature and provide the heat necessary to supply ORC plants. An example of this configuration is reported in the study

of Sharaf et al [152], where the thermal energy produced by a field of PTC is used to drive the ORC via evaporator heat exchanger. In this plant, the exhausted energy from the ORC turbine is also used in the first effect of a MED process, by producing power and desalted water (power and solar desalination with MED, PSDMED). This system was compared with a further system, where the solar energy is directly utilized from the via evaporator heat exchanger to the first effect of MED process, by producing only potable water (solar desalination with MED, SDMED). By considering a MED plant with a capacity of 5000 m^3/day, the most important parameters obtained in the both systems are summarised in Table 10.

Table 10. Results for both systems based on 5000 m^3/day.

Parameter	Unit	SDMED	PSDMED
Solar field area	m^2	1.009×10^5	1.32×10^5
Specific power consumption	kWh/m^3	2.17	2.67
Gain ratio* *Distillate mass flow rate / Steam mass flow rate	-	7.56	3
Total water price	$\$/m^3$	1.645	1.845
Total investment, operating and maintenance cost	$/h		
Total exergy destruction	MW	155.7	157.8
Overall exergy efficiency	%	31.82	33.1
Turbine power	MW	–	5.381
Steam mass flow rate	kg/s	7.65	46.05

It is evident that PSDMED gives slightly higher values against the SDMED comparing the total water price, solar field area, and total exergy destruction rate. However, it is considered attractive based on the results of exergy efficiency and the developed power by the organic turbine.

The power generation by ORC supplied by biomass, combined with the water desalination is studied by Maraver et al. [85]. In this work, aim of authors was to provide an assessment of a polygeneration system, based on biomass combustion for the production of desalted water, power, heat and cold. The investigated system consists of a small scale ORC engine, acting as the polygeneration system prime mover, by producing power and heat, recovered for directly heating purposes or DHW, and to generate cooling by a $LiBr/H_2O$ ACH and to produce desalted water in a MED unit. ORC subsystem was modelled using the Aspen Plus process simulator. Configuration proposed is compared to stand-alone systems producing the same energy and material outputs. Author investigated the behaviour of the plant by varying main parameters of each components and determined the optimal distribution of the heat generated by the ORC, obtaining the highest savings with larger amounts of heat destined for heating or DHW. This aspect limits the amount of heat used for the activation of MED and ACH to 40% when the comparison of the proposed polygeneration with high performance stand-alone one is carried out. Moreover, 33 working fluid for ORC unit were considered and the economic feasibility was assessed. Fluorobenzene and octamethyltrisiloxane offer good cycle efficiencies as well as acceptable densities and specific power capacities compared with other efficient fluids. SPB ranged between 4.00 and 20.0 years depending on biomass fuel price and MED capital cost, which is function of daily capacity.

3.2.5 Internal Combustion Engine (ICE)

Internal combustion engines (ICEs) convert the heat produced from combustion into mechanical work [153]. Such engines were the most widely used prime movers in small- and

medium-scale distributed energy resource (DER) systems [154] due to its low initial cost and robustness [155]. ICE technology is mature, and has flexibility in design for different fuels (natural gas, biogas, biodiesel, etc.) [90]. Some limitations are frequent maintenance, vibration, noise and emission issues [154]. It must be noted that in an ICE, only 30–40% of an engine's fuel combustion energy is converted into electricity [156]. The rest is waste heat dissipated mainly by the engine exhaust system and the cooling system. In order to recover such waste heat, the conventional ICEs are often coupled to heat exchangers. In addition, ICEs can be easily coupled to cooling devices (adsorption [157], heat pumps and electric chillers [86, 158, 159], absorption systems [160]) in trigeneration systems.

An example of this application is investigated in the simulation and experimental work carried out by Wu et al. [157]. In this work, they investigated a micro-CCHP based on a 16 kW_e ICE which supplies by the exhaust heat a 7.5 kW adsorption chiller. A thermal management controller (TMC) is also included in order to manage the recovered waste heat. The TMC has three stages of heating output: the first stage has the top priority of heating output while the third one, the lowest priority of heating output. Specifically, the recovery of the waste heat will be initially sent to the buffer tank cycle, then to the hot water cycle, and finally to the cooling water cycle (Figure 73).

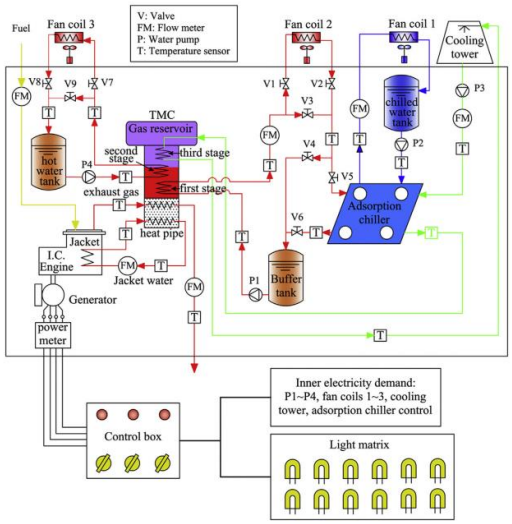

Figure 73. Layout of experimental micro-CCHP system [157].

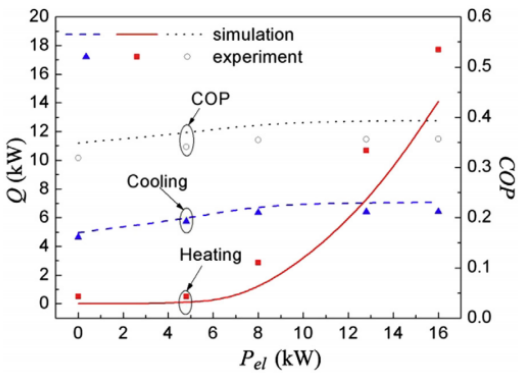

Figure 74. Influence of electric output on heating and cooling output [157].

This depends on the buffer tank set point temperature and hot water tank set point temperature. The heating load is controlled by fan coil 2 and fan coil 3, whereas the cooling load by fan coil 1. The model of ICE is based on the statistical data provided by ASHRAE for naturally aspirated small ICE. The authors assess that experimental results agree with the simulative results. It resulted that with the help of TMC, the system can realize 17.7 kW heating output, 6.5 kW cooling output and 16 kW electric output simultaneously (Figure 74). In particular, as shown in this figure, when the electric output is low, the heating output is nearly 0, namely all the waste heat is absorbed by the adsorber. When the electric output is over 6.4 kW, the heating output starts to increase while the cooling output and COP of adsorber both change slightly. Namely, when the electric output is over 6.4 kW, the waste heat recovered by TMC exceeds the heat transfer capacity of the first stage and part of waste heat is assigned to the second stage.

A further application regarding the simulation of a small size ICE, by the Aspen Plus software, is investigated by Chen et al. [86]. In particular, here the waste heat contained in the jacket water (at 90 °) and exhaust gas (at 500°C) of 300 kW ICE is efficiently recovered to generate power and cooling energy simultaneously, by an ammonia-water system. The waste heat carried by the exhaust gas and the jacket water reach 36.7% and 23.0% of the energy input, respectively. The results show that, at rated load, the heat recovered from the exhaust gas and jacket water is 242.80 kW and 180.47 kW, respectively. The turbine work reaches 35.61 kW, and the net power output of the combined system is 14.76 kW. In addition, the refrigeration output is 225.72 kW. The equivalent heat-to-power efficiency of the combined power and cooling system is 19.76%. The total equivalent power output is quite high, 92.86 kW. From the carried out exergy and economic analysis results that the exergy efficiency and the payback period of the proposed system are respectively, 33.69% and 2.84 years.

A combustion engine included in a CHCP system for a small supermarket was simulated by Maidment et al. [160]. The combustion engine produces: i) electricity to drive a low-temperature vapour-compression refrigeration cycle and operate store lighting, equipment and the HVAC system; ii) heat, recovered by heat exchangers from engine jacket and exhaust gas, used to satisfy the space-heating and hot-water demands; iii) cool, by an ACH used to refrigerate propylene glycol to −10°C for cooling the chilled-food cabinets in a supermarket. A gas-fired boiler is also included in the system to supplement the heat provided by the combustion engine when necessary and a waste-heat exchanger is used to reject unwanted heat to the atmosphere. The carried-out investigation has shown that this configuration to be extremely efficient, as PES of 20% are achievable. A payback period of 6 years has been calculated. For larger stores, better payback periods, between 4 and 5 years, may be achieved as the unit cost of the ACH significantly reduces.

Sibilio et al. [90] simulated an innovative building-integrated micro-trigeneration system, based on a 6.0 kW_e / 11.7 kW_{th} natural gas-fuelled ICE micro-cogeneration unit feeding an electric air-cooled vapour compression water chiller for heating, cooling and DHW purposes in a multi-family house (Figure 75). The same plant configuration is simulated also in [161], by evaluating the energy, environmental and economic effects of electric vehicle charging. The feasibility of the investigated trigeneration plant was dynamically investigated by the developed model using the simulation software TRNSYS, by comparing it with the conventional separate energy production (a natural gas-fired boiler, air-cooled water electric chiller, electric grid). The proposed system also includes

a hot water tank with three internal heat exchangers, an auxiliary boiler, an electric air-cooled water chiller, a heat exchanger, thermostats, pumps, diverters, and a group of fan-coils installed in the building. The model of the ICE unit was calibrated and validated based on measured data and it is based on the operation strategy following the heat load. The system was analysed for three different Italian cities (Palermo, Naples and Milan), by evaluating the equivalent CO_2 emissions, PES and operating costs (OC). The Figure 76 highlights that PES ranging from 0.2% to 4.3%, ΔCO_2 ranging from 3.9% to 10.6%, ΔOC ranging from 11.3% to 19.9%, with the best results in Milan. Although the PES and ΔCO_2 are negative during summer, the system allows to reduce the electric load peaking of electric grid, alleviating the risk of network congestion and failure events.

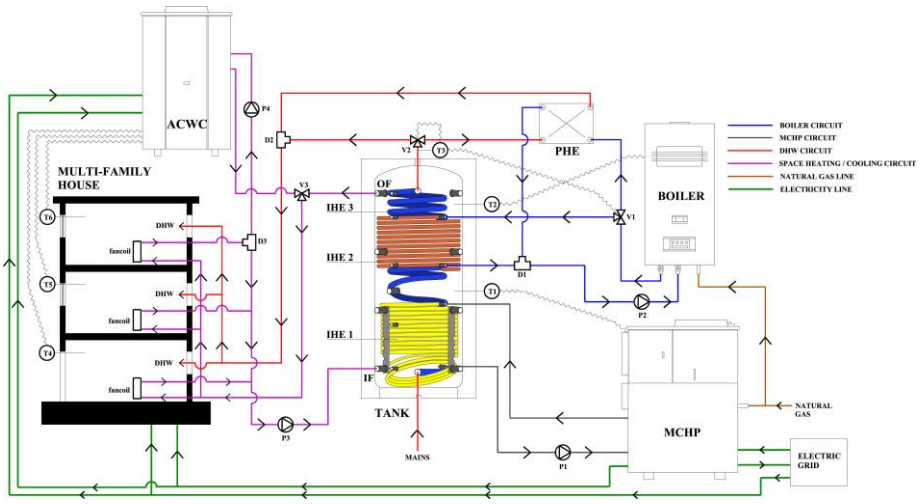

Figure 75. Scheme of the proposed system in [90].

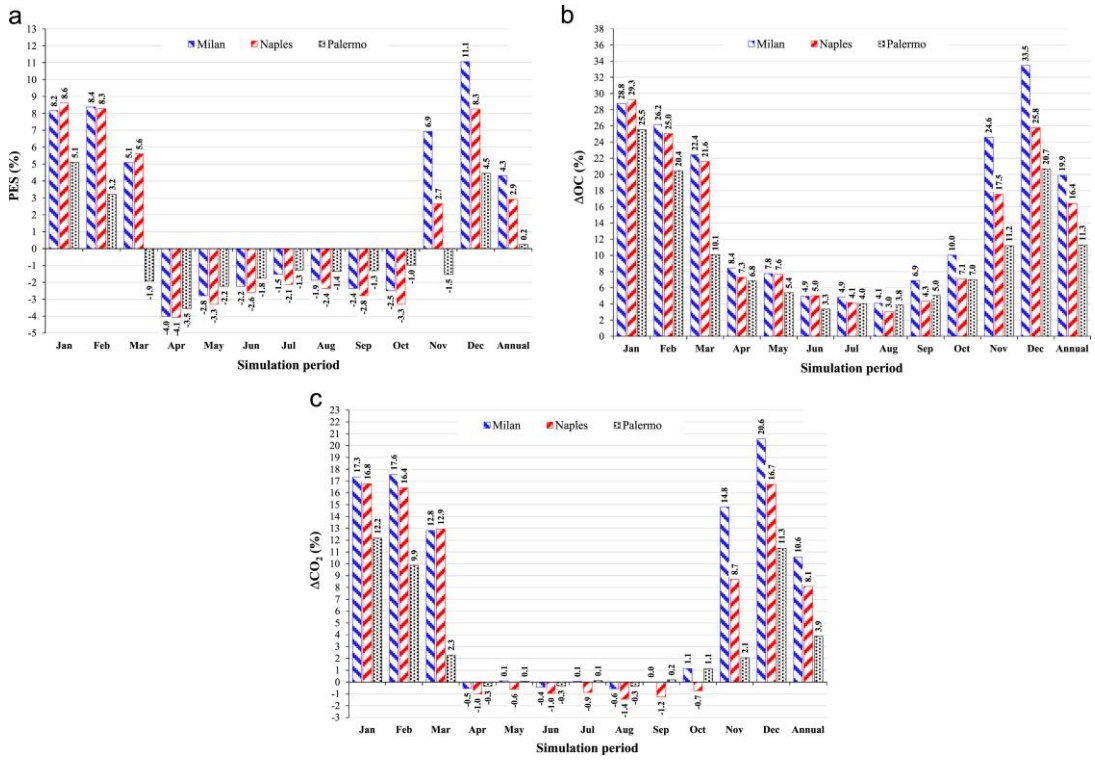

Figure 76. Values of (a) PES, (b) ΔCO_2 and (c) ΔOC for the three investigated city [90].

Rey et al. [162] designed, built, tested and dynamically simulated a gasoline ICE micro CHP system, whose exhaust gases and engine cooling fluid are recovered for a recreational sailing boats used as mobile homes. The system, producing heating, DHW and electricity, was designed to work independently, and therefore no auxiliary system was considered, whereas an electricity and thermal energy storage to match the demand and production were included (Figure 77).

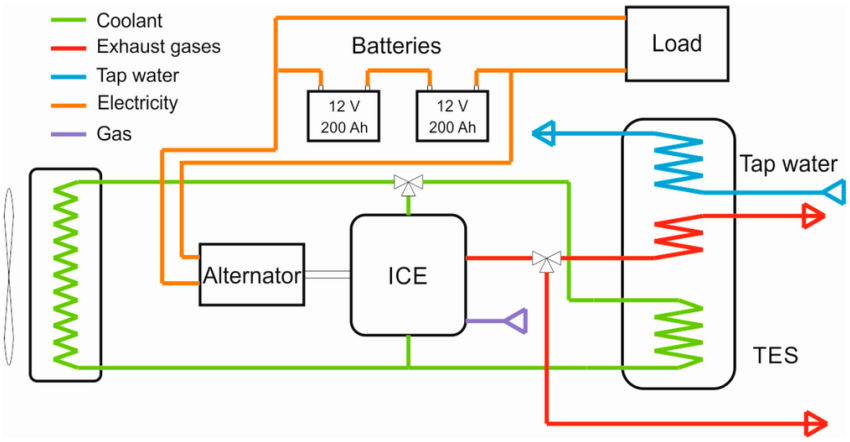

Figure 77. ICE-based micro CHP unit layout [162].

In order to model and simulate the micro-CHP system TRNSYS simulation software was used. The performance of the ICE was compared with similar system based on a Stirling engine (SE). The transient simulations were performed by considering the boat under three different European climates (Helsinki (Finland), Breskens (The Netherlands), and Malaga (Spain)) and the electricity storage size variation. Authors present their experimental results showing electric and thermal capacities of ICE system equal to 0.653 kW and 5.414 kW, respectively. From the simulations, it resulted that the system guaranteed the heat demands in all studied climates. The results of SE and ICE were similar as for electric and thermal energy production, for all the locations because the simulations are performed by the following thermal load control strategy. The slight differences in heat production results are due to the small differences in heating power of the two systems (5.93 kW for SE). Annual electric coverage never reaches 100% (Figure 78). Nevertheless, ICE supplies less electricity because of its lower electric/thermal energy flow rate ratio: 13% compared to 15% with SE. The parametric analysis showed that the optimal capacity of the electricity storage system was double with respect to the initial configuration (24 V/100 Ah), leading to a significant increase (up to 11% for Malaga) of the electric production.

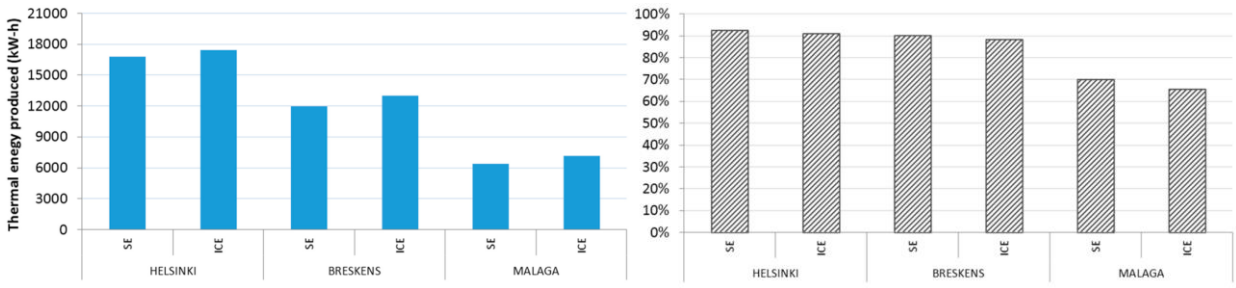

Figure 78. Annual thermal production in kWh (left) and electric coverage (right) [162].

3.2.6 Fuel cells (FC)

Fuel cells are based on direct conversion of several types of fuels into electricity, without any mechanical drive or generator, by coproducing heat and other outputs which make them attractive for polygeneration applications (Figure 79). These are well-known as the most efficient small-scale power plants, by showing high electric efficiency (up to 60%) and overall efficiency (up to 90%) [90]. They have several benefits, such as almost zero emissions, a good match with the residential thermal to power ratio, reliability, quiet operation, potential for low maintenance, excellent part load management [163, 164].

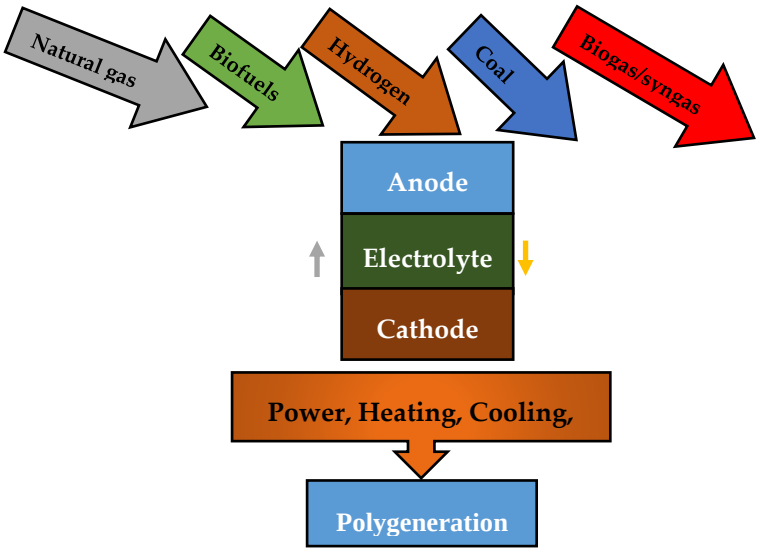

Figure 79. Polygeneration system based on FC technology.

Therefore, their integration within polygeneration systems for power generation is particularly attractive. The work carried out by Soutullo et al. [79], reported above, is not the only one considering the integration of FCs into polygeneration systems. In fact, a number of possible configurations are investigated in literature, such as solid oxide fuel cells (SOFC) [165] or PEMFCs [166] integrated with solar heating and cooling systems, as well as PEM integrated with CPVT and an electrolyzer. This last configuration was dynamically simulated in TRNSYS environment and analysed from the energy and economic point of view in the work of Calise et al. [167]. In fact, this polygeneration system consists of a 600 m^2 CPVT field (PTC with triple-junction solar PV cells), PEMFCs (180 kW_e and 153 kW_{th}), a 375 kW single-stage $LiBr/H_2O$ ACH, a 216 kW_e alkaline water electrolyzer and an auxiliary gas boiler (Figure 80) and produces space heating / cooling, DHW, electricity for a small real university building. In particular, the electrolyzer system is powered only by the CPVT electricity and produces hydrogen, used to supply the FC and oxygen, which, instead, is sold. The results of yearly dynamic simulations, obtained for Naples (South Italy) regarding system efficiency and economic parameters achieved are reported in Table 11. CPVT thermal efficiency, calculated with respect to the beam radiation, is 63.4%. The electric one is 19%, due to the use of a multijunction PV cells. The overall efficiency at full load of the FC is 78.4%. 26.8% of the electric energy supplied by CPVT to produce hydrogen is dissipated due to the EL inefficiencies.

The yearly mean ACH COP is about 0.70. In case of a capital investment subsidy of 50%, SPB significantly decreases to about 6 years, in such a way the system can became profitable. A parametric analysis on the PEMFC electric power variation is also carried out, and from the economic point of view results that when an optimal FC nominal power of 100 kW is selected, SPB in case of incentive, is about 5 years. Therefore, global results of this work prove the technical and economic feasibility of such innovative polygeneration system, considered as an efficient design option for several possible users.

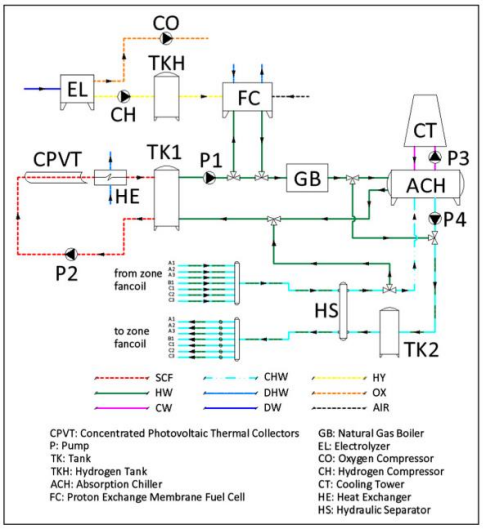

Figure 80. System layout [167].

Table 11. Efficiency and economic parameters, yearly results.

Parameter	Value	Unit
$\eta_{th,CPVT}$	0.634	–
$\eta_{el,CPVT}$	0.189	
$\eta_{th,FC}$	0.434	
$\eta_{el,FC}$	0.35	
η_{EL}	0.732	
COP_{ACH}	0.729	
SPB	12.5	years
SPB with 50% subsidy	5.84	

A polygeneration microgrid including a lead acid battery bank, wind turbine, monocrystalline PV panels, a Proton Exchange Membrane (PEM) fuel cell, a PEM electrolyzer, a metal hydride tank, a reverse osmosis (RO) desalination unit using energy recovery, a H_2 vehicle and control system was simulated in TRNSYS 16 [168]. In particular, the hydrogen vehicle is a hybrid fuel cell – battery scooter with an average hydrogen consumption of 2.4 Nm^3/100 km. The polygeneration microgrid covers the electricity and potable water needs for two households and, by producing hydrogen, covers also the transport need. This is considered to be installed on a small island in the Aegean Sea, Greece. In this work, the proposed system was evaluated from the economic point of view (by evaluating NPV and SPB) and a detailed optimization procedure aiming at low investment

and operational cost, was also carried out. Results showed that, due to current high H_2 operating cost, it was preferable to store the produced electricity in a bigger battery bank (1000 Ah at 48 V), by reducing the size of the H_2 electricity storage. The FC optimal size resulted equal to 300 W, therefore, FC is used as a backup energy producer, since its produced energy is significantly lower with respect to the ones produced by PV panels and wind turbine (Figure 81). In any case, the authors state that this result does not suggest removing FC in their configuration, since the use of FC electricity avoids to completely discharge the battery and the problems connected with inverter synchronization operation. Therefore, the employment of the fuel cell is considered as necessary. The NPV for the polygeneration micro grid is 21,236 €.

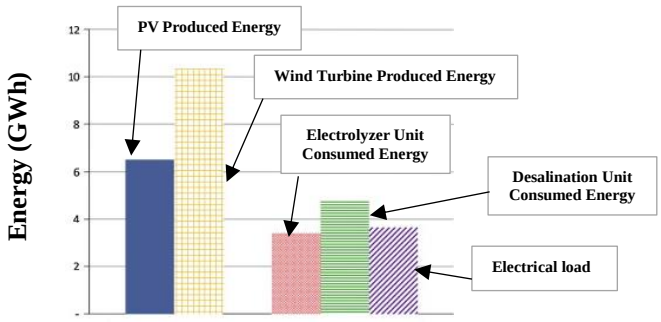

Figure 81. Yearly produced and consumed energy [168].

The previous papers investigated FC polygeneration systems as hybrid systems, that is, the FC integration into another electricity generation system. Whereas an application regarding polygeneration systems based on SOFC as prime mover solely is carried out in reference [169]. Here, a planar 5-kW low-temperature SOFC polygeneration system, based on nanocomposite materials, is designed and analysed. The SOFC operating temperature reaches 550°C and its power density is 0.4 and 0.7 W/cm^2 in the case it is supplied by hydrogen or syngas, respectively. In this work, the system design and the energy and mass balances, based on lumped-parameter model, are presented and a simulation based of the use of syngas as input fuel is performed. The simulation results showed that the SOFC electric and thermal efficiencyare equal to 19.5% and 57.6%, respectively. In addition, the authors state that there is a considerable amount of heat at the FC outlet, which can be harvested for further use despite the fact that this SOFC has lower operating temperature than common SOFC systems. Therefore, there is a high potential in low temperature SOFCs for polygeneration application because they do not have the common problems of high temperature SOFCs and are less expensive. Besides, usage of waste heat of the SOFC stack enhanced the efficiency to about 75% based on the operating parameters.

Becker et al. [170] presented the model, design and techno economic performance analysis of a 1 MW SOFC polygeneration system for combined production of heat, hydrogen, and power. The system was simulated by Aspen Plus™ in order to calculate system and components thermodynamic performance. SOFC electric efficiency at rated power is estimated at 48.8% and the overall plant efficiency is 85.2%.

In references [171, 172], the trigeneration system proposed is based on SOFC, which was completely analysed by energetic, exergy and exergoeconomic point of view. Heating and cooling production is performed by recovering heat from the gases exiting the SOFC. As regard the energy

analysis, authors investigated the influences of two significant SOFC parameters, such as current density and the inlet flow temperature, on several output variables are. Findings show that the minimum energy efficiency of the trigeneration system is 33% higher than the SOFC power cycle one. Furthermore, the maximum energy efficiencies are 79% in case of trigeneration, 69% in case of power-heat cogeneration, 58% in case of power-cooling cogeneration and 46% in case of electricity production. The maximum trigeneration exergy efficiency is about 47%. The exergy analysis showed that the main exergy destructions occur in the air heat exchanger, the SOFC stack and the after burner, which was supposed to oxidize all the non-reacted gases exiting the SOFC. As regards the exergoeconomic analysis, authors investigated the effects of three important SOFC parameters, such as the current density, inlet flow temperature and fuel utilization factor, on several output variables such as the unit cost of the electric power, the unit cost of the cooling and the unit cost of the heating and total unit cost of the products.

3.3 By-products of polygeneration systems

The majority of the systems shown above report the analysis of polygeneration systems where the main goal of the system is the production of energy vectors. However, several other studies presented novel polygeneration systems which were purposely developed in order to produce a specific product. In particular, the potential outputs of polygeneration systems can be power, space heating and cooling, DHW, chemical products, desalinated water, synthetic fuels, etc. and depend on the inputs and user demands. Several simulation models are available in literature regarding polygeneration systems aiming to produce desalinated water. In fact, in many polygeneration plants, the desalination technologies fuelled by thermal energy, could be economically profitable when fed by heat wastes recovered from power plants through cogeneration [173]. For example, a polygeneration scheme based on 24.7 MW natural-gas GT exhaust heat conversion to drive a seawater RO desalination process was adopted in [174]. In particular, GT cycle is thermally coupled to a bottoming ORC, mechanically coupled to the RO unit. The system was developed for on-site hydrocarbon production applications in Arabian Gulf.

The thermodynamic performance of the combined power cycle and of RO process are calculated by Aspen process modelling software V8.4 and Dow Chemical Company RO System Analysis (ROSA) software, respectively. The energy, exergy and economic analyses are carried out for four organic fluids but are mainly focused on octamethyltrisiloxane, which yields 6 MW of net power output at ideal and overall exhaust gas heat recovery efficiencies of 14% and 10%, respectively, 37 MW of process heat, and 1380 m^3/hour of permeate. The reverse osmosis unit operates at a specific energy consumption and exergy efficiency of 4.1 kWh/m^3 and 29%, respectively. The exergy efficiency of the polygeneration system is estimated at 32%, thereby enhancing the efficiency of the original GT power generation system by 6%. The system becomes profitable after approximately 3 years for subsidized local water and prices.

Rather than waste heat obtained by a fossil fuel prime mover as shown in the previous work, the use of renewable energy sources (solar, biomass, geothermal) to power desalination processes in polygeneration systems was also emphasized. In fact, an interesting study of dynamic simulation, carried out by TRNSYS software, regards a solar MED polygeneration system [175]. In particular, in this study a PTC field coupled to a 50 MW_e power Rankine cycle is considered. The necessary amount of heat to drive the MED unit, modelled by using Matlab software, is provided by Rankine

cycle condenser. The system was dynamically simulated and analysed from both thermodynamic and economic points of view and for two case studies, Venezuela and northern Chile. It was found that the polygeneration system can provide electricity and water for more than 85,000 inhabitants at favourable prices, increasing the total plant annual cost of only 6%-12%. The plant was also optimized, and it resulted that the optimum configuration would produce 29,323 m^3/day for Venezuela and 22,160 m^3/day for Chile, and could supply electricity and freshwater to 117,000 and 87,000 inhabitants respectively.

A further study regards a solar thermal polygeneration system integrating membrane distillation was also investigated by Mohan et al. for United Arab Emirates locations [176]. Here, with respect to the previous solar polygeneration system, the solar energy is directly provided to the desalination unit, as shown in Figure 82.

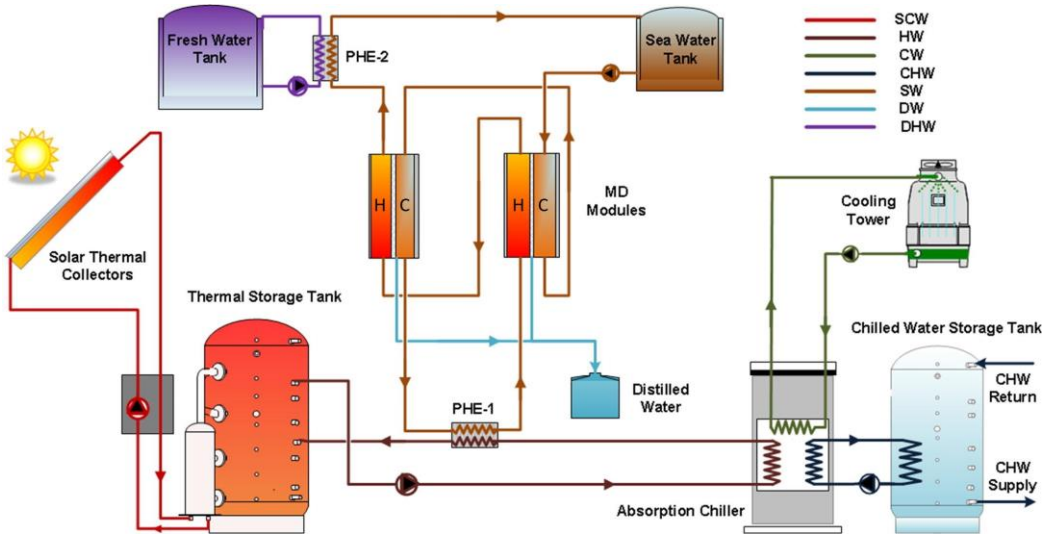

Figure 82. Schematic layout of solar polygeneration system [176].

A 35.2 kW single stage LiBr/H_2O ACH is also include in the system in order to meet the cooling load in a portacabins building, modelled in TRNBUILD and located in Rakric. The whole system, designed for also producing DHW as coproduct, is modelled in TRNSYS environment and validated by the experimental data achieved from on-site testing of polygeneration system. In this study, three different solar technologies were compared: flat plate, evacuated tube and compound parabolic collectors. Dynamic simulations, developed in TRNSYS environment, showed that the best pay-back value, equal to 6.75 years, was achieved in case of evacuated tube collectors having gross area of 216 m^2. The best performance in terms of daily production of membrane distillation and DHW production 92.8 kg/day and 301.67 kg/day, respectively.

Alternative configurations were also studied by replacing or coupling the solar collectors with geothermal wells. Such kind of polygeneration system results optimal to operate in some of the several small volcanic islands, where the availability of solar and geothermal energy is high whereas the availability of fresh water is scarce and its cost consequently high [77]. This idea was also investigated in the works reported in references. [77, 88, 113, 114].

In the framework of polygeneration systems, the conversion of fossil fuels or of renewable energy source, aiming at producing useful chemical products and reducing the environmental pollution, mainly in the transportation sector, has recently attracted a significant interest. Among the numerous possible chemical coproducts of a polygeneration plant (depending by the configuration, technique and input), several works are focused on the production of methanol [82, 87, 92], ethanol [81, 84, 102, 139] and hydrogen [94, 140, 144, 167].

The integration of a methanol-producing biorefinery with an existing CHP unit and a local industry (butchery) in the Danish city of Horsens is designed and optimized in reference [177]. In this work, the concept of flexible multi-generation system (FMG, defined as integrated systems that generate multiple energy services and are able to adjust operation in response to fluctuating demand patterns and varying price schemes in the overarching energy system) is highlighted. FMG was developed for producing methanol from renewable biomass, in particular wood chips, and covers the local district heating demand and the thermal utility demand of the butchery. Technologies considered include a two-stage biomass gasifier, a solid oxide electrolysis cell, a methanol production facility, industrial heat pumps, and novel heat and gas infrastructures. To simulate each system component the energy system modelling tool SIFRE is used; a detailed procedure of optimization with the aim of maximizing NPV and minimizing the total CO_2 emission impact, is also described. For the optimized design, the NPV was estimated to vary within the range 252.5–1471.6 M€ in response to parameter value changes of ±25% of investments costs and methanol price that has a significant impact on the FMGs estimated performances. In addition, a change in the applied interest rate from 5% to 20% in the reference scenario would reduce the NPV to 181.3 M€.

A techno-economic analysis of a polygeneration plant which coproduces methanol through methanol synthesis, diesel, gasoline and a sizeable amount of electricity, by converting coal and natural gas is presented by Adams and Barton [178]. In this work, a new strategy regarding the natural gas reforming for efficient polygeneration systems is also proposed. In particular, this strategy, defined ‘’internal reforming’’ is based on fact that the gasifier cooling is provided by reforming of natural gas, rather than generation of steam. Simulations show that the ’’internal reforming’’ provides increased energy efficiency and can be the optimal design choice in many market scenario. In particular, internal reforming had up to 2% points more efficiency than external one due to the improved heat integration when about half or more of the output was liquid fuels.

Regarding the ethanol production, a research work aiming at analysing the effects of introducing a lignocellulosic ethanol polygeneration plant into the district heating system in Stockholm, Sweden, was carried out [179]. The plant has an ethanol capacity of 95 MW with biogas, electricity and heat as coproducts. The system was studied using MODEST, a model framework based on linear programming, developed for optimisation of dynamic energy systems with time-dependent components and boundary conditions. The results show that such system would produce 110 GWh of electricity annually and furtherly, income from the sale of the biofuels and electricity produced would be about €76 million and €130 million annually, respectively, which is an increase of 70% compared to the income from the electricity produced in the system today. A reduction in global CO_2 emissions of about 0.7 million tonnes annually, would be also reached. If the electricity price would increase by 20%, the system global CO_2 emissions would be even lower and the income from the sold coproducts would be about €232 million annually.

Hydrogen production is another interesting process coupled to a polygeneration systems [180, 181]. H_2 is used to produce electricity with low carbon emissions in a GT [182], or in SOFCs [183, 184]. Alternatively, H2 can be properly used for PEMFCs. In this case, high purity H2 is needed. Pure hydrogen is generated from syngas by the pressure swing adsorption (PSA) technique, with 85% hydrogen separation efficiency [185, 186].

An interesting polygeneration system, aiming at producing hydrogen, oxygen, power, heat and cool, involving the application of both fossil and renewable energy sources is investigated in [187]. Here a solar power tower is combined with a coal gasification system, a GT fuelled by syngas, a ST supplied by wasted heat of GT cycle, a single effect ACH, a hot water production unit, and a hydrogen production unit (Figure 83).

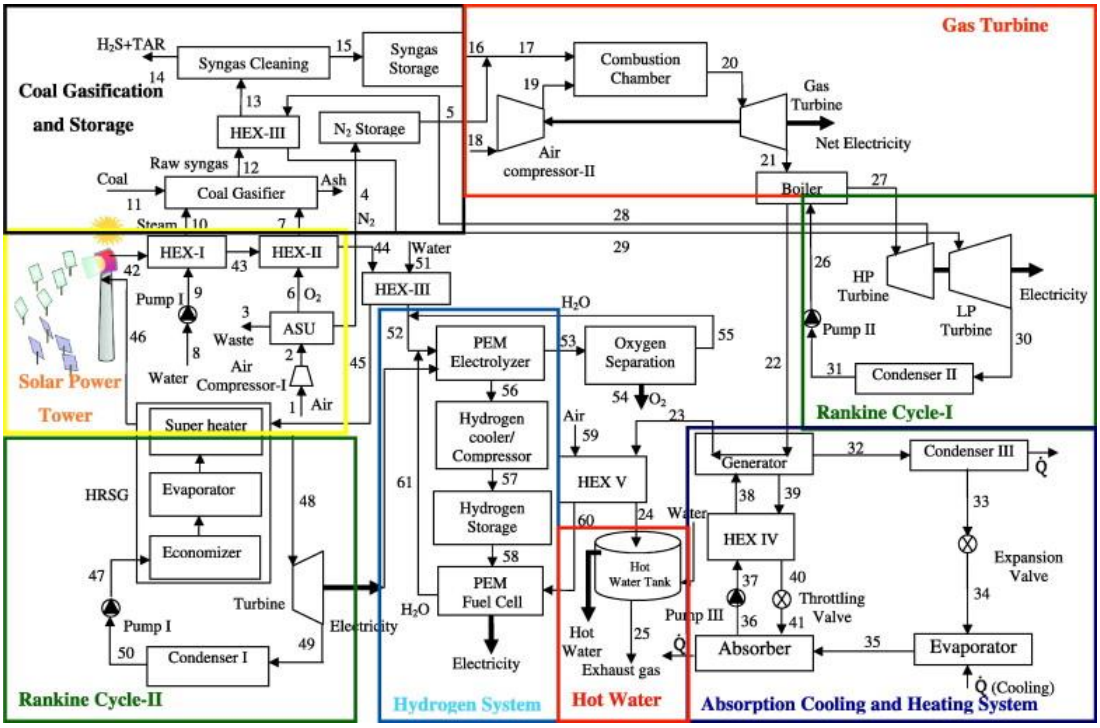

Figure 83. Schematic diagram of the multi-generation energy production system [187].

In particular, the heat produced from the solar tower is converted by a Rankine cycle into power, in turn used to supply an electrolyser which produces hydrogen. The thermodynamic properties of the working fluids involved into system are calculated by using EES software. The energy efficiencies for the different sub-systems, i.e. coal gasification system, Rankine cycles, GT system, ACH and heating unit, hydrogen production unit, and of the overall multi-generation system, were evaluated, from both the energetic and exergy point of view. In particular, regarding the hydrogen production, the reached energy and exergy efficiencies were equal to 19.43% and 14.41%, respectively; the obtained energy and exergy efficiencies of multi-generation system were equal to 54.04% and 57.72%, respectively.

Chapter 4 Polygeneration systems for building

Trigeneration and polygeneration systems are currently considered as a viable opportunity for energy saving in buildings; in particular technologies able to provide to the Buildings Combined Cooling, Heating and power (BCCHP) are often considered [154]. In fact, the integration of small polygeneration systems based on renewable energy technologies, mainly the solar ones, within buildings is of crucial importance for the reduction of energy consumptions in buildings, which is responsible for about 40% of global energy consumption. In the last few years, the share of energy consumption of the residential sector surpassed that of industries, contributing to about 46% of the EU global greenhouse gases emissions. Therefore, polygeneration systems can be designed at lower capacity levels, in order to integrate them in small buildings or single family houses. The design of small-scale, efficient systems is crucial to achieve the targets in terms of reduction of fossil fuels and emissions. Therefore, the development and the adoption of building energy performance simulation (BEPS) tools is crucial and highly recommended for promoting the building integration of renewable energy technologies, toward the design of the next generation of buildings (e.g., NZEBs).

In this framework, the integration of solar technologies within the building in polygeneration systems [25, 88, 121, 123], as well as the use of natural-gas-driven BCCHP systems [88, 89, 188-190], have been widely investigated.

In the following subsections (4.1 and 4.2), some studies regarding the simulation, the modelling and the energy, exergy, economic and environmental analysis of this kind of polygeneration systems for several building applications, are reported. In such studies, the system performance was evaluated by taking into account the hourly weather data and hourly power, heating and cooling loads of the users simulated. Therefore, the analyses were performed by a dynamic simulation tool, the well-knew TRNSYS software. Such software, diffusely adopted by the academic community, enables transient energy simulations, providing a library of built-in components (e.g. pumps, mixers, diverters, valves, controllers, auxiliary heaters, heat exchangers, etc.) often based on experimental data [191]. This methodology has been successfully adopted to perform dynamic analyses of several solar systems [192, 193]. Therefore, all the obtained simulations results can be intrinsically considered as reliable for carrying out simulations of building energy performance [194].

4.1 Dynamic simulation of polygeneration systems coupled to BIPVT solar collectors for several building applications: energy, exergy, economic and environmental analysis

Study 1

Applications: Residential **Analysis:** Energy and economic

Technologies: roof and façades BIPVT solar collectors, heat pumps/chillers, gas-fired condensation boiler

The case study concerns the comparison among innovative building-plant system configurations, based on BIPVT collectors for the polygeneration of electricity, space heating and DHW. In particular, in this study, partially reported in reference [29], the energy and economic performance analysis of BIPVT collectors was carried out, to assess the summer and winter active and passive effects on energy consumptions due to building integration of solar technologies. Energy and economic simulation models of the layouts under evaluation were designed and implemented in TRNSYS 17. The model, including all the components required for operating the system, also includes suitable control strategies for the maximization of system energy utilization in all the operating conditions and the calculation of space heating and cooling demands, on the basis of a 3-D building model, implemented in TRNBUILD (included in the TRNSYS package). In particular, the analysis carried out is referred to:

- 4 different configurations, namely: Case A) conventional building without PVT (reference case); Case B) stand-alone PVT collectors; Case C) roof BIPVT collectors; Case D) roof and south-façade BIPVT collectors;
- different values of many design parameters regarding the building envelope, with the aim to study their influence on the primary energy demand for space heating and cooling, DHW and electricity production;
- 16 different European weather conditions.

The energy and economic analysis carried out in this study is completely new, with respect to the literature review reported in subsection 2.3, in fact, none of the papers available in literature investigated both active and passive effects related to the BIPVT by means of dynamic simulations of the building-plant system as a whole.

System layout - Study 1

The BIPVT system considered consists of flat-plate PVT collectors, integrated into the building roof and/or south-façade of a 3-floor residential building, consisting of three different thermal zones. A description of the configurations analysed is provided in Figure 84:

Case A: Conventional building without PVT collectors. Here, electric air-to-water Heat Pumps/chillers (HP) provide space heating and cooling, whereas DHW is obtained by means of a gas-fired Condensing Boiler (CB).

Case B: In this building system configuration, a stand-alone PVT (unglazed) solar field (sited on a land adjacent to the building) is taken into account. The hot water produced through the PVT collectors is supplied to a heat storage TanK (TK), through an internal Heat Exchanger (HE1). During winter, TK hot water is exploited through a suitable Radiant Floor (RF) for the space heating

of the thermal Zone 3. Depending on the availability of solar radiation, the RF heating capacity may be also lower than the Zone 3 heating demand. Therefore, suitable auxiliary systems (electric HP units) are taken into account. The heat pump works in parallel with the RF (independently by PVT collectors/TK system) in order to adequately control the indoor air temperature. Space heating in Zones 1 and 2, and space cooling in all the three building zones, are only provided by the HP (similarly to the reference Case A). In the heating season, internal heat exchanger, HE2, (used for DHW preparation) is often bypassed, i.e. the solar heat is supplied in priority to the Zone 3 RF. Conversely, when the RF is not active (e.g. in summer or when the indoor temperature is higher than the selected set point), the solar thermal energy stored in the TK is used to preheat the DHW by means of HE2 (included in TK). In this case, tap water supplied by the grid is preheated through HE2.

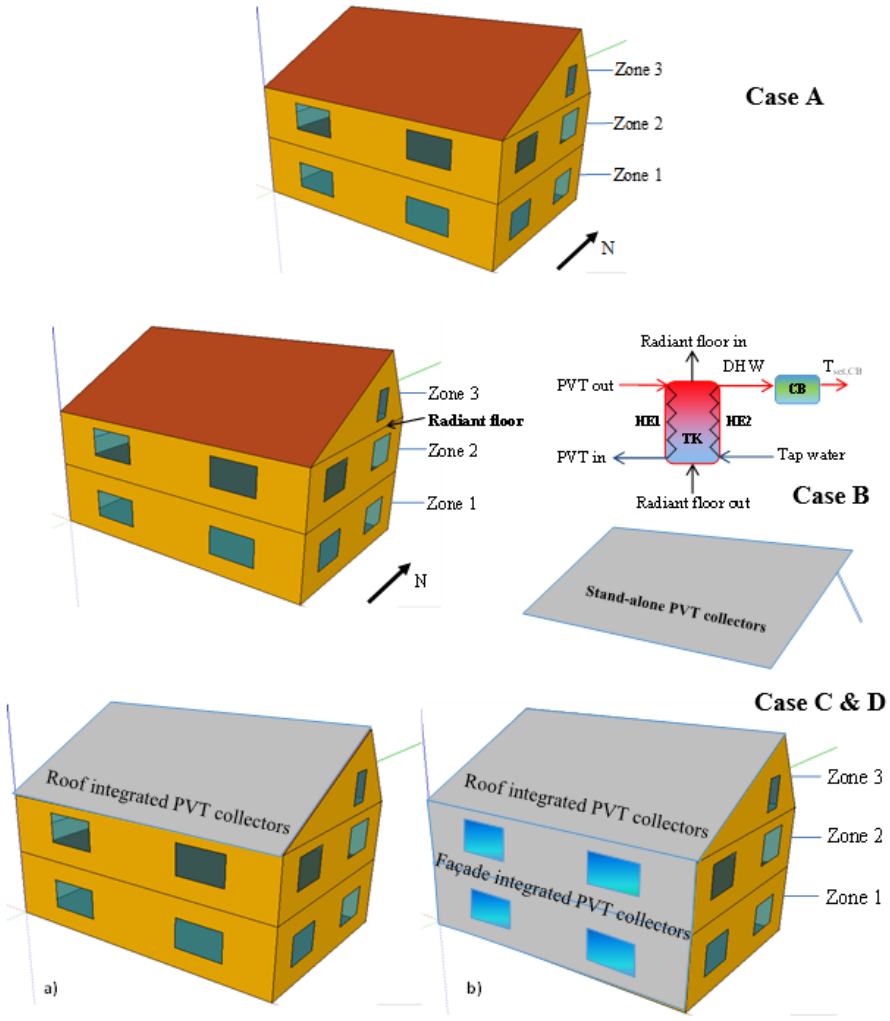

Figure 84. Cases A-D.

Case C: Here, a south-facing roof unglazed BIPVT collectors field (with the same area as Case B) is taken into account. The back surface of the collectors coincides with the external surface of the tilted roof. Such arrangement is compliant with the Italian legislation, which requires the installation of solar collectors as integrated (or adjacent) to the building external surfaces.

Case D: In this building system configuration, a south facing roof and south-façade unglazed BIPVT collectors field is taken into account. For the roofing integration the same solar field area as

Case B and C is assumed, whereas an additional BIPVT area is modelled for the building façade. In order to achieve an optimal control of the output temperature, the modelled BIPVT collectors are equipped with three different separate water circulating loops.

The system layout for Cases B, C and D is depicted in Figure 85. In particular, three main system loops are modelled:

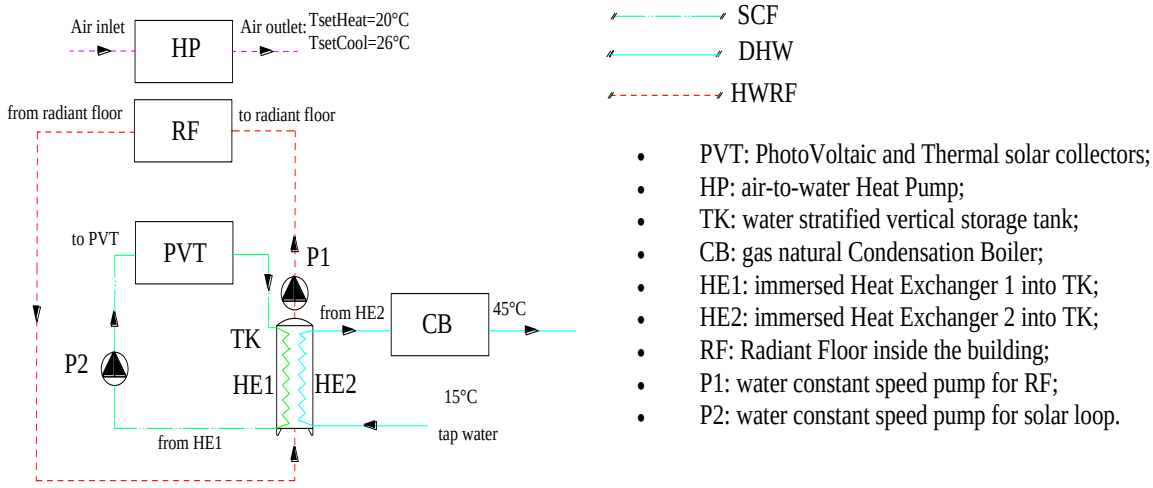

Figure 85. Plant layout.

- SCF (Solar Collector Fluid) loop – the outlet hot water from the PVT solar field is supplied by means of a water constant speed pump (P2) to a water stratified vertical energy storage TK through the internal heat exchanger HE1;
- DHW (Domestic Hot Water) loop – the tap water from the grid is preheated through the heat exchanger HE2 and heated to the DHW set point temperature by a gas-fired condensation boiler, CB (activated if necessary);
- HWRF (Hot Water of the Radiant Floor) loop – the outlet hot water from TK is supplied by means of a water constant speed pump (P1) to the Zone 3 RF for indoor space heating.

The operating principle of the systems under study and the related control strategies can be summarized as follows. The PVT collectors are managed by a suitable controller operating on the P2 pump. Such controller receives temperature readings from the outlet of HE1 heat exchanger (i.e.: the solar collector inlet temperature) and the outlet pipe of the solar collector loop. Hot water produced by the solar loop is supplied to TK through HE1. The controller stops P2 pump when solar collector outlet temperature is lower than inlet one, in order to prevent heat dissipation. CB is activated only if the outlet water temperature from the HE2 heat exchanger is lower than DHW set point one. HE2 volume is sufficiently high for fulfilling the required DHW storage capacity (see Table 12, V_{HE2}/V_{TK}). The tap water enters HE2 only if: i) no thermal energy is required by the RF (i.e. when the P1 pump is off); ii) a simultaneous occupants DHW demand occurs (see Table 13). Therefore, a suitable controller manages the activation of the P1 pump. In particular, such controller receives temperature readings from the top of TK and from the indoor air of the thermal Zone 3 (where the RF is installed). The controller produces the ON signal for the pump activation if: i) the TK top temperature is higher than $T_{TK,topSET}$ (Table 12); ii) the indoor air temperature of the Zone 3 is lower than $T_{in,RF}$ (Table 14). Hot water from the top of TK directly supplies the RF for space heating.

Table 12. Main system design parameters.

	Parameter	Description	Value	Unit
SOLAR FIELD	$A_{SC\ Roof}$	BIPVT Solar Collector roof aperture area (PVT for Case B)	125	m^2
	$A_{SC\ 1/2}$	BIPVT Solar Collector façade aperture area (Zones 1 and 2)	45.0/37.5	m^2
	q_{P2}/A_{PVT}	P2 rated flow rate per unit of BIPVT aperture area	10	kg/h m^2
	λ_{abs}	Thickness of the absorber plate	0.3	mm
	k_a	Thermal conductivity of the absorber plate	385	W/mK
	N_{tubes}	Number of identical fluid tubes bonded to the absorber plate	700	-
	W_b	Average bond width (between tube and absorber plate)	0.01	m
	k_b	Thermal conductivity of the bond	385	W/mK
	R_1	Thermal resistance of the material between PV cells and absorber plate	0.04	m^2K/W
	R_b	Thermal resistance of the panel back material (Case B)	2.50	m^2K/W
		Thermal resistance of the panel back material (Case C, D)	0.04	m^2K/W
	λ_p	Thickness of the panel back material (Case B only)	0.10	m
	k_p	Conductivity of panel back material (Case B only)	0.04	W/mK
	b_0	Incidence angle modifier: 1st order coefficient	0.10	-
	ρ_s	Reflectance of the collector surface at normal incidence	0.15	-
	ε	Emissivity of the collector surface	0.90	-
	η_0	PV efficiency at the reference condition	12	%
	β_{wall}	Collector slope (façade integrated)	90	°
	β_{roof}	Collector slope (roof integrated)	30	°
	α	Collector azimuth	0	°
	Eff_T	Efficiency modifier temperature	-0.005	1/°C
	Eff_G	Efficiency modifier radiation	$7.0 \cdot 10^{-6}$	m^2/W
TANK	H_{TK}	Height	2	m
	q_{HE1}/A_{PVT}	Heat Exchanger 1 flow rate per unit of BIPVT aperture area	10	kg/m^2h
	q_{HE2}	Heat Exchanger 2 maximum flow rate	117	kg/h
	$V_{HE1/2}/V_{TK}$	HE1 and HE2 volume per unit of TK volume	1/20	-
	$T_{TK,topSET}$	Tank TK top temperature for radiant floor activation	22	°C
BOILER	$P_{CB,rated}$	Rated CB heat power	25000	W
	$\eta_{RS,DHW}$	Efficiency of the condensation boiler (also for RS = Case A)	95	%
	q_{DHW}	DHW flow rate per person	65	l/p day
	$T_{set,CB}$	CB outlet set point temperature	45	°C
HEAT PUMP/CHILLER	COP_N	Nominal coefficient of performance (heating)	3.5	-
	EER_N	Nominal energy efficiency ratio (cooling)	3.0	-
	Milan and Freiburg		**Heating**	**Cooling**
	$P_{heat/cool,rated1}$	Rated heating and cooling capacity for zone 1	9840 W	7880 W
	$P_{heat/cool,rated2}$	Rated heating and cooling capacity for zone 2	8440 W	6750 W
	$P_{heat/cool,rated3}$	Rated heating and cooling capacity for zone 3	5270 W	4220 W
	Naples and Almeria		**Heating**	**Cooling**
	$P_{heat/cool,rated1}$	Rated heating and cooling capacity for zone 1	7880 W	6300 W
	$P_{heat/cool,rated2}$	Rated heating and cooling capacity for zone 2	6750 W	5400 W
	$P_{heat/cool,rated3}$	Rated heating and cooling capacity for zone 3	4220 W	3370 W

Table 13. Simulation assumptions.

Set point indoor air temperature [°C]	Heating: $T_{setHeat}$ = 20 Cooling: $T_{setCool}$ = 26
Occupancy schedule [h]	24:00 - 9:00; 13:00 - 15:00; 18:00 - 24:00
Number of occupants per zone	3
People heat gain [W/p]	Sensible: 75 Latent: 75
Light + machineries heat gains schedule [h]	18:00 - 23:00
Light + machineries heat gains [W/m^2]	8.0
Air infiltration and free cooling ventilation rate [vol/h]	0.3/2.0
DHW set point temperature [°C]	45
Tap water temperature [°C]	15
DHW usage schedule [h]	07:00 - 09:00; 13:00 - 15:00; 20:00 - 22:00

Then, the outlet water from the RF enters the bottom of the TK (i.e. return water) by means of the inlet of the adopted double port. When the indoor air of Zone 3 is higher than $T_{in,RF}$ + 2.1°C or TK top temperature is lower than $T_{TK,topSET}$ – 1.0°C, P1 pump is switched off and the stored thermal energy is exploited for DHW production, i.e. tap water enters HE2 heat exchanger. An auxiliary HP is also used for heating/cooling each building thermal zone at the selected set-point temperatures.

Table 14. Layers features and design parameters of the radiant floor (Zone 3 only).

Layers	**Thickness**	**Unit**
Interior plasterboard	0.020	m
Thermal insulation (= 0.023 W/mK)	0.020	
Concrete slab	0.150	
Cement based-mortar (above and below the pipes)	0.060	
Ceramic tiles	0.020	
D_{pipe}, Pipe outside diameter	0.018	
S_{pipe}, Pipe Spacing (centre to centre)	0.20	
T_{pipe}, Pipe wall thickness	0.002	
Design parameters	**Value**	**Unit**
$T_{in,RF}$, Zone 3 indoor air temperature for radiant floor activation	19	°C
qP1, P1 rated flow rate for supplying the radiant floor	1,100	kg/h
λ_{pipe}, Pipe wall conductivity	0.35	W/mK

System model – Study 1

Thermodynamic models related to the most significant system components, included in the developed simulation model, is here provided. For details about the models of the remaining devices, see reference [191].

a) BIPVT collectors

BIPVT collectors are modelled by adopting the component included in the TRNSYS TESS library (Type 563, [191]). The thermal model is based on algorithms presented in reference [195]. Specifically, each of sheet and tube PVT collector includes several components, such as an absorber encapsulating the PV film, flow channels for the cooling fluid and thermal insulation. A dual purpose is obtained by such devices: i) producing electricity through the embedded PV cells; ii) generating thermal energy by transferring heat to the water flowing in tubes bonded to an absorber plate underlying the cells. The model of this BIPVT collector can be connected to the one of a multi zone building (Type 56, described in the following paragraphs) with the aim to assess the influence of the integrated PVT modules on the building heating and cooling loads (i.e.: passive effects).

The collector model relies on linear factors linking the electricity efficiency of the PV cells to the related temperature and to the incident solar radiation. The cells are assumed to be operating at their maximum power conditions. The mathematical model is based on a derivation of the standard tube-fin solar collector algorithm and it assumes constant overall energy loss coefficient and absorber absorbance [195]. Here, the collector electricity efficiency is calculated as a function of the cell average temperature T_{cell} and of the incident solar radiation (G_t) [191]:

$$\eta_{PV} = \eta_0 \cdot \left[1 + Eff_T \cdot \left(T_{cell} - T_{ref}\right)\right] \cdot \left[1 + Eff_G \cdot \left(G_T - G_{ref}\right)\right] \quad (1)$$

where: η_0 is the PV efficiency at the reference conditions; Eff_T and Eff_G are the temperature and radiation efficiency modifiers; T_{ref} is the reference temperature and G_{ref} is the reference incident solar radiation.

Several energy balances are suitably solved in order to assess: i) the outlet temperature of the fluid ($T_{f,out}$); ii) the temperature distribution along the PV surface (T_{cell}), the absorber plate and the interface between the collector and the upper surface of the roof (T_{back}) [191, 195]. The fluid outlet temperature is calculated as:

$$T_{f,out} = \left(T_{f,in} + \frac{\varepsilon}{\kappa}\right)\exp\left(\frac{N_{tubes}}{\dot{m}\cdot c_p}\cdot\frac{\kappa}{\theta}\cdot L\right) - \frac{\varepsilon}{\kappa} \tag{2}$$

where: $T_{f,in}$ is the inlet fluid temperature; $\dot{m}$ is the fluid mass flow rate; N_{tubes} is the number of identical tubes carrying the fluid through the collector. ε, κ and θ depend on the collector geometry, heat transfer coefficients, thermal resistances and temperatures of sky, ambient and back collector surface, as detailed in [195]. As a function of $T_{f,out}$, the collector useful energy gain is calculated as:

$$Q_u = \dot{m}\cdot c_p\left(T_{f,out} - T_{f,in}\right) \tag{3}$$

The design and operating parameters of the collectors are selected according to the data included in reference [60] and [196]. All the design parameters for the analysed case studies are shown in Table 12.

b) Energy storage tank

In order to model the dynamics of a stratified fluid storage tank, the TRNSYS built-in Type 340 is used. In this model four optional internal heat exchangers and ten connections (double ports), for direct TK charge and discharge, can be modelled (necessary to the DHW and space heating purposes) [121]. For the simulated systems, one double port and two heat exchangers are taken into account:

- the double port on the modelled storage TK is linked to the RF for the Zone 3 space heating;
- the HE1 heat exchanger supplies TK with the heat produced by BIPVT collectors;
- the HE2 heat exchanger is exploited for producing DHW.

The TK model is based on the assumption that the thermal storage is subjected to thermal stratification and is divided into *N* fully-mixed equal sub-volumes. The temperatures of the nodes are calculated by solving a set of differential equations, related to a virtual matrix made of a triple array of *N* columns. The first column (*j*=1) includes the data of the first heat exchanger (HE1), the second one (*j*=2) the data of the storage TK and the last one (*j*=3) the data of the second heat exchanger (HE2). One mass flow rate ($\dot{m}_f$) through the double port is taken into account in each *n*-th node. The temperatures of the TK nodes are calculated on the basis of unsteady energy and mass balances, by solving a set of differential equations. The change of internal energy with the time occurring in the *n*-th node of the store (*j=2*) is calculated as:

$$\begin{aligned} M_n c_f \frac{dT_{n,j}}{d\vartheta} &= \dot{m}_f c_f\left[\xi_1\cdot\left(T_{n-1,j} - T_{n,j}\right) + \xi_2\cdot\left(T_{n,j} - T_{n+1,j}\right)\right] + \frac{S_n\lambda}{\delta_n}\left[\left(T_{n-1,j} - T_{n,j}\right) + \left(T_{n+1,j} - T_{n,j}\right)\right] + \\ &+ UA_n\left(T_a - T_{n,j}\right) + \sum_{k=1}^{\Gamma}\gamma^j UA_n^j\left(T_{n,k} - T_{n,j}\right) \end{aligned} \tag{4}$$

The first sum on the right hand side of Eq. (4) represents the heat transfer due to the mass flows through the double port (linked to the RF). Here, a positive mass flow rate from the bottom to the top is taken into account ($\xi_1 = 1$ if $\dot{m}_f > 0$, else $\xi_1 = 0$) and vice versa ($\xi_2 = 1$ if $\dot{m}_f < 0$, else $\xi_2 = 0$). The second sum takes into account the conductivity between the vertical boundary layers of the TK. The heat losses are taken into account by the third term of Eq. (4). Here, UA_n represents the heat transfer capacity rate between the store *n*-th node and the outdoor environment. Thus, the fourth term on the right hand side of the same equation represents the heat transfer between the heat exchanger nodes, on the boundary vertical partitions, and the store ones. Here, $\gamma^j = 1$ if the *n*-th store node is in contact with the *n*-th node of the horizontal boundary of the heat exchanger, otherwise $\gamma^j = 0$. Similarly, UA_n^j is the heat transfer capacity rate between the *n*-th node related the heat exchanger and the storage TK. The energy balance for an *n*-th heat exchanger (*j =1* and *j =3* vertical partitions) node is:

$$M_n c_{f,HE} \frac{dT_{n,j}}{d\vartheta} = \dot{m}_{f,HE} c_{f,HE} \left[\left(T_{n-1,j} - T_{n,j} \right) + \left(T_{n,j} - T_{n+1,j} \right) \right] + UA_n \left(T_a - T_{n,j} \right) + \gamma^j UA_n^j \left(T_{n,2} - T_{n,j} \right) \quad (5)$$

where the vertical temperature boundary nodes ($T_{n-1,j}$ and $T_{n+1,j}$) represent the inlet and outlet temperatures of the considered heat exchanger. In addition, on the right hand side of Eq. (5), the second and third terms take into account the heat loss capacity rates: i) from the heat exchangers to the surroundings; ii) from the heat exchanger to the storage TK (*j=2*).

c) Building and radiant floor model

In order to calculate the space heating and cooling and DHW demands, a suitable building was modelled by means of the Type 56 of TRNSYS (version 17), coupled to the Google SketchUp TRNSYS3d plug-in [197]. The detailed procedure for using these tools is reported in reference [198]. Details about both the building physics and energy systems simulation models are available in [191]. A validation report about the whole Type 56, performed by using detailed measurements from the CEC research program PASSYS, is presented in reference [199]. TRNSYS 17 introduces new features regarding radiation [200], glasses and windows (with and without shading devices), as successfully performed by facilities test cells [201]. In general, the outputs achieved by such software, or others standard simulation tools, are nowadays considered sufficiently reliable for carrying out building energy performance simulations [194].

Through the Type 56 it is possible to model the thermal behaviour of a RF for indoor space heating. In the proposed model, an “active layer” is added to the floor surface of thermal Zone 3 (Figure 84). The layer is called “active” since it includes a fluid filled pipeline for supplying heat to the system. Such layer is described by several parameters referred to: floor and pipes geometries, inlet mass flow rate, inlet fluid temperature, number of loops (for calculating the pipeline length) and additional energy gain at the fluid level (Table 14).

d1) Energy and economic model

A detailed energy-economic model was also developed in order to assess the energy and economic profitability of the system under investigation. As mentioned above, in such analyses, in case of the Reference System (RS, corresponding to Case A), space heating and cooling is provided

by the electric HP, whereas DHW is provided by the CB and electricity by the national grid. Primary energy savings, achieved by the proposed systems (Cases B, C and D) with respect to the RS (Case A) are suitably calculated. Obviously, it is assumed that all systems provide the same amount of DHW and electricity, with the same indoor set point temperatures. The primary energy saving, calculated as a function of the annual total energy produced by RS, is:

$$\Delta PE = \sum_i \left(\frac{E_{el,BIPVT} - E_{el,aux}}{\eta_{RS,el}} - \frac{Q_{DHW,CB}}{\eta_{RS,DHW}} + \frac{Q_{heat,RS}}{COP_{RS,Heat}\eta_{RS,el}} - \frac{Q_{heat,PC}}{COP_{PC,Heat}\eta_{RS,el}} + \frac{Q_{cool,RS}}{COP_{RS,Cool}\eta_{RS,el}} - \frac{Q_{cool,PC}}{COP_{PC,Cool}\eta_{RS,el}} \right)_i \quad (6)$$

where: $E_{el,BIPVT}$ is the electricity produced by the BIPVT; $Q_{DHW,CB}$ is the energy consumption of the CB; $Q_{heat,RS}$ is the energy for heating and $Q_{cool,RS}$ is the energy for cooling, supplied by the RS; $Q_{heat,PC}$ and $Q_{cool,PC}$ are the energies supplied by the HP for space heating and cooling, respectively; $E_{el,aux}$ is the electricity supplied to the auxiliary devices (e.g. pumps); $\eta_{RS,DHW}$ is the thermal efficiency of the CB; $\eta_{RS,el}$ is the efficiency for conventional electric power production. Index *i* is related to the *i-th* time step of the simulation. Note that, in Eq. (6) the variable coefficients are referred to both the RS (Case A) and the PS (corresponding to Cases B, C and D). Note also that, the Coefficient of Performances of the air-to-water HP ($COP_{PC,heat}$ and $COP_{PC,cool}$), are calculated by the methods recommended by the UNI/TS 11300 (Italian release of ISO EN 13790). As a result, the nominal COP_N *and* EER_N given by the constructors, and their variation due to the occurring operating conditions are suitably taken into account.

$$COP_{PS,heat} = \frac{COP_N}{COP_{MAX}} \cdot \frac{\vartheta_c + \Delta\theta_c}{(\vartheta_c + \Delta\theta_c) - (T_{ba} - \Delta\theta_f)} \cdot (4 \cdot f_{PLR}) / (0.1 + 3.6 \cdot f_{PLR})$$
$$COP_{PS,cool} = EER_N \cdot \frac{\frac{\vartheta_{e,out} - \vartheta_c + T_{ba} + \vartheta_e}{2}}{\vartheta_c - \vartheta_e} \cdot (a \cdot f_{PLR}^3 + b \cdot f_{PLR}^2 + c \cdot f_{PLR} + d) \quad (7)$$

In particular, $COP_{PS,heat/cool}$ are calculated as a function of the part-load ratio f_{PLR}, the ambient temperature T_{ba} and the condenser/evaporator temperatures (further details are available in [202]).

An economic analysis of the proposed system is also carried out. In particular, a suitable model is developed in order to assess the economic feasibility of the system. Here, the total capital cost (J_{tot}) of the proposed system (including BIPVT solar field or PVT collectors for Case B, pumps, valves, controllers, tank, etc.) is calculated as a function of the solar field surface area, according to the data provided in reference [203]:

$$J_{tot} = 660 \cdot A_{PVT} \quad (8)$$

The PSs yearly savings are reported in terms of operating costs with respect to those of the RS configuration. For electricity, it is assumed that the net power production is entirely delivered to the national grid (the producer can benefit of a feed-in tariff, j_{el}). The unit cost of natural gas, j_{NG}, was used to calculate the cost related to thermal energy. System operating costs are due to: i) pumps electricity consumption; ii) HP electricity demands; iii) CB natural gas consumption. As a result, the savings obtained by the proposed system, PC, are due to: i) produced solar electricity; ii) reduced use of the heat pump (due to the RF supplied by the solar collectors); iii) DHW production obtained by solar thermal energy. Thus, the annual savings are calculated as:

$$\Delta C = \left[\left(E_{el,BIPVT} - E_{el,aux} \right) + \left(\frac{Q_{heat,RS}}{COP_{RS,Heat}} - \frac{Q_{heat,PC}}{COP_{PC,Heat}} + \frac{Q_{cool,RS}}{COP_{RS,Cool}} - \frac{Q_{cool,PC}}{COP_{PC,Cool}} \right) \right] j_{el} - \frac{Q_{DHW,CB}}{LCV_{NG}\eta_{RS,DHW}} j_{NG} \quad (9)$$

At last, the economic profitability analysis also includes the assessment of the Simple Pay Back (*SPB*) period, the ratio between the extra cost of the proposed system (the difference between the capital cost of the PS system and the one of RS) and the savings in terms of operating costs.

$$SPB = \frac{J_{tot}}{\Delta C} \quad (10)$$

Case studies

The selection of the case studies was carefully performed in order to analyse a residential application, which is well-representative of the next generation of buildings [204]. Therefore, a residential 3-floors building, complying with the present EU energy efficiency regulation (low U-values, solar energy applications, etc.), is simulated. For such building, a rectangular plant shape (15 m x10 m) with an East-West oriented longitudinal axis is taken into account. Here, the south facing surface of the pitched roof is 30 degrees tilted. Three different thermal zones related to the indoor spaces of the ground, the 1st and 2nd floors, are modelled. Details about the building surfaces/volumes are provided in Table 15, the envelope features are reported in Table 16. Simulations are mainly carried out by taking into account four different European weather zones selected among those representatives of European climates. They refer to the climate of Freiburg, (South-Germany), Milan (North-Italy), Naples (South-Italy) and Almeria (South-Spain), whose hourly weather data files are obtained by Meteonorm database [191]. For such weather zones, a detailed parametric analysis is also performed in order to find out the influence of the building envelope features on the performance of the examined BIPVT layouts. Additional weather zones, reported in Table 17, are also investigated in order to carefully analyse the relationship between performance and weather conditions by comparing the obtained heating and cooling demands of Case C (BIPVT collectors) and Case B (PVT stand-alone collectors). With the purpose of performing a correlational analysis, several climatic indexes are also calculated, such as: Heating Degree Days (*HDD*); Cooling Degree Days (*CDD*) and Incident Solar Radiation (ISR). In Table 17, all the weather zones considered are sorted by decreasing *HDDs. HDDs* and *CDDs* are calculated by considering as a reference temperature, for both heating and cooling, 18°C [205]. Note that, according to the climate, different heating periods are taken into account for the simulated weather zones [203]. Table 17 also includes the cooling period and the HVAC system activation hours.

Table 15. Building thermal zones.

Zone (Floor)	**Height** [m]	**Volume** [m^3]	**Floor area** [m^2]	**Glass area** [m^2]
1 (Ground)	3.5	525	150	19.5
2 (1st)	3.0	450		19.5
3 (2nd)	3.75 (max) 1.88 (average)	281		6.0
Total	10.25	1256	450	45.0

Table 16. Study 1 opaque/transparent elements features.

Building element	**U-value** [W/m^{2}K]	**Thickness** [m]	ρ_s [-]	ε [-]
Roof and façades without BIPVT panels	0.31	0.30	0.40	0.90
Internal floor/ceiling (tile flooring)	0.66	0.33		
Ground floor (tile flooring)	0.81	0.18		
Windows glass	2.83	0.004/0.016 (air)/0.004	0.13	0.18

Table 17. Weather zones indexes and HVAC system schedules.

Weather zone	**HDD** [Kd]	**CDD** [Kd]	**ISR** [kWh/m^{2}y]	**Winter season**	**Heating schedule** [h]	**Cooling season**	**Cooling schedule** [h]
Prague (Czech Republic)	3854	150	998	15/10 - 15/04	06:30 - 08:30; 12:00 - 15:00; 17:00 - 20:00	01/05 - 30/09	13:00 - 15:00; 18:00 - 20:00
Copenhagen (Denmark)	3738	85	987				
Berlin (Germany)	3397	264	1001				
Vienna (Austria)	3277	269	1112				
London (UK)	3155	82	998				
Paris (France)	3122	155	1036				
Freiburg (Germany)	3052	255	1112				
Milan (Italy)	2734	436	1246				
Bolzano (Italy)	2646	473	1242				
Turin (Italy)	2585	453	1291				
Madrid (Spain)	2179	687	1662	01/11 - 15/04			
Pescara (Italy)	1899	606	1518				
Pisa (Italy)	1851	566	1447				
Rome (Italy)	1687	671	1563				
Naples (Italy)	1480	729	1512	15/11 - 31/03			
Brindisi (Italy)	1239	775	1518	15/11 - 31/03			
Larnaca (Cyprus)	842	1199	1847	01/12 - 15/03			
Almeria (Spain)	785	963	1733				

For all the investigated cases, the following solar field are considered: i) in Cases C and D, the BIPVT collectors are mounted on the south facing surface of the pitched roof. Case C surface is 125 m^2 and tilt is 30°; ii) in Case B, the stand-alone PVT area has the same size and tilt as Case C; iii) in Case D, an additional solar surface area, on south-façade, is considered, for a total BIPVT area of 207.5 m^2 (45 m^2 at Zone 1 and 37.5 m^2 at Zone 2). For free cooling purposes a specific windows opening strategy is assumed during the no-heating season and from 20:00 to 09:00. During heating season, in order to simulate the occupants' behaviour in case of overheating (indoor air temperature > 25°C), a 2 vol/h outdoor air ventilation rate (simulated by the windows opening) is modelled. Subsequently, the closing of the windows occurs when the indoor air temperature falls below 23°C. Design and operating parameters of all the simulated components are shown in Table 12, whereas those related to the RF, serving only the Zone 3, are reported in Table 14. Note that RF is supplied only by solar energy and that the thermal capacity of the modelled solar field (limited by the available surface area) is sufficient for providing space heating to Zone 3 only. Additional assumptions taken into account in the analysis are: i) efficiency for conventional electricity production ($\eta_{RS,el}$) equal to 46%; ii) electricity feed-in tariff (j_{el}) equal to 0.35 €/kWh; iii) natural gas cost (j_{NG}) equal to 1.0 €/Nm^3; iv) natural gas lower heating value equal to 9.59 kWh/Nm^3.

Results of Study 1

In order to investigate the effect due to the building integration of PVT panels on the production of electricity, DHW and space heating, a comprehensive analysis based on dynamic simulations is

carried out. This section includes a plurality of parametric analyses which are carried out in order to assess the effect of several building envelope parameters on the overall building primary energy demands. In the following sections, yearly, weekly, and daily results are discussed with the aim to provide useful results for benchmarking purposes. Most of the detailed results refer to weather zones of Freiburg, Milan, Naples, and Almeria, whereas further results are referred to the analysis related to a larger group of investigated weather zones.

Yearly results

In this session energy and economic performances of Cases B, C and D are compared to those obtained for the RS, Case A. for the climate zone of Naples. In particular, in Table 18 the calculated primary energy demands are reported for each investigated building-plant system layout.

Table 18. Yearly results.

	Case A		**Case B**		**Case C**		**Case D**	
	[MWh/y]	[kWh/m^{3}y]	[MWh/y]	[kWh/m^{3}y]	[MWh/y]	[kWh/m^{3}y]	[MWh/y]	[kWh/m^{3}y]
PE_{DHW}	7.85	6.25	5.33	4.24	5.36	4.27	4.68	3.72
$PE_{Auxiliaries}$	-	-	$6.69 \cdot 10^{-2}$	$5.33 \cdot 10^{-2}$	$6.66 \cdot 10^{-2}$	$5.30 \cdot 10^{-2}$	$9.14 \cdot 10^{-2}$	$7.27 \cdot 10^{-2}$
$PE_{el,PVT}$	-	-	37.68	29.99	37.63	29.96	52.83	42.05
$PE_{Heating}$	2.91	2.31	2.14	1.70	1.96	1.56	1.81	1.44
$PE_{Cooling}$	1.47	1.17	1.49	1.18	1.75	1.39	2.03	1.61
$PE_{Heat\&Cool}$	4.38	3.48	3.62	2.88	3.71	2.95	3.84	3.06
PE_{tot}	12.23	9.73	-28.66	-22.82	-28.50	-22.69	-44.22	-35.20

The overall primary energy requirement (PE_{tot}) of Case A is mainly due to the DHW preparation (64%), produced through a much less energy efficient technology (a gas-fired CB). This condition strongly affects all the achieved results. In fact, any energy efficiency measure aiming at reducing the building demands of space heating and cooling (including BIPVT collectors) has a minor influence on the overall energy savings. The lower values of primary energy for space heating and cooling are due to the very low U-values of the building considered, equipped with a high efficiency electric HP. The combination of these two circumstances determines the high ratio obtained between PE_{DHW} and total primary energy demands PE_{tot}. Conversely, in case of existing buildings, the primary energy required for space heating ($PE_{Heating}$) is generally higher than the DHW one, because of the typically scarce envelope thermal insulation and low energy efficiency of the heating systems. Comparing Cases B, C and D vs. Case A, a significant saving of $PE_{Heating}$ and PE_{DHW} is obtained. This is due to the amount of solar energy exploited for both DHW production and space heating purposes. PE_{DHW} related to Case C is slightly higher than the one reported for Case B, due to the adopted assumptions and the different temperature level within the heat storage TK. In particular:

- solar DHW is provided only if the RF does not need to be activated (i.e. hot water from the TK is supplied to the RF).
- the temperature of the hot water stored in the TK of Case C is averagely higher than the one of Case B during the no-heating months. This is due to lower thermal losses of BIPVT collectors vs. stand-alone PVT panels ones (i.e. the back surfaces of the collectors face the building indoor air Zone 3 in Case C and the outside air in Case B).

Clearly, the larger solar field area of Case D, compared to those of Cases B and C, leads to: i) higher electricity production ($PE_{el,PVT}$); ii) higher solar hot water production for the RF use and DHW preparation; iii) higher cooling primary energy demand ($PE_{Cooling}$) due to the indoor air temperature overheating in summer. Table 18 also shows that, for the considered building, located in the weather zone of Naples, the space heating primary energy demand ($PE_{Heating}$) is significantly higher than the cooling one ($PE_{Cooling}$) for all case studies. This is an unexpected result for the average climatic conditions of Naples (Mediterranean climate). This result is due to the selected space cooling daily schedule (four hours per day) vs. the heating one (eight hours per day), to the adopted free cooling strategy and windows solar shadings. Table 18 also shows that for Cases B, C and D, significant savings are achieved in terms of PE_{tot} vs. Case A (from 40.7 to 56.5 MWh/y), basically due to the electricity produced of collectors, of about 37.6 MWh/y for Cases B and C and 52.8 MWh/y for Case D. Obviously, the higher amount of electricity production shown by Case D is due to its larger BIPVT solar field area (south roof + south façade). Note that, negative values of PE_{tot}, shown in Table 18, basically identify a yearly electricity production $PE_{el,PVT}$ higher than the building demand. In addition, Table 18 also shows that a negligible difference is detected between $PE_{el,PVT}$ of Cases B and C. This result shows that the Case C determines a marginal increase of the PV cells average temperature, with a negligible reduction of the annual electricity efficiency and production vs. Case B. For all Cases (B, C and D), an important decrease with respect to Case A of $PE_{heating}$ is detected, due to the utilization of thermal energy produced by solar collectors and delivered to the Zone 3 RF, with a consequent reduction of the electricity required by the backup heat pump. Obviously, this saving is even greater for Case D, because of the larger solar field. $PE_{Heating}$ is lower for Case C with respect to Case B: therefore, BIPVT collectors are beneficial for the reduction of the space heating demand (useful winter passive effect of BIPVT collectors). Opposite effect occurs for $PE_{Cooling}$, which in Cases C resulted higher than that one calculated in Case B (unwanted summer passive effect of BIPVT collectors causing a higher mean radiant temperature of Zone 3). Evidently, in case of additional south-façade BIPVT collectors (Case D), a higher $PE_{Cooling}$ vs. Case C is obtained (higher mean radiant temperatures of Zone 1 and Zone 2). In the weather zone of Naples, these two effects are almost counterbalanced so that the overall primary energy consumption (PE_{tot}) reported for Case C is similar to the one calculated for Case B.

Weekly results

The effects of the weather conditions on the weekly BIPVT performance are studied through a suitable comparative analysis by taking into account, in addition to Naples, the weather zones of Freiburg, Milan and Almeria. It is worth noting that for all such weather zones, the simulations are performed by assuming the same collectors tilt angle, without varying it as a function of the latitude. For all the weather zones, weekly building heating and cooling demands (E_{heat} and E_{cool}) are shown for Case A, B, C and D in Figure 86. By comparing the results reported in these figures, the potential heating energy saving achieved through the solar heated RF (Cases B, C and D) and the passive heating effect due to roof BIPVT collectors (Case C) and roof/façades BIPVT collectors (Case D) can be detected. The highest energy saving for the space heating is obtained in Freiburg by comparing Case D vs. Case A. Obviously, during the winter, shorter heat pump running times are obtained also due to the BIPVT collectors passive effect.

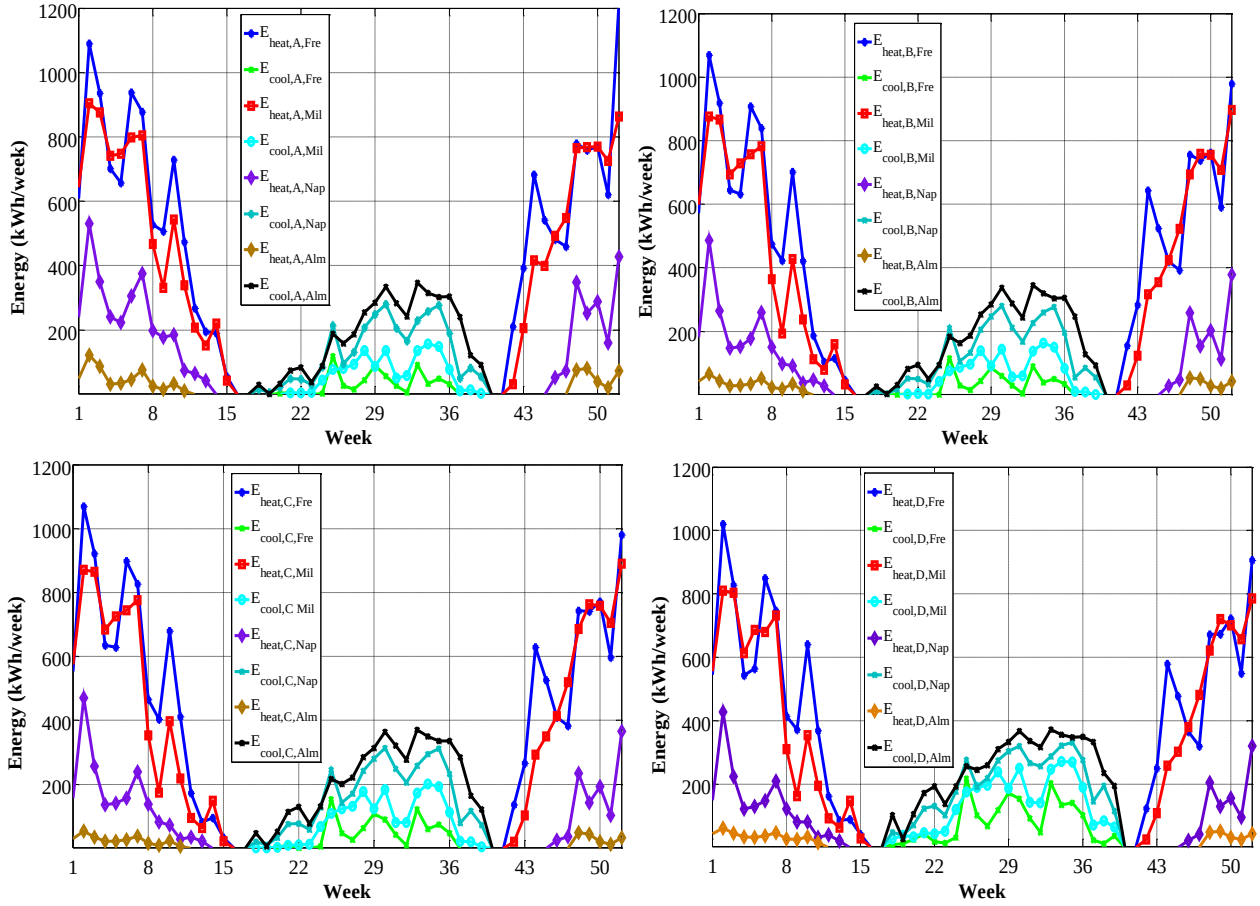

Figure 86. Weekly heating and cooling energy demand for Case A, B, C and D in Freiburg, Milan, Naples and Almeria.

Lower savings are observed in Milan, Naples and Almeria vs. those obtained in Freiburg. According to the adopted assumptions, no differences are observed in terms of cooling energy demands, between Cases B and A. As expected, the roof and roof/façades BIPVT collectors (Cases C and D, respectively) lead to higher cooling energy requirements with respect to Case A along all the summer season. This unwanted result is due to the hot water flowing through the BIPVT collectors (which heat up the interior surfaces of the building roof and south-façade). The passive effect of BIPVT overheating causes an increase of the cooling energy demand (higher in Case D vs. Case C because of the larger building integrated solar field area). Obviously, this phenomenon is more evident in Almeria (black line in Figure 86).

Daily dynamic results

In this section, the results of hourly simulation are discussed. In particular, in Figure 87, for one winter sample day in Naples, the time histories of the occurring operating temperatures are reported for: i) the Case B roof and the corresponding stand-alone PVT panels; ii) the Case C roof BIPVT system. It is clearly shown that no significant differences are detected between PVT front temperatures (T_{pv}) for Case B vs. Case C. For Case B, the obtained collector back surface temperatures ($T_{back,SC,B}$) are always higher than the outdoor ambient air ones (T_{amb}), whereas for Case C, this behaviour ($T_{back,SC,C} > T_{amb}$) is observed only during the daily hours in which a significant incident solar radiation occurs. During these hours, the temperature of the roof external surface of Case B ($T_{outside,roof,B}$) is always lower than the corresponding temperature of Case C, as

expected. Note that, for Case C $T_{back,SC,C}$ is equal to $T_{outside,roof,C}$. Similar results are obtained during the summer season.

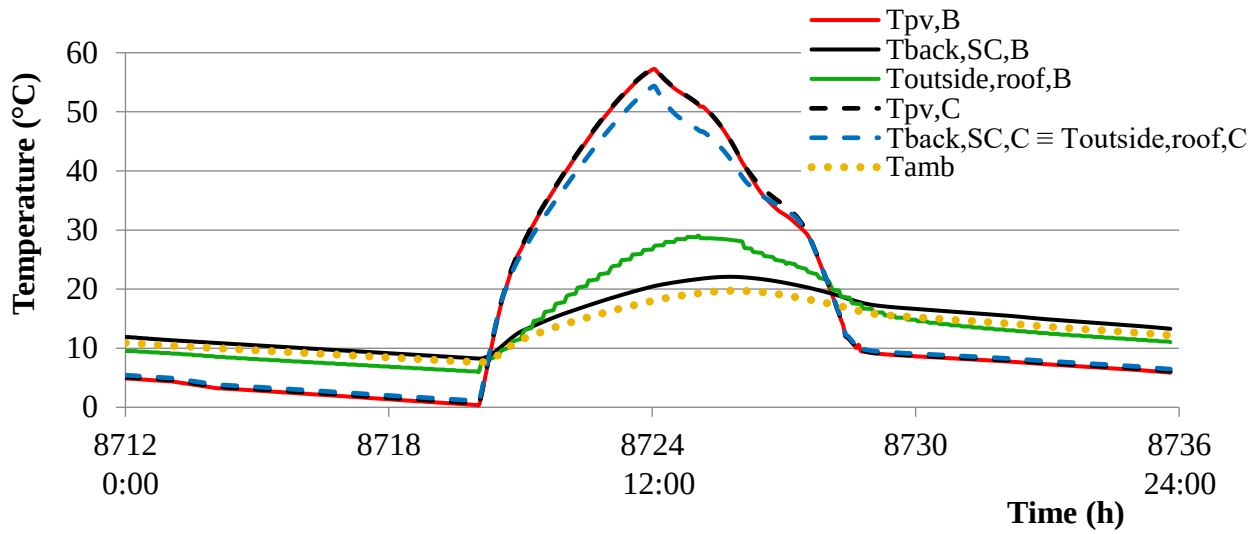

Figure 87. Zone 3: winter day in Naples.

With regard to the passive effects of BIPVT panels on the heat transfer across the roof (Case C) with respect to the traditional roof (Case B), the following results, also shown in Figure 87, are obtained:

- During day hours with significant incident solar radiation it is obtained: $T_{pv,C} > T_{outside,roof,B}$ (i.e. the external BIPVT collectors temperatures (Case C) are much higher than the corresponding ones of the Case B roof). For this reason, according to the inertial behaviour of the building structure, in the heating (cooling) season a potential helpful (unwanted) passive effect of the roof BIPVT collectors vs. the traditional roof is produced;
- During all the remaining hours the opposite trend is detected: $T_{pv,C} < T_{outside,roof,B}$. This result is consistent with the findings reported in literature [43, 206, 207]. Therefore, according to the inertial behaviour of the building structure, in the heating (cooling) season a potential unwanted (helpful) passive effect of the roof BIPVT panels vs. the traditional roof is produced.

As is well known, the comfort depends also on the mean radiant temperature of the building envelope, which for the Zone 3 is affected by the temperature of the south roof internal surface ($T_{inside,roof}$).

In Figure 88, for one summer sample day, the time histories of the Zone 3 indoor air temperatures ($T_{indoor,air}$), south roof internal surface temperatures ($T_{inside,roof}$) and cooling loads (Q_{Cool}) are reported for Cases B and C. In this figure, an unwanted roof BIPVT passive effect is detected during all the afternoon hours ($T_{inside,roof,C} > T_{inside,roof,B}$). Note that, the peak of $T_{inside,roof}$ is shifted (vs. $T_{outside,roof}$, occurring about at 12:00) late in the afternoon because of the thermal inertia effect of the simulated roof structure. During these hours, increased cooling loads and demands are detected for Case C vs. Case B ($Q_{Cool,C} > Q_{Cool,B}$). Conversely, during the night and early in the morning, a helpful passive effect is obtained in terms of occupants comfort ($T_{inside,roof,C} < T_{inside,roof,B}$ and $T_{indoor,air,C} < T_{indoor,\ air,B}$). In these hours the cooling system is simulated as switched off, as typically occurs in residential buildings.

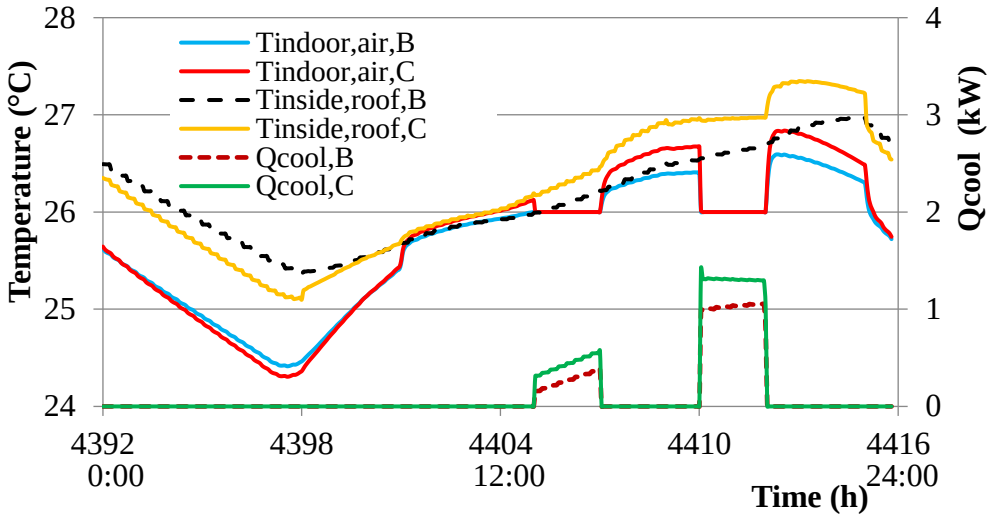

Figure 88. Zone 3 summer day in Naples.

Parametric analysis

For the building-plant system layouts examined, a parametric analysis was carried out in order to assess the effects of some building envelope design parameters on the electricity and DHW production, as well as on the space heating and cooling demands. The investigated parameters are:

- thermal transmittance (*U-value*), of the building roof and façades: 0.32, 0.80 and 1.20 W/m^{2}K.
- density (ρ) of concrete slabs included in the building roof and façades walls layers. The simulated densities are: 600 (very lightweight concrete), 800, 1000 and 1200 kg/m^3 (common concrete). Note that, for each investigated density a different thermal conductivity was adopted.

The combinations of U-values and ρ taken into account in this analysis are shown in Table 19.

Table 19. Façade/roof layers and heating/cooling capacities.

Concrete slab		**Thermal insulation**	**U-value**	**Milan and Freiburg**		**Naples**		**Almeria**	
Density	**Conductivity**	**Thickness**		**Heating**	**Cooling**	**Heating**	**Cooling**	**Heating**	**Cooling**
[kg/m^3]	[W/mK]	[m]	[W/m^{2}K]	[W/m^3]					
600	0.36	0.054	0.30	18.8	15.0	15.0	12.0	15.0	12.0
		0.011	0.80	35.0	28.0	23.6	18.9	16.3	13.0
		0.002	1.20	43.1	34.5	31.3	25.0	17.5	14.0
800	0.41	0.056	0.30	18.8	15.0	15.0	12.0	15.0	12.0
		0.013	0.80	35.0	28.0	23.6	18.9	16.3	13.0
		0.003	1.20	43.1	34.5	31.3	25.0	17.5	14.0
1000	0.47	0.057	0.30	18.8	15.0	15.0	12.0	15.0	12.0
		0.014	0.80	35.0	28.0	23.6	18.9	16.3	13.0
		0.004	1.20	43.1	34.5	31.3	25.0	17.5	14.0
1200	0.54	0.059	0.30	18.8	15.0	15.0	12.0	15.0	12.0
		0.015	0.80	35.0	28.0	23.6	18.9	16.3	13.0
		0.005	1.20	43.1	34.5	31.3	25.0	17.5	14.0

In all such combinations for roof and façades, the thicknesses of external/internal plasterboard layer are 0.02 m, that of concrete slab layer is 0.20 m. The analysis is carried out for the weather zones of Freiburg, Milan, Naples and Almeria. The adopted simulation assumptions (e.g. free cooling strategy, building envelope features, internal loads due to people, electric devices, lighting, ventilation and infiltration rates through windows, daily heating/cooling periods, etc.) are summarised in Table 13. In addition, in Table 19, the installed cooling and heating capacities of the simulated HVAC system (fan coil units) are also shown. Details about the heating and cooling capacities of the modelled fan coil units are reported in Table 12. Note that, for all the simulated system layouts, the installed heating capacity is higher than the cooling one. This is due to the coil heat exchange capacity that is always higher for the heating operation than for cooling one. The first result of this analysis regards the differences of the electricity production between Cases C and B (equal solar PV field area). In particular, a very slight growth of electricity production is obtained by increasing the roof U-values, whereas it is almost independent of the related slabs density. The calculated differences resulted quite low, ranging from -0.12 to 0.38%. Figure 89 shows the $PE_{Heating}$ and $PE_{Cooling,}$ for Case A of the four investigated weather zones, as a function of the U-values and densities ρ. In this figure, each bundle of lines (delimited by the coloured regions) shows the obtained trend for the different densities and for a single weather zone. For each obtained coloured region, the bottom line is always related to the highest investigated density (ρ equal to 1200 kg/m^3), while the top line refers to the lowest one (ρ equal to 600 kg/m^3). As expected, the *U-values* have a high impact on the heating and cooling consumptions, whereas a very slight dependence of the building envelope density ρ on the primary energy demands is observed. On the other hand, the higher the *U-value*, the higher the ρ influence. The parametric analysis carried out for Case A allows one to obtain an interpolating equation of the simulated results, useful for designers and benchmark purposes. The detected linear functions for the heating and cooling energy consumptions are:

$$PE_{Heating} = \left[HDD \cdot \left(3.0 \cdot 10^{-3} + \frac{\rho}{3.0 \cdot 10^{6}} \right) \right] \cdot U \cdot + \left(2.8 \cdot 10^{-3} \cdot HDD + \frac{\rho \cdot HDD}{10 \cdot b} - 2.8 \cdot 10^{0} \right) \quad (11)$$

$$PE_{Cooling} = \left(\frac{\rho \cdot -4.0 \cdot 10^{-1} \cdot 3.0 \cdot 10^{-1}}{ISR} \right) \cdot U + \left(1.7 \cdot 10^{-3} \cdot CDD - \frac{4.2 \cdot 10^{1}}{CDD} \right) \quad (12)$$

Where *HDD* and *CDD* are the heating and cooling degree days, *ISR* is the incident solar radiation. For all the analysed cases, the obtained corresponding R^2 are higher than 0.97. Such easy to use correlations can be adopted as a swift tool for the assessment of $PE_{Heating}$ and $PE_{Cooling}$ by simply selecting and implementing in the Eqs. (11) and (12), the occurring climate index and building envelope features.

The results achieved by such equations for Case A can be also combined to the ones obtained by the carried out parametric analysis for Cases B, C and D. In Table 20, the percentage differences of primary energy (*ΔPE*) demand due to space heating, cooling and DHW production, between the Case A and the other simulated Cases B, C and D, are shown. Note that the primary energy demand for the DHW preparation is equal to 7.84 MWh/y for all investigated parameters combinations and weather conditions. The following comments can be made by observing Table 20.

- *ΔPE* Case A vs. Case B - The maximum primary energy savings for space heating are achieved in Almeria, Naples, Milan and Freiburg about 47, 26, 10 and 6%, respectively, due to the solar heat gain achieved through the stand-alone PVT collectors exploited by the RF. High energy savings are

also achieved for the DHW preparation. In particular, the maximum savings range from 15% in Freiburg to 28% in Almeria.

- *ΔPE* Case A vs. Case C - In all the weather zones higher primary energy savings for space heating are obtained vs. the previous case (*ΔPE* Case A vs. Case B). The maximum savings obtained in Almeria, Naples, Milan and Freiburg are about 62, 33, 12 and 8%, respectively. In Case C, the achieved savings are due to the solar heat gain obtained through the roof BIPVT collectors exploited by the RF (as for Case B) and to the useful passive effect due to the BIPVT collectors. The minimum growth of the cooling demand, due to the unwanted summer passive effect of the BIPVT collectors for Almeria, Naples, Milan and Freiburg is about 16, 15, 23 and 25%, respectively. The dependence of the cooling demand growth on the roof slabs density appears significant only in Freiburg and Milan for U = 1.20 W/m^{2}K. Weaker density influences are detected in the remaining examined cases. In general, the higher the CDD, the lower the ρ influence. In all the weather zones the best energy results regarding the energy savings of DHW preparation are achieved for U = 0.32 W/m^{2}K, equal to 14, 18, 25 and 27% for Freiburg, Milan, Naples and Almeria, respectively.

Table 20. *ΔPE* for space heating/cooling and DHW between Case A and Cases B, C and D.

Walls/Roof ***U-value***	***ΔPE*** **Case A vs. Case B**		***ΔPE*** **Case A vs. Case C**			***ΔPE*** **Case A vs. Case D**		
	Heating	**DHW**	**Heating**	**Cooling**	**DHW**	**Heating**	**Cooling**	**DHW**
[W/m^{2}K]	[%]							
Freiburg								
0.32	6.46	14.58	8.24	-25.53	14.34	15.68	-58.60	20.31
0.80	4.61	12.70	7.96	-42.74	12.11	14.47	-61.19	18.56
1.20	3.45	11.64	7.83	-56.67	10.36	11.72	-67.51	16.85
Milan								
0.32	9.54	18.06	11.79	-23.45	17.82	18.79	-49.42	24.74
0.80	7.23	16.83	11.44	-34.93	15.75	18.20	-47.67	23.16
1.20	5.56	15.61	10.99	-44.03	14.18	15.12	-50.56	21.85
Naples								
0.32	26.41	25.03	32.54	-14.91	24.77	37.59	-27.36	34.16
0.80	20.35	23.10	28.89	-22.45	22.31	37.41	-27.03	33.04
1.20	14.73	22.19	24.81	-28.86	20.48	31.47	-29.26	31.09
Almeria								
0.32	27.43	28.30	45.07	-15.96	27.10	27.34	-26.79	35.23
0.80	47.45	27.39	61.56	-21.67	25.60	56.83	-23.29	34.17
1.20	40.98	26.57	58.45	-25.56	24.32	56.87	-22.78	34.52

- *ΔPE* Case A vs. Case D - Because of the larger solar field area, higher heating primary energy savings in Naples, Milan and Freiburg (38, 19 and 16%, respectively) were obtained vs. the previous case (*ΔPE* Case A vs. Case C). Note that in Almeria lower savings are obtained with respect to those obtained by comparing Case A to Case C. In this case study, the savings achieved are due to the solar heat gain obtained through the roof and façade BIPVT collectors exploited through the RF and to the useful passive effect due to the BIPVT collectors. The saving dependence on the roof slabs density appears weak in Freiburg and Milan whereas rather significant for Naples and Almeria

where the best heating energy performance is obtained for the ρ = 1000 and 1200 kg/m^3, respectively. The minimum growth of the cooling energy consumptions ($PE_{Cooling}$) due to the unwanted summer passive effect of the BIPVT collectors for Almeria, Naples, Milan and Freiburg is about 23, 27, 48 and 58%, respectively. Despite of such high percentage growths, the real cooling demands are still rather low. The dependence of the cooling demand growth on the façade and roof slabs density appears weak in Freiburg whereas rather significant for Milan, Naples and Almeria where the minimum cooling demand is obtained for ρ = 1200 kg/m^3. The maximum energy savings for the DHW production range from 20% in Freiburg to 35% in Almeria.

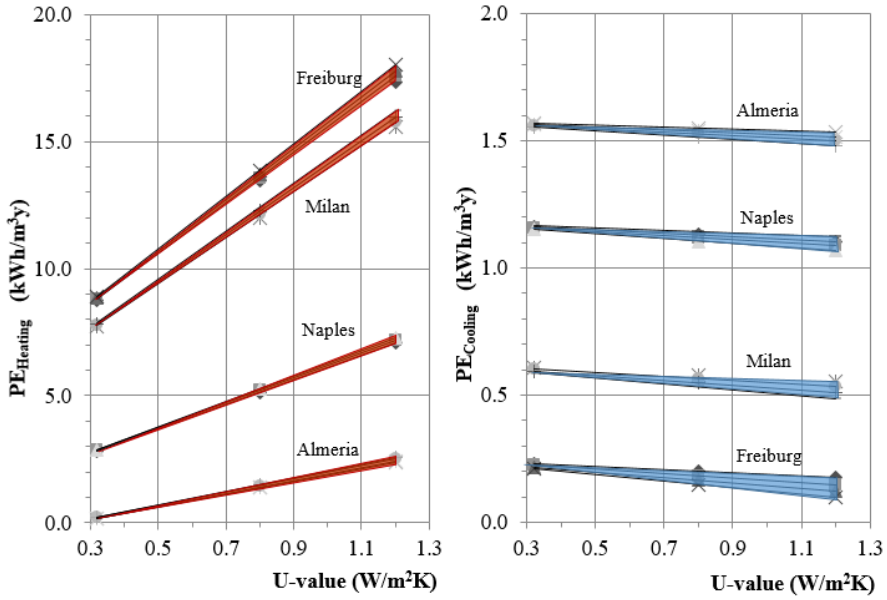

Figure 89. Case A: $PE_{Heating}$ and $PE_{Cooling}$ vs *U-values*, densities ρ of the simulated envelopes and *HDD / CDD.*

From the above discussed remarks, it is possible to observe that:

- the hot Mediterranean weather zone of Almeria shows for the space heating energy savings a different results trend with respect to those observed in Naples, Milan and Freiburg (cooler or colder weather zones). In particular, Almeria shows higher heating energy savings for Cases B and C vs. Case A (Table 20) because of the related averagely higher outdoor temperature and solar radiation during the winter season. In this case, the highest external heat gains are achieved with U = 0.8 W/m^{2}K (longest switched off time intervals of the electric heat pump). In Almeria, during the heating season, the water circuits integrated in the building façade BIPVT collectors reduce such helpful heat gains. Therefore, lower amounts of transferred solar radiation are obtained through the Case D building envelope vs. the Case C one. For this reason, the heating savings of Case D vs. Case A are lower than the ones assessed for Case C vs. Case A;
- for Case A vs. Cases B, C and D (Table 20), it is observed that the best heating energy performance is achieved for U = 0.8 W/m^{2}K for the weather zone of Almeria, and for U = 0.32 W/m^{2}K for the other climate zones. By comparing Case A vs. Case C, for all the four investigated weather zones, the best cooling energy performance is achieved for U = 0.32 W/m^{2}K, whereas by comparing Case A vs. Case D, the higher the CDD, the higher the *U-values* that maximizes the cooling savings. In fact, for Freiburg the best energy performance is achieved for U = 0.32 W/m^{2}K whereas in Naples for U = 0.8 W/m^{2}K and in Almeria for U = 1.2 W/m^{2}K. The maximum savings

for the DHW production in all the weather zones are achieved for U = 0.32 W/m^{2}K, and the savings dependence on the façades and roof slabs density appears negligible.

- due to the adopted assumptions (i.e. residential building usage), for the weather zones of Freiburg, Milan and Naples, the heating primary energy demands are remarkably higher than the cooling ones, except for Almeria, which are of the same order of magnitude, especially for low *U-values.*

The total primary energy consumptions for space heating and cooling ($PE_{Heating\&Cooling}$) vs. *U-values*, for the different ρ and for all Cases (A, B, C and D) are shown in Figure 90, for Freiburg and Almeria.

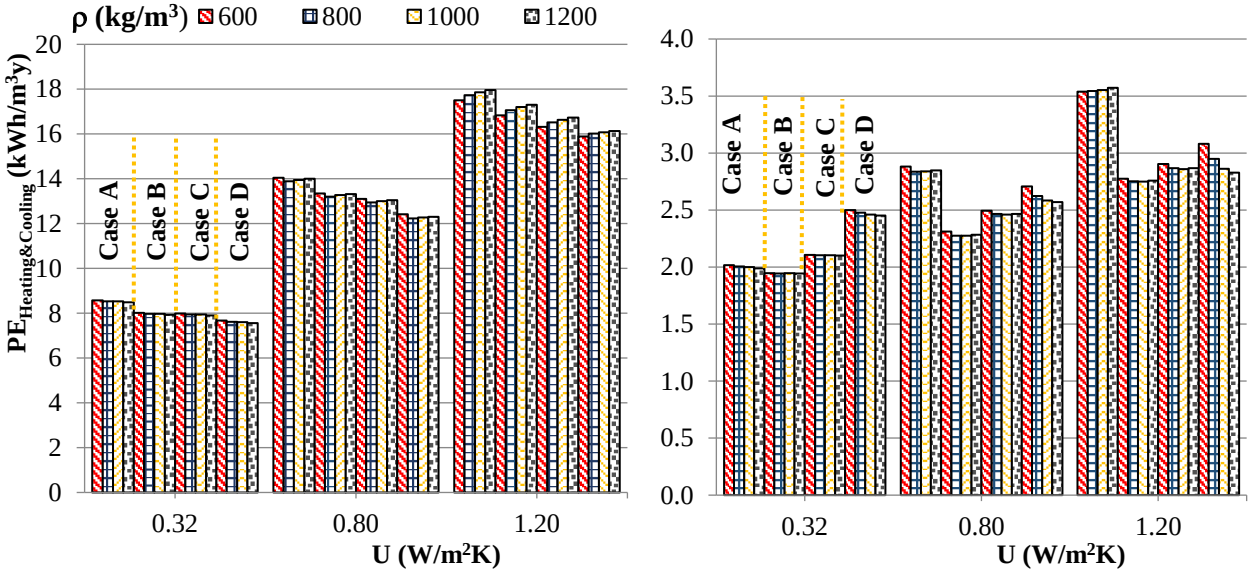

Figure 90. Freiburg (left), Almeria (right): $PE_{Heating\&Cooling}$ *vs. U-value* and different densities.

In Freiburg, due to the positive passive effect (i.e. additional heat gains) of the building integration, passing from Case A to Case D, $PE_{Heating\&Cooling}$ decreases. Contrarily, in Almeria, due to the significant cooling demand, $PE_{Heating\&Cooling}$ of Case C and Case D is always higher than those achieved in Cases B, for all the simulated U-values. Thus, the BIPVT collectors passive effects cause an increase of $PE_{Cooling}$ that counterbalances the decrease of $PE_{Heating}$. As above reported, shows that $PE_{Heating\&Cooling}$ remarkably increase with the building U-values (as expected) while are rather independent of the thermal mass of the building envelope. Note that, for the considered building-plant system layouts, BIPVT collectors show a remarkable passive energy effect only in the building Zone 3. For this reason, a specific analysis is carried out for analysing the Zone 3 heating and cooling demands. The results of this additional investigation, assuming U = 0.32 W/m^{2}K and ρ = 1200 kg/m^3, are summarized in Figure 91- Figure 92. In particular, Figure 91 shows the difference ($\Delta E_{Heating}$) between the Zone 3 unitary heating / cooling demand for Case C and Case B as a function of *HDD/CDD* and *ISR*. In Figure 91 the same analysis is carried out for the cooling demand as a function of *CDD* and *ISR*. Basically, by these figures the energy passive effects reached through roof BIPVT collectors with respect to the stand-alone ones, are assessed. Each marker reported in these graphs is representative of a simulated weather zone among the 20 listed in Table 17. By observing Figure 91 an almost linearly increase with *HDDs* and decrease with *ISRs* (the minus sign means a reduction of the heating demand) can be detected. This is due to the enhanced

winter passive heating/insulating effect of roof BIPVT collectors in the cold winter climate zones (high *HDDs* and low *ISRs*). Figure 91 confirms that the unitary cooling demands ($\Delta E_{Cooling}$), corresponding to the occurring overheating unwanted effects, are higher for hot climate zones (high *CDDs* and *ISRs*). Note that, the differences (ΔE) reported in Figure 91 range from -0.7 to nearly 0 kWh/m^{3}y and in Figure 91 from 0 to 0.32 kWh/m^{3}y. Therefore, for all the considered weather zones, a minor influence of BIPVT collectors on the overall energy demands for space heating and cooling of Zone 3 is detected. This result is confirmed by observing Table 21. Here, for the investigated weather zones of Freiburg, Milan, Naples and Almeria the heating and cooling energy demands of Case B Zone 3, as well as the related overall primary heating and cooling demands, are reported. In Figure 92, Zone 3 differences, between Case C and Case B, in terms of overall primary energy for space heating and cooling ($\Delta PE_{Heating\&Cooling}$) are shown vs. *CDD* and *HDD* (the minus sign denotes a reduction of the energy demand).

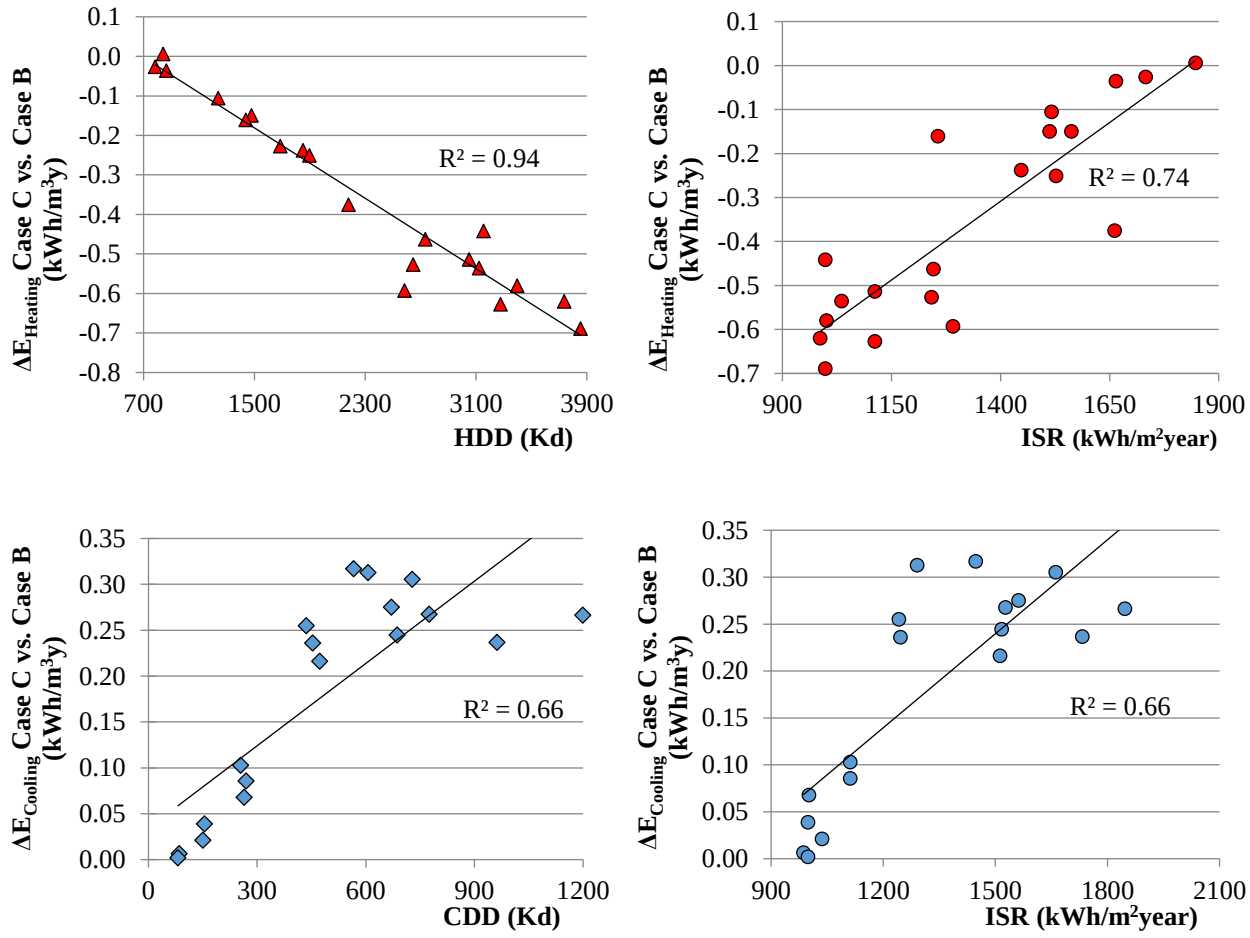

Figure 91. Zone 3: heating (above) and cooling (below) energy saving between Case C and B.

This figure shows that for the weather zones with high HDD and low *CDD* the roof integration of PVT collectors leads to slight overall savings, whereas for zones with high *CDD* (e.g. Larnaca, Almeria, Palermo and Naples) the negative (unwanted) passive effect of summer overheating is dominant with respect to the positive (useful) winter heating one. However, once again, such variations are small with respect to the overall building primary energy consumption.

Table 21. Zone 3: Energy and primary energy for space heating and cooling for Case B.

Weather Zone	$E_{Heating}$	$E_{Cooling}$	$PE_{Heating}$	$PE_{Cooling}$	$PE_{Heating\&Cooling}$
	[kWh/m^{3}y]				
Freiburg	13.17	0.06	8.71	0.04	8.75
Milan	11.07	0.44	7.35	0.26	7.61
Naples	1.81	1.85	1.15	0.93	2.09
Almeria	0.06	3.11	0.04	1.61	1.65

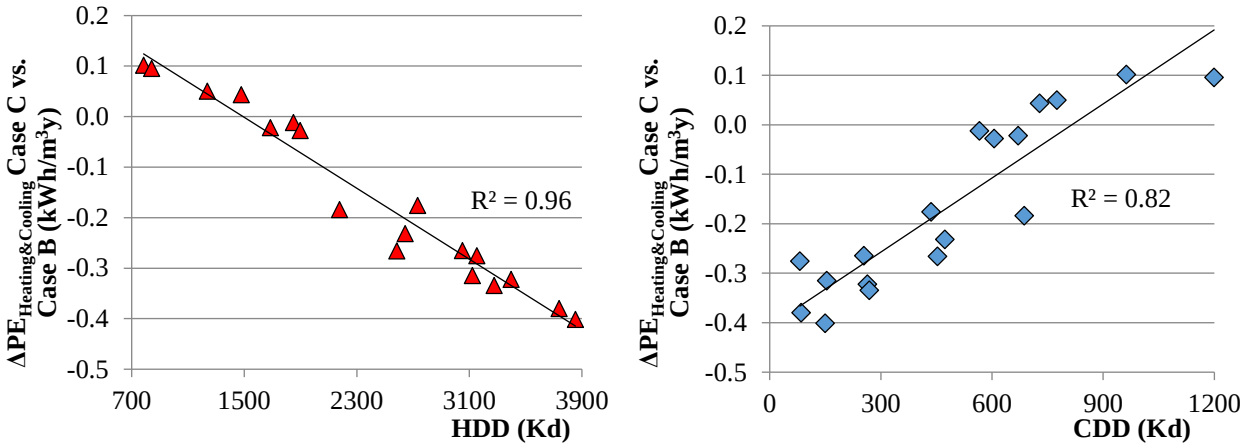

Figure 92. Zone 3: primary energy difference for space heating and cooling, Case C vs. Case B.

Thermo-economic analysis

In order to assess the economic performance of the examined building-plant system layouts, a suitable thermo-economic analysis is carried out. The obtained results are shown in Table 22. Here, for Freiburg, Milan, Naples and Almeria and for Cases B, C and D, by taking into account Case A as RS, the differences of Primary Energy demand (ΔPE), total Primary Energy Savings (PES), Primary Energy Savings for space heating and cooling (PES^*), savings in terms of operating costs (ΔC), extra capital costs (ΔI_0), SPB periods are reported. As an example, by comparing Case D vs. Case A, remarkable $PESs$ of about 73, 77, 87 and 89% are achieved for Freiburg, Milan, Naples and Almeria, respectively. These results are mainly due to the high electricity production obtained through the façade and roof BIPVT collectors. Conversely, PES^* results much lower than the related PES. Note that they may become also negative (see Almeria) if the unwanted summer overheating effects are higher than the helpful winter ones due to the BIPVT collectors. The calculated SPB indexes resulted rather high for all the investigated weather zones and system layouts, ranging from about 11 years for Almeria (Case A vs. B) to 20 years for Freiburg (Case A vs. D). As expected, SPB indexes decrease as a function of the related available solar radiation. This result is mainly due to the achieved electricity production. By comparing the calculated $SPBs$ and $PESs$ for Cases B and C (vs. Case A) in Table 22, minor differences are observed among all the examined weather zones. In other words, Cases B and C are almost equivalent from the economic point of view. It is worth noting that such result was obtained considering the conservative assumptions to neglect PVT panels landing costs for Case B and to assume the same installation costs of the PVT collectors in Cases B and C. Consequently, if in the next future

such extra costs (for Case B) and savings for BIPVT devices will be taken into account, Case C economic profitability could be enhanced.

Table 22. *ΔPE*, *PES*, *PES**, *ΔC*, *ΔI*$_0$, *SPB* between Case A and Cases B, C and D.

Case	*ΔPE* [MWh/y]	*PES* [%]	*PES** [%]	*ΔC* [k€/y]	*ΔI*$_0$ [k€]	*SPB* [y]
Freiburg						
Case A vs. Case B	30.83	65.67	6.26	4.86	80.69	16.6
Case A vs. Case C	31.58	67.32	6.96	4.94	80.69	16.3
Case A vs. Case D	43.11	72.75	10.92	6.87	135.14	19.7
Milan						
Case A vs. Case B	34.25	69.50	8.75	5.40	80.69	15.0
Case A vs. Case C	34.20	69.45	8.82	5.39	80.69	15.0
Case A vs. Case D	47.92	76.91	10.63	7.57	135.14	17.8
Naples						
Case A vs. Case B	40.89	81.93	17.23	6.44	80.69	12.5
Case A vs. Case C	40.73	81.68	15.29	6.42	80.69	12.6
Case A vs. Case D	56.44	86.77	12.35	8.91	135.14	15.2
Almeria						
Case A vs. Case B	44.88	85.50	2.00	7.07	80.69	11.4
Case A vs. Case C	44.55	84.95	-5.73	7.02	80.69	11.5
Case A vs. Case D	61.39	88.76	-23.35	9.70	135.14	14.0

In Figure 93, *ΔPES** between Cases A-B and Cases A-C is plotted vs. HDD for Freiburg, Milan, Naples and Almeria. A negative *ΔPES**, equal to -2% for Naples and -8% for Almeria, is detected. Therefore, in mild Mediterranean or hot summer climates, stand-alone PVT collectors result more efficient than the BIPVT ones. In general, the adoption of façade BIPVT collectors results not much attractive (vs. roof applications) because of the low related ISR. In fact, for all the investigated weather zones, the roof BIPVT system layout (Case C) resulted much more economically convenient than the façade/roof BIPVT one (Case D). In other words, the capital cost of the façade PV solar fields is paid back in longer times (vs. roof applications) because of the lower thermal energy and electricity production per unit of the façade BIPVT surface area.

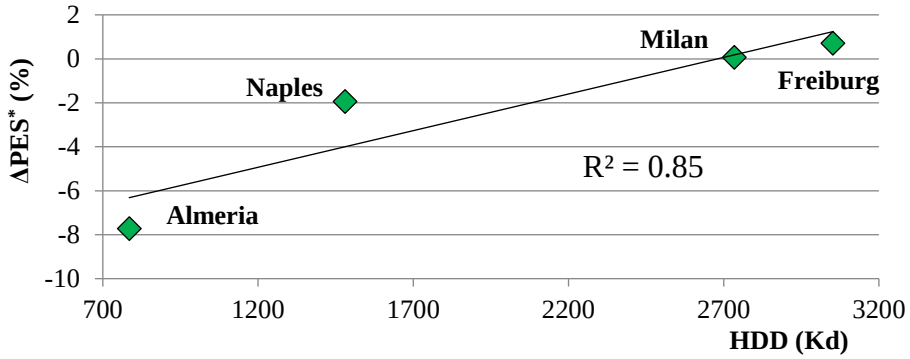

Figure 93. Primary energy saving difference for space heating and cooling between Cases A-B and Cases A-C.

Study 2

Applications: Offices **Analysis:** Energy, economic and environmental

Technologies: roof BIPVT solar collectors, heat pump/chiller, gas-fired condensing boiler, lead acid battery, adsorption chiller

The study 2 concerns the modelling and simulation of an innovative polygeneration system layout based on a BIPVT system coupled to an adsorption chiller and an electricity storage system, for a 3-floors office building, well-representative of the traditional Italian buildings. Such study, concerning the energy, economic and environmental analysis is reported in reference [208]. The system produces solar heating by RF, solar cooling by a low-temperature adsorption chiller, solar DHW and electricity. The electricity produced by BIPVT collectors is used to satisfy the building needs. The eventual extra-production is delivered to the grid or stored in lead-acid batteries, with the purpose of mitigating the effects of solar energy intermittency. Auxiliary heat pumps/chillers and a gas-fired condensing boiler are included in the model in order to integrate the demands of heating, cooling and DHW production.

This work was developed in order to fill the lack of literature reported in subsection 2.3, showing that none of the papers available in literature is focused on the dynamic energy performance evaluation of solar heating and cooling systems, including BIPVT collectors coupled to the solar cooling and electric energy storage systems. In addition, it is also wort noting that this study allows one to evaluate the active and the passive effects due the building integration, under dynamic conditions, that is still mostly neglected in literature. By means of the developed dynamic simulation model, implemented in TRNSYS 17 environment, the system performances are assessed by varying:

- the main system design and operating parameters with respect to the value of reference case ones;
- the building U-values as a function of four well representative Italian weather conditions (Palermo, Naples, Florence and Turin).

System layout - Study 2

The developed dynamic simulation model is applied to a suitable case study building for office use, consisting of 3-floors corresponding to 3 different thermal zones. For comparison purposes two different building configurations are modelled, namely, Reference System (RS) and proposed System (PS). Both configurations are implemented in TRNSYS environment. For such configurations, building space heating and cooling, DHW and electricity demands consumption are dynamically calculated. The simulation model is completed by an additional computer tool for the assessment of the system economic and the environmental impact performance. In the following, more details about the PS layouts are provided, whereas for RS see the description reported in Study 1, Case A.

Proposed System. In Figure 94, the building-plant configuration of the PS is depicted. Here, the building is modelled by implementing a south facing roof BIPVT collectors field (consisting of water unglazed flat-plate panels). The back surface of the solar collectors is considered as coincident with the external surface of the tilted roof. Note that such arrangement is compliant with many present and future national rules (e.g. the Italian legislation), which recommend or oblige, especially for new buildings, the installation of solar collectors as integrated (or adjacent) to the building external surfaces [21].

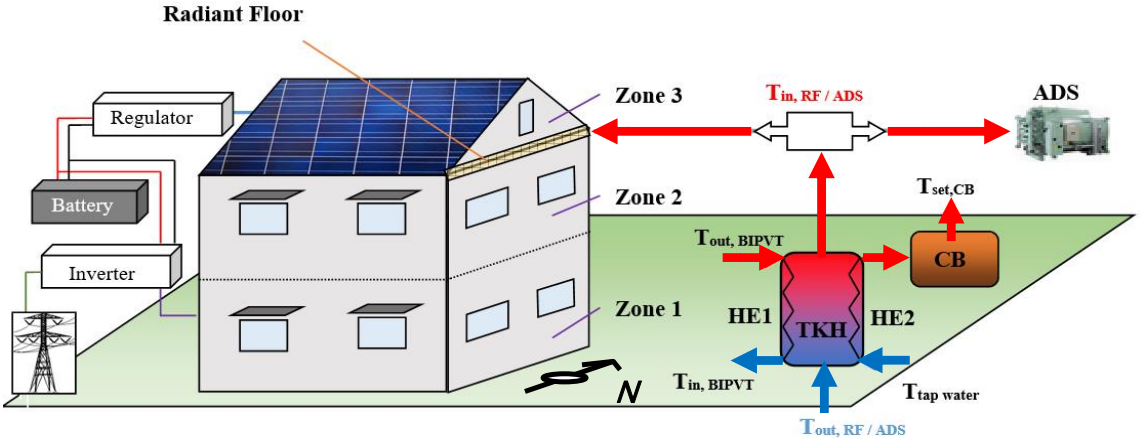

Figure 94. Roof BIPVT collectors with electricity storage and adsorption chiller.

In Figure 95, the considered proposed building-plant system, with five system loops, is shown:

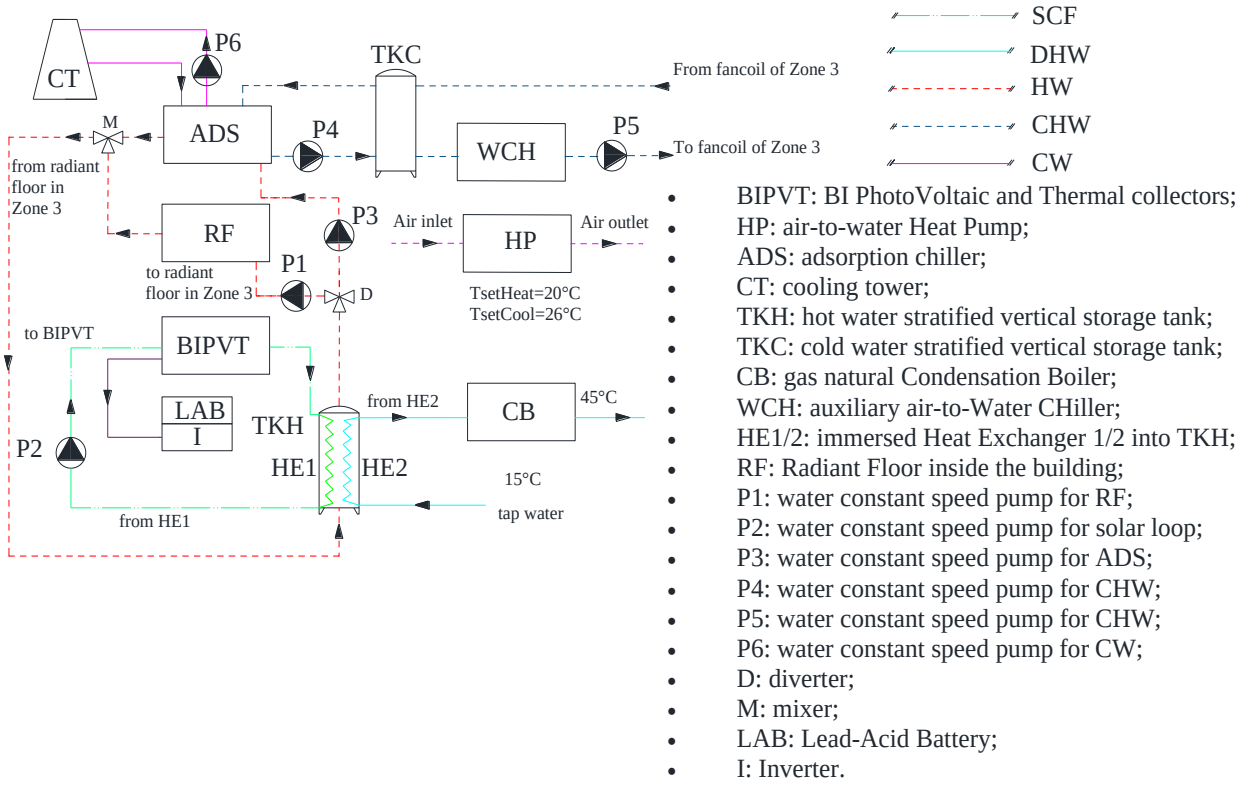

- BIPVT: BI PhotoVoltaic and Thermal collectors;
- HP: air-to-water Heat Pump;
- ADS: adsorption chiller;
- CT: cooling tower;
- TKH: hot water stratified vertical storage tank;
- TKC: cold water stratified vertical storage tank;
- CB: gas natural Condensation Boiler;
- WCH: auxiliary air-to-Water CHiller;
- HE1/2: immersed Heat Exchanger 1/2 into TKH;
- RF: Radiant Floor inside the building;
- P1: water constant speed pump for RF;
- P2: water constant speed pump for solar loop;
- P3: water constant speed pump for ADS;
- P4: water constant speed pump for CHW;
- P5: water constant speed pump for CHW;
- P6: water constant speed pump for CW;
- D: diverter;
- M: mixer;
- LAB: Lead-Acid Battery;
- I: Inverter.

Figure 95. PS: plant layout.

- SCF& DHW loop – see Study 1, Figure 85.
- Hot Water (HW) loop – the outlet water from the stratified vertical energy storage TK for Hot water (TKH) is supplied by means of two water constant speed Pumps (P1 and P3) to the Zone 3 RF for indoor space heating and to an ADSorption chiller (ADS) for indoor space cooling,
- CHilled Water (CHW) loop – the chilled water produced by the adsorption chiller is stored in an energy storage TK for Cold water (TKC) through the P4 pump. Then the chilled water is supplied to the building fan coils through the P5 pump;

- Cooling Water (CW) loop – the cooling water from the Cooling Tower (CT) is supplied to the adsorption chiller through the P6 pump.

The operating principle of the PS and the related control strategies about the BIPVT, HE2 outlet temperature, the schedule DHW demand and the hot TK top temperature during winter operation are the same as those summarized in the subsection "System layout - Study 1" (see Table 12 for $T_{TK,topSET} = T_{TKH,topSET}$; Table 14 for $T_{in,RF}$). Note that although the control of the activation of solar DHW production is the same of the Study 1, the schedule is different since it is related to the office user. Regarding the summer operation, the controller, which controls the TKH top temperature, produces the ON signal, for the P3 pump activation of inlet hot water flow rate required by the adsorption chiller, if TKH top temperature is higher than $T_{ON,ADS}$ +0.5°C (upper dead band), as shown in Table 23. $T_{ON,ADS}$ is the minimum TKH top temperature for the ADS activation. Consequently, the adsorption chiller, the P4 and P6 pumps are switched on and chilled water is produced. Auxiliary electric HP are also used for the heating/cooling of the building thermal Zones 1 and 2 at the selected set-point temperatures. For the thermal Zone 3, the auxiliary system for space heating is obtained by an electric heat pump (in case of low or zero thermal energy production for the RF activation), whereas the auxiliary system for space cooling is an electric air-to-Water CHiller (WCH, Figure 95). In particular, such auxiliary device is included in the proposed plant layout as backup of the adsorption chiller in case of scarce solar radiation or high internal heat gain in the thermal Zone 3. Such electric chiller is designed with the same rated cooling capacity as the ADS (to balance all the Zone 3 cooling loads when the ADS is deactivated).

A suitable controller is taken into account in order to manage the WCH activation. In particular, such controller receives temperature readings from the bottom of the cold storage TKC and produces the ON signal for the chiller activation if the TKC bottom temperature is higher than $T_{ON,WCH}$ (Table 23). A further specific controller is used in order to manage the activation of the P5 pump. In particular, such controller receives temperature readings from the indoor air of the thermal Zone 3 (where the fan coil system is installed) and the controller produces the ON signal for the pump activation if the Zone 3 indoor air temperature is higher than $T_{setCool}$ (Table 24).

The whole system operation is guaranteed only during the occupation office time (Monday – Friday, 08:00 – 17:00). In order to mitigate the effects of intermittency of solar energy, the use of an electricity storage system (obtained by Lead-Acid Batteries, LABs), coupled to an inverter / regulator system, is taken into account (their operating parameters are listed in Table 23). In this way, the electricity produced by BIPVT collectors and not directly self-consumed is stored into the LABs. If their maximum state of charge is reached, the extra produced electricity is supplied to the grid.

System model – Study 2

In this section, a detailed description of the thermodynamic model related to ADSorption chiller is only provided. The model of the Building (TRNSYS Type 56), BIPVT collectors (TRNSYS Type 563) and RF, are in detail explained in the previous study (Study 1). For the remaining system components, the main features are reported in the following list:

- Lead-acid storage batteries (LABs). They are modelled through TRNSYS Type 47, which specifies how the battery state of charge varies over the time, given the rate of charge or discharge.
- Regulator and inverter. They are modelled through TRNSYS Type 48. The regulator distributes Direct Current (DC) power from BIPVT collectors to/from the batteries and to the inverter, which

converts the DC power to Alternating Current (AC), sending it first to the user and then to the grid, if the batteries are fully charged.

For additional details about the simulation models of such devices, see reference [191].

e) Adsorption chiller

A hot water driven adsorption chiller, ADS, is adopted in order to provide cooling to the Zone 3 of the building during the summer season. In the model, this component is simulated by the component TRNSYS Type 909. This component is based on user-supplied data files, which consists of manufacturer catalogue data, including the trend of the cooling capacity and the COP for different operating conditions. The data files are generated on the basis of the hot, chilled and cooling side inlet temperatures and liquid mass flow rates. In particular, an *InvenSor® LTC 10 vario* adsorption chiller is selected, with a nominal capacity of 6.3 kW. The thermodynamic model of the adsorption chiller is based on the energy balance. The thermal energy flow rate removed from the chilled water is computed as:

$$\dot{Q}_{chw} = \min\left(\dot{Q}_{capacity}, \dot{m}_{chw} \cdot c_p (T_{chw,in} - T_{chw,set})\right) \quad (13)$$

where: $T_{chw,set}$ is the set point temperature for the outlet chilled water stream (such parameter is an input to the model). The adsorption chiller operates with the regeneration of a desiccant matrix and the required power for this process is:

$$\dot{Q}_{hw} = \frac{\dot{Q}_{chw}}{COP_{ADS}} \quad (14)$$

In addition, adsorption chiller operation requires that thermal energy flow rate must be rejected by the cooling water stream. This power flow is calculated as follows:

$$\dot{Q}_{cw} = \dot{Q}_{chw} + \dot{Q}_{hw} + \dot{Q}_{aux} \quad (15)$$

where: $\dot{Q}_{aux}$ is the auxiliary power required to run pumps and controllers of the chiller. Once all the power terms are defined (hot, chilled and cooling sides of the adsorption chiller), the outlet water streams temperatures can be calculated as:

$$T_{chw,set} = \begin{cases} T_{chw,set} \text{ if } \dot{Q}_{capacity} \geq (\dot{m}_{chw} \cdot c_{p,chw} \cdot (T_{chw,in} - T_{chw,set})) \\ T_{chw,in} - \dfrac{\dot{Q}_{capacity}}{\dot{m}_{chw} \cdot c_{p,chw}} \text{ if } \dot{Q}_{capacity} < (\dot{m}_{chw} \cdot c_{p,chw} \cdot (T_{chw,in} - T_{chw,set})) \end{cases} \quad (16)$$

$$T_{cw,out} = T_{cw,in} + \frac{\dot{Q}_{cw}}{\dot{m}_{cw} \cdot c_{p,chw}} \quad (17) \qquad T_{hw,out} = T_{hw,in} - \frac{\dot{Q}_{hw}}{\dot{m}_{hw} \cdot c_{p,chw}} \quad (18)$$

Finally, the adsorption chiller COP (COP_{ADS}) is calculated as follows:

$$COP_{ADS} = \frac{\dot{Q}_{chw}}{\dot{Q}_{aux} + \dot{Q}_{hw}} \quad (19)$$

d2) Energy and economic model

In order to calculate the primary energy saving and the economic profitability of PS vs. RS, the consumptions of both systems are analysed. The energy needs of RS are due to: i) the electricity demand of HP for space heating and cooling, by calculating the related variable COPs as reported in

Eq. (7)), appliances and artificial lights; ii) the natural gas consumption of CB for DHW production. The consumptions of PS are due to the energy integration of the DHW condensing boiler and to the electricity for space heating and cooling, appliances, lighting, and auxiliary electric devices (e.g. the pumps of the RF system, the ADS chiller, the cooling tower and the solar field). Then, for the PS, the primary energy saving is calculated by considering, for each simulation time step, the electricity produced by BIPVT collectors, the electricity power from/to the batteries, the electricity supplied by the grid and the primary energy due to the DHW consumption. For this reason, the primary energy saving of electricity and DHW is calculated in each *i*-th time step as follows:

$$\Delta PE_{el,DHW} = \sum_i \left(\frac{E_{el,BIPVT} - E_{el,toLAB}\eta_R\eta_I + E_{el,fromLAB}\eta_R\eta_I\eta_{LAB}}{\eta_{RS,el}} - \frac{Q_{DHW,CB,RS} - Q_{DHW,CB,PS}}{\eta_{RS,DHW}} \right)_i \quad (20)$$

where: $E_{el,BIPVT}$ is the produced electricity by the BIPVT system; $E_{el,toLAB}$ is the electricity stored by the batteries; $E_{el,fromLAB}$ is the electricity from the batteries to the load; $Q_{DHW,CB,RS}$ and $Q_{DHW,CB,PS}$ are the energy consumption of the CB in RS and PS; $\eta_{RS,DHW}$ is the thermal efficiency of the CB; $\eta_{RS,el}$ is the efficiency for conventional electricity power production; η_R, η_I and η_{LAB} are the efficiency of the regulator, inverter and batteries, respectively. Eq (20) shows the calculation of the annual primary energy savings obtained by the PS. It is obtained by a summation for all the i-th time steps of the primary energy savings obtained in each time interval. In particular, the first term in the summation is representative of the primary energy saved due to the lower electric energy demanded to the grid. Obviously, this term considers BIPVT electric production, inlet and outlet LAB electricity. The second term in the summation is the saving of primary energy due to the lower amount of thermal energy demanded to the gas-fired boiler. Obviously, this saving is strictly related to the BIVT thermal production. In addition, for assessing the effects of the BIPVT system on the space heating and cooling energy demand of building, the primary energy saving due to energy consumption for space heating and cooling $PES_{heat\&cool}$ is computed as:

$$PES_{heat\&cool} = \sum_i \frac{1}{\eta_{RS,el}} \left(\frac{\frac{Q_{heat,RS}}{COP_{RS,Heat}} - \frac{Q_{heat,PS}}{COP_{PS,Heat}} + \frac{Q_{cool,RS}}{COP_{RS,Cool}} - \frac{Q_{cool,PS}}{COP_{PS,Cool}}}{\frac{Q_{heat,RS}}{COP_{RS,Heat}} + \frac{Q_{cool,RS}}{COP_{RS,Cool}}} \right)_i \quad (21)$$

where: $Q_{heat,RS}$, $Q_{cool,RS}$, $Q_{heat,PS}$ and $Q_{cool,PS}$, are the energy for space heating and cooling supplied by the HP, in case of RS and PS, respectively.

The primary energy saving due only to DHW (PES_{DHW}) is calculated as:

$$PES_{DHW} = \sum_i \frac{1}{\eta_{RS,DHW}} \left(\frac{Q_{DHW,CB,RS} - Q_{DHW,CB,PS}}{Q_{DHW,CB,RS}} \right)_i \quad (22)$$

The total capital cost ($J_{PS,tot}$), calculated to assess the economic feasibility of PS, includes the initial cost of all the main components (BIPVT solar collectors, tanks, adsorption chiller, cooling tower, storage lead-acid batteries, inverter / regulator). The single cost (computed in €) of such components is reported in the following. The BIPVT solar field cost is computed as [209]:

$$C_{BIPVT} = 200 \cdot A_{PVT} \quad (23)$$

The costs of the TKH and TKC are assessed as a function of their storage volumes [192]:

$$C_{TK} = 494.9 + 808.0 \cdot V_{TK} \quad (24)$$

The specific cost per kW of the ADS chiller is estimated to be 500 €/kW_{cool} [209]. Therefore, the initial cost of the ADS chiller is:

$$C_{ADS} = 500 \cdot \dot{Q}_{chw} \quad (25)$$

The initial cost of the cooling tower is calculated as a function of the cooling power [210]:

$$C_{TOWER} = 0.005 \cdot \dot{Q}_{cw}^{\ 2} + 13.31 \cdot \dot{Q}_{cw} + 885.5 \quad (26)$$

The initial cost of batteries, according to the market analysis [211], is calculated as a function of the specific cost per kWh of the energy capacity of LAB ($Capacity_{LAB}$) system (equal to 200 €/kWh [212], obtained by literature data), as

$$C_{LAB} = 200 \cdot Capacity_{LAB} \quad (27)$$

The LABs energy capacity is calculated by taking into account a ratio between the LABs useful energy capacity and the BIPVT system rated electricity production equal to 0.5, with the aim to reach a trade-off between capital cost and energy capacity.:

The capital cost of the inverter is calculated as a function of the nominal electric power of BIPVT collectors ($\dot{P}_{el,BIPVT}$). The following function is obtained by literature data and manufacturers' market data [213]:

$$C_I = 180 \cdot \dot{P}_{el,BIPVT} \quad (28)$$

The economic yearly saving of PS takes into account the economic gains and operating costs with respect to those of RS. In PS and RS, the operating costs are due to electricity demand from the grid ($E_{el,fromGRID,PS}$ and $E_{el,fromGRID,RS}$), by considering the hourly unitary cost ($j_{el,GRID}$) and the thermal energy consumption due to the CB, assessed in terms of natural gas unitary cost (j_{NG}).

Note that, the operating costs and the economic gains for PS are here assessed by considering the Italian rules regarding the electricity exchange with the national grid. In Italy, small PV systems (below 20 kW) may benefit of the net metering program. Here, the national grid is virtually used as an infinite electric storage. Therefore, when the PV produces electricity in excess with respect to the demand, such electricity is delivered to the grid. Then, when the demand is higher than PV production, the grid can return back the previous amount of electricity. This balance is performed on a yearly basis. Thus, at the end of the year the user pays only the difference between the overall energy withdrawn from the grid and the energy produced by the PV system. In addition, a small additional cost (fixed, independent from the amount of electricity exchanged) must be paid [214]. In particular, an annual constant cost for the electricity exchange (C_{EX}) and the additional costs for the withdrawn electricity from grid are taken into account [215].

The economic gains, i.e. the surplus of BIPVT system electricity production dumped to the national grid ($E_{el,toGRID,PS}$, electricity no self-consumed as well as no stored in batteries) and the further economic compensation (when electricity dumped to the grid is greater than the withdrawn one) are also taken into consideration. As a result, the annual savings obtained by IS, are calculated as:

$$\Delta C = \max\left(E_{el,toGRID,PS} \cdot ZP - E_{el,fromGRID,PS} \cdot NSP, 0\right) + \min\left(E_{el,fromGRID,PS} \cdot NSP, E_{el,toGRID,PS} \cdot ZP\right) +$$
$$C_{charges} \cdot \min\left(E_{el,fromGRID,PS}, E_{el,toGRID,PS}\right) + j_{el,grid} \cdot \left(E_{el,fromGRID,RS} - E_{el,fromGRID,PS}\right) \quad (29)$$
$$-C_{EX} - j_{NG} \cdot \frac{Q_{DHW,CB}}{LCV_{NG}\eta_{RS,DHW}}$$

where: $C_{charges}$ is the economic compensation due to grid and general charges received on the minimum between electricity exchanged to/from the grid; *NSP* is the hourly National Single Price; *ZP* is the hourly Zone Price. Eq. (29) is derived on the basis of the algorithm included in Italian

national legislation dealing with net metering. All the terms are strictly calculated according to those rules. In particular, the first term represents the cost of the electricity taken from the grid to the user. The second term is the revenue related to the electricity sold to the grid. The third term is an economic compensation due to the grid and general charges, which is proportional (through $C_{charges}$) to the minimum value between the electricity taken from the grid and the electricity delivered to the grid. The fourth term is representative of the savings related to cost of electricity which is proportional to the difference between the electricity taken from the grid by the RS and the one taken from the grid by the PS. C_{ex} is an annual constant cost required to benefit of the net metering. Finally, the last term shows the savings in terms of natural gas consumed by the boiler.

At last, the economic profitability analysis also includes the assessment of the SPB period, as calculated in Eq.10. Note that for the calculation of the extra costs, the costs of the components included in both RS and PS do not have to be considered since their difference is obviously equal to zero. Therefore, considering that the WCH is included in both PS and RS (to balance the cooling loads of the thermal Zone 3), its capital cost is not included in the calculation of the extra cost.

f) Environmental analysis

Due to the increasing environmental concerns and specifically global warming issue, in this study the environmental performance of PS, is also calculated. This assessment is performed by comparing the yearly equivalent carbon dioxide (CO_2) emissions of PS vs. the RS ones. In order to carry out this analysis, the equivalent avoided CO_2 emissions (ΔCO_2) are calculated as:

$$\Delta CO_2 = \sum_i \left(\left(E_{el,\,fromGRID,RS} - E_{el,\,fromGRID,PS} \right) \cdot F_{el} + \frac{Q_{DHW,CB,RS} - Q_{DHW,CB,PS}}{\eta_{RS,DHW}} \cdot F_{NG} \right)_i \quad (30)$$

where: F_{NG} and F_{el} are the CO_2 equivalent emission factor for natural gas and for electricity, respectively. ΔCO_2 is calculated by assuming that in PS and RS, equivalent CO_2 emissions are due to the primary energy consumption of the CB and to the electricity withdrawn from the national grid. In PS, no equivalent CO_2 emission associated to the electricity produced by the BIPVT collectors and to the energy required by ADS is considered, because both systems are supplied by renewable solar energy.

Case study

The dynamic simulations for both RS and PS are carried out by taking into account the hourly Meteonorm weather data file for the weather zone of Naples (South-Italy) [191]. A traditional 3-floors office building, with HVAC system activation schedule ranging from 8:00 0 to 17:00 (during weekdays), is simulated. According to the Italian rules [216], the considered heating season is between November 15th and March 31st whereas the cooling one is set from June 1st to September 30th. The same building geometry considered in the Study 1 was taken into account (See Figure 84). Therefore, details about the building surfaces/volumes are provided in Table 15. Conversely, the properties of opaque and transparent elements of the modelled building are different with respect to the Study 1 ones (Table 16); in fact in this study the features are selected as well-representative of the traditional Italian buildings [217]) and reported in Table 25. The design and operating parameter assumptions for the polycrystalline PVT collectors are listed in Table 12. The design parameters regarding the components of the investigated system, as well as additional simulation assumptions regards the heating and cooling set points and HVAC system activation hours, are reported in Table

23 and Table 24, respectively. The TKH design parameters are the same as in Study 1 (see Table 12, Tank). The values of $\eta_{RS,el}$, j_{NG} and natural gas lower heating value, adopted in the carried out energy-economic and environmental analysis are equal to those assumed in Study 1. Additional assumptions are: i) the annual constant cost of electricity exchange (C_{EX}) equal to 30 €/year; ii) CO_2 equivalent emission factors for natural gas and for the electricity, F_{NG} and F_{el}, equal to 0.20 $kgCO_2/kWh_{PE}$ and 0.48 $kgCO_2/kWh_{el}$, respectively.

Table 23. Case study: main system design parameters.

	Parameter	Description	Value	Unit
INVERTER	P_L	Power output Limit	20	kW
	$FSOC$	High and low limit on Fractional State Of Charge	0.9 - 0.4	-
	$\eta_{I,AC,to,DC}$	Efficiency (AC to DC)	1	
	$\eta_{I,DC,to,AC}$	Efficiency (DC to AC)	0.96	
	η_R	Regulator efficiency	0.95	
BATTERY	C_{cell}	Cell energy Capacity	16.7	Ah
	$N_S \cdot N_P$	Number cells in Series and in Parallel	24·14	-
	η_{LAB}	Battery efficiency	0.9	
BOILER	q_{HE2}	Heat Exchanger 2 maximum flow rate	18	kg/h
	$P_{CB,rated}$	Rated condensing boiler heating power	0.754	kW
	$\eta_{RS,DHW}$	CB efficiency (also for RS)	0.95	-
	q_{DHW}	DHW flow rate per day	90	l/day
COLD TANK	H_{TK}	Height	1	m
	V_{TKC}	Cold water tank (TKC) volume	1	m^3
	$T_{ON,WCH}$	TKC top temperature for electric chiller activation	20	°C
ADSORPTION CHILLER& COOLING TOWER	Q_{chw}	Rated adsorption chilled capacity	6.3	kW
	COP_{ADS}	Nominal Coefficient Of Performance	0.6	-
	q_{P3}	P3 rated flow rate for supplying adsorption chiller	1130	kg/h
	q_{P4}	P4 rated chilled flow rate for supplying Tank TKC	1085	
	q_{P6}	P6 rated flow rate for cooling adsorption chiller	2893	
	$T_{SET,chw}$	Chilled water set point temperature	12	°C
	$T_{ON,ADS}$	Tank TKH top temperature for adsorption chiller activation	55	
	$Q_{ch,TOWER}$	Rated cooling tower capacity	18.75	kW
FAN COIL	q_{P5}	Rated P5 flow rate (fan coil circuit)	1085	kg/h
	q_{air}	Rated air flow rate (fan coil)	3788	
HEAT PUMP / CHILLER	COP_N	Nominal Coefficient Of Performance (heating)	3.5	-
	EER_N	Nominal energy efficiency ratio (cooling)	3.0	
	$P_{heat/cool,rated1}$	Rated heating / cooling capacity Zone 1	15 / 12	kW
	$P_{heat/cool,rated2}$	Rated heating / cooling capacity Zone 2	13 / 10	
	$P_{heat/cool,rated3}$	Rated heating / cooling capacity Zone 3	8/ 6	

Table 24. Simulation assumptions.

Set point indoor air temperature [°C]	Heating: $T_{setHeat}$ = 20 Cooling: $T_{setCool}$ = 26
Occupancy schedule [h]	08:00 - 17:00
Number of occupants per zone	5
People heat gain [W/p]	Sensible: 75 Latent: 75
Machineries heat gains schedule [h]	08:00 - 17:00
Machineries heat gains per zone [W/m^2]	4.7 (5 computers, 140 W each one)
Light [W/m^2]	5
Air infiltration and free cooling ventilation rate [vol/h]	0.4/2.0
Air ventilation rate [l/s p]	11
DHW set point temperature [°C]	45
Tap water temperature [°C]	15
DHW usage schedule [h]	08:00 - 17:00

Table 25. Study 2 opaque/transparent elements features.

Building element	***U-value*** [W/m^{2}K]	**Thickness** [m]	ρ_s [-]	ε [-]
Roof (without BIPVT panels) and façades	0.98	0.30	0.40	0.90
Internal floor/ceiling (tile flooring)	0.68	0.33		
Ground floor (tile flooring)	0.81	0.18		
Windows glass	2.83	0.004/0.016 (air)/0.004	0.13	0.18

Results of Study 2

In the following a detailed discussion of the obtained yearly, monthly, weekly and daily simulation results as well as of the outcomes achieved by a suitable sensitivity analysis performed on the main design system parameters and on the weather conditions, is presented.

Yearly results

In this paragraph, the results of simulations are discussed, related to both PS and RS referred to the weather zone of Naples, calculated on the yearly basis. In particular, in Figure 96, it is evident that during winter season, the building heating energy demand of PS vs. RS decreases from 5.26 to 3.79 MWh/year (for the Zone 3 from 2.14 to 1.22 MWh/year, not shown in the figure).

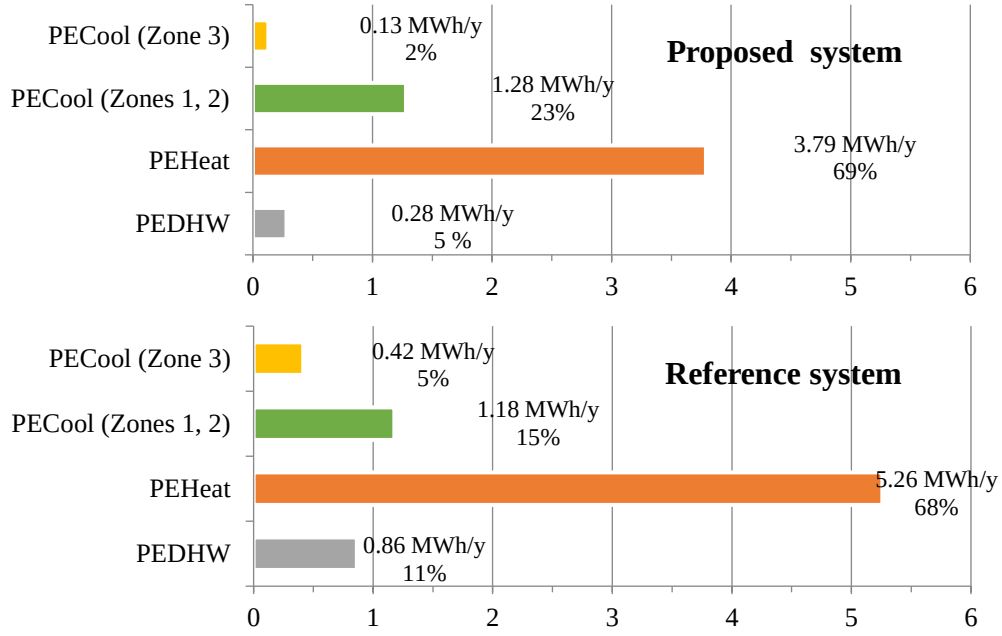

Figure 96. Yearly primary energy demands for heating, cooling and DHW preparation.

This benefit is due to the BIPVT collectors thermal energy supplied to the Zone 3 RF and to the useful heating passive effect due to the BIPVT collectors. This positive result is basically due to the higher temperature of south-facing roof internal surface of PS vs. the RS one. Note that, PS south-facing roof external surface is coincident with the back surface of the solar collectors, whose temperature is higher than the ambient one. To this positive free heating effect, obtained during winter, corresponds a negative overheating one in summer (lower or no heat dissipation through the building roof can be detected). Because of the considered weather zone (Naples, South-Italy), as well as the

considered free cooling strategy, *U-values*, windows solar shadings and overhangs, the calculated primary energy demand for space cooling ($PE_{Cool\ Zone\ 3}$ + $PE_{Cool\ Zones\ 1,\ 2}$) is considerably lower than the space heating one (PE_{Heat}). Note that, $PE_{Cool\ Zone\ 3}$ of PS takes into account only the primary energy demand due to the auxiliary electric chiller. Therefore, the adopted solar cooling technology reduces the amount of space cooling energy provided through the air-to-water heat chillers of the whole building (from 1.6 MWh/y of RS to 1.4 MWh/y of PS), though the cooling energy increase of Zones 1 and 2, due to BIPVT collectors heating passive effect (see $PE_{Cool\ Zones\ 1,\ 2}$ of RS vs. $PE_{Cool\ Zones\ 1,\ 2}$ of PS). Regarding the primary energy for DHW production, a primary energy saving obtained by the PS is detected thanks to the solar energy use. The general lower amount of energy vs. space heating and cooling is basically due to the building use (office) considered in this case study. In Figure 96 the percentage of the above mentioned yearly primary energy demands are also reported. In Table 26 the yearly performance of the PS vs. the traditional one is summarised. A remarkable primary energy saving is achieved by the PS vs. the traditional system (ΔPE = 37.5 MWh/y).

Table 26. Yearly performance of the PS vs. RS.

ΔPE [MWh/y]	$PES_{el,DHW}$ [%]	PES_{DHW} [%]	$PES_{heat\&cool}$ [%]	$J_{PS,tot}$ [k€]	ΔC [k€/y]	SPB [y]	$\Delta CO_2^{\%}$ [%]
37.5	63.5	67.5	24.1	18.3	1.80	10.1	83.9

In particular, the total primary energy saving for both electricity consumptions and DHW production ($PES_{el,DHW}$) resulted about 64%, whereas the primary energy saving for DHW preparation only (PES_{DHW}) is equal to about 67%. An overall primary energy saving for space heating and cooling ($PES_{heat\&cool}$), about 24% is reached. Note that, such achievement is obtained by suitably taking into account the combination of the above mentioned negative (in summer) and positive (in winter) passive effect of the BIPVT system. Such results, in terms of $PES_{el,DHW}$ and $PES_{heat\&cool}$, agree with those obtained by the Study 1. The capital cost of the considered PS ($J_{PS,tot}$) is 18.3 k€; the yearly economic saving vs. the RS one (ΔC) resulted equal to 1.80 k€/y. Assuming a capital cost incentive equal to 50%, the *SPB* resulted approximately 10 years. Although the economic feasibility of the PS is not so optimistic, the calculated equivalent CO_2 avoided emissions ($\Delta CO_2^{\%}$) resulted higher than 83%.

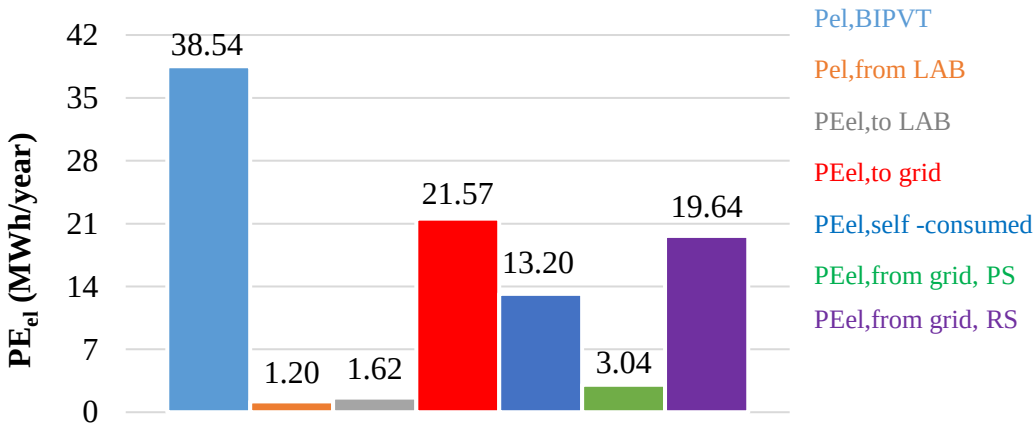

Figure 97. Yearly primary energies for the PS and RS.

In Figure 97 the yearly primary energy due to the different calculated electric energies in both PS and RS are depicted. The above mentioned $PES_{heat\&cool}$ allows to the PS vs. RS one to remarkably

reduce the overall electricity consumption and the related operating economic costs. In fact, the electricity primary energy provided by the grid to the PS building ($PE_{el,from\ grid,\ PS}$) is much lower than the one supplied to RS ($PE_{el,from\ grid,\ RS}$): 3.0 vs. 19.6 MWh/y. Such positive achievement is also due to the electricity produced by the BIPVT collectors and self-consumed by the building ($PE_{el,self\text{-}consumed}$) or stored through the battery storage system ($PE_{el,from\ LAB}$). Note that a significant amount of primary energy due to electricity production ($PE_{el,BIPVT}$) is delivered to the grid ($PE_{el,to\ grid}$).

Monthly and weekly results

In this section, the yearly energy system performances are presented on monthly and weekly bases. In particular, in Figure 98 the monthly results regarding the ratios between the systems electric energy exchanges (i.e. self-consumed by the user, produced by the BIPVT system, fed to and supplied by the grid, provided by the batteries) and the building electricity demand are reported.

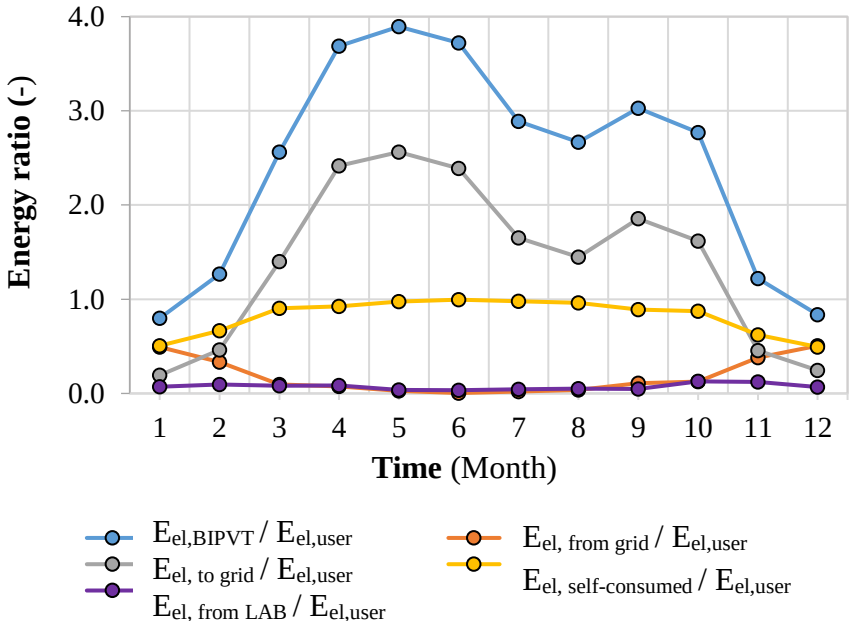

Figure 98. Monthly electricity ratios.

In this figure, it is possible to observe that the ratio related to self-consumed energy ($E_{el,\ self\text{-}consumed} / E_{el,\ user}$) is always much higher than the ratio related to the electricity demand from the grid ($E_{el,\ from\ grid} / E_{el,\ user}$). In fact, mainly during the summer months, thanks to the electricity production of the BIPVT system and the use of LABs, an almost virtually grid-independent building-plant system is reached. This is mainly due to the relevant BIPVT electricity production that during the summer season is constantly higher than the user demand (average summer $E_{el,\ BIPVT} / E_{el,\ user} = 3$). Therefore, LABs are often fully charged and the significant amount of the exceeding electricity is delivered to the grid (average summer $E_{el,\ to\ grid} / E_{el,\ user} = 2$). Obviously, this circumstance mainly occurs during the weekends when the offices are closed (104 days per year). This is particularly visible from May to August, when the electricity demand from the grid ($E_{el,\ from\ grid} / E_{el,\ user}$) and the electricity supplied by the batteries to the building ($E_{el,\ from\ LAB} / E_{el,\ user}$) are negligible. This result is due to the selected capacity of the batteries, which is low vs. the BIPVT system one. In fact, during such months, the BIPVT produced electricity ($E_{el,\ BIPVT} / E_{el,\ user}$) is much higher than the self-consumed ($E_{el,\ self\text{-}consumed} / E_{el,\ user}$) one. It is worth noting that in this case study, the LABs capacity

was selected on the basis of an economic criterion (minimum *SPB*). Thus, results show that for the present capital costs of LABs and the present electricity selling prices, large LABs are not profitable. However, this scenario is expected to vary in the next few years due to the simultaneous reduction of LABs capital costs and due to the reduction of electricity selling prices.

In Figure 99, several system thermal energy ratios are reported on weekly basis. During the winter weeks, the electricity efficiency of the BIPVT collectors ($\eta_{el,BIPVT}$) approaches 9%, whereas it decreases under 8% in summer weeks (because of the high BIPVT collectors surfaces temperatures). Such results agree with those obtained by in-field measurements on polycrystalline flat glazed polycrystalline silicon PVT collectors [218], and are higher than those measured by the authors on similar unglazed collectors [219], as expected.

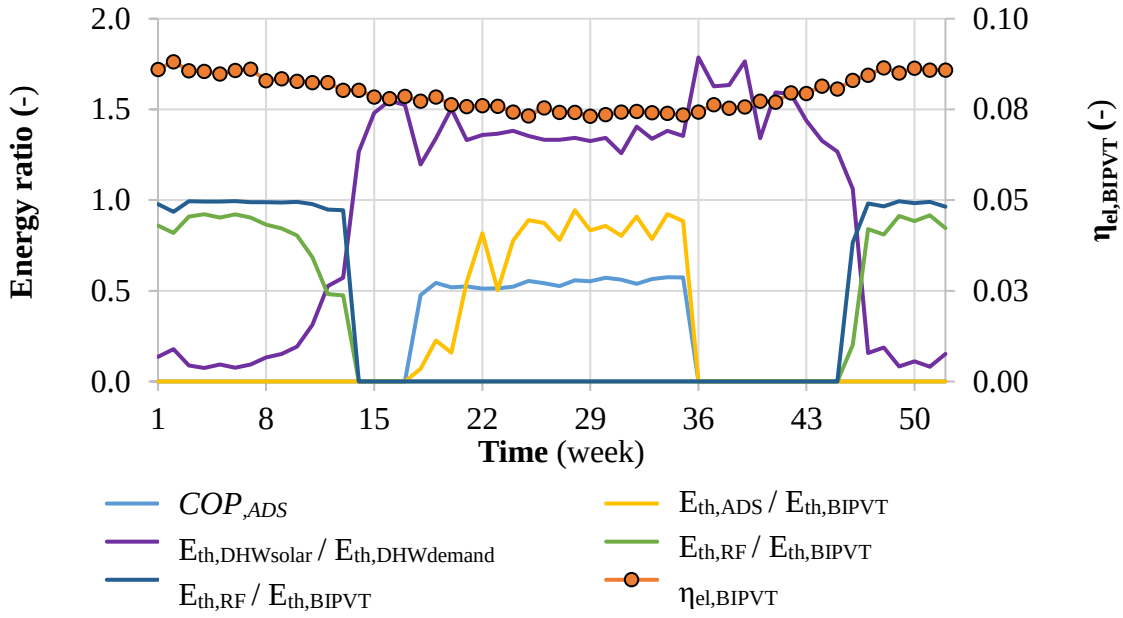

Figure 99. Weekly energy ratios.

The trends of the BIPVT thermal energy utilization are shown in Figure 99. Here, it is possible to observe that the PS, during both winter and summer seasons, shows an almost full utilization of the thermal energy produced by the BIPVT. In fact, the ratio between the energy provided by the RF and that one produced by the BIPVT collectors, $E_{th,RF}$ / $E_{th,BIPVT}$, approaches the unity (full utilization of $E_{th,BIPVT}$) during winter. Nevertheless, due to the utilization of BIPVT thermal energy by the RF, a remarkable use of the CB, $E_{th,CB}$, is necessary to produce DHW. In particular, $E_{th,CB}$ / $E_{th,DHWdemand}$ almost reaches the unity, decreasing during spring/autumns weeks and becoming null during summer, where $E_{th,BIPVT}$ is capable to completely balance the DHW demand, resulted to be totally covered by solar energy. In Figure 99, it is also worth noting that the ratio between the thermal energy need of the adsorption chiller and that one produced by the BIPVT, $E_{th,ADS}$ / $E_{th,BIPVT}$, reaches about 0.9 during the summer warmest weeks, showing an almost full utilization of the solar thermal energy. During the summer season, the *COP* of the investigated adsorption chiller technology approaches the nominal value of 0.6. The range of variation of the *COP* (calculated at different operating conditions and without including the electric consumption due to auxiliaries) is consistent with results obtained through experimental investigations, such as those reported in recent studies where different operational parameters [220] and low regeneration temperature working pairs [221] of the adsorption chiller are taken into account, as well as those obtained by optimization

procedures focused on the device itself [222]. The ratio between the thermal energy for the DHW produced by BIPVT collectors and the user DHW energy demand ($E_{th,DHWsolar}$ / $E_{th,DHWdemand}$) in no-winter time is always greater than 1. This is due to greater outlet temperatures from the heat exchanger HE2 (used for the DHW production) in the TKH with respect to the set point temperature (assumed equal to 45°C).

Daily dynamic results

In this section, for a representative summer day several daily simulation results are shown, Figure 100.

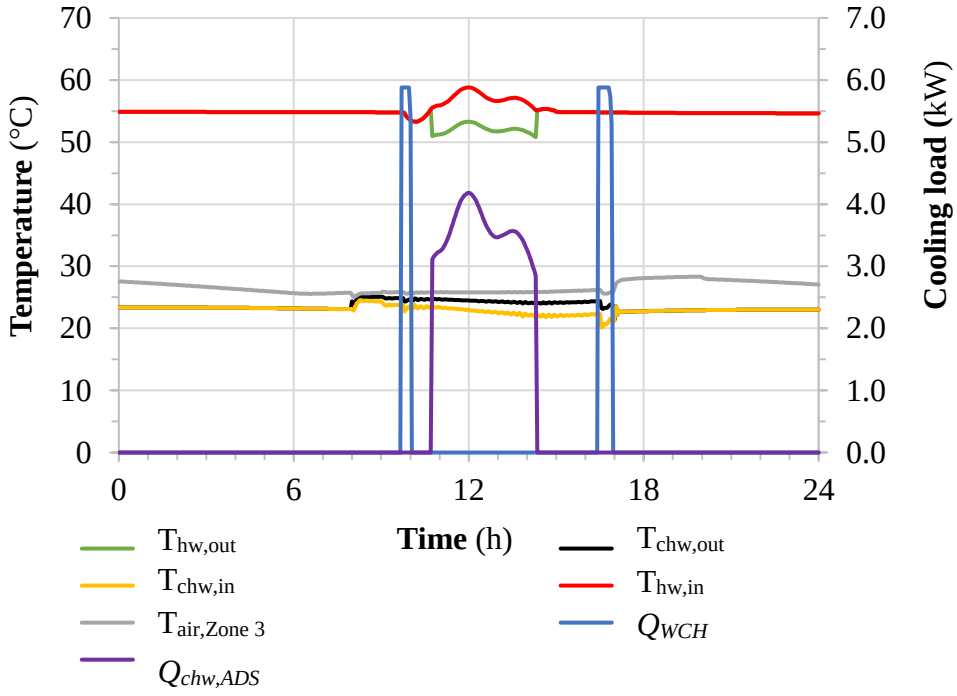

Figure 100. A sample summer day

In particular, the selected day is September 6th, ranging from simulation hour 5928 to 5952. In this figure, the time histories of the main operating temperatures of the HVAC system are reported. Early in the morning, the inlet hot water temperature at the top of TKH (53°C) is lower than the adsorption chiller activation temperature ($T_{ON,ADS}$ = 55°C). As it is clearly shown in Figure 100 from 10:40 to 14:20, the obtained levels of $T_{hw,in}$ (> $T_{ON,ADS}$) allow the adsorption chiller running for the space cooling of thermal Zone 3 by reaching its summer set point temperature ($T_{air,\ Zone\ 3}$) of 26°C. In these hours, the chilled power of adsorption chiller $Q_{chw,ADS}$ ranges between 3.0 to 4.2 kW, with the higher value reached at 12:00. From 08:00 to 09:40 and from 14:20 to 16:20, this required set point temperature is obtained only by the chilled water stored in TKC (without chillers activation), whereas from 09:40 to 11:00 and from 16:20 to 17:00, it is obtained by the backup electric chiller (Q_{WCH} = 6.0 kW). Note that, when at 17:00 the Zone 3 fan coil units are switched off, an increase of $T_{air,\ Zone\ 3}$ is detected (reaching almost 28°C). According to the design assumptions, the difference between the inlet and outlet hot water temperature of the adsorption chiller during its activation ($T_{hw,in}$ - $T_{hw,out}$) is about 5°C. The outlet chilled water temperatures from the fan coil units to TKC storage ($T_{chw,out}$) range between 23 and 25°C. In Figure 100 the time history of the inlet chilled water

temperature to the fan coil units ($T_{chw,in}$) is also depicted. Note that, the temperature differences ($T_{chw,out}$ - $T_{chw,in}$) are about 2°C. Regarding the calculated adsorption chiller *COP*, a level approaching the nominal value is reached. It is noted also that the $COP_{,ADS}$ decreases with $T_{hw,\ in}$, i.e. the lower $T_{hw,\ in}$ the lower the adsorption chiller efficiency.

Sensitivity analysis: system design-operating parameters and weather condition

In this section, the results of the carried out sensitivity analysis are reported. Such analysis aims to investigate the variation of the above discussed results, by varying the main design and operating parameters of the plant. A discussion of the results related only to the parameters showing the highest influence on the system energy and economic performance are reported. Such parameters are: the Zone 3 indoor air temperature for RF activation ($T_{in,RF}$); TKH top temperature for RF activation ($T_{TKH,topSET}$); the TKH volume per m^2 of BIPVT collectors ($v_{TKH,spec}$); the number of LABs cells in parallel (N_P). In particular, the primary energy saving on DHW production and on building heating and cooling (PES_{DHW} and $PES_{heat\&cool}$) as well as to the payback period (*SPB*) are discussed. Figure 101 shows the Primary Energy Saving for DHW preparation (PES_{DHW}) as a function of $T_{in,RF}$ and $T_{TKH,topSET}$.

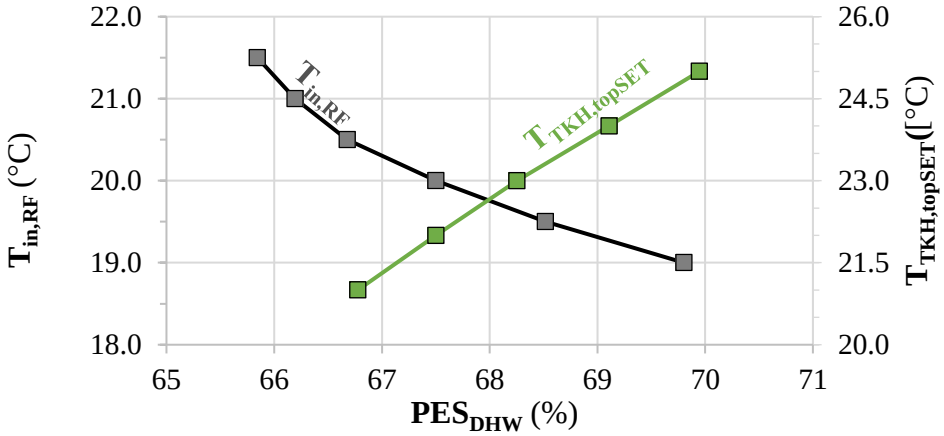

Figure 101. PES_{DHW} as a function of T_{inRF} (left) and $T_{TKH,topSET}$ (right).

Varying such parameters, a modification of the control strategy on the activation of the P1 pump is achieved. In particular, the increase of $T_{TKH,topSET}$ leads to exploit the stored thermal energy into TKH for the DHW production, instead to produce Zone 3 space heating by the RF system. In fact, the higher the $T_{TKH,topSET,}$ the shorter the P1 pump activation time in winter. By this approach, an increase of PES_{DHW} is obtained, with a maximum of about 70%. An opposite result is obtained by increasing $T_{in,RF}$, Figure 101. In fact, by increasing $T_{in,RF}$ with respect to the starting value reported in Table 23 ($T_{in,RF}$ = 19°C), an RF activation is obtained (by switching on the P1 pump), although the indoor air temperature exceeds the winter set point ($T_{setHeat}$ = 20°C). Therefore, in this case, the control strategy leads to exploit the stored thermal energy into TKH for RF activation, by reducing its use for DHW production. PES_{DHW} and $PES_{heat\&cool}$ trends, depending on $v_{TKH,spec}$, are depicted in Figure 102. Here, it can be observed that an increase of $v_{TKH,spec}$ is always useful from the energy saving point of view. In fact, the higher $v_{TKH,spec}$, the higher the obtained *PES* for both the DHW production and space heating and cooling.

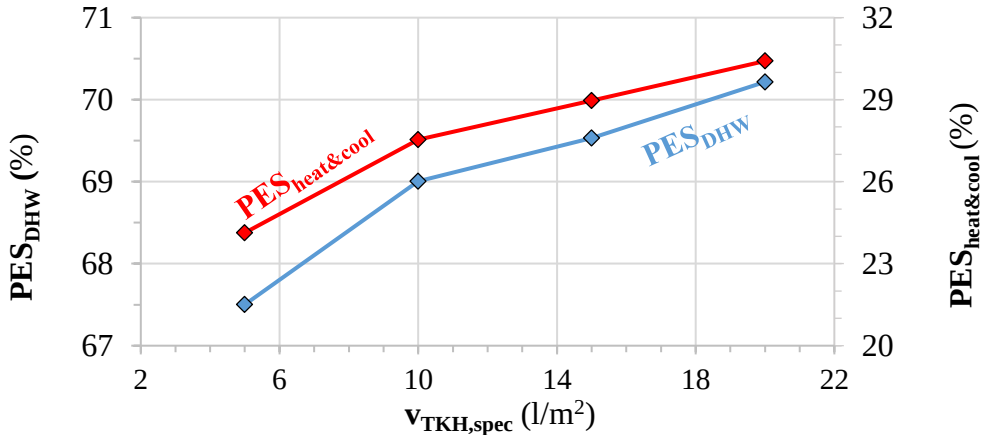

Figure 102. PES_{DHW} (left) and $PES_{heat\&cool}$ (right) as a function of $v_{TKH,spec}$.

This is mainly due to the higher solar thermal energy stored into TKH (also during the afternoon, when the solar radiation decreases) exploited for DHW and space heating and cooling purposes. The maximum PES_{DHW} and $PES_{heat\&cool}$ are 70 and 30%, respectively. Figure 103 shows the variation of the *SPB* as a function of N_P and $v_{TKH,spec}$. It can be observed that for this office building, the lower the N_P the shorter the *SPB* (the minimum is about 9.8 years). In addition, the smaller the $v_{TKH,spec}$ the shorter the *SPB*; the increase of the energy saving obtained with high TKH volumes, showed in Figure 102, is not significant to attain relevant increases of the economic saving: higher volumes lead to reduced economic profitability of the PS. In this section, the economic and environmental results of a sensitivity analysis are reported, by taking into account:

- four different Italian weather zones (Turin, Florence, Naples, Palermo). For each weather zone, the corresponding *HDD*, the *ISR* and the considered heating period [203], as well as the cooling season period and the HVAC system activation schedules are reported in Table 27.

Table 27. Weather zones indexes and HVAC system schedules.

Weather zone	***HDD*** [Kd]	***ISR*** [kWh/m²y]	**Winter season**	**Cooling season**	**Heating / cooling schedule** [h]
Turin (North-Italy)	2617	1291	15/10 - 15/04	01/06 - 30/09	08:00 - 17:00
Florence (Middle-Italy)	1821	1440	01/11 - 15/04		
Naples (South-Italy)	1034	1512	15/11 - 31/03		
Palermo (South-Italy)	751	1664	01/12 - 31/03		

- new heating/cooling capacities of the building-plant system, in order to comply with the corresponding maximum heating and cooling loads according to the selected weather zones (Table 28);

- new *U-values*, thicknesses, solar reflectance and emissivity of the opaque/transparent building envelope elements according to the selected weather zones. In particular, such parameters follow the Italian law for the energy efficiency of new buildings (Table 28).

The results of this parametric analysis are reported from Figure 104 to Figure 106. In particular, in Figure 104 the obtained overall primary energy saving ($PES_{el,DHW}$, due to electricity demand for the building heating and cooling and natural gas consumption for DHW production) of PS vs. RS, calculated as a function of *HDD* and *ISR*, is reported for the four considered weather zones.

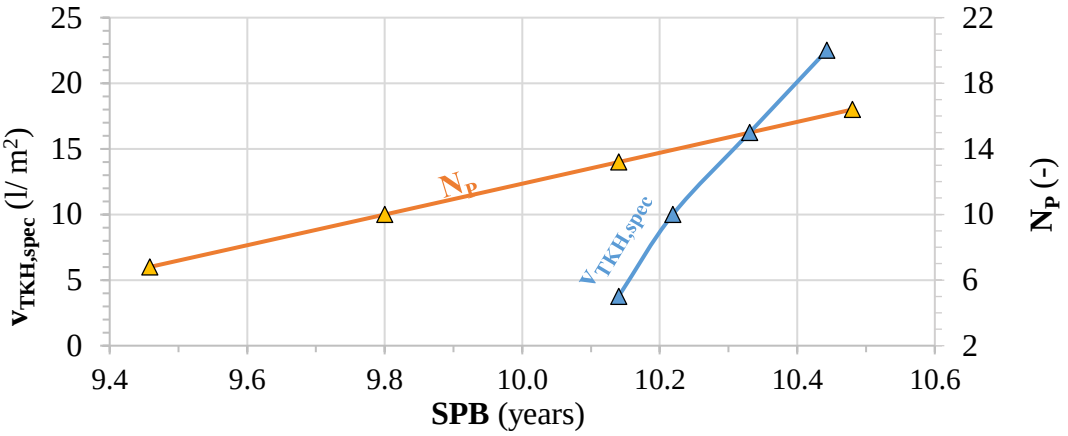

Figure 103. *SPB* as a function of $v_{TKH,spec}$ (left) and N_P (right).

Table 28. Parametric analysis building-plant systems: heating/cooling capacities and opaque/transparent elements features.

Weather zone	Zone	Heating [kW]	Cooling [kW]	Building element	*U-value* [W/m²K]	Thickness [m]	ρ_s [-]	ε [-]
Turin	1 2 3	14 12 7	11 9 6	Roof without BIPVT panels	0.22	0.33	0.40	0.90
				Façades	0.26	0.32		
				Internal floor/ceiling (tile flooring)	0.76	0.27		
				Ground floor (tile flooring)	0.26	0.24		
				Windows glass	0.86	0.004/0.016 (Kr)/0.004	0.27	0.31
Florence	1 2 3	13 11 7	10 9 5	Roof without BIPVT panels	0.26	0.32	0.40	0.90
				Façades	0.29	0.31		
				Internal floor/ceiling (tile flooring)	0.76	0.27		
				Ground floor (tile flooring)	0.29	0.23		
				Windows glass	1.27	0.004/0.016 (Ar)/0.004	0.24	0.31
Naples	1 2 3	13 11 7	10 9 5	Roof without BIPVT panels	0.33	0.30	0.40	0.90
				Façades	0.34	0.29		
				Internal floor/ceiling (tile flooring)	0.76	0.27		
				Ground floor (tile flooring)	0.38	0.21		
				Windows glass	1.40	0.004/0.016 (Ar)/0.004	0.27	0.31
Palermo	1 2 3	9 8 5	7 6 4	Roof without BIPVT panels	0.35	0.29	0.40	0.90
				Façades	0.43	0.28		
				Internal floor/ceiling (tile flooring)	0.76	0.27		
				Ground floor (tile flooring)	0.44	0.76		
				Windows glass	1.40	0.004/0.016 (Ar)/0.004	0.27	0.31

The results show an almost linear correlation between $PES_{el,DHW}$ and the selected weather condition indexes. In particular, $PES_{el,DHW}$ linearly increases with ISRs and decreases with HDDs, ranging between 68.8% for Palermo and 58.5% for Turin. The higher $PES_{el,DHW}$ obtained for Palermo is justified by the higher electricity production of BIPVT collectors with respect to the electricity production achieved in Turin (+20%). In Figure 105, a linear increasing trend is obtained also for the equivalent avoided CO_2 emissions of PS vs. RS ($\Delta CO_2^{\%}$), reported as function of *ISRs* for the analysed weather zones. The best environmental performance is obtained in Palermo, where the CO_2 saving of the PS surpasses 90%. Anyway, remarkable equivalent avoided CO_2 emissions are also achieved in Naples, Florence and Turin, being always higher than 76%.

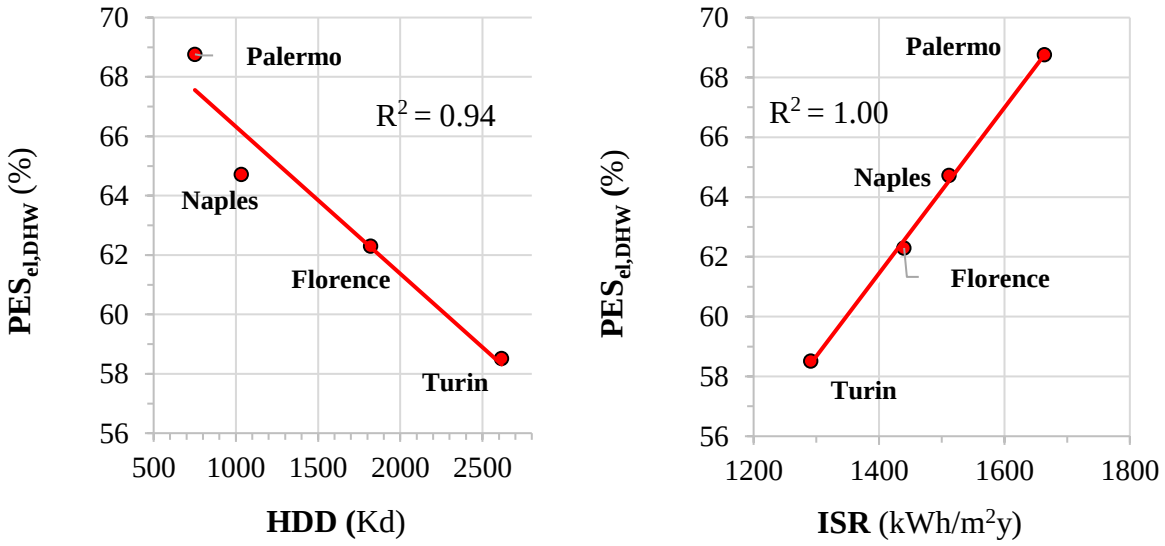

Figure 104. *$PES_{el,DHW}$* vs. *HDD (left)* and *ISR* (right).

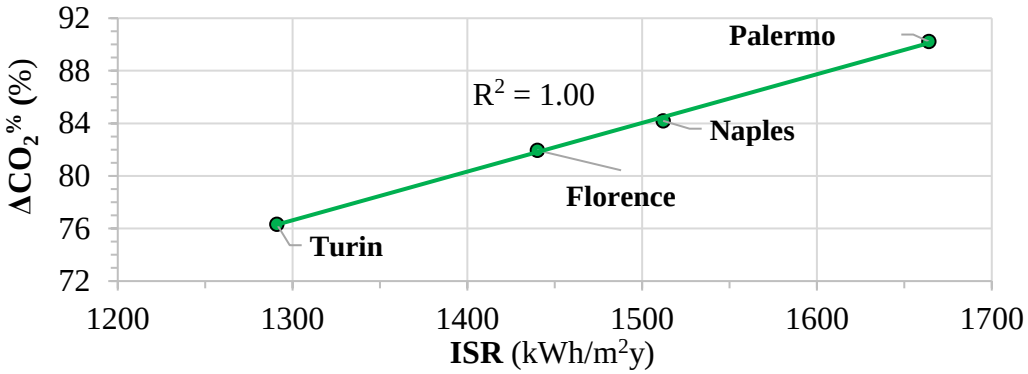

Figure 105. Equivalent CO_2 avoided emissions (*$\Delta CO_2^{\%}$*) vs. *ISR*.

In Figure 106, the trend of *SPB* is plotted for the analysed weather zones as a function of *HDD* and *ISR*. Also, in this case an almost linear decrease with *HDD* and increase with *ISR* is detected. The best *SPB*, equal to 10.6 years, is obtained for Turin, the worst one for Palermo (11.3 years). It is worth noting that this trend is different with respect to the one achieved in the case of *PES*. This is mainly justified by the different selling/purchasing costs of electricity. In fact, such result is due to the high economic saving obtained in Turin, by comparing the total cost of PS and RS (electricity cost for space heating / cooling + natural gas cost for DHW), higher than the one calculated for Palermo (1793 vs. 1635 €/year). The difference in capital costs between the two cities is negligible (about 4%). Conversely, the higher amount of electricity produced in Palermo (determining a better *PES*, compared to Turin) does not correspond to similar monetary savings. In fact, the overall savings due to electricity production in Palermo and Turin are 1062 and 1254 €/year, respectively. In other words, a 20% of higher electricity production in Palermo (with respect to Turin) corresponds to only 15% of higher monetary incomes. This due to the fact, that the extra production achieved in Palermo is mainly delivered to the grid at very low prices. Conversely, the higher thermal BIPVT production (for DHW, space heating and cooling) of Turin determines an income, which is higher than the corresponding one achieved in Palermo. The overall result is that the savings in Turin are higher than the ones achieved in Palermo, determining a lower *SPB* period.

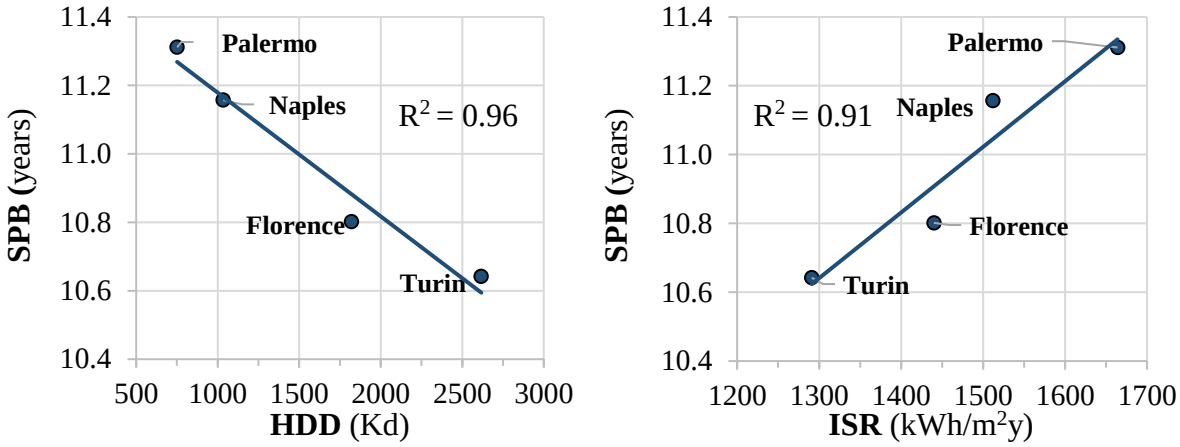

Figure 106. *SPB* vs. *HDD* (left) and *ISR* (right).

Study 3

Applications: Offices and fitness center **Analysis:** Energy, exergy and economic

Technologies: façades BIPVT solar collectors, heat pump/chiller, gas-fired condensing boiler, lead acid battery

The study 3 concerns an exergy and technoeconomic analysis of BIPVT collectors integrated in the south facing façade of a non-residential high-rise building. BIPVT collectors produce: i) thermal energy for space heating purposes, by a radiant floor system; ii) DHW; iii) electricity. Electric air-to-water heat pumps/chillers and a condensing gas fired boiler are used as auxiliary systems for space heating / cooling and DHW, respectively. The system also includes an electricity storage system coupled to the BIPVTs in order to mitigate the effects of solar energy intermittency and to obtain a virtually grid-independent system. The comparison of such system and the conventional one is performed for three thermal zones, well representative of the thermal behaviour of the whole building. The detailed dynamic simulation model is developed by means of TRNSYS 17, in order to predict the transient behaviour of BIPVT system. With respect to the studies 1 and 2 and the others reported in subsection 2.3, the study 3 presents the following novelties:

- a dynamic exergy analysis, together with a dynamic energy and economic analysis of facades BIPVT collectors coupled to an electricity storage system by dynamic simulations;
- the whole building-plant system, by considering the effects of BIPVT collectors exergy on the thermal loads for space heating and cooling and the electricity load of building, is taken into account;
- the evaluation of the exergy destructions and exergy efficiencies of each of the investigated components;
- an exergy efficiency map for several European weather zones of BIPVT collectors;
- a parametric exergy analysis by varying the size of the electricity storage system, by analysing the effect on the destroyed exergy and exergy efficiency.

The economic viability of the PS, evaluated in terms of *SPB*, is also discussed.

The façade integrated PVT collectors configuration modelled in this study, reported in reference [223], is selected because: i) solar systems are mainly used in rural areas, where they can be simply installed on the roof. While in large densely populated cities, high-rise buildings are very common in the urban districts and roof space of the building is often limited and its ownership is controversial; ii) the roof is often shaded by other buildings; iii) the integration of solar collectors on the roof has the disadvantages of serious thermal loss led by long pipelines [224].

System layout - Study 3

The RS and PS are depicted in Figure 107. Here, only three Zones, well-representative of all the other Zones, of a conventional office high-rise building, are taken into account. In fact, all floors are designed for office building usage except for a floor, where a fitness center is located. This assumption allows one to reduce the simulations computation time of the developed building-plant model and the obtained results can be easily extended to whole building. The RS corresponds to the considered conventional building without building integrated PVT collectors, including HP for producing space heating and cooling, a natural gas CB for DHW production, whilst the electricity is provided by the national grid.

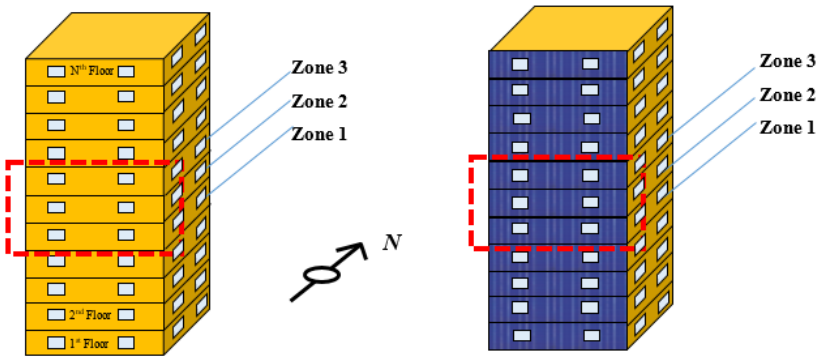

Figure 107. RS (left), PS: façade BIPVT collectors (right).

The PS configuration consists of south facing façade unglazed BIPVTs, designed for the same building considered in the RS. BIPVTs produce thermal energy exploited through a suitable RF system for the space heating of Zone 3 (Figure 108) and electricity is used for the building energy demand.

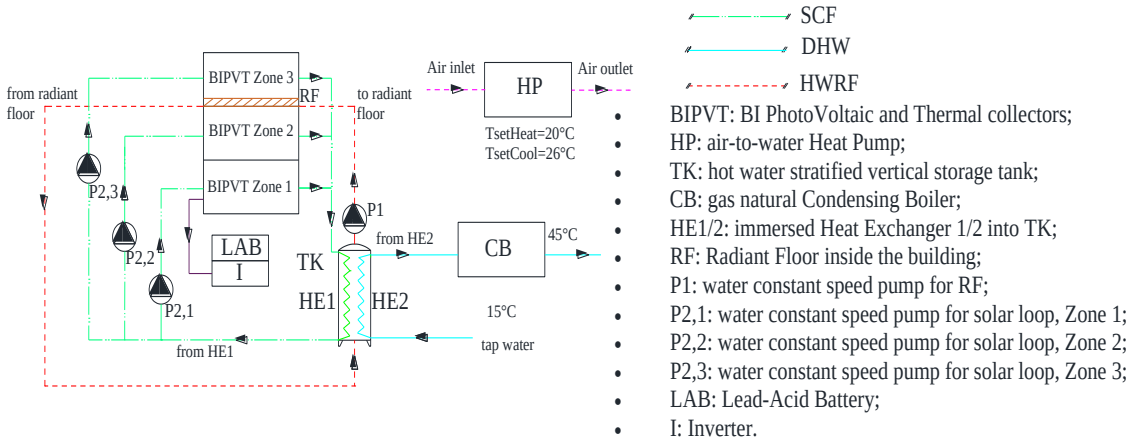

Figure 108. System layout

Table 29. Simulation assumptions

Zone 1	Number of occupants per occupancy schedule [occ·hour]	20 × 9:00 - 13:00; 30 × 13:00 - 18:00; 60 × 18:00 - 22:00
	Occupants heat gain [W/occ]	Sensible: 185. Latent: 340
	Air ventilation rate [l/s occ]	16.5
	DHW demand [l/day occ]	50
	DHW demand schedule	09:00 - 22:00
Zone 2&3	Number of occupants per occupancy schedule [occ·hour]	Zone 2: 18 × 9:00 - 19:00 Zone 3: 9 × 9:00 - 19:00
	Occupant heat gain [W/occ]	Sensible: 75. Latent: 75
	Air ventilation rate [l/s occ]	11.5
	DHW demand [l/day]	30 (0.2 l/day m^2)
	DHW demand and machineries schedule	9:00 - 19:00
Zone 1&2&3	Light [W/m^2]	5
	Air infiltration rate [vol/h]	0.4
	Free cooling ventilation rate [vol/h]	2.0
	DHW set point temperature [°C]	45
	Set point indoor air temperature [°C]	Heating: TsetHeat = 20 Cooling: TsetCool = 26
	Tap water temperature [°C]	15

The excess of BIPVT thermal energy is used to produce DHW for an open space office at Zone 2, a single office at Zone 3 and of fitness center at Zone 1. In layout of PS, 3 main loops are modelled: the Solar Collector Fluid (SCF) loops; the Hot Water of the RF (HWRF) loop; the DHW loop. BIPVTs are arranged in 3 separate hydraulic loops, controlling separately BIPVT outlet water temperature for the 3 zones by suitable controllers. Each controller receives the temperature readings from the outlet of HE1 heat exchanger (i.e., solar collector inlet temperature) and the outlet pipe of its solar collector loop. Hot water produced by the solar loop can be supplied to TK through HE1. The controllers stop their controlled pumps (P2,1, P2,2 or P2,3, depending on the Zone loop) when the respective collectors outlet temperature is lower than the inlet one, in order to avoid heat dissipation. CB is activated only if HE2 outlet temperature is lower than user DHW set point one. The tap water enters HE2 only if: i) the thermal energy for RF is not required (i.e. when P1 pump is off); ii) a simultaneous demand of DHW occurs (Table 29). Consequently, a suitable controller manages the activation of P1 pump. In particular, the control strategy managing the operation of P1 pump is detailed in [29, 208].

System model – Study 3

This section presents a detailed discussion of dynamic exergy balances of the investigated building-plant system, in order to dynamically calculate the destroyed exergy and other exergy performance parameters for each component of the system. To this scope, the system is first modelled from a thermodynamic point of view, calculating the thermodynamic properties for the key state points and the energy flows for all of the time-steps of the simulations. Then, on the basis of the energy results (temperatures, pressures, heat, work, etc.) exergy analysis can be also applied in order to calculate the related exergy performance parameters. Exergy analysis accuracy is strictly related to the energetic model reliability, which must dynamically simulate the performance of the system components. To this scope, a special effort is performed in order to develop suitable dynamic building-plant simulation models (for the PS and RS) by means of TRNSYS 17.

The used significant components of the developed building-plant model are:

- the BIPVT unglazed collectors, Type 563;
- the stratified hot TK, Type 340;
- the radiant floor for the thermal Zone 3 space heating;
- the building, Type 56;
- the Lead-Acid storage Battery (LAB), Type 47;
- the regulator and inverter Type 48.

For Types 563, 340 and 56 see Study 1, for Types 47, 48 see Study 2. For additional details about the remaining models of used devices (TRNSYS fluid properties routine to calculate the thermodynamic properties Type 58, the condensing boiler Type 751, the differential controllers Type 2 and controllers used as delayed output devices Type 661), see reference [191].

g) exergy model

The exergy analysis carried out in this work is based on the definition of unsteady exergy balances for all the components of the system. As a consequence, for each time-step of the 1-year dynamic simulation, the conventional (energy-based) dynamic simulation model returns nodes state

point properties (typically temperature and pressure) and mass flow rates along with components energy flows (heat and work). Then, for each single time-step such data are used as an input by the exergy model, which is able to calculate the corresponding destroyed exergy for all the components. Additional algorithms are implemented in order to calculate the exergy efficiency of the main components. It is worth noting that the majority of the system components do not involve chemical processes. Then, exergy balances can be written considering the sole physical exergy related to the material and energy streams entering and exiting each component. Conversely, in case of CB, important chemical processes occur also when a larger control volume is considered. Therefore, in this case exergy balances must also consider the chemical exergy. Furthermore, it is worth noting that for all the liquid fluids of the systems, the physical exergy can be calculated as:

$$ex_{ph} = (h - h_a) - T_a (s - s_a) = c\left[(T - T_a) + v(p - p_a)\right] - T_a \, c \ln\left(\frac{T}{T_a}\right) \quad (31)$$

However, as usual in liquids, the term $v(p - p_a)$ is often negligible. For example, reference [225] shows that exergy related to pressure drops is definitively negligible with respect to the one related to temperature differences. Therefore, the previous equation can be simplified as follows:

$$ex_{ph} = (h - h_a) - T_a (s - s_a) \quad (32)$$

where T_a is the temperature of the considered dead state. In such equation, thermodynamic properties (enthalpy, entropy, etc.) of all the streams water are calculated in detail using the correlations included in TRNSYS environment. In particular, Type 58 is used to calculate water properties in all the states (liquid, saturated or superheated). Fixed values of dead-state temperature and pressures are assumed, according to the approach reported in reference [226].

The exergy flow due to power produced is numerically equal to the electricity produced [227]. The exergy flows due to a thermal flow can be evaluated correcting the heat flow by the corresponding Carnot factor [227].

$$\dot{E}x_{\dot{Q}} = \dot{Q}\left(1 - \frac{T_a}{T}\right) \quad (33)$$

Thus, the exergy theory can be applied in order to calculate destroyed exergy rates and exergy efficiencies for all components [225, 227]. In the followings, these calculations are shown for the main system components:

BIPVT collectors

Some special calculations must be performed in order to evaluate the exergy stream due to renewable energy sources. In particular, the calculation of the exergy flow due to the solar radiation can be performed using different approaches (Jeter, Petela and others) [228]. Such approaches ("technical boundary approaches") differ for the selection of the temperature of the sun. A completely different approach ("physical boundary approach") disregards the conversion of solar energy into heat in the solar collector. In this study, according to the best practice available in literature for the "technical boundary approach" [228], this calculation is performed by the Petela theorem, in which the sun temperature is set at 4077°C (3/4 of the corresponding black body temperature) [229]:

$$\dot{E}x_{sun} = A_{BIPVT} G \left(1 - \frac{T_a}{T_{sun}}\right) \quad (34)$$

Therefore, considering a control volume containing the BIPVT collectors, including the back surface in contact with the outside surface of building façade, the destroyed exergy is as follows:

$$\dot{E}x_{d,BIPVT} = \dot{E}x_{sun} - \left[\begin{array}{l} \dot{E}x_{BIPVT,o} - \dot{E}x_{BIPVT,i} + \dot{P}_{el,BIPVT} \\ + \left(\dot{Q}_{conv} + \dot{Q}_{rad} \right) \left(1 - \frac{T_a}{T_{top}} \right) + \dot{Q}_{back} \left(1 - \frac{T_a}{T_{back}} \right) \end{array} \right] \quad (35)$$

where: T_{top} and T_{back} are the temperature of the PV cells and the temperature of the back surface of the collector (the interface between the collector and the façade). $\dot{E}x_{SC,o/i}$ is the outlet/ inlet physical exergy of collectors; $\dot{P}_{el,BIPVT}$ is the exergy flow due to electricity produced by collectors, $\dot{Q}_{conv}$ is the heat flow lost to the environment through convection from the top surface of the collectors; $\dot{Q}_{rad}$ is the heat flow lost to the environment through radiation losses from the top surface of the collectors; $\dot{Q}_{back}$ is the transferred heat flow through the back surface of the collectors to the building façade. Note that these last three terms, representing the exergy of the heat lost to the environment, should be considered as an exergy residual as defined by Kotas [227].

This last exergy term, called $\dot{E}x_{back,BIPVT} = \dot{Q}_{back} \left(1 - \frac{T_a}{T_{back}} \right)$, is very significant, and represents the useful winter passive effect of BIPVT collectors, reducing the space heating demand and simultaneously affects the destroyed exergy of collectors. Note that the computation of destroyed exergy must be carried out for the 3 fields of BIPVT collectors, equipped with 3 different separate water circulating loops. In fact, for the 3 considered BIPVT loops, different inlet and outlet temperatures can be achieved. As a consequence, exergy balances must be mandatory written separately for the three considered loops. Finally, the BIPVT collectors exergy efficiency is:

$$\eta_{ex,BIPVT} = \frac{\dot{E}x_{BIPVT,o} - \dot{E}x_{BIPVT,i} + \dot{P}_{el,BIPVT}}{\dot{E}x_{sun}} \quad (36)$$

Condensing boiler

The exergy flow related to the fuel entering the CB can be calculated, considering its specific chemical exergy of reaction, ε_{NG}. Exergy flow related to the fuel used by the CB is:

$$\dot{E}x_{NG} = \dot{m}_{NG} \varepsilon_{NG} \quad (37)$$

Therefore, the destroyed exergy and the exergy efficiency are calculated, respectively, as follows:

$$\dot{E}x_{d,CB} = \dot{E}x_{NG} - \left(\dot{E}x_{CB,o} - \dot{E}x_{CB,i} \right) \quad (38) \qquad \eta_{ex,CB} = \frac{\dot{E}x_{CB,o} - \dot{E}x_{CB,i}}{\dot{E}x_{NG}} \quad (39)$$

Tank

The exergy balance of tank must also consider the stored exergy in the system, i.e. its thermal capacity. The destroyed exergy is:

$$\dot{E}x_{d,TK} = \dot{E}x_{SCF,TK,i} + \dot{E}x_{HWRF,TK,i} + \dot{E}x_{DHW,i} - \dot{E}x_{SCF,TK,o} - \dot{E}x_{HWRF,TK,o} - \dot{E}x_{DHW,o} - \dot{E}x_{TK,stored} \quad (40)$$

$$\dot{E}x_{TK,stored} = \rho V_{TK} c_p \frac{\left(T_{TK,avg,\vartheta} - T_{TK,avg,\vartheta-1}\right) - T_a \ln \frac{T_{TK,avg,\vartheta}}{T_{TK,avg,\vartheta-1}}}{\Delta\vartheta} \quad (41)$$

It is worth noting that the previous equation considers the TK average temperature, $T_{TK,avg,\vartheta}$. The term V_{TK} takes into account the whole volume of tank including the stored water and the inner heat exchangers, HE1 and HE2. In order to calculate the exergy stored $\dot{E}x_{TK,stored}$, the Eq. (41) considers the difference between the TK average temperature at time step ϑ and one at previous time step, ϑ*-1*. $T_{TK,avg,\vartheta-1}$ is achieved by Type 661, a controller reproducing the values of a variable from a user-defined previous time step.

Finally, in the case of tank, no specific exergy product can be considered, therefore, the definition of the exergy efficiency is meaningful. In any case, a process exergy efficiency can be evaluated as follows:

$$\eta_{ex,\mathrm{TK}} = \frac{\dot{E}x_{DHW,o} + \dot{E}x_{HWRF,TK,o} + \dot{E}x_{SCF,TK,o}}{\dot{E}x_{DHW,i} + \dot{E}x_{HWRF,TK,i} + \dot{E}x_{SCF,TK,i}} \quad (42)$$

Lead Acid Battery

The exergy balance of battery can be simply written considering the inlet power to battery $\dot{P}_{el,toLAB}$ (> 0), the power going from the battery $\dot{P}_{el,fromLAB}$ (< 0) to the load and stored power into battery $\dot{P}_{el,LAB,stored}$. The stored power is obtained by the difference between the state of charge *SoC* (Ah) at time step ϑ and one at previous time step, ϑ*-1*, multiplied for the total *voltage* (V) and the number of cells N_{cells} connected in parallel in the battery. Then, the destroyed exergy is:

$$\dot{E}x_{d,LAB} = \dot{P}_{el,toLAB} - \dot{P}_{el,fromLAB} - \dot{P}_{el,LAB,stored} = \dot{P}_{el,toLAB} - \dot{P}_{el,fromLAB} - \frac{voltage \cdot (SoC_{\vartheta} - SoC_{\vartheta-1}) \cdot N_{cells}}{\Delta\vartheta} \quad (43)$$

The dynamic exergy efficiency of battery is calculated by considering the charge and discharge phases, which are not simultaneous. In particular, in the discharge phase, the term $\dot{P}_{el,toLAB}$, considered as exergy fuel, is equal to 0, conversely, in the charge phase the term $\dot{P}_{el,fromLAB}$, considered as exergy product, is equal to 0. For this reason, to evaluate the exergy efficiency also the stored power into battery is taken into account:

$$\eta_{ex,LAB} = \frac{\dot{P}_{el,fromLAB} + \varepsilon^{+}_{LAB} \left|\dot{P}_{el,LAB,stored}\right|}{\dot{P}_{el,toLAB} + \varepsilon^{-}_{LAB} \left|\dot{P}_{el,LAB,stored}\right|} \quad (44)$$

where ε^{+}_{LAB} and ε^{-}_{LAB} are dimensionless coefficients, equal to 0 or 1. In particular, during the discharge phase ε^{+}_{LAB} = 0 and ε^{-}_{LAB} = 1, conversely, during the charge phase.

Building

The exergy analysis of building is performed by taking into account that the system building boundary includes the envelope external surface at external temperature $T_{external,surface,i}$. This boundary is considered both in RS and PS. Note that in PS system, the building boundary of south

façades is in contact with the back surface of the BIPVT collectors. All energy flows through the building boundary are shown in Figure 109.

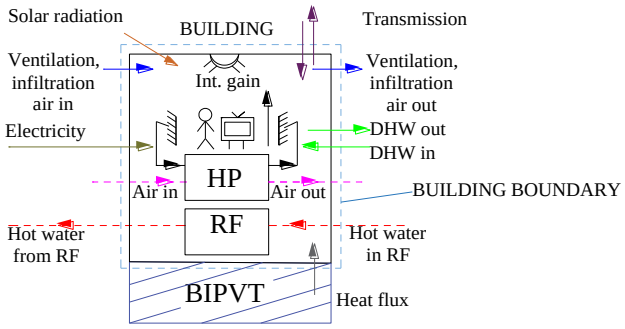

Figure 109. Energy and exergy flows through the building boundary.

The developed exergy model evaluates in detail each exergy flow by considering individually each wall and each window of the building zone at its temperature. This is performed because the temperature of several building components assumes different value during the time-steps of the simulation and, in this way, the calculation of the exergy flow results more accurate. In particular, the developed exergy model of building takes into account:

- the exergy of heat flux due to the total radiation incident on external surfaces (windows and opaque walls) $\dot{E}x_{sun,BUILDING}$ of whole building, evaluated as:

$$\dot{E}x_{sun,BUILDING} = \sum_{z}^{1,2,3} \sum_{i} A_{external,surface,i} G \left(1 - \frac{T_a}{T_{sun}} \right) \tag{45}$$

Note that this computation is carried out for all external surfaces of the 3 considered thermal Zones *z*.

- the exergy of heat flux due to the thermal transmission:

$$\dot{E}x_{transmission,BUILDING} = \sum_{z}^{1,2,3} \sum_{i} \dot{Q}_{transmission,i} \left(1 - \frac{T_a}{T_{external,surface,i}} \right) \tag{46}$$

where: $\dot{Q}_{transmission,i}$ is the thermal energy flow rate due to transmission heat of the surface *i* at external temperature $T_{external,surface,i}$.

- the exergy of heat flux due to the inlet and outlet air ventilation and infiltration:

$$\begin{aligned} \dot{E}x_{ventilation,BUILDING,in} &= \sum_{z}^{1,2,3} n_{vent,z} V_z \rho c_p \left(\left(T_{amb} - T_a \right) - T_a \ln \left(\frac{T_{amb}}{T_a} \right) \right) \\ \dot{E}x_{ventilation,BUILDING,out} &= \sum_{z}^{1,2,3} n_{vent,z} V_z \rho c_p \left(\left(T_{indoor,air,z} - T_a \right) - T_a \ln \left(\frac{T_{indoor,air,z}}{T_a} \right) \right) \end{aligned} \tag{47}$$

$$\begin{aligned} \dot{E}x_{\text{infiltration},BUILDING,in} &= \sum_{z}^{1,2,3} n_{\text{inf},z} V_z \rho c_p \left(\left(T_{amb} - T_a \right) - T_a \ln \left(\frac{T_{amb}}{T_a} \right) \right) \\ \dot{E}x_{\text{infiltration},BUILDING,out} &= \sum_{z}^{1,2,3} n_{\text{inf},z} V_z \rho c_p \left(\left(T_{indoor,air,z} - T_a \right) - T_a \ln \left(\frac{T_{indoor,air,z}}{T_a} \right) \right) \end{aligned} \tag{48}$$

where $n_{vent,z}$ and $n_{\text{inf},z}$ are the air change rate for ventilation and infiltration (1/h) and V_z is the volume of each thermal Zone.

- the exergy of the internal gain of occupants, equipment and light, evaluated as in Eqs. (49)-(51):

$$\dot{E}x_{occupants,BUILDING} = \sum_{z}^{1,2,3} \dot{Q}_{lat+sens,occ} n_{occ,z} \left(1 - \frac{T_a}{T_{occ}}\right) \quad (49)$$

$$\dot{E}x_{equipment,BUILDING} = \sum_{z}^{1,2,3} \dot{Q}_{equipment,z} \left(1 - \frac{T_a}{T_{equipment}}\right) \quad (50)$$

$$\dot{E}x_{light,BUILDING} = \sum_{z}^{1,2,3} \dot{q}_{light} A_z \left(1 - \frac{T_a}{T_{light}}\right) \quad (51)$$

where: in Eq. (49) $\dot{Q}_{lat+sens,occ}$ is the total heat gain (latent and sensible) due to the degree of activity of occupants (kW); $n_{occ,z}$ is the number of occupants in each thermal Zone (-); in Eq. (50 $\dot{Q}_{equipment,z}$ is the heat gain rate due to equipment of each from thermal Zone (kW); in (51) $\dot{q}_{light}$ is the specific lighting power per m^2 (kW/m^2) of each thermal Zone with area A_z. T_{occ} $T_{equipment}$ and T_{light} are the reference temperature of occupants, equipment and light, respectively (K).

- the exergy flow due to electricity to supply the load of user (HP $\dot{P}_{el,HP}$, equipment $\dot{P}_{el,equipment}$ and light consumption $\dot{P}_{el,ligh}$);

$$\dot{E}x_{electricity,BUILDING} = \dot{P}_{el,toUSER} = \dot{P}_{el,HP} + \dot{P}_{el,equipment} + \dot{P}_{el,ligh} \quad (52)$$

$\dot{P}_{el,HP}$ takes into account only the exergy flow due to electricity to supply the HP, whereas no exergy flow due to heat flow dissipated from condenser and evaporator included in heat pump system is considered, because the corresponding inlet and outlet exergy flows are calculated with respect to the same temperature and pressure (the environment state, the dead state), and therefore, their physical exergy is zero.

- the physical exergy due to DHW and hot water supplying the RF system (inlet / outlet to /from building), evaluated by using the Eq. (32). Obviously, the physical exergy of RF system is computed only for the PS.

Finally, the destroyed exergy of the whole building is evaluated by considering all the previous inlet and outlet exergy flows, as defined in the following Eq. (53):

$$\begin{aligned}
&\dot{E}x_{d,BUILDING} = \dot{E}x_{BUILDING,in} - \dot{E}x_{BUILDING,out} \\
&\dot{E}x_{BUILDING,in} = \dot{E}x_{sun,BUILDING,in} + \dot{E}x_{transmission,BUILDING,in} + \dot{E}x_{electricity,BUILDING,in} + \dot{E}x_{ventilation,BUILDING,in} + \\
&+\dot{E}x_{\text{infiltration},BUILDING,in} + \dot{E}x_{occupants,BUILDING,in} + \dot{E}x_{equipment,BUILDING,in} + \dot{E}x_{light,BUILDING,in} + \dot{E}x_{DHW,BUILDING,in} \\
&+\dot{E}x_{RF,BUILDING,in} + \dot{Q}_{back}\left(1 - \frac{T_a}{T_{back}}\right) \\
&\dot{E}x_{BUILDING,out} = \dot{E}x_{transmission,BUILDING,out} + \dot{E}x_{ventilation,BUILDING,out} + \dot{E}x_{\text{infiltration},BUILDING,out} + \dot{E}x_{DHW,BUILDING,out} + \\
&+\dot{E}x_{RF,BUILDING,out}
\end{aligned} \quad (53)$$

Note that in the Eq. (53) the last term of the total inlet exergy flow takes into account also the exergy due to the passive effect of PVT collectors integrated into Zone 1, 2 and 3 south façades of the building. In addition, it must be taken into account that this term, during the whole yearly simulation, can be considered also as an outlet exergy flow, when the Carnot factor assumes opposite sign.

d3) Energy and economic model

By the developed energy-economic model, the primary energy saving and economic profitability of the PS with respect to the RS one is suitably calculated. In RS, the electric load is due to consumption for space heating and cooling of HP, equipment and lighting loads. In PS, the electric load is also due to the installation of auxiliary electric devices of the RF system and the solar field (e.g. pumps). For each simulation time step, the electric load of PS is electricity produced by the BIPVTs, the electric power from and to the battery and the one supplied by the grid. The Primary Energy Saving due to electricity consumption (PES_{el}) is calculated as follows:

$$PES_{el} = \sum_i \frac{1}{\eta_{RS,el}} \left(\frac{E_{el,BIPVT} - E_{el,toLAB}\eta_R\eta_I + E_{el,fromLAB}\eta_R\eta_I\eta_{LAB}}{E_{el,BIPVT} + E_{el,RS}} \right)_i \quad (54)$$

where: $E_{el,BIPVT}$ is the produced electricity by the BIPVT; $E_{el,toLAB}$ is the electricity stored by the battery; $E_{el,fromLAB}$ is the electricity from the battery to the load; $E_{el,RS}$ is the electricity consumption of RS; $\eta_{RS,el}$ is the efficiency for conventional electricity production; η_R, η_I and η_{LAB} are the efficiency of the regulator, inverter and battery, respectively.

The primary energy saving due to DHW consumption PES_{DHW} and due to space heating and cooling $PES_{heat\&cool}$ are evaluated as Eq. (21) and (22). In order to assess the economic feasibility of the PS, the cost functions for all components are taken into account by calculating the total capital cost ($J_{PS,tot}$) that includes the cost of BIPVT solar field Eq. (23), TK Eq. (24), storage LAB Eq. (27), and inverter/regulator Eq. (28). The economic yearly saving of PS taking into account the economic gains and operating costs with respect to those of RS, was evaluated as Eq. (29), as well as the *SPB*, see Eq. (10).

Case study

The simulations of RS and PS refer to a high-rise building, well-representative of conventional Italian constructions. The building, located in Naples (South-Italy), is simulated by using the hourly weather data file from the Meteonorm database [191]. According to the Italian regulation [216], the heating period goes from November 15th to March 31st; the cooling period is set from June 1st to September 30th. As mentioned in system layout section, the exergy and the energy-economic analysis is performed on three thermal Zones of building: the thermal Zone 1 designed for the fitness center and the thermal Zones 2 and 3 designed for open space office and for single offices, respectively. The building has a rectangular shape with an East-West oriented longitudinal axis; the height, the floor area and the glazed area of each thermal Zone are equal to 3.5 m, 150 m^2 and 19.5 m^2, respectively. Note that the windows are located only at the south, west and east facing façades. The same envelope features assumed in Study 2 (see Table 25) were considered; the simulation assumptions of the three thermal Zones are reported in Table 29. In both systems, a specific windows opening strategy is considered (free cooling strategy). In particular, during the heating season and during the occupation

hours, when the indoor air temperature is higher than 24°C, a 2 vol/h outdoor air ventilation rate (simulated by the windows opening) is modelled. Then, windows are closed when the indoor air temperature falls below 22°C. A similar strategy is adopted also during the no-heating season and occurs also during the night hours: the windows opening is expected for indoor air temperature higher than 25°C, and simultaneously, the indoor air temperature is higher that outdoor one. Subsequently, the closing of the windows occurs when the indoor air temperature falls below 23°C. In the PS, the BIPVT collectors are mounted on the south facing façades (90° tilted), occupying a surface area of 45 m^2 for each thermal Zone, for a total BIPVT surface area of 135 m^2. All the design parameters of BIPVT collectors , as well as the operating parameters related to the RF, serving only the thermal Zone 3, are reported in reference [29]. The design parameters regarding the battery (in this Study N_p is 11), inverter and TK are shown in Table 12, whereas the CB and HP ones in Table 30.

Table 30. Main system design parameters.

	Parameter	Description	Value	Unit
CB	$P_{CB,rated}$	Rated CB heat power	88.24	kW
	$\eta_{RS,DHW}$	Efficiency of the condensing boiler (also for RS)	95	%
	q_{DHW}	DHW flow rate per day	17210	kg/ day
	q_{HE2}	Heat Exchanger 2 maximum flow rate	2106	kg/h
HEAT PUMP/ CHILLER	COP	Nominal coefficient of performance heating / cooling	3.5/3.0	-
	$Q_{heat/cool,rated1}$	Rated heating / cooling capacity Zone 1	16/13	kW
	$Q_{heat/cool,rated2}$	Rated heating / cooling capacity Zone 2	12/9	
	$Q_{heat/cool,rated3}$	Rated heating / cooling capacity Zone 3	11/9	

Note that both in RS and PS, the same rated power values are considered for CB and HP and the DHW and the indoor set point temperatures of building thermal Zones are the same in both modelled systems.

Additional assumptions adopted in the carried out exergy and energy-economic analysis are: i) the constant dead state ambient temperature, T_a = 298 K (value rather close to the annual average outdoor air temperature) and the constant dead state pressure, p_a =101325 Pa; ii) the specific chemical exergy, ε_{NG}, that in case of natural gas is estimated in 49925 kJ/kg [230-232]; iii) the temperature of occupants, equipment and light, T_{occ}, $T_{equipment}$ *and* T_{light} assumed equal to 309 K, 313 K and 4000 K, respectively. The values of $\eta_{RS,el}$, j_{NG}, natural gas lower heating value and C_{EX} adopted in the carried out energy-economic are equal to those assumed in Study 2. Finally, a detailed parametric analysis by taking into account several representative European weather zones as well as a suitable exergy analysis by varying the electricity storage system capacity, are also performed. The analysis on the European climates is carried out at the aim to assess the effects of the climate conditions on the exergy and energy-economic performance of the investigated BIPVT collectors.

Results of Study 3

In this section the yearly, weekly, and daily results in terms of temperatures, powers, energy, exergy, and economic parameters are discussed in detail for the weather zone of Naples.

Yearly results

In Figure 110, the primary energy in RS and PS for the electricity taken from national grid and produced by BIPVT collectors, for space heating/cooling by HPs and DHW preparation are displayed. The *PE* for DHW is significantly higher than the space heating one (PE_{heat}).

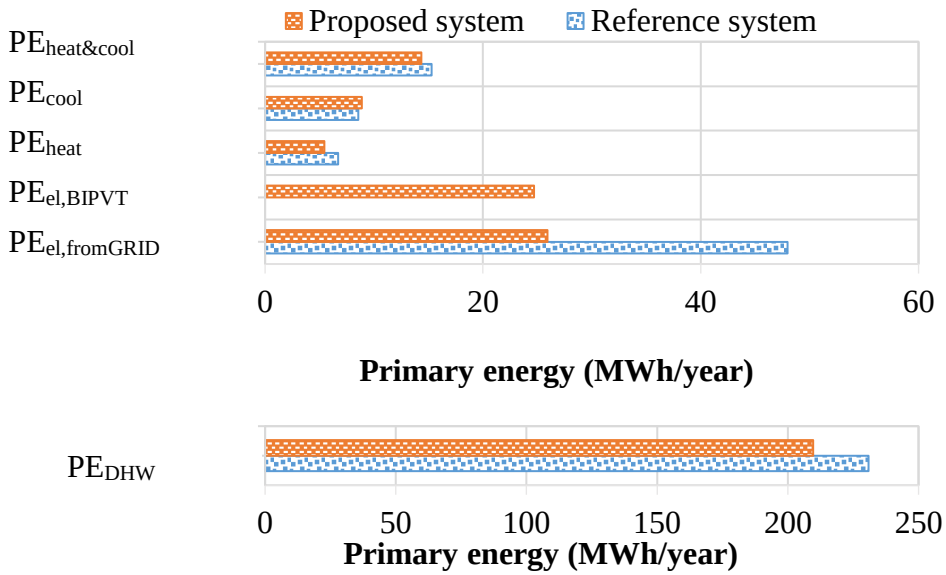

Figure 110. Primary energy of RS and PS for heating / cooling by HPs, DHW preparation, electricity production by BIPVT, and electricity from grid.

This is due to the assumption about the thermal Zone 1 destination use, the fitness centre, featured by a remarkable DHW demand. In PS layout, by exploiting the BIPVT thermal energy to produce DHW, the yearly demand decreases from 230.9 to about 209.7 MWh/year. During the winter, by comparing the RS with the PS layout, the PE_{heat} decreases from 7.6 to 5.5 MWh/year. This effect is due to the adoption of the RF system in the thermal Zone 3 and to the BIPVT positive passive effect during the winter operation. In particular, the winter passive effect is justified by the hot water flowing through the BIPVT collectors, which heats the exterior surfaces of the south-façades, in contact with the back surface of the collectors, at a temperature higher than the ambient one. This determines a useful reduction of the primary energy for space heating of the HPs. During summer, the overheating due to PVT integration leads to a slight increase of primary energy for space cooling of the PS (summer negative passive effect), but it is not significant, because the summer overheating is balanced by the reduction of solar incident radiation, about 40% (lower solar gain) on the south external facades, covering an area equal to 135 m^2 on the total area of all external facades (331.5 m^2). The decrease of primary energy for space heating and cooling, together with the self - consumed BIPVT collectors electricity and to the adoption of electricity storage system, lead to a reduction of the electricity required from national grid, passing from 48.0 to 25.9 MWh/year. In Table 31, the yearly exergies, exergy and energy efficiencies, energy, and economic savings of PS are summarised. Note that the efficiency defect, defined as the ratio between the destroyed exergy by the i^{th} component of the plant and the inlet fuel to the whole plant, is also calculated. In order to perform this calculation, the system boundary includes all components (building, battery, TK, CB and BIPVT collectors), whereas the inlet fuel of the plant includes the solar exergy, the fuel of the CB and the exergy due to electricity withdrawn from grid. The highest value of destroyed exergy is achieved by the CB, due to its irreversible chemical reactions. Note that, the destroyed exergy of the CB in PS ($Ex_{d,CB,PS}$) decreases with respect to the one obtained in RS ($Ex_{d,CB,RS}$), by reducing the irreversibilities of the innovative system. This is mainly due to the reduction of the exergy input (higher inlet temperature at CB for the solar preheating of the DHW) and of the chemical exergy of reaction (lower primary energy consumption of CB). A remarkable destroyed exergy, equal to about 126.1 MWh/year, is shown for the BIPVT solar collectors, being a typical

value for any solar technology. This result is due to the very large temperature difference between the solar collector surface and the sun, although the high exergy product due to the BIPVT electricity production. In any case, the BIPVT destroyed exergy is not the most important parameter to be considered, since they use the solar exergy input, which is a free renewable and environmental-friendly source. In addition, the solar exergy input converted by solar collectors would be intrinsically destroyed when no BIPVT collector is considered. Therefore, the high destroyed exergies obtained absolutely do not suggest avoiding the use of such renewable energy technologies. A remarkable reduction of the building destroyed exergy, equal to about 31%, is achieved by comparing the destroyed exergy of PS and RS ($Ex_{d,BUI,PS}$ vs $Ex_{d,BUI,RS}$). This is due to specifically the following reasons:

Table 31. Yearly exergy flows, exergy and energy efficiencies, energy and economic savings

Parameter	Description	Value	Unit
$Ex_{d,CB,PS}$	Destroyed exergy of condensing boiler in PS	239.0	MWh/year
$Ex_{d,BIPVT}$	Destroyed exergy of BIPVT collectors	126.1	
$Ex_{d,TK}$	Destroyed exergy of tank	0.7	
$Ex_{d,LAB}$	Destroyed exergy of lead acid battery	0.3	
$Ex_{d,aux}$	Destroyed exergy of auxiliaries (pumps)	0.03	
$Ex_{d,BUI,PS}$	Destroyed exergy of building in PS	308.7	
$Ex_{d,tot,PS}$	Total destroyed exergy in PS	674.9	
$Ex_{d,CB,RS}$	Destroyed exergy of condensing boiler in RS	263.8	
$Ex_{d,BUI,RS}$	Destroyed exergy of building in RS	450.0	
$Ex_{d,tot,RS}$	Total destroyed exergy in RS	713.8	
$\eta_{ex,LAB}$	Lead acid battery exergy efficiency	85.5	%
$\eta_{ex,TK}$	Tank exergy efficiency	74.2	
$\eta_{ex,BIPVT}$	BIPVT collectors exergy efficiency	8.4	
$\eta_{ex,CB}$	Condensing boiler exergy efficiency	2.0	
d_{LAB}	Lead acid battery efficiency defect	0.1	
d_{TK}	Tank efficiency defect	0.1	
d_{BIPVT}	BIPVT collectors efficiency defect	18.9	
d_{CB}	Condensing boiler efficiency defect	35.9	
$\eta_{t,BIPVT}$	BIPVT collectors thermal efficiency	8.6	
$\eta_{el,BIPVT}$	BIPVT collectors electric efficiency	7.5	
PES_{el}	Primary Energy Saving for electricity	32.8	
PES_{DHW}	Primary Energy Saving for DHW	9.2	
$PES_{heat\&cool}$	Primary Energy Saving for space heating and cooling	6.2	
ΔC	Yearly economic saving	4.0	k€/year
$J_{PS,tot}$	Total capital cost of proposed system	15.7	k€
SPB	Simple Pay Back	3.9	year

- in RS the inlet solar exergy to the building, is higher than the PS one, since in PS it is converted by south façades BIPVTs and is not directly absorbed by the walls;
- the exergy due to heat transmission through the external walls in PS is lower, mainly for the useful winter passive effect of BIPVTs;
- the inlet exergy due to electricity supplying the HPs for producing space heating is lower in PS (for the previous point and for the effect of RF system).

A significant result can be clarified by observing the values of total destroyed exergies, $Ex_{d,tot,RS}$ and $Ex_{d,tot,PS}$. Note that when the whole building - plant system is considered, although in the PS layout further components with respect to those of the RS layout are included (extra components are the BIPVTs, TK, LAB, and auxiliaries), by taking into account the system boundary including all components, $Ex_{d,tot,PS}$ is lower than $Ex_{d,tot,RS}$. This is mainly due to the reduction of $Ex_{d,BUI,PS}$. The obtained values exergy efficiency are equal to 2.0, 8.4, 74.2 and 85.5%, respectively for $\eta_{ex,CB}$,

$\eta_{ex,BIPVT}$, $\eta_{ex,TK}$ and $\eta_{ex,LAB}$. Focusing on the solar collectors (unglazed PVT building integrated collectors), the obtained value of the exergy efficiency is in accordance with the results reported in literature, showing for the coverless PVT water collectors, an exergy efficiency equal to about 11% [233]. The BIPVT yearly thermal and electric efficiencies are 8.6 and 7.5%, respectively. In Table 31, the results of the developed energy and economic analysis are also reported. By assuming a capital cost contribution equal to 50% of total capital cost, the *SPB* is equal about to 3.9 years. Such positive result is mainly due to high saving of natural gas cost of the PS for DHW preparation. This occurs although the PES_{DHW} is not that high, being 9.2% only due to the noteworthy DHW demand of RS. $PES_{heat\&cool}$ is equal only to 6.2%, mainly because of the useful passive effect of BIPVTs winter overheating is slightly higher than the unwanted summer cooling one. Such saving is also due to the use of the RF system providing space heating for the Zone 3. The *PES* for electricity is also shown, 32.8%.

Weekly results

In this section, the results of exergy analysis aggregated on a weekly basis are presented in - Figure 111 and Figure 112. Figure 111 shows the cumulated weekly exergy destructions of the main components of the investigated building - plant system.

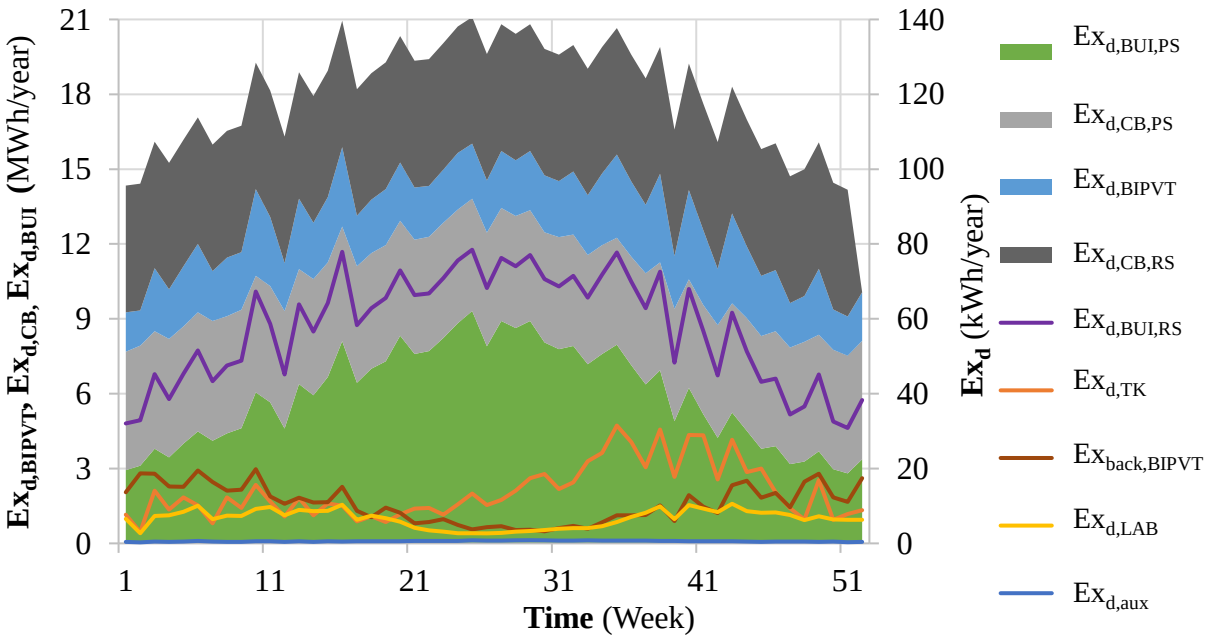

Figure 111. Weekly destroyed exergy

It is clearly shown that the weekly trends of building destroyed exergy $Ex_{d,BUI}$ of RS and PS are growing during the summer weeks, basically due to the higher demand electricity of HPs for space cooling. $Ex_{d,BUI,RS}$ is noticeably greater than $Ex_{d,BUI,PS}$, according to the yearly exergy results. In both RS and PS, $Ex_{d,CB}$ and $Ex_{d,BUI,}$ show that CB and BUI are the main sources of system irreversibilities. This occurs for the highly irreversible chemical reaction occurring in CB, and because in BUI several conversion processes occur. Such irreversibility cannot be reduced. $Ex_{d,CB}$ is slightly higher in winter. The weekly values of $Ex_{d,CB,PS}$ decrease with respect to $Ex_{d,CB,RS}$, according to the yearly

results obtained in the previous section. BIPVTs also represent a remarkable source of irreversibilities for the system, showing a destroyed exergy rate $Ex_{d,BIPVT}$ variable all year long, as a consequence of the variations of exergy fuel related to solar energy. In fact, higher exergy destructions are achieved during winter weeks, as a consequence of the higher winter exergy fuel and the lower summer exergy products. This is mainly due to the collectors slope, equal to 90°, corresponding to a lower summer incident radiation with respect to the winter one, for the latitude of Naples. The significant value of $Ex_{d,BIPVT}$ is consistent with the theories available in literature regarding exergy analysis of solar systems. In fact, heat transfer within the collector suffers for the huge temperature differences between the sun and the collector itself. Therefore, the exergy analysis suggests that solar collectors are affected by large unavoidable irreversibilities. On the other hand, it must be considered that such technology uses a renewable and free source energy and, therefore, such irreversibilities can be also considered acceptable. Anyway, $Ex_{d,BIPVT}$ is usefully reduced by $Ex_{,back,BIPVT}$ (reported on the right axis), which represents the transferred exergy through the back surface of the collectors to the building façades, which is higher in winter. This term reduces the space heating demand, as explained-above, and simultaneously $Ex_{d,BIPVT}$, with respect to the stand-alone ones. In fact, at the same conditions, the exergy of collector back surface will be lower in case of the stand-alone collectors, mainly during the winter when the back surface temperature of the collectors is higher than the ambient one. In any case, such effect is negligible with respect to the global $Ex_{d,BIPVT}$. The destroyed exergy of the TK and LAB are negligible with respect to $Ex_{d,BUI}$, $Ex_{d,CB}$, and $Ex_{d,BIPVT}$. In Figure 112, the weekly exergy and energy efficiencies of the main components of the plant are depicted.

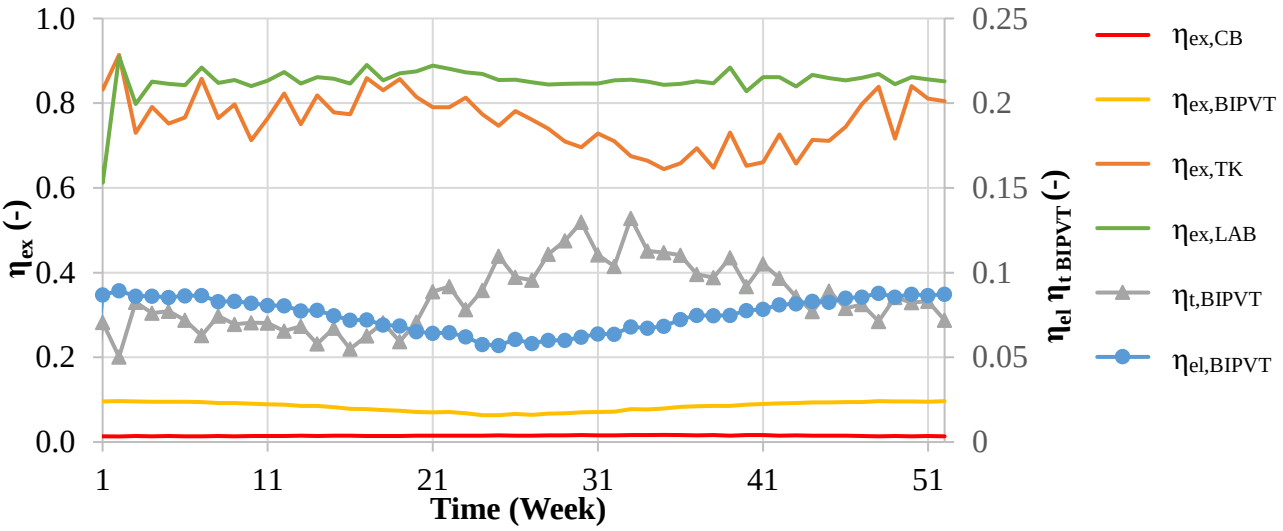

Figure 112. Weekly exergy and energy efficiency.

BIPVT collectors electric efficiency $\eta_{el,BIPVT}$ ranges between 6 to about 9% and lowers in hotter weeks, when higher ambient and BIPVT back surface temperatures are reached. This result also affects the exergy efficiency trend. Conversely, in summer, thermal losses decrease due to the higher outdoor temperature: this trend justifies the increase of BIPVT thermal efficiency $\eta_{t,BIPVT}$. The highest value, equal to 13%, is achieved at 33rd week. The trend of TK exergy efficiency $\eta_{ex,TK}$ is consistent with its exergy destruction curve: the lowest exergy efficiencies are obtained during the weeks from 35th to 45th featured by the highest exergy destructions. During winter weeks, this

component shows an exergy efficiency very high and reaches, as expected for the evaluation of a process exergy efficiency, a maximum of almost 91%. The high values of battery exergy efficiency $\eta_{ex,LAB}$ are almost constant during all the weeks of year. The lowest exergy efficiencies are obtained for CB (close to 2% all year long) and BIPVT collectors (between 10% and 6%). The winter increase of $\eta_{ex,BIPVT}$ is correlated to the higher exergy product due to the greater winter electricity production of BIPVT collectors.

Daily dynamic results

The hourly exergy efficiencies and destroyed exergies of BIPVTs, CB, TK and LAB, are reported in Figure 113 and Figure 114, respectively, for a representative summer day.

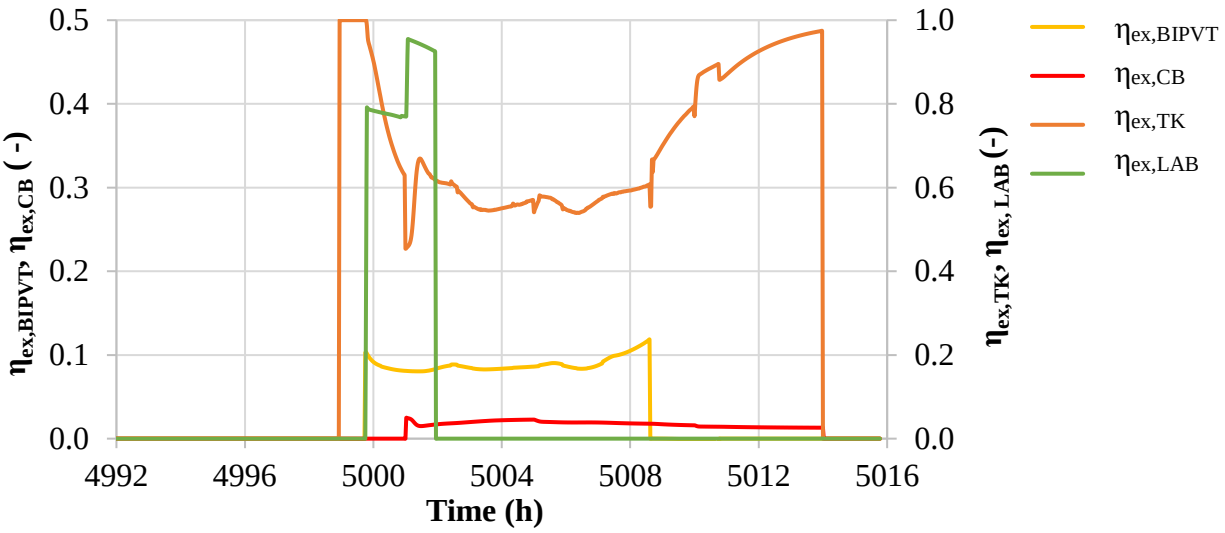

Figure 113. Hourly exergy efficiency, for a sample summer day in Naples.

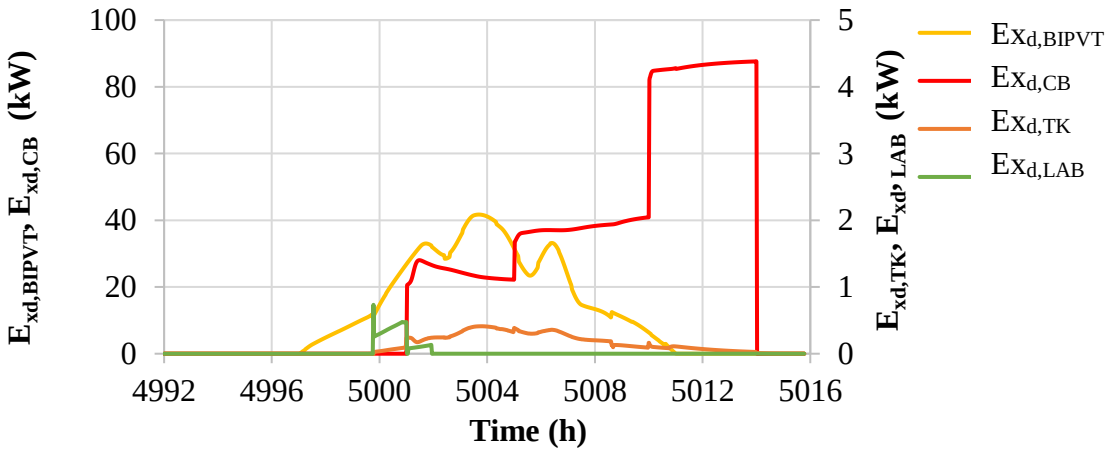

Figure 114. Hourly destroyed exergy, for a sample summer day in Naples.

An interesting result regards $\eta_{ex,LAB}$, assuming lower values during charging phase, about 77.0%, and higher ones during discharging one, about 94.0%. By averaging both values, an average

exergy efficiency equal to 85.5% (corresponding to yearly efficiency). $\eta_{ex,TK}$ shows a maximum close to 100% during early morning hours, when the TK exergy input due to thermal energy flow rate production by BIPVTs is zero and, for the same reason, in the late evening, when a significant TK exergy output due to DHW demand also occurs. $Ex_{d,\ CB}$ shows a maximum of about 90 kW, simultaneous with the high DHW demand. The huge $Ex_{d,\ BIPVT}$ is due to conversion of solar radiation into heat and power by the BIPVTs occurs mainly at midday when the incident radiation is at the maximum value. This corresponds to the significant temperature difference between BIPVTs and the sun, in accordance with theory by Petela. LAB and TK destroyed exergies are negligible with respect to $Ex_{d,\ BIPVT}$ and $Ex_{d,\ CB}$.

Parametric analysis

In this section, a parametric analysis is also carried out at the aim to assess the effects of the climate conditions on the exergy efficiency and destroyed exergy of BIPVT collectors in the investigated system for four European weather zones. The selected weather zones, featured by different incident solar radiation on vertical surface (G_{90}) and latitude, are Belfast (North Ireland; 762 kWh/year; 54°), Freiburg (Germany; 867 kWh/year; 47°), Naples (Italy; 1114 kWh/year; 40°) and Larnaca (Cyprus; 1323 kWh/year; 34°). The ratio between G_{90} and the incident solar radiation on horizontal surface $G_{horizontal}$ for the four investigated weather zones, are 0.85, 0.78, 0.73 and 0.72. for Belfast, Freiburg, Naples and Larnaca, respectively. The highest value of $G_{90}/G_{horizontal}$ obtained is in Belfast, featured by the highest latitude and the lowest one resulted in Larnaca, with the lowest latitude value. Such aspect is very significant for the carried out exergy analysis, because the weather zone location and incident solar radiation affects the exergy input (the solar exergy) and exergy product (electricity) of BIPVT collectors, and as consequence, their exergy efficiency and destroyed exergy. In order to perform such analysis, the values of thermal transmittance (*U-value*), thicknesses, solar reflectance, and emissivity of building façades and windows are selected according to the weather zone, as well as the heating / cooling capacities of the four investigated weather zones (For further details see reference [223]). Note that heating/cooling capacities are fixed, by considering that the HVAC system is able to comply the corresponding maximum heating and cooling loads occurring in winter and summer season, respectively. In particular, the cooling season is between June 1st to September 30th for all weather zones, whereas the heating one is set from November 15th to March 31st for Naples (according to the Italian rules [216]), whereas for Larnaca and Freiburg & Belfast is set from December 1st to March 15st, and October 15th to April 15st, respectively. In Table 32, the yearly destroyed exergy and exergy efficiency of BIPVT collectors for the investigated weather zones are summarised.

Table 32. Yearly destroyed exergy and exergy efficiency of BIPVT collectors.

Parameter	Larnaca	Naples	Freiburg	Belfast
$Ex_{d,BIPVT}$ [MWh/year]	150.0	125.9	98.9	87.1
$\eta_{ex,BIPVT}$ [%]	8.4	8.4	8.7	8.8
Ex_{sun} [MWh/year]	169.0	140.5	109.2	96.0
$Ex_{back,BIPVT}$ / $Ex_{d,BIPVT}$ [%]	0.18	0.19	0.31	0.34

It is clearly shown an increasing trend between the destroyed exergy of BIPVT collectors $Ex_{d,BIPVT}$ and the exergy due to the incident solar radiation on BIPVT collectors Ex_{sun} of selected weather zones: the higher the Ex_{sun}, the greater the $Ex_{d,BIPVT}$. The highest destroyed exergy occurs in Larnaca, equal to 150 MWh/year. Conversely, the lowest destroyed exergy, of about 87 MWh/year, is obtained in Belfast. In addition, it is shown also that the highest exergy efficiency of BIPVT collectors $\eta_{ex,BIPVT}$, equal to 8.84% for Belfast, is correlated with lowest destroyed exergy. From this analysis, it resulted that the variation in exergy efficiency $\eta_{ex,BIPVT}$ among the investigated weather zones is negligible, because the decrease / increase of the exergy input Ex_{sun} is balanced by reduction / increase of exergy product (the exergy due to electricity produced by BIPVT collectors) occurring in Belfast/Larnaca. In Table 32, the ratio between the exergy output of BIPVT collectors $Ex_{back,BIPVT}$ and $Ex_{d,BIPVT}$ is also reported. Note that $Ex_{back,BIPVT}$ is the exergy transferred through the back surface of the collector to the building façade and it affects the destroyed exergy of collectors, as well as the space heating demand of building. In fact, by such ratio, it is possible to show the useful winter passive effect of BIPVT collectors on reducing of $Ex_{d,BIPVT}$. This useful effect is predominant in cold weather zones (Belfast), where the ratio is about 0.34% and reduces in hot weather zones (Larnaca) by assuming the value of 0.18%. Anyway, the obtained values of $Ex_{back,BIPVT}$ are negligible with respect to the obtained ones for $Ex_{d,BIPVT}$.

Finally, parametric analysis results, in order to investigate the variation of the number cells in parallel N_P of LAB system on the destroyed exergy $Ex_{d,LAB}$ and exergy efficiency $\eta_{ex,LAB}$ of LAB system, is also reported. In particular, N_P is varied from 5 to 23 with step 2. The obtained results are depicted in Figure 115 and are reported for the weather zone of Naples.

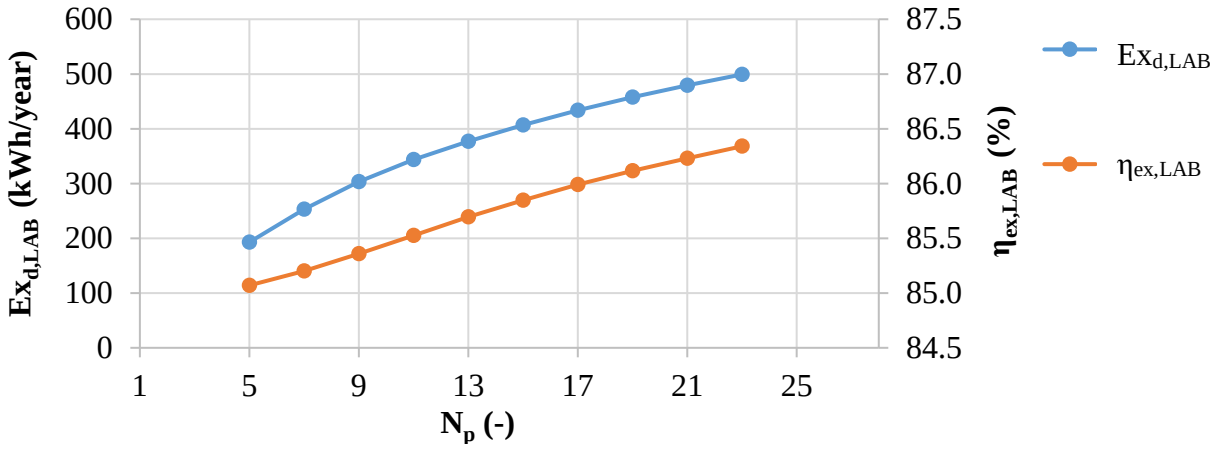

Figure 115. Destroyed exergy (left) and exergy efficiency (right) of LAB vs N_P.

A linear increasing trend is detected between $\eta_{ex,LAB}$ and N_P due to the higher growing of the electricity going from the battery, considered as exergy product, with respect to the obtained growing of the inlet electricity to battery, considered as exergy input. The term due to the accumulated exergy (not showed) equally grows with N_p. From the exergy point of view, in order to obtain high $\eta_{ex,LAB}$ a greater N_p is recommended: the highest value is 86.3% obtained for N_p equal to 23. The irreversibilities of battery increase with its size, by varying from 193 to 499 MWh/year.

4.2 Dynamic simulation of a natural-gas-driven BCCHP system

Study 4

Applications: factory **Analysis:** Energy and economic
Technologies: gas fired reciprocating engine, absorption chiller

The study 4 regards a CCHP system developed to produce electricity, space heating / cooling and DHW for a real factory application, namely a Diesel engines factory located in Potenza (South Italy). The system layout includes a reciprocating engine fuelled by natural gas, heat exchangers for waste-heat recovery, pumps, storage tanks, a single-stage LiBr/H_2O ACH, a cooling tower, mixers and valves. This study is reported in reference [89].

Real measured data were used to estimate the electric energy demand of the factory, whereas a detailed building simulation model was used to calculate heating and cooling demands. A detailed economic analysis was carried out, aiming at evaluating:

- the optimal size of the CCHP system;
- the optimum control strategy, from a thermo-economic point of view, comparing three different cases: Base-Load operation, electric load tracking and a new hybrid strategy based on the simultaneous tracking of electric and thermal-loads.

The final goal of this study lies in the proposal of innovative approach, based on detailed dynamic simulations, predicting the system performance on a very short time basis (seconds or minutes) and evaluating the energy, economic and environmental feasibility of such system. The novel methodology overcomes the main drawbacks of this technology, i.e. the scarce reliability of the feasibility analysis often performed, based on dramatic simplifications used in the prediction of system performance. In addition, in this study, with respect to the others literature works, only a unique dynamic model, including simultaneously the building and CCHP system, able to simulate the real behaviour of the whole system is considered. Whereas in other studies, often building and plant are separated, and the heating and cooling demands of the building are calculated by external tools and then used as input data for the CCHP simulation model, leading to significant errors. The novelty of this study is also for the investigated building application, i.e. the factory, with respect to the residential one usually analysed. In addition to the developed new hybrid strategy, in this study several detailed control strategies, in order to guarantee the exact operation of all the included components, as expected from the real project, were developed. This was done by including numerous temperature controllers, managing the temperatures of heat recovery exchangers on jacket and waste gas loops correctly, the activation temperature of ACH and fan coil units, the production of DHW, the activation of engine etc.

System layout Study 4

The CCHP layout is depicted in Figure 116. The Prime Mover (PM), i.e. the natural gas-fired reciprocating engine producing power and heat; the heat is obtained from two heat exchangers: a shell-and-tube heat exchanger Exhaust gases-Jacket water (ExJw), in which the exhaust gases heat up the jacket water leaving the engine, and a plate-fin heat exchanger Jacket water-Heating water (JwHw), in which the hot jacket water supplies thermal energy to the heating water, used for heating purposes, for DHW production and to drive the single-stage LiBr/H_2O ACH. The system layout

includes six main loops: exhaust gases, air, heating water, cooling water, hot water and chilled water. In ExJw, the hot water exiting from the engine is heated up to the set-point temperature $T_{out,JwHw,ExJw}$ (Table 33).

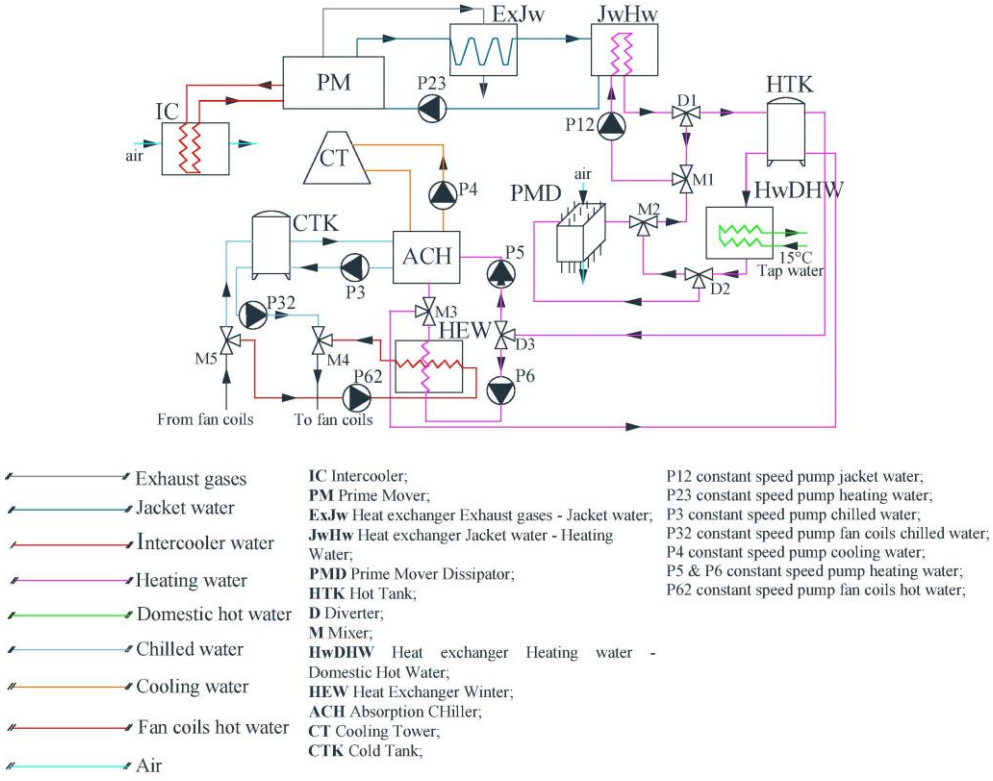

Figure 116. System layout [89].

JwHw provides heat to the Hot storage TanK (HTK), through the heating water loop. When space cooling is required, the diverter D3 directs the hot water coming from the HTK top, through the pump P5, to the ACH, producing chilled water sent by the pump P3 in a variable inlets Cold stratified storage TanK (CTK). The chilled water coming from the CTK bottom is sent by the pump P32 to the fan coils (FC). ACH is cooled by the Cooling Tower (CT), through the pump P4. When space heating is required, the diverter D3 directs the hot water coming from HTK to the cross-flow Heat Exchanger for Winter (HEW); the hot water obtained is sent to the FC through the pump P62.

The thermal energy provided by the PM unit is also used to produce DHW, through the heat exchanger Heating water-Domestic Hot Water (HwDHW). The excess thermal energy is dissipated in the PM Dissipator (PMD); to this scope, a controller, managing the diverter D2, receives temperature data from the outlet of mixer M2 and varies the inlet flow rate to PMD to reach the set-point temperature at the inlet of the heat exchanger JwHw, $T_{in,set,JwHw}$ (Table 33). If $T_{in,JwHw}$ is lower than $T_{in,set,JwHw}$, the same control diverts the inlet flow rate to HTK, through D1, by mixing in M1 the inlet and outlet flows of JwHw, in order to avoid any thermal shock for the engine. Some controllers were implemented in order to reach the set-point temperature values $T_{set,ACH}$ and $T_{set,HEW}$ (Table 34) and to activate the ACH, the CT and the HEW. In fact, an ON/OFF hysteresis controller checks the temperature of the hot water coming from the top of the HTK: when such temperature is too low, the controller switches off the pump P6 (or P5), to prevent the heating and cooling systems from operating at low efficiency and capacity. When the pumps P5 and P6 are deactivated, the hot stored water can reach the set-point temperature (also considering the dead bands ΔT_{ACH} and ΔT_{HEW},

indispensable to reduce the number of ON/OFF events) required to activate the ACH and HEW. A further ON/OFF hysteresis controller manages the pump P32, by comparing the temperature of the chilled water at the CTK bottom, $T_{CTK,BOTTOM}$ with the set-point value fixed for supplying the fan coils ($T_{set,chw,FC}$) and verifying the presence of a cooling demand. Therefore, the fan coils units are activated only when the chilled water temperature is below the fixed set-point.

Table 33. Main design parameters (1).

Component	Parameter	Value	Unit
Prime Mover	Model name	Vitobloc 200 EM-401/549	
	Manufacturer	Viessmann	
	$Q_{th,rated,PM}$ – rated thermal capacity	549	kW
	$P_{el,rated,PM}$ – rated electric capacity	401	
	Rated fuel input	1053	
	Rated electric efficiency	38.1	%
	Rated thermal efficiency	52.1	
	Global rated efficiency	92.8	
Intercooler	Model name	WH1163.BD/10VEF	
	Manufacturer	ThermoKey	
	Water flow rate	4200	
	Air flow rate	18,375	
Heat exchanger exhaust Gases – Jacket water	$T_{out,ExJw,rated}$ Jacket water outlet rated temperature	84–89	°C
	Exhaust Gases flow rate	2200	kg/h
	Jacket water flow rate (pump P23)	54,900	
Heat exchanger Jacket water/heating Water	$T_{in,set,JwHw}$ JwHw inlet set-point temperature	70	°C
Heat exchanger Jacket water/heating Water	Heating Water flow rate (pump P12)	23,500	kg/h
Prime Mover Dissipator	Model name	WH1463.CDVEFS	
	Manufacturer	ThermoKey	
	Heating Water flow rate (pump P12)	23,500	kg/h
	Air flow rate	69,580	
Heat exchanger heating Water/ Domestic Hot Water	Heating Water flow rate (pump P12)	23,500	kg/h
	Domestic Hot Water flow rate (average)	8	

As for the operation strategy, in the reference case the PM unit was assumed to “follow” the electric load, namely: (i) if the ratio between the electric demand, $P_{el,req}$, and the PM rated power, $P_{el,rated,PM,}$ is lower than 50%, the engine is switched off; (ii) when such ratio ranges from 50% to 100%, the engine works at part load, matching the electric demand ($P_{el,req} = P_{el,PM} < P_{el,rated,PM}$); (iii) when the electric demand is equal or higher than engine maximum capacity ($P_{el,req} > P_{el,rated,PM}$), the engine works at its rated power ($P_{el,rated,PM}$).

Table 34. Main design parameters (2).

Component	Parameter	Value	Unit
Heat Exchanger Winter	Heating water flow rate (pump P6)	14,400	kg/h
	Fan coils hot water flow rate (pump P62)	5158	
	ΔT_{HEW} Tolerance on HEW activation temperature	2	°C
	$T_{set,HEW}$ Set-point temperature for space heating activation	75	
LiBr-H_2O absorption chiller	Model name	16LJ-13	
	Manufacturer	Carrier	
	$T_{in,chw,rated,ACH}$ Inlet chilled water rated temperature	12	°C
	Chilled water set-point temperature	7	
	$T_{in,cool,rated,ACH}$ Inlet cooling water rated temperature	30	
	$T_{out,cool,rated,ACH}$ Outlet cooling water rated temperature	35	
	$T_{set,ACH}$ Set-point temperature for space cooling activation	80	
	$T_{in,hot,rated,ACH}$ Inlet hot water rated temperature for ACH operation	90	
	ΔT_{ACH} Tolerance on ACH activation temperature	5	
	$T_{out,hot,rated,ACH}$ Outlet hot water rated temperature for ACH operation	72	
	Chilled water flow rate (pump P3)	33,768	kg/h
	Cooling water flow rate (pump P4)	84,240	
	Hot water flow rate (pump P5)	14,400	
	Fan coils chilled water flow rate (pump P32)	44,760	
	Coefficient of Performance	0.67	–
	Rated cooling capacity	196	kW
	Rated Heat Input	294	
Cooling Tower	Model name	EVAPCO	
	Manufacturer	Carrier	
	Operating fluid	Water	
	Number of fans	1	-
	Fan power	4	-
	Evaporated water flow rate	792	kg/h
	Air flow rate	45000	
	Rated cooling capacity	488	kW
Cold Tank Hot Tank	Volume	2	m^3
Fan coils	Rated heating and cooling capacity for Production Zone	21/208	kW
	Rated heating and cooling capacity for Office Zone	69/53	
	$T_{set,chw,FC}$ Set-point of the chilled water temperature for activating the Fan Coils in cooling mode	15	°C

System model – Study 4

In this section only a detailed description of the thermodynamic model related to internal combustion engine and of the ACH as well as the energy and economic model of the BCCHP system, is provided. The building model is developed by TRNSYS3d plug-in of TRNSYS, as explained in

Study 1, model (c). For additional details about the simulation models of the other components, see reference [191].

h) Absorption chiller

The single-effect LiBr–H_2O ACH (Type 107) is simulated through a normalized catalogue data look-up principle [234]. The user must numerically calibrate a map that regulates the ACH performance. In this study, the operating map was calibrated on the performance data of the real installed chiller, Carrier model 16LJ-13 [235]. This accurate calibration was performed in order to simulate a system as much as possible close to the real one to be installed at the factory. The ACH nominal capacity is calculated as:

$$\dot{Q}_{cool,ACH,rated} = f_{ACH}\dot{m}c_p\Delta T_{chw} \tag{55}$$

The cooling ratio factor and the input heat ratio factor are useful to numerically express the performance data, as shown in following equations:

$$f_{Q_{cool}} = \frac{\dot{Q}_{cool,ACH}}{\dot{Q}_{cool,ACH,rated}} = \vartheta\left(T_{set,out,chw}, T_{in,cw}, T_{in,hw}, T_{in,chw}, f_{DL}\right) \tag{56}$$

$$f_{Q_h} = \frac{\dot{Q}_{h,ACH}}{\dot{Q}_{h,ACH,rated}} = \vartheta\left(T_{set,out,chw}, T_{in,cw}, T_{in,hw}, T_{in,chw}, f_{DL}\right) \tag{57}$$

A fixed value of the ACH coefficient of performance is assumed, and the hot water input rate in design conditions $\dot{Q}_{h,ACH,rated}$ is calculated as follows:

$$\dot{Q}_{h,ACH,rated} = \frac{\dot{Q}_{cool,ACH,rated}}{COP_{ACH,rated}} \tag{58}$$

The heat rejection rate from the absorption chiller is calculated as:

$$\dot{Q}_{ACH,cool,req} = \dot{m}_{chw}c_{p,chw}\left(T_{in,chw} - T_{set,out,chw}\right) \tag{59}$$

Therefore, the design load ratio is:

$$f_{DL} = \frac{\dot{Q}_{ACH,cool,req}}{\dot{Q}_{ACH,cool,rated}} \tag{60}$$

The factors defined in Eqs. (56) and (57) calculate the cooling and the heating rates at any time, which are then introduced in the energy balances to calculate the outlet temperatures of hot, chilled and cooling water.

i) Internal combustion engine

Type 907 (present in TRNSYS library [191]) models the internal combustion engine. The engine performance is influenced by the temperatures and flow rates of the jacket water, oil cooling water and after-cooling water, as well as by the temperature of ambient air. This model is realized through energy and mass balances, based on the data provided by the manufacturer [236]. The user must numerically calibrate a map that regulates the engine performance. Such calibration allows one to accurately simulate the real engine to be installed at the factory. Several equations are implemented in the model and the most important ones are reported in the followings.

The partial load ratio of PM is defined in Eq. (61), and depends on the electric load, $\dot{P}_{req}$, and on the PM rated power, $\dot{P}_{el,rated,PM}$.

$$PLR = \min\left(1, \frac{\dot{P}_{req}}{\dot{P}_{el,rated,PM}}\right) \tag{61}$$

The mechanical efficiency and electric efficiency of the internal combustion engine, in converting shaft power to electric energy output, are calculated as:

$$\eta_m = \frac{\dot{P}_{shaft}}{\dot{Q}_{fuel}} \tag{62}$$

$$\eta_{el} = \frac{\dot{P}_{el,rated,PM} PLR}{\dot{P}_{shaft}} \tag{63}$$

Considering the fraction of thermal energy recovered, *F*, the jacket water temperature (Jw) at the outlet of the engine can be calculated through an energy balance as:

$$T_{Jw,out} = T_{Jw,in} + \frac{F_{Jw}\left(\dot{Q}_{fuel} - \dot{P}_{shaft}\right)}{\dot{m}_{Jw} c_{p,Jw}} \tag{64}$$

Finally, the outlet temperatures of the water flowing through the Oil Cooler (OC), of the InterCooler (IC) and of the exhaust gases (exh) leaving ExJw are calculated through the following Eqs.:

$$T_{OC,out} = T_{OC,in} + \frac{F_{OC}\left(\dot{Q}_{fuel} - \dot{P}_{shaft}\right)}{\dot{m}_{OC} c_{p,OC}} \tag{65}$$

$$T_{IC,out} = T_{IC,in} + \frac{F_{IC}\left(\dot{Q}_{fuel} - \dot{P}_{shaft}\right)}{\dot{m}_{IC} c_{p,IC}} \tag{66}$$

$$T_{exh,out} = T_{intake} + \frac{F_{exh}\left(\dot{Q}_{fuel} - \dot{P}_{shaft}\right)}{F_{exh,\,flow}\dot{m}_{rated,exh} c_{p,exh}} \tag{67}$$

d3) Energy and economic model

In this section, the model used to assess the energy and economic profitability of the system is presented. It is worth to note that the calculation of the possible savings in terms of primary energy and operating costs dramatically depends on the system assumed as a reference. For the specific case study, the RS is the one currently installed at the factory, that is: the public electric grid for electricity, gas-fired boilers for heating and an air-to-water electric vapour-compression chillers for cooling. So, the corresponding thermodynamic *PES* can be calculated as:

$$PES_{thd} = 1 - \frac{E_{fuel,CHP}}{\frac{E_{el,CHP}}{\eta_{el,ref}} + \frac{E_{th,CHP}}{\eta_{th,ref}} + \frac{E_{cool,CHP}}{\eta_{el,ref} COP_{ref}}} \tag{68}$$

However, the economic calculations also require to calculate the *PES* with a different criterion, defined by the Italian legislation [83–86], and derived from the European Regulation 2004/08/EC [82]. According to such laws, the classification of a CHP plant as a “High-Efficiency Cogeneration” unit (HEC), needed to obtain a series of economic incentives and benefits, is based on the following condition, to be verified on a yearly base for the entire lifetime of the system:

$$PES = 1 - \frac{E_{fuel,CHP}}{\frac{E_{el,CHP}}{\eta_{el,ref}} + \frac{E_{th,CHP}}{\eta_{th,ref}}} \geq PES_{\min} \tag{69}$$

$\eta_{el,ref}$ and $\eta_{th,ref}$ are the reference efficiencies for the separate production of electricity and thermal energy, respectively. $E_{th,PM}$ is the waste thermal energy actually recovered and used in a given year (including the amount eventually used to drive an ACH); $E_{el,CHP}$ is the electric energy

produced in cogeneration in the same year. $E_{fuel,CHP}$ is the corresponding fuel consumption; PES_{min}, is 0 when the rated CHP power is below 1 MW and 0.10 in the remaining cases. As can be easily understood, the *PES* index introduced by the European Regulation 2004/08/EC represents a conventional Primary Energy Saving value, different from the Thermodynamic *PES*, and in a certain sense less realistic; anyway, such "legal" *PES* must be considered in order to assess the economic incentives and benefits granted to the system. Among other benefits, HEC units can obtain a number of marketable certificates, known as Energy Savings Certificates (*ESC*), proportional to the primary energy saving formally acknowledged (each *ESC* corresponds to an energy saving of 1 toe): usually, such certificates have a market value or a Selling Price (SP_{ESC}) around 100 €/toe. So, the overall economic CCHP system saving is:

$$\Delta \mathrm{C} = SP_{ESC} ESC + \left(\frac{E_{ch,ACH}}{COP_{RS,HP}} + E_{el,CHP} \right) \cdot c_{el,RS} + \frac{E_{th,HEW} + E_{th,HwDHW}}{\eta_{th,RS,boiler} LCV_{NG}} \cdot c_{NG,RS} - Ma - C_{el,system} - C_{fuel} - C_{\mathrm{fees},el} \tag{70}$$

$E_{ch,ACH}$ is the ACH produced chilled energy; $E_{th,HEW}$ and $E_{th,HwDHW}$ are the HEW and HwDHW heat exchangers produced thermal energies; *Ma* is the cost for the maintenance; $C_{el,system}$ are the system general charges; C_{fuel} is the natural gas cost; $C_{fees,el}$ are the costs related to the fees caused by the electric energy production and producer self-consumption. The last four terms of Eq. (70) are calculated as follows:

$$\begin{cases} Ma = E_{el,PM} \cdot c_{Ma} \\ C_{el,system} = i \cdot E_{el,rated,PM} \end{cases} \qquad \begin{cases} C_{fuel} = V_{NG,taxfree} \cdot c_{NG,taxfree} + \left(V_{NG,tot} - V_{NG,taxfree} \right) \cdot \left(c_{NG,taxfree} + c_{fees} \right) \\ C_{fees,el} = E_{el,PM} \cdot c_{fees,el} \end{cases} \tag{71}$$

All the parameters included in Eqs. (70) and (71) are reported in reference [89], as well as further details about the whole presented energy/economic model. The economic analysis includes the assessment of the *SPB* period, as calculated in Eq.10, as well as the Net Present Value (*NPV*), the Profit Index (*PI*) and the Internal Rate of Return (*IRR*).

$$NPV = \Delta C \cdot AF - J_{tot} \tag{72}$$

$$PI = \frac{NPV}{J_{tot}} \tag{73}$$

$$IRR = a \,/\, NPV = 0 \tag{74}$$

ACH, CT and PM costs are included in the total capital cost J_{tot}. Based on the values reported in commercial catalogues, the following unit costs were assumed: 36€ per kW of cooling capacity for the CT; 310€ per kW of cooling capacity for the ACH; 944€ per kW of rated power for the PM. *AF* is the annuity factor: for a time horizon of 10 years and a discount rate of 5%, is equal to 7.72 years.

Case studies

Analysed case study consists of a factory application, located in Potenza, south Italy, where the CCHP system described above aims at improving the energy efficiency and the economic sustainability of the productive process. All the design parameters were accurately calibrated on the basis of the real performance data of the equipment to be installed. In this way, it was possible to simulate with high accuracy the real operation of the CCHP plant. For this case study, the electric energy produced by the engine will be mainly used for the production process, whereas the waste heat will be used for heating and cooling purposes and DHW production. By a 1-year campaign measures the real electric demand of the factory is achieved, whereas by a detailed building

simulation, the thermal and cooling demands were calculated (Figure 117). Note that the dashed lines represent the rated thermal, cooling and electric capacity of CCHP system.

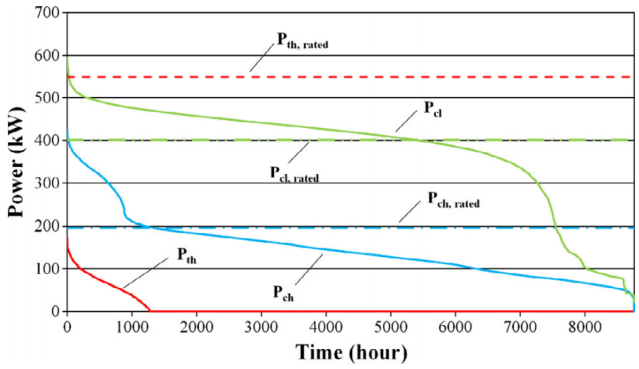

Figure 117. Aggregate electric (measured), cooling and thermal (calculated) power demand.

The factory has a predominant and almost constant power demand, higher than 400 kW for more than 5000 h. Furthermore, the combined heating and cooling demand during the winter is much lower than in other seasons, and this would affect negatively the global efficiency and economic profitability in case of electric-tracking operating strategy, because the system could not really operate in cogeneration, since a lot of waste heat should be rejected to the environment. Therefore, according to the indications provided by the designers, the CCHP was assumed to run from March 1st to October 31st. The factory 3D building (Figure 118, Table 35 and Table 36) was divided into two thermal zones: the Production Zone and the Office Zone, including offices, hall, dressing rooms, bathrooms and lunch room.

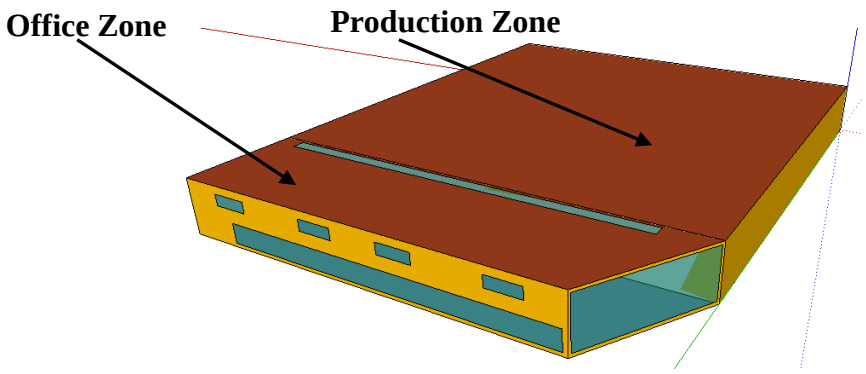

Figure 118. 3D buildings.

Table 35. Features of the opaque elements (U-values, thicknesses).

Zone	Building element	*U-value* [W/m²K]	Thickness [m]	Zone	*U-value* [W/m²K]	Thickness [m]
Office	Adjacent wall	2.1	0.36	**Production**	2.1	0.36
	Roof	1.39	0.13		0.54	0.34
	External wall	0.45	0.26		1.32	0.29
	Ground floor (tile flooring)	2.67	0.18		2.74	0.14
	Windows glass	5.68	0.004		5.68	0.004

Table 36. Building characteristics.

Thermal Zone	Production Zone	Offices Zone

Set point indoor air temperature [°C]	Cooling: $T_{set,cool,Winter}$ = 20±1 $T_{set,cool,Summer}$ = 24±1	Heating: $T_{set,h}$ = 20±1 Cooling: $T_{set,cool}$ = 24±1
Winter season	-	15/10 – 15/04
Summer season	01/03 – 31/10	01/06 – 30/09
Occupancy schedule [h]	00:00–24:00	08:00–17:00 (working days)
Number of occupants per zone	20	14
People heat gain [W/p]	Sensible: 100 Latent: 130	Sensible: 90 Latent: 95
Light heat gains schedule [h]	00:00–24:00	
Machineries heat gains schedule [h]	00:00–24:00	08:00–17:00 (working days)
Light + machineries heat gains [W/m^2]	65	10
Air infiltration rate [vol/h]	0.3	0.5
DHW set point temperature [°C]	45	
Tap water temperature [°C]	15	
DHW usage schedule [h]	08:00 – 17:00 (working days)	

Results of Study 4

The presented results refer to: the Electric-Load tracking strategy, in which the engine follows the user power demand; the yearly results of Base-Load operation, in which the power is always equal to the rated PM capacity, for the operating time scheduled by the designer and a new strategy denoted as "Hybrid Electric/Thermal-Load tracking".

Yearly results

The results from March 1st to October 31st are summarized in Table 37 and Table 38. In Table 37, Electric-Load tracking strategy was compared with the case of Base-Load operation. The electricity consumption of the auxiliary devices, $E_{el,aux}$, and the thermal energy used for heating purposes and domestic hot water, $E_{th,HEW}$ and $E_{th,DHW}$, respectively, are negligible compared to electricity, $E_{el,PM}$, and thermal energy, $E_{th,JwHw.}$ A certain amount of the engine waste energy is used to drive the ACH, $E_{th,ACH}$. However, such energy is also significantly lower than the overall thermal energy available to the heat exchanger JwHw, $E_{th,JwHw}$. It is worth to note that the demand for space cooling $E_{th,ACH}$, 1132 MWh/year, is dominant with respect to the space heating one $E_{th,HEW}$, 25 MWh/year. This is due to the high internal gain in the Production Zone. Then, the CCHP system energy performance is poor, with a very low global efficiency (η_{glob} = 0.57). but sufficient to obtain some public subsidies, namely: (i) marketable Energy Saving Certificates, *ESC*, which can be obtained when the Legal *PES* is positive; (ii) exemption from paying very high extra-fees (>50€/MWh) on the electricity produced in cogeneration and self-consumed; such benefit can be obtained only when the electric energy acknowledged as produced in HEC mode ($E_{el,CHP}$) is higher than 50% of the overall electric energy produced ($E_{el,PM}$). It is worth to note that, in case a running time extended to the whole year is considered, the ratio $E_{el,CHP}/E_{el,PM}$ would decrease below 50%, and the above-mentioned extra-fees would affect negatively the economic performance of the cogeneration system, that would become largely unprofitable.

Table 37. Yearly energy results.

Strategy	$E_{el,\ PM}$	$E_{el,\ aux}$	$E_{ch,\ ACH}$	$E_{cool,\ ACH}$	$E_{th,\ ACH}$	$E_{th,\ ExJw}$	$E_{th,\ JwHw}$	$E_{th,\ HEW}$	$E_{th,\ DHW}$

-	MWh/year								
Electricity-tracking	1947	18	786	1926	1132	1065	2674	25	2
Base-load operation	2358	21	894	2197	1293	1322	3247	29	2

Table 38. Yearly economic and energy results.

Description	Parameter	Control strategy		Unit
		Electricity-tracking	Base-load operation	
Global efficiency	η_{glob}	0.566	0.559	-
Operation equivalent Hours	H_{eq}	4855	5880	hours
Prime mover required Energy	E_{fuel}	5480	6591	MWh/year
Yearly electricity	$E_{el,PM}$	1947	2358	
Useful thermal Energy	$E_{th,useful}=E_{th,HwDHW}+E_{th,HEW}+E_{th,ACH}$	1156	1324	
CHP yearly Electricity	$E_{el,CHP}= C_{eff}\cdot E_{th,useful}$	1043	1207	
Legal primary energy saving	PES	0.140	0.143	
Thermodynamic primary energy saving	PES_{thd}	-0.272	-0.269	
Effective Coefficient	C_{eff}	0.899	0.912	-
Ratio of electric energy produced in HEC mode to the overall electricity production	$E_{el,CHP}/E_{el,PM}$	0.534	0.512	-
Total Fuel consumption	$V_{NG,tot}$	571485	687246	Sm^3/year
Tax free volume fuel consumption	$V_{NG,taxfree}$	428270	518734	
Energy Savings Certificates	ESC	13846	16454	€/year
Economic Saving for Cooling	S_{cool}	38002	43254	
Economic Saving for Heating and DHW	S_h+S_{DHW}	1084	1225	
Economic Saving for electricity	S_{el}	279647	308952	
Total Economic Saving	$S_{tot}= S_{cool} + S_h+S_{DHW} + S_{el}$	318733	353431	
Electric operating cost	$C_{op,el}$	24334	29474	
Gains	$G=ESC + S_{tot} - C_{op,el}$	308235	340411	
Fuel Cost	C_{fuel}	156979	188708	
System Cost	$C_{el,system}$	3284	3978	
Maintenance Cost	Ma	29200	35368	
Total cost	$C_{tot}=Ma+ C_{el,system} +C_{fuel}$	189463	228054	
Yearly economic saving	$\Delta C= G-C_{tot}$	118772	113051	
Total capital cost	$J_{tot}=J_{CT}+J_{ACH}+J_{COG}$	489352	489352	€
Simple Pay Back	SPB	4.1	4.3	years
Net Present Value	NPV	429920	385754	€
Profit Index	PI	0.883	0.792	-
Internal rate of return	IRR	0.205	0.191	-

In Table 38, a remarkable difference between the Legal *PES* (around 14%) and the Thermodynamic *PES* (−27%) results, due to the different reference systems assumed in the two cases. In fact, in Legal *PES* no difference is made between the heat used as is and that used to drive ACH: according to the rules stated by the Directive 2004/08/EC, it is assumed that, in the RS, the

same amount of thermal energy should be produced by a conventional boiler. On the contrary, in the thermodynamic *PES* the cooling provided by the ACH is taken into consideration, and the corresponding energy saving is calculated assuming that, in the real RS, such cooling would have been provided by a conventional air-to-water electric chiller, with a rated *COP* of 3. The value of the PES_{thd} suggests that the PS, based on the real design data of the CCHP to be installed in the factory, is not appropriately sized for the case under investigation. However, in spite of its poor energy performance, the system under evaluation is reasonably profitable form the economic point of view, also due to the incentives provided by the Italian laws. This result shows that the definition of a Legal *PES* only based on the amount of thermal energy recovered, regardless the way in which such energy is actually used, can be seriously misleading in case of CCHP systems. In fact, when the percentage of waste heat used to drive an ACH is significantly high, as in the case under study, the difference between legal and Thermodynamic *PES* values increases, so that also a CCHP system with bad energy performance can be legally classified as a "High-Efficiency Cogeneration" device and obtain undeserved public incentives. As expected, the Base-Load strategy, compared to the Electricity-Tracking mode, shows higher values of the energy flows provided by the CCHP unit, but worst values as for *SPB* and η_{glob}. In this case, in fact, the CCHP system is always set to work at the maximum rated capacity, also when there is a low electricity or thermal demand, and often this affects negatively the system energy and economic performance.

Weekly results

In Figure 119, the thermal energy flows provided by the following heat exchangers are shown for: jacket water ($E_{th,JwHw}$), gases-jacket water ($E_{th,ExJw}$), domestic hot water ($E_{th,HwDHW}$). The graphs also report the electric energy provided by the PM, $E_{el,PM}$, and the electric energy consumed by the auxiliary devices, $E_{el,aux}$. It is clear that $E_{el,aux}$ and $E_{th,HwDHW}$ are negligible compared to the remaining energy flows. The minimum energy production values are reached at the 26th and 36th week. In fact, the engine is following the real electric load, which is quite low in that period (summer holidays). The slightly seasonal trend in the energy production is a consequence of the activity scheduled in the factory and is not an effect of the variations in weather conditions. In fact, in this specific case, space heating and cooling demands are dominated by the internal gains due to the manufacturing process. Conversely, the results depicted in Figure 120 show a remarkable seasonal trend. In fact, by observing the cooling energy produced by ACH $E_{ch,ACH}$, an increase of the cooling demand can be noted during summer season. The thermal energy used for heating purpose, $E_{th,HEW}$, is a small fraction of the total thermal energy, $E_{th,JwHw}$, and also the thermal energy used in the ACH loop $E_{th,ACH}$ is, in the best case, lower than 50% of the available energy. This occurs especially during the month of March, when the energy demands for space cooling and heating are simultaneously low. This leads to the conclusion that, the CCHP system size to be installed in the factory is not optimized, in terms of thermal capacity.

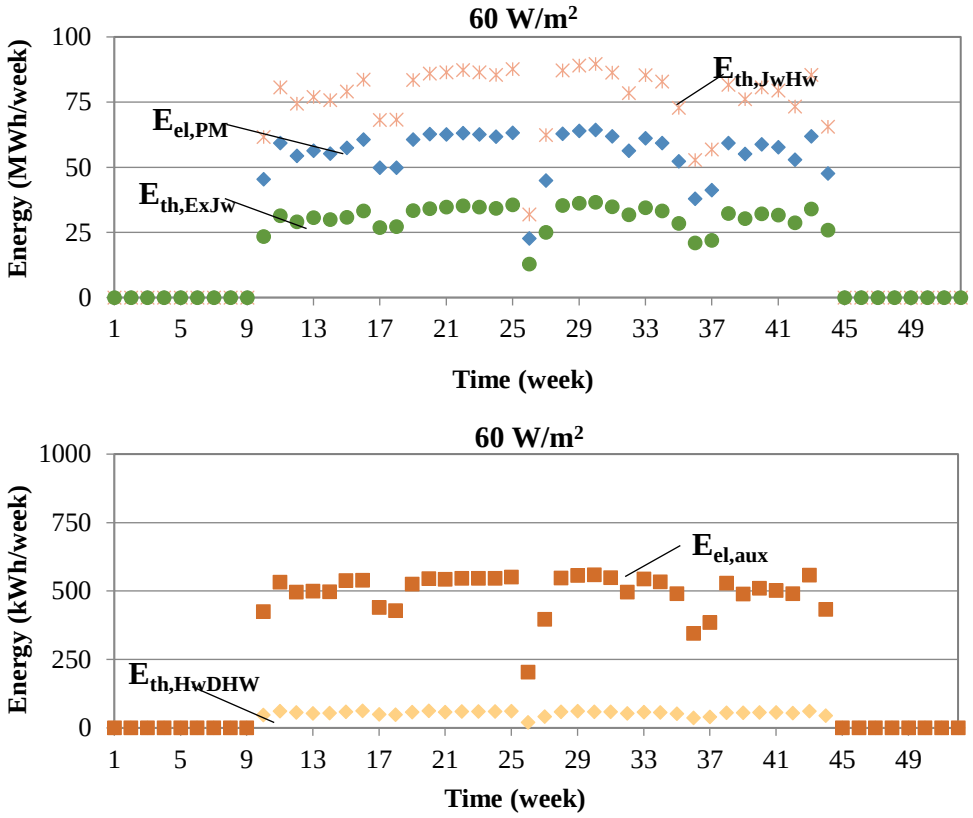

Figure 119. Weekly energy.

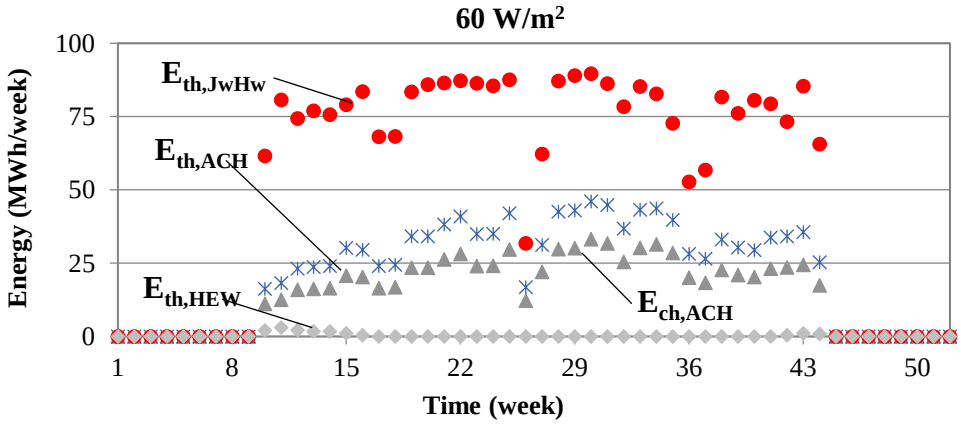

Figure 120. Weekly energy.

Daily dynamic results

Dynamic results are reported for a typical summer day (August 1st), and are referred to the Electricity-Tracking operation mode. Figure 121 and Figure 122 show the main operating temperatures of the CCHP system. In particular, Figure 121 reports the inlet/outlet temperatures of the hot water in the heat exchanger Jacket-Water ($T_{in,JwHw,hotside}$ and $T_{out,JwHw,hotside}$) and the inlet/outlet temperatures of the hot water used to drive the ACH ($T_{in,hot,ACH}$ and $T_{out,hot,ACH}$). $T_{in,JwHw,hotside}$ and $T_{out,JwHw,hotside}$ are about 93°C and 85°C, respectively, and are very close to the design values. This result confirms the accuracy of the model used for determining the performance of the PM, by performing an accurate calibration of all the parameters affecting the engine model and the heat exchangers included in the system.

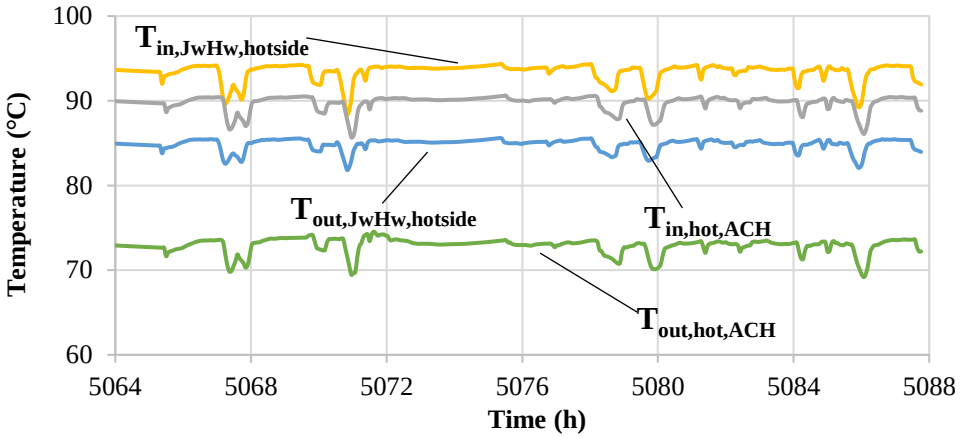

Figure 121. Temperatures for a sample summer day (1).

The water of the heating loop is heated and stored in HTK, by the JwHw heat exchanger. When the HTK top temperature reaches the set-point value ($T_{set,ACH}$=80°C), ACH is switched on. For the day selected, $T_{in,hot,ACH}$ is about 90°C, equal to the rated value $T_{in,hot,rated,ACH}$ (Table 34) while $T_{out,hot,ACH}$ is about 73°C, so that a temperature difference of about 17°C is obtained. The slightly oscillating trend of such temperatures is due to following reasons: (i) the fluctuations of the iterative feedback controller, managing the comfort temperature of Office Zone, operating according to a secant method; (ii) the Electricity-Tracking strategy adopted, that also affects the temperatures at the outlet of the engine jacket. The oscillating trend mainly occurs: (i) when the fan coil units are switched on (at 08:00) (ii) when the cooling system is operating in the Office Zone where the set-point indoor air temperature is set at 24±1°C; (iii) at 17:00, when the fan coil units are switched off. It is also worth noting that the a very low set-point temperature (24°C) is required by the production process. In Figure 122, the time trends of the following temperatures are shown: indoor air for the Office and Production Zones, $T_{air,OFF}$ and $T_{air,PROD}$; ambient, T_{amb}; inlet chilled water, $T_{in,water,FC,PROD}$; outlet cold air of the fan coil units in the Production Zone, $T_{out,air,FC,PROD,}$; inlet chilled water at the CTK, $T_{in,water,CTK}$.

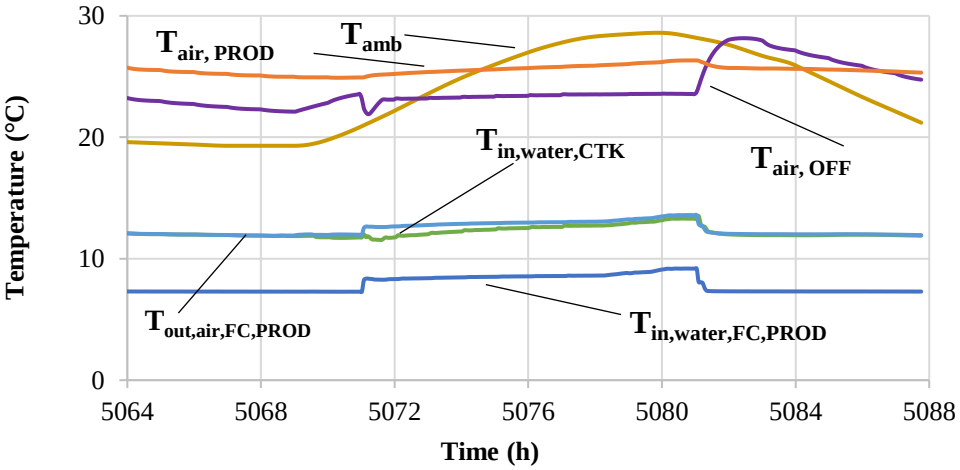

Figure 122. Temperatures for a sample summer day (2).

The set-point value of the temperature in the summer, $T_{set,cool,Summer}$ (Table 36), is only reached in the Office Zone during the occupancy schedule, while in the Production Zone the indoor air

temperature $T_{air,PROD}$ is higher than $T_{set,cool,Summer}$, equal to 24°C, also if the fan coil units operates all day long. This is due to the high internal thermal load in the Production Zone. $\underline{T_{air,PROD}}$ and $T_{air,OFF}$ follow the trend of T_{amb}. However, the building thermal inertia shifts the maximum to the afternoon. This graph clearly shows that, in the reference case, in hot days the Production Zone temperature is higher than the set-point value, due to the selected ACH capacity, lower than the maximum cooling load of the Production Zone. Once again, the developed simulation tool allowed one to detect a possible lack of the design of the CCHP which is going to be installed at the factory. $T_{in,water,FC,PROD}$ is constantly equal to the rated value (7°C) and rises to about 8.5°C when the fan coil units of both thermal Zones operate simultaneously, while $T_{in,water,CTK}$ (i.e. the outlet temperature of chilled water loop from fan coil units) is about 12°C, as designed. In Figure 123, the following results are shown: PM thermal and electric efficiencies ($\eta_{th,PM}$, $\eta_{el,PM}$), PM electric and thermal energy flow rate ($P_{el,PM}$, $P_{th,PM}$) and ACH *COP*, COP_{ACH}. COP_{ACH} is close to the rated value (0.67), since ACH usually works at full load, and COP_{ACH} slightly exceeds such value up to almost 0.8 during the Office Zone occupancy schedule. In fact, it linearly depends on the inlet temperature of the hot water used to drive the chiller, $T_{in,hot,ACH}$, that reaches high values (compatible with the ACH map) in these periods, due to the Electricity-Tracking strategy, that causes a surplus in the availability of thermal energy. Besides, COP_{ACH} is inversely proportional to the ambient temperature, T_{amb}, that is lower than the indoor air temperature. $\eta_{th,PM}$ is always lower than the rated value of 0.30 meaning that significant dissipation of thermal energy is present, negatively affecting the CCHP system global performance. When the engine works at the rated electric power capacity, $P_{el,PM}$=401 kW, $\eta_{el,PM}$ reaches the rated value, 0.38. Some small reductions occur in case of part-load operation. In this work special attention was also paid to new hybrid strategy. This expects that the prime mover follows the power demand until the temperature of the DHW outlet water reaches a set-point temperature equal to 75.5°C. Then, the system is partialized at a fixed point, defined by the ratio between the power actually produced by the prime mover and its rated capacity, $P_{el,PM}/P_{el,rated,PM}$, until the temperature reaches a value of 69.5°C.

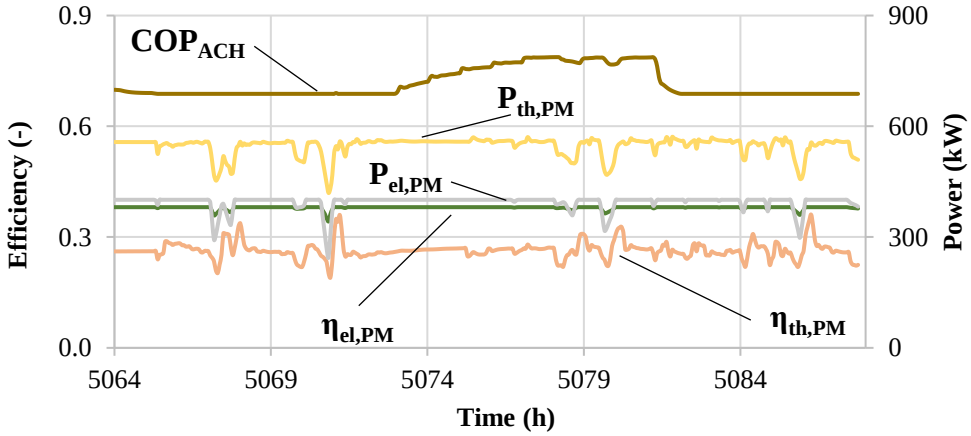

Figure 123. Efficiency (left) and power (right) for a sample summer day.

The fixed value of $P_{el,PM}/P_{el,rated,PM}$ is selected to simulate the operating strategy of a real prime mover. When the partialization is activated, the electric demand ($P_{el,PM,dem}$) is also checked, and it must be higher than a fixed ratio, defined as $P_{el,PM,dem}/P_{el,rated,PM}$. This last condition is set in order to obtain a minimum electric load. Conversely, with the present energy price and legislation, the

economic feasibility would be negatively affected. Results regards the new control strategy showing *SPB*, electric economic saving ($\Delta C_{el,user}$), global efficiency (η_{glob}) and economic gain due to excess electricity sold to the grid vs. the ratio $P_{el,PM}/P_{el,rated,PM}$ are reported in Figure 124. The lines in the graphs represent the minimum value of $P_{el,PM,dem}/P_{el,rated,PM}$ that has to be satisfied in order to activate the prime mover. For low values of the $P_{el,PM,dem}/P_{el,rated,PM}$, η_{glob} decreases, due to the longtime of part-load operation of the engine; the electricity sold to the grid significantly increases, because the production is greater than the demand. A good value of η_{glob} about 0.8 is reached for $P_{el,PM}/P_{el,rated,PM}$ = 0.5. Conversely, for the same value a reduction of economic saving and an increase of SPB is observed. This result is mainly due to adoption of rules of the Italian electricity energy market which boost more electric – driven strategies than efficiency ones. Anyway, it is noted that with this new hybrid control strategy the best *SPB* is equal to 3.8 years with respect to the value of 4.1 and 4.3 years of the electricity tracking and base-load operation strategy, respectively.

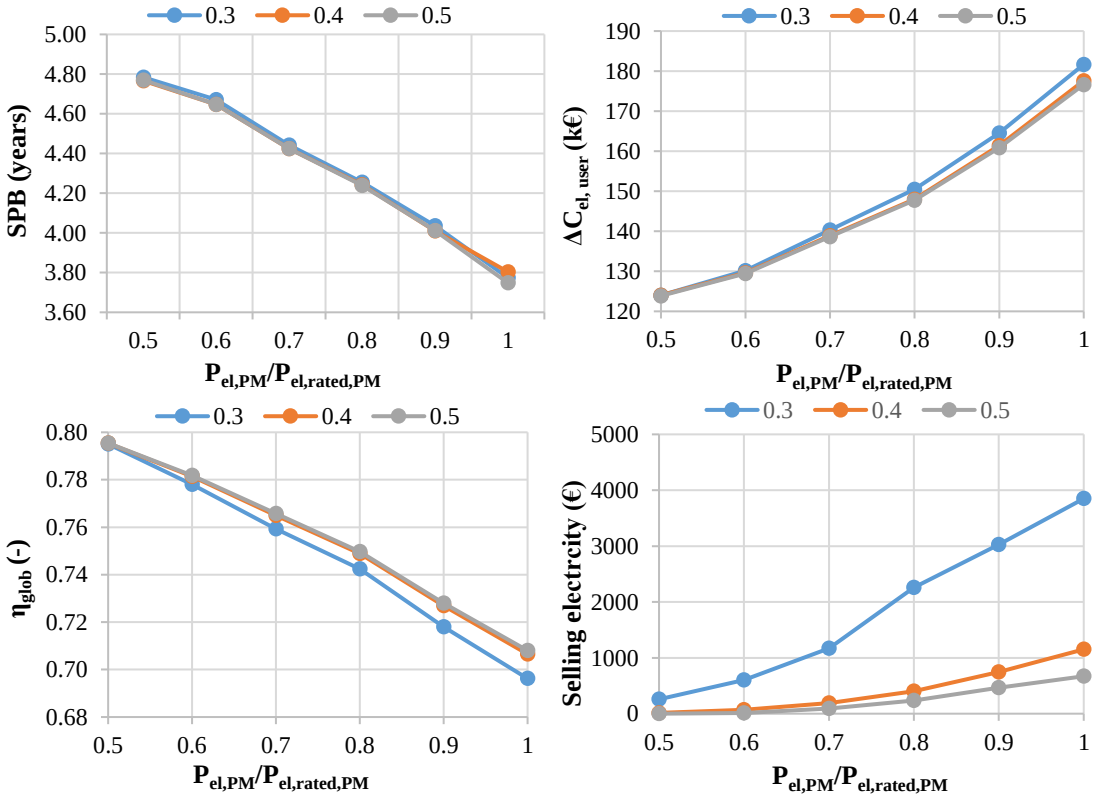

Figure 124. Efficiency and economic results.

Study 5

Applications: hospital **Analysis:** Energy and economic

Technologies: gas fired reciprocating engine, absorption chiller

This study presents a numerical analysis of a trigeneration system serving a hospital, aiming at determining the best economic operating strategy. Here, the novel approach, presented already in Study 4, based on dynamic simulations developed in TRNSYS environment able to predict real CCHP performance preceding its installation, aims at optimizing the operation control strategy of this trigeneration plant. This consists of a natural gas fired reciprocating engine, heat exchangers for waste-heat recovery, a single-stage LiBr-H_2O ACH, a cooling tower, pumps, a backup boiler, a backup vapor-compression electric chiller, storage tanks, valves and mixers. Three different operating strategies were evaluated in order to minimize the plant cost and maximize the performance of the system, namely: Thermal Load Tracking mode (TLT), Maximum Power Thermal Load Tracking mode (MPTLT) and Electricity Load Tracking mode (ELT). In the MPTLT strategy, the thermal energy flow rate provided by the engine is always lower or equal to the thermal demand; in the TLT strategy, the engine operates according to an On/Off strategy; in the ELT strategy, the electric power provided by the engine is always lower or equal to the electric demand. For ELT control strategy 256 simulations were also performed by varying the main model parameters, in order to determine the combination showing the lowest *SPB* value and the highest *PES* value. The optimum and the analysis of the optimum response surface was obtained by using Design of Experiments (DoE) method [237], which allow one to design a pre-optimized CCHP system.

The analysis presented, see reference [238], is new because between the several papers of chapter 3, very few papers:

- carried out thermoeconomic analyses and optimizations based on system dynamic simulations of polygeneration systems. In addition, those few papers were mainly focused on micro-polygeneration systems which dramatically suffer for the low operating hours typical of the residential application and for the high capital costs due to low capacity;
- investigated simultaneously the relationship between CCHP system and building by implementing a detailed model of the hydronic system strictly related to a building dynamic simulation model;
- carried out a thermoeconomic comparison among the different control strategies for the optimal management of the CCHP system.

System layout Study 5

The system layout is shown in Figure 125 [239]. It is similar to Study 4 one, but some differences concerning the dissipation of the heat not used can be noted. In particular, it consists of a gas-fired reciprocating engine producing power and heat, recovered from the engine cooling jacket water and from the exhaust hot gases. Power is utilised for lighting and hospital equipment; the heat for heating/DHW and cooling purposes, by a single-stage LiBr-H_2O ACH. The modelled main loops (exhaust gases, hot water, chilled water, DHW (sanitary hot water, SHW), heating and cooling water) are shown in Figure 125. For heat recovery, two heat exchangers were considered: the Exhaust gases – Jacket water ExJ (a shell-and-tube heat exchanger) and the Jacket water / heating

Water JW (a plate-fin heat exchanger). ExJ supplies heat to the heating loop hot water increasing its temperature up to the set point, $T_{out,Jw,ExJ}$ (Table 41). JW heats the heating water supplying the hot stratified storage tank (TKH).

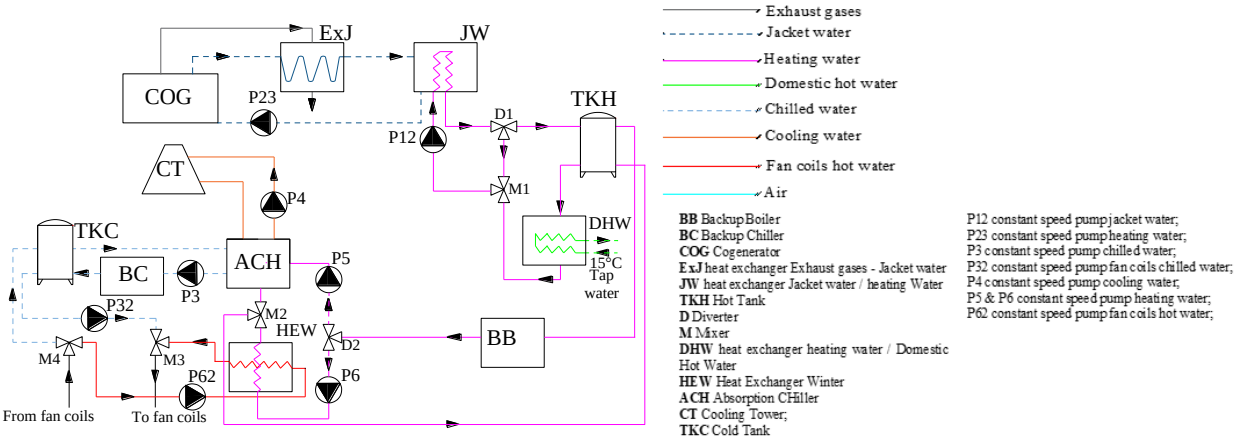

Figure 125. System layout.

Then, the water coming from the top of the tank, TKH, passes through Backup Boiler (BB) and is diverted by D2 to the ACH (when space cooling is required) and to the cross-flow Heat Exchanger Winter (HEW) (when space heating is required), through pumps P5 and P6, respectively. Pump P3 supplies the produced chilled water (CHW) to the Backup electric Chiller (BC) and subsequently stored into a cold stratified storage tank TKC equipped with variable inlets. The chilled water coming from the bottom of TKC, then, goes to the cooling fan coils system. Pump P4 pumps cooling water from tower CT to the ACH. Winter heat exchanger HEW provides the hot water to the heating fan coil system. A certain amount of the produced thermal energy is used by the heat exchanger heating Water / Sanitary Hot Water, SHW to produce DHW.

The system was also equipped with suitable controllers in order to implement conventional and innovative control strategies. In particular, as shown in Figure 126, the pump P6, which feeds the HEW, is activated only when these three conditions are respected: the space heating is required, the engine is ON and the inlet HEW hot water temperature is higher than 70°C. On the other hand, as shown in Figure 127, the ACH and the pumps P5 and P3, which feed the chilled water loop, operate only when these three conditions are fulfilled: space cooling is demanded, engine is ON and the inlet ACH hot water temperature is higher than 75°C.

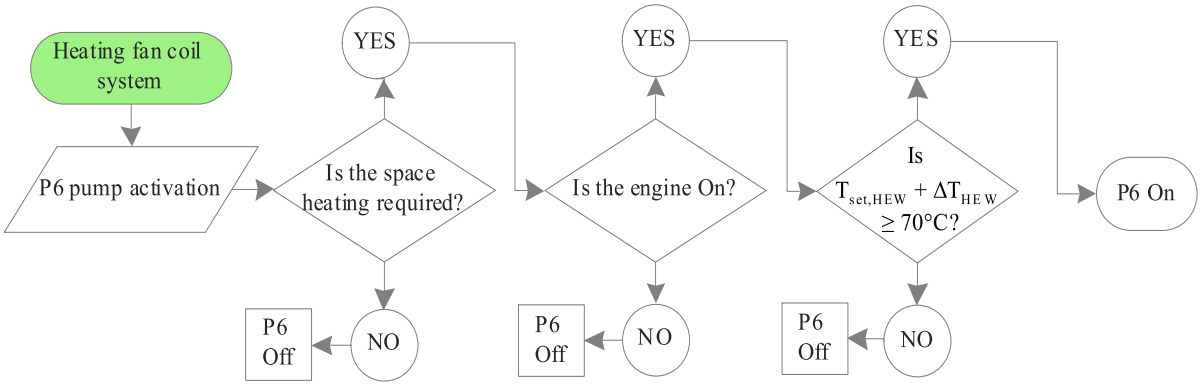

Figure 126. Heating fan coil system control strategy.

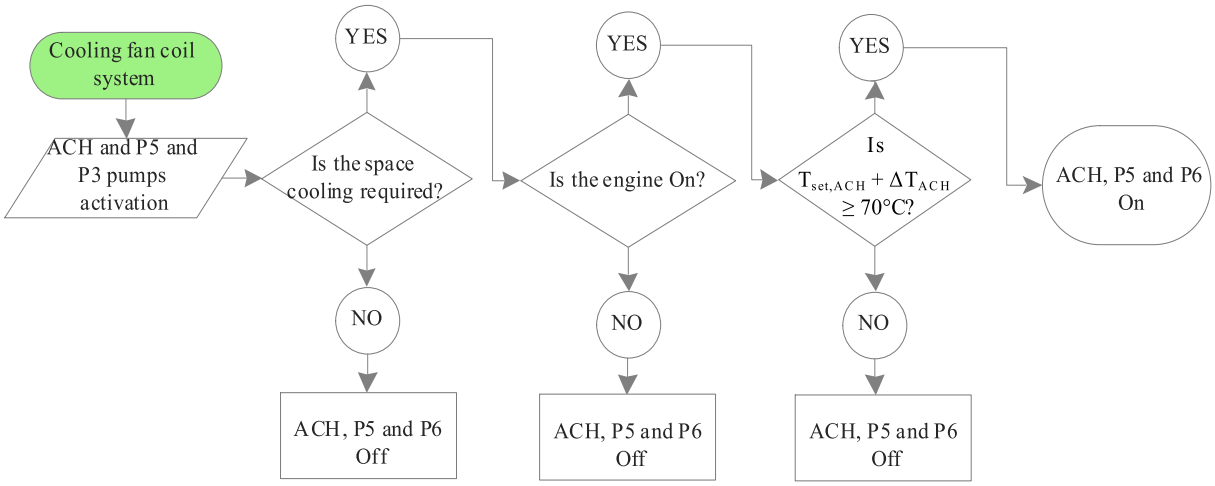

Figure 127. Cooling fan coil system control strategy.

Other suitable controllers were implemented for the ACH, the cooling tower and the HEW, in order to achieve the desired activation value of temperatures, $T_{set,\,ACH}$ and $T_{set,\,HEW}$ (Table 39). In particular, ACH and HEW are managed by an On/Off hysteresis controller that checks the TKH top temperature and turns off the ACH and HEW (pumps P5 and P6, respectively) when such value is lower than the set point temperatures, in order to avoid a system operation at low capacity and efficiency. The ACH and HEW switch on only when these temperatures overcome the set points, increased of a dead band ΔT_{ACH}, that is necessary to reduce the number of start-up and shut-down events. The pump P32 is managed by an On/Off hysteresis controller that monitors the TKC bottom temperatures, $T_{THC,BOTTOM}$, in order to check the inlet chilled water temperature (set point $T_{set,chw,FC}$) to the cooling fan coil system and simultaneously the cooling energy demand of the building. In this way, when the chilled water temperature is too high, the fan coils are not supplied.

The cogenerator (i.e. PM), instead, was assumed to follow the thermal load. When the temperature coming from the SHW is equal or higher than 72°C, the PM turns off managed by another On/Off hysteresis controller and it turns on again when this temperature is lower than 67.5°C. When this temperature is too low, the system is managed by a suitable feedback controller that bypasses a part of the heating water flow rate that comes out from the JW heat exchanger. In this way, all the design operating constraints of the PM required by the manufacturer are fulfilled. Finally, a proportional control allows the PM to work at part-load operation from 50% to 100% of the maximum power, as a function of the engine inlet temperature. All these PM controls are shown in Figure 128. The backup boiler controls are depicted the Figure 129. It is activated only when the PM is on and it works in full-load conditions, the heating demand is high, the external air temperature is lower than 10°C and the inlet temperature is lower than 85°C; then, when the temperature of the water coming from the SHW is lower than 64°C, the backup boiler turns on, while, when it is higher than 70°C, the backup boiler turns off. The backup boiler can modulate the outlet water temperature from 83°C to 87°C as a function of the external air temperature. The backup electric chiller, instead, is managed by an On/Off hysteresis controller. It is switched on when the ACH is on (and so when the ACH control strategy is respected too) and the temperature of the chilled water produced by it is higher than 10°C, as it is possible to see in Figure 130.

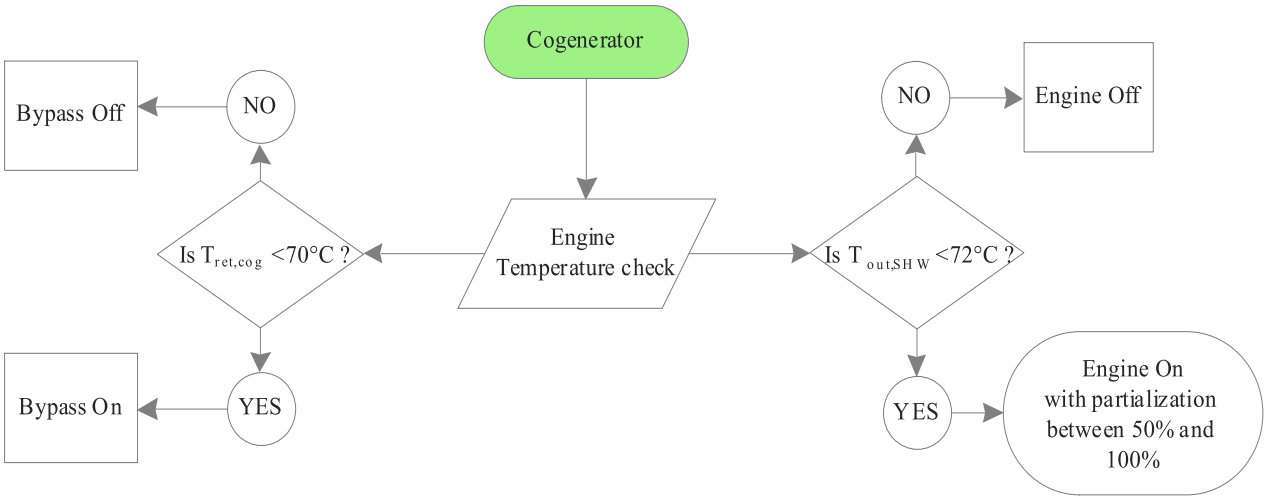

Figure 128. Prime mover control strategy.

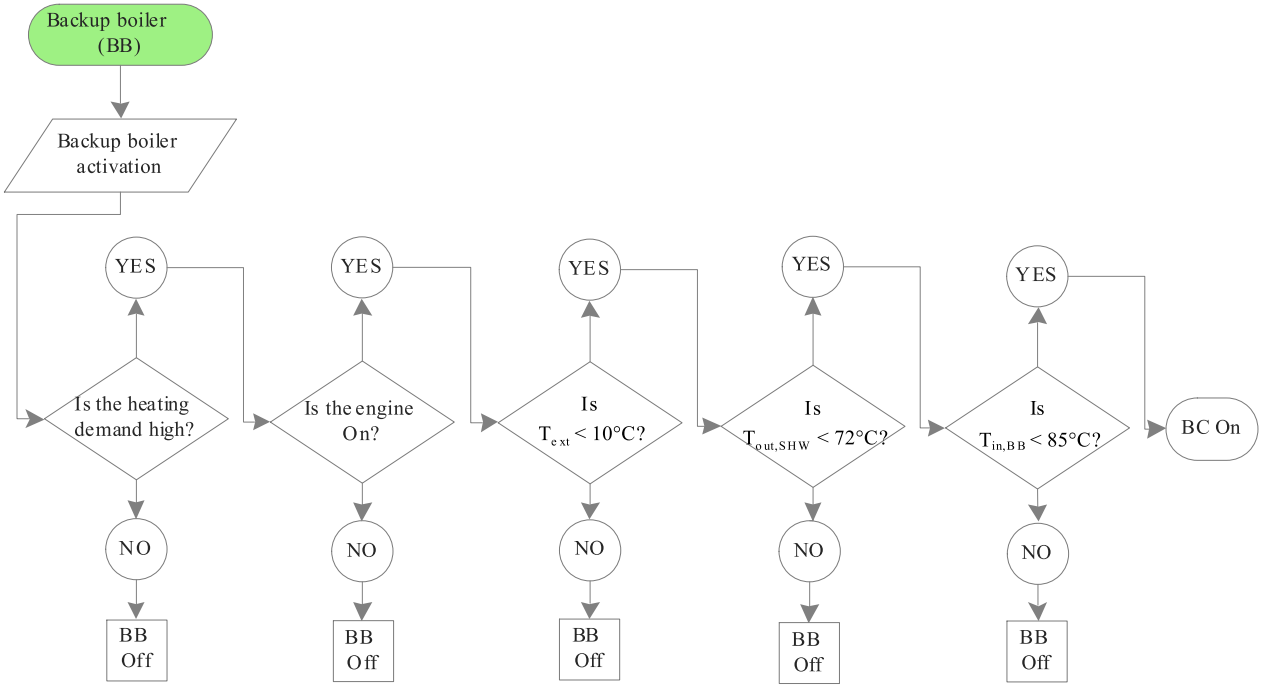

Figure 129. Backup boiler control strategy.

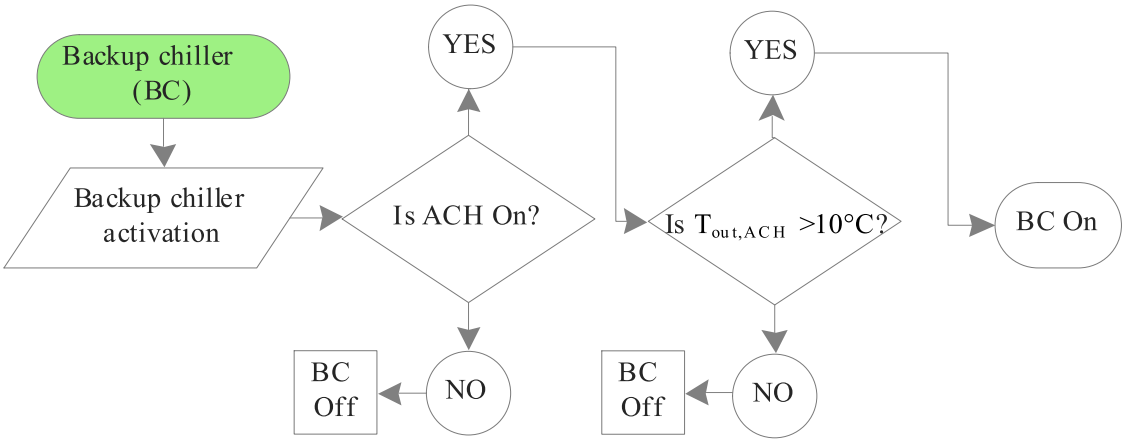

Figure 130. Backup chiller control strategy.

Generally, the operating strategy adopted for hospitals is based on the Thermal Load Tracking mode (TLT), due to the high thermal energy request that extends also during the night. TLT strategy is a thermal load tracking mode in which the engine partializes to follow the thermal building request. Anyway, in this case study the numerical and dynamic results will be shown also for the Maximum Power Thermal Load Tracking mode (MPTLT) and the Electricity Load Tracking mode (ELT) strategies. Most of the implemented controls are true also for these two new operating strategies. MPTLT strategy is a thermal load tracking mode in which the engine does not partialize and so it works always at maximum power. To obtain this operating strategy from the previous one, the proportional controller, which operated on the engine partialization, was removed. ELT strategy, instead, is an electric load tracking mode in which the engine partializes to follow the electric request. This operating strategy can be applied only through another heat exchanger, which must reject excess heat. In fact, following the electric load, it is possible to get excess heat to reject. This rejecting heat exchanger is also controlled by a PID controller, which forces the water coming back to the PM, to go into the rejecting heat exchanger. In this way, there is a dissipation of the thermal surplus and no problems occur to the engine operations.

System model – Study 5

The layout described in the previous section was dynamically simulated in TRNSYS environment. For the description of the components models as the internal combustion engine and the ACH, see Study 4 section, for the building model, see Study 1 section. The remaining models are reported in TRNSYS library. Regarding the internal combustion engine, in Figure 131, the mechanical and electric efficiency of the engine (left) and the fraction of thermal energy recovered to jacket water, engine oil, after cooler and exhaust gases (right) as function of the engine partial load ratio, on the basis of the numerical map adopted in the model are depicted. In particular, the represented data correspond to the operation ones of the engine Vitobloc 200, EM-140/207 (Viessmann).

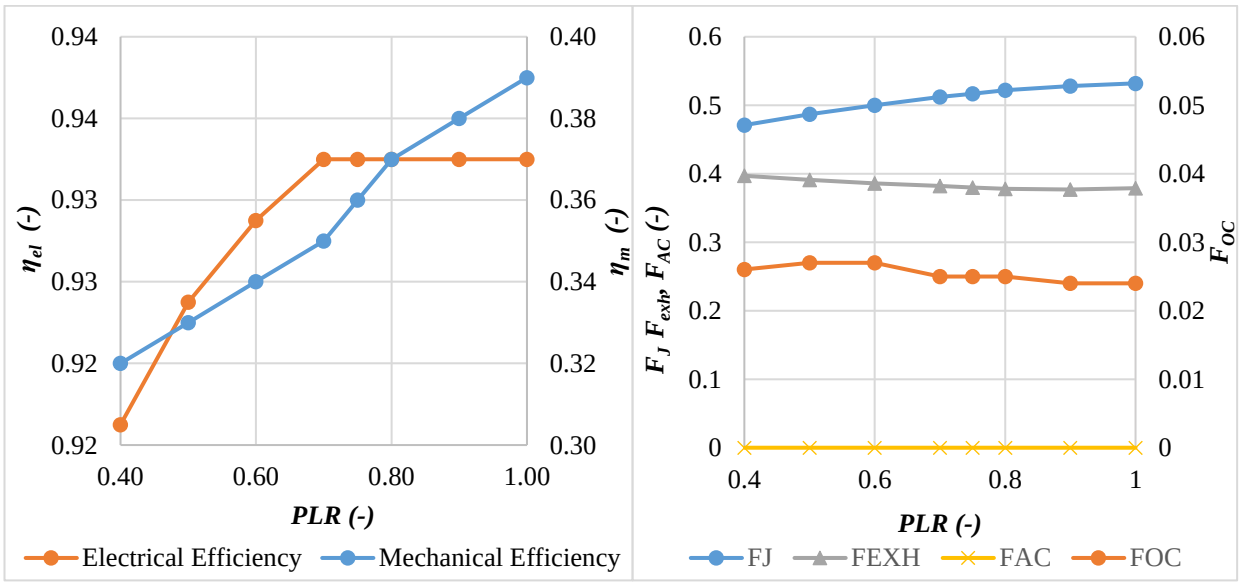

Figure 131. Mechanical and electric efficiency of the engine (left) and fraction of thermal energy recovered to the jacket water, engine oil, after cooler and exhaust gases (right) as function of the engine partial load ratio.

The detailed thermo-economic analysis included in order to assess the energy and economic profitability of the trigeneration system under investigation is reported in Study 4 section. For further details see reference [238].

Case study

The investigated case study consists of a private hospital, located in Central Italy. The private hospital includes 147 beds, 35 clinics and 3 operating rooms that allow one to perform a plurality hospital activity. The annual electric demand is 1527.8 MWh and the natural gas consumption is equal to 165104 m^3 (data referred to year 2015). The building includes six floors, one of which is the basement that is two meters below the ground floor. The three operating rooms are located at the third floor; the fifth floor, instead, only includes technical rooms. The analysed building in the 3D model was divided into four different thermal zones (Floors, Basement, Attic and Operating Rooms), as shown in Figure 132.

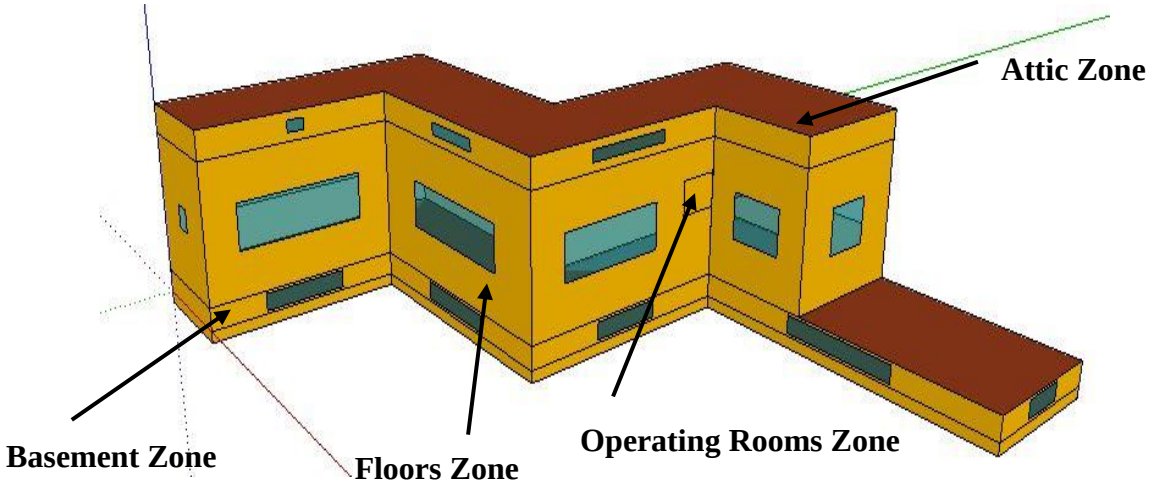

Figure 132. 3D Building.

The four different thermal zones are managed by different control strategies, implementing different values of winter and summer comfort temperatures. Zones are also different for: time occupancy scheduling, air change rates, internal loads and walls stratigraphy. The simulation assumptions regarding the building are shown in the Table 40 and Table 42. Note that the values of thermophysical proprieties of the building (for opaque and transparent elements), the air infiltration / ventilation rate, the people / light / machineries heat gains, schedulers, etc. were fixed by taking into account the literature values regarding the hospital buildings [198] and by considering the Italian President of the Republic's Decree of the 1997, which establishes the minimum plant requirements for operating rooms and hospital buildings. Design parameters of the system were accurately calibrated in order to match the performance data and the features of the real cogeneration system to be installed. The trigeneration system consists of a reciprocating internal combustion engine from 140 kW_e and 207 kW_t, able to produce power and heat by means of heat recoveries from the exhaust gases, the oil and jacket cooling water. In summer, when the thermal demand is low and approximately equal to that required for the production of DHW, the hot water produced by the cogenerator is sent to the 175.8 kW_f ACH, connected with a 425 kW cooling tower (Table 39). In this way, the designed trigeneration system is able to satisfy a large amount of the building energy demand; the remaining amount of electricity, not used to match the electricity load of the

hospital, is purchased from the grid. A backup boiler and an auxiliary electric chiller are used to completely match user heating and cooling energy demand. The economic analysis, taking into account the evaluation of *SPB*, the *NPV* and the *PI*, was carried out by considering the total capital cost J_{tot} assessed by the costs of main components (ACH, cooling tower and cogenerator unit), obtained by commercial catalogues and provided by manufacturers' data: 1043 €/kW for the cogeneration unit and 41 €/kW and 540 €/kW for cooling tower and ACH, respectively. AF, is equal to 10.38, being calculated by assuming a discount rate of 0.05 and a time horizon of 15 years. The design parameters of the whole CCHP plant, of the internal combustion engine and the assumptions regarding the building are shown in Table 39-Table 42.

Table 39. Main design parameters (1).

Component	Parameter	Value	Unit
Heat exchanger winter	Heating water flow rate (pump P6)	17200	kg/h
	Fan coils hot water flow rate (pump P62)	71428	
	ΔT_{HEW} Tolerance on HEW activation temperature	2	°C
	$T_{set,\,HEW}$ Set point temperature for space heating activation	70	
Chiller	Chilled water set point temperature	7	
	$T_{set,\,ACH}$ Set point temperature for space cooling activation	75	
	ΔT_{ACH} Tolerance on ACH activation temperature	5	
	Hot water flow rate (pump P5)	32400	kg/h
	Chilled water flow rate (pump P3)	27500	
	Fan coils chilled water flow rate (pump P32)	59143	
	Rated cooling capacity	175.8	kW
Cooling tower	Cooling water flow rate (pump P4)	91800	kg/h
	Air flow rate	33480	
	Rated cooling capacity	425	kW
Cold tank	Volume	3	m^3
Hot tank		6	
Fan coils	Rated heating and cooling capacity for floors zone	280/271	kW
	Rated heating and cooling capacity for basement zone	146/85	
	Rated heating and cooling capacity for attic zone	105/110	
	Rated heating and cooling capacity for operating rooms zone	103/86	
	$T_{set,chw,FC}$ Set point inlet chilled water temperature	15	°C

Table 40. Assumptions for the simulation of the hospital building.

	Thermal zone			
	Floors	**Attic**	**Basement**	**Operating rooms**
Set point indoor air temperature [°C]	$T_{setHeat}$: 21±1 $T_{setCool}$: 26±1			$T_{setHeat}$:21 $T_{setCool}$:24
Occupancy schedule [h]	00:00-24:00	8:00-17:00 (working days)	00:00-24:00	7:00-21:00
Number of occupants per zone	400	10	100	15
People heat gain [W/p]	Sensible: 90 Latent:95	Sensible: 165 Latent:300	Sensible: 100 Latent: 130	Sensible: 100 Latent: 205
Light heat gains schedule [h]	00:00-24:00	8:00-17:00 (working days)	00:00-24:00	7:00-21:00
Machineries heat gains schedule [h]	00:00-24:00	8:00-17:00 (working days)	00:00-24:00	7:00-21:00
Light + machineries heat gains [W/m^2]	10	13	13	100
Air infiltration rate [vol/h]	2	1	2	20
DHW set point temperature [°C]	45			
Tap water temperature [°C]	14			

Table 41. Main design parameters (2).

Component	Parameter	Value	Unit
Cogenerator	$Q_{th,rated,COG}$ Thermal rated power	207	kW
	$P_{el,rated,cog}$ Electric rated power	140	
Heat exchanger exhaust Gases-Jacket water	$T_{in,out,ExJ,JW}$ Jacket water inlet and outlet rated temperatures	88-92	°C
	Exhaust Gases flow rate	520	kg/h
	Jacket water flow rate (pump P23)	17780	
Heat exchanger jacket water/heating water	$T_{in,\,set,\,JW}$ JW inlet set point temperature	70	°C
	Heating Water flow rate (pump P12)	8903	kg/h
Heat exchanger heating water/sanitary hot water	Heating Water flow rate (pump P12)	8903	
	Sanitary hot water flow rate (average)	1333	

Table 42. Features of the opaque elements (U-values, thicknesses).

Thermal zone	Building element	U-value [W/m^{2}K]	Thickness [m]
Attic	Roof	0.670	0.220
	External wall	0.714	0.245
	Adjacent ceiling (Floors)	1.110	0.440
	Windows glass	2.830	0.004
Floors	Adjacent ceiling (Attic)	1.110	0.440
	External wall	0.714	0.245
	Adjacent ceiling (Basement)	1.110	0.440
	Windows glass	2.830	0.004
	Adjacent wall (Operating Rooms)	1.306	0.340
Basement	Adjacent ceiling (Floors)	1.110	0.440
	External wall	1.306	0.245
	Ground floor	0.794	0.550
	Windows glass	2.830	0.004
Operating rooms	Adjacent ceiling (Floors)	1.110	0.440
	External wall	1.306	0.245
	Adjacent wall (Floors)	1.306	0.340

Results of Study 5

Discussion of the results first presents integrated (yearly, weekly) results of the base case (TLT strategy). Afterwards, integrated and dynamic results of the other proposed strategies (MPTLT strategy and ELT strategy) were discussed. For each strategy, optimizations were performed in order to find the best solution.

Yearly results

In Table 43 a comprehensive overview of system overall performance is reported. In particular, Table 43 reports the electric energy produced by the CHP system, electric energy consumed by the auxiliaries (circulating pumps, electric chiller, ACH, CT fan), chilled energy, ACH thermal energy and cooling energy, thermal energy produced by the auxiliary boiler, chilled energy produced by the auxiliary electric chiller, thermal energy of the Exhaust gases-Jacket water heat exchanger (ExJ), Jacket water/heating Water heat exchanger (JW), Heat Exchanger for Winter (HEW), heating water/Sanitary Hot Water heat exchanger (SHW). It is noticeable that the auxiliary electric energy is negligible with respect to the electric production. Thermal energy is mainly supplied by the engine jacket and from the exhaust gases, providing a thermal production equal to 1261 MWh/year. This energy is not sufficient to meet all the thermal request; for this reason, a 330 MWh/year BB thermal

production is required. The highest rate of the produced thermal energy is used for space heating purposes and it is equal to 995 MWh/year; ACH thermal demand is equal to 192 MWh/year and the one needed to supply the sanitary hot water heat exchanger is equal to 393 MWh/year. In Table 44 the heating and cooling energy demands by each building thermal zone are shown.

Table 43. Annual produced energies.

Energy	[MWh/year]
CHP electric energy	808
Absorbed electric energy	9
ACH chilled water energy	156
ACH heating water energy	192
ACH cooling water energy	350
BB thermal energy	330
BC chilled energy	90
ExJ thermal energy	479
JW thermal energy	1261
HEW thermal energy	995
SHW thermal energy	393

Table 44. Annual heating and cooling energy demands

Zone	Heating	Cooling
	[MWh/year]	
Floors	552	148
Basement	233	31
Attic	52	12
Operating rooms	111	49
Total	948	240

The previous tables show that the CCHP system is able to supply about 54% of the electric energy demand, 78% of the thermal energy demand and the 64% of the cooling energy demand. The CCHP system uses 2301 MWh/year of primary energy, instead of 2969 MWh/year required by the conventional system. Thus, the *PES* is about 670 MWh/year, corresponding to a CO_2 emission reduction equal to 134 tons of CO_2.

Weekly results

In order to better evaluate the variation of energy flows and system performance during the year, in Figure 133 (above), the following weekly thermal energy flows were reported: jacket water, gases-jacket water, SHW heat exchangers and boiler ($E_{th,JW}$, $E_{th,GJ}$ and $E_{th,SHW}$, $E_{th,BB}$, respectively). Such Figure also shows the electric production of the PM, $E_{el,cog}$ and the electricity consumption of the auxiliary devices, $E_{el,aux}$, clearly negligible compared to the other terms. The trends of all the parameters show minimum values in summer. This is due to fact that the PM is following the real thermal demand of the hospital. $E_{th,SHW}$ is quite constant during the year, while the BB produces thermal energy, $E_{th,BB}$, only in winter, when the thermal demand is very high. Conversely, the results reported in Figure 133 (below) show a remarkable seasonal trend. In fact, by observing the cooling energy produced by ACH $E_{ch,ACH}$ and by the electric chiller $E_{ch,el,BC}$, an increase of the cooling demand can be detected during the summer. In this period, the thermal energy used for heating purpose, $E_{th,HEW}$, is equal to zero and so the thermal energy request, $E_{th,req}$, is only due to the SHW; for this reason it is possible to use the thermal energy produced by cogenerator to drive the ACH.

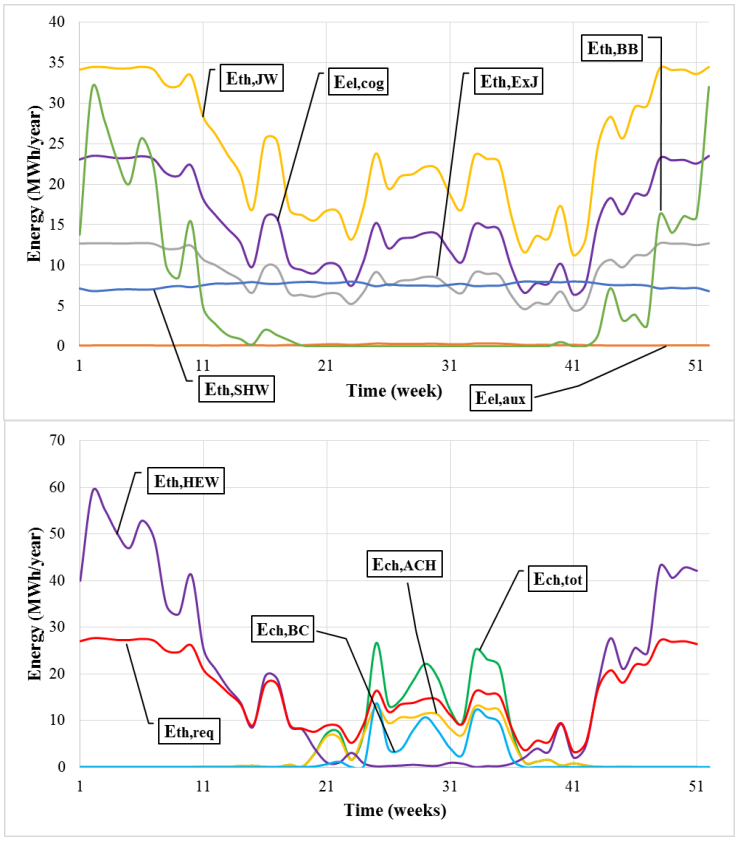

Figure 133. Weekly energy.

Annual dynamic results

In Figure 134 - Figure 136 the thermal, cooling and electric (obtained by measured historical data) cumulative load diagrams are shown.

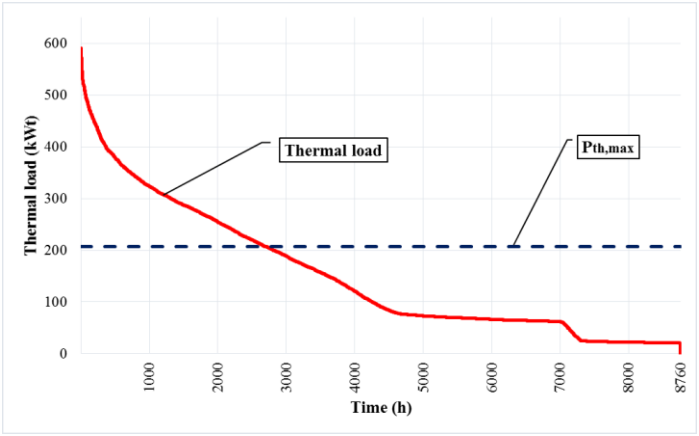

Figure 134. Thermal load.

The interpretation of these figures is crucial for a preliminary evaluation of the trigeneration system feasibility, suitable only if the electric and thermal loads are high, constant and simultaneous. The maximum value of the thermal load is about 600 kW. The cooling load extends for about 2000 hours, reaching a peak of about 450 kW. The electric load varies between 100 and 300 kW, and only for about 2000 hours the request is lower than the PM rated power (140 kW), making possible

to sell a small amount of the electricity in excess. In Figure 137 the thermal load diagram is shown, having added to the thermal energy flow rate required, also the cooling power converted into thermal energy flow rate (by the cooling capacity and ACH *COP* ratio, equal to 0.7), so as to give virtually all the thermal load of PM. By this operation, the intercept between $P_{t,min}$ and the thermal load curve is shifted forward in time, to about 5500 hours.

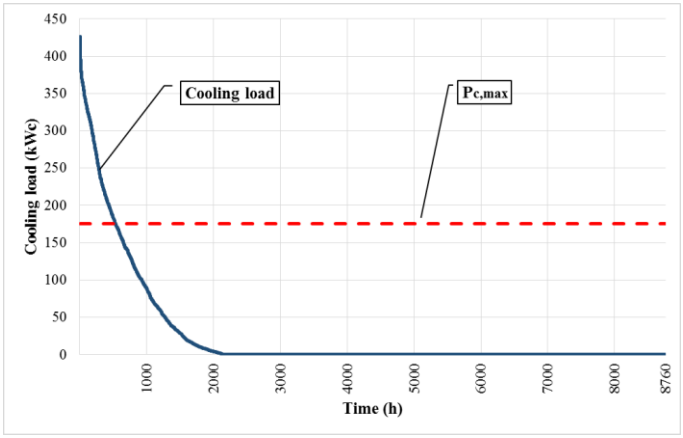

Figure 135. Cooling load.

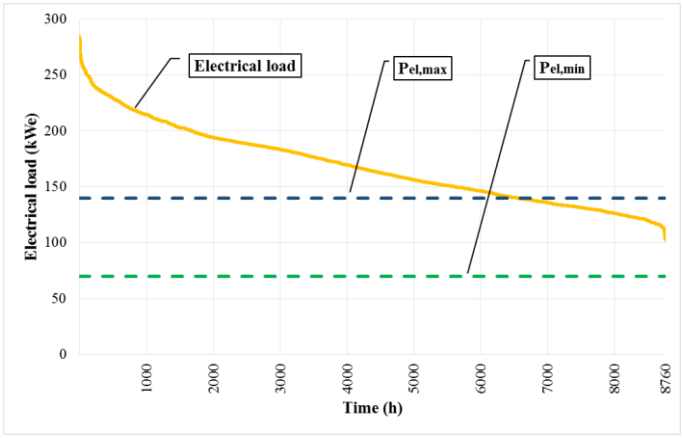

Figure 136. Electric load.

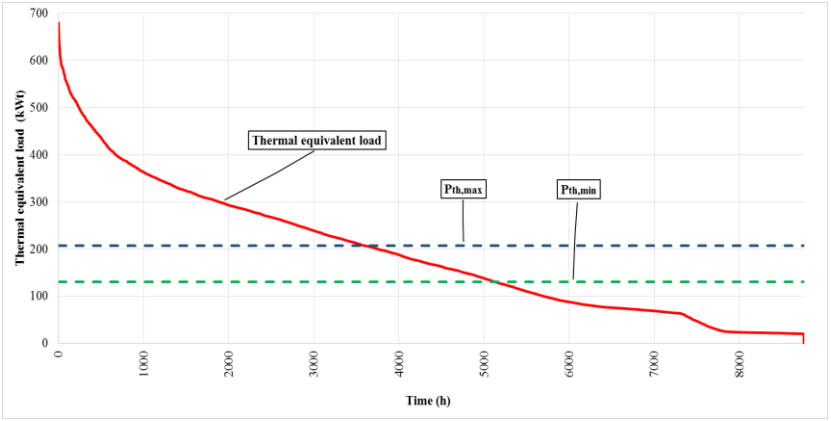

Figure 137. Thermal equivalent load.

Weekly dynamic results

The weekly dynamic results are here reported to show the operation of the designed control strategies. In particular, Figure 138 shows the operation of the thermostats installed within the buildings controlling thermal zone temperatures at their respective set point.

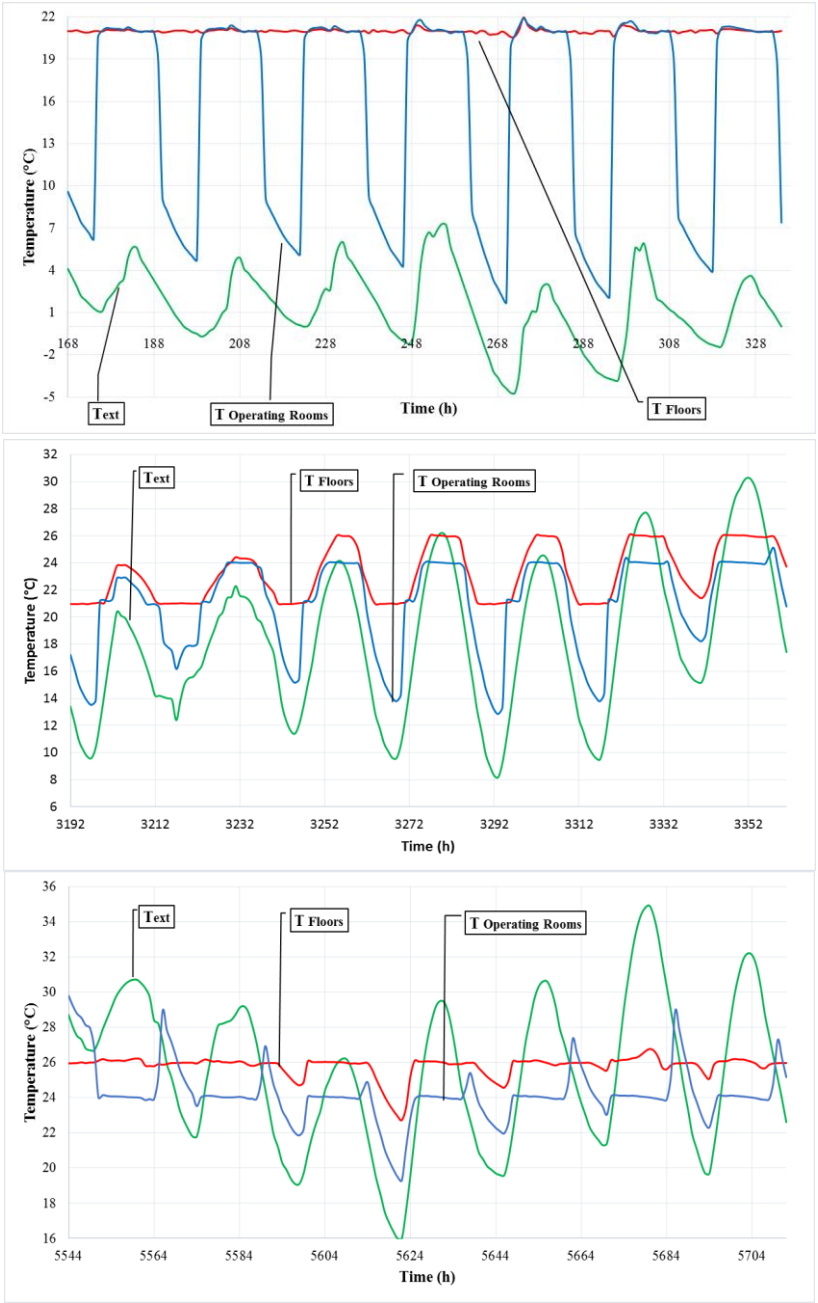

Figure 138. External, Floors and Operating Rooms temperature (above January 8-14; central May 14-20; below August 20-26).

Here, it is possible to observe the trend of the comfort temperatures for the Floors and Operating Rooms Zones in a typical winter, spring or autumn, and summer week. It is clearly observed that, by the implemented PID controls, the set point temperatures are always fulfilled, 24/24h in the Floors Zone, and during the scheduled occupying period of the Zone operating rooms. It is also worth noting that when the operating rooms are closed, the internal air temperature dramatically

decreases, approaching the external air one. This is due to the fact that in that period Air Handling Unit fan is continuously in operation (although heating and cooling coils are deactivated) providing a huge air change with external air. This is required in order to maintain pressure difference between indoor and outdoor air, preventing any contamination of the operating room. In order to save energy, when the external temperature is not too high (or low in winter), the controls turn the cooling (or the heating, in winter) system off. In some spring or autumn days, when the outdoor temperatures are cold in the middle of the night and hot in the middle of the day, either the heating or the cooling systems are switch on during the same day. This is possible since the rooms are all equipped with 4-pipe fan coils (i.e. each fan coil includes both heating and cooling coils), as it is shown in the Figure 138.

Daily dynamic results

In this section, for a representative winter day, March 8th, the operating temperatures of the heat exchanger JW (included within the cogenerator) are reported in Figure 139.

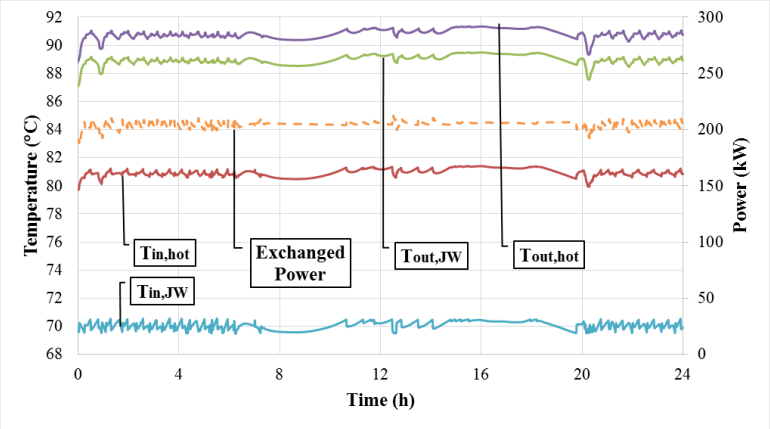

Figure 139. Heat exchanger JW operating temperatures.

It is possible to note that, by the detailed PM map calibration, the heating water increases its temperature from 70°C ($T_{in,JW}$) to 90°C ($T_{out,JW}$) while the hot source water decreases its temperature from 92°C ($T_{in,hot}$) to 82°C ($T_{out,hot}$), according to manufacturer design values. Such result is also due to the detailed calibration of the entire model to the specific PM under investigation, with special reference to the parameters of the heat exchangers (number of shell passes, overall heat transfer coefficient in the heat exchangers, heat exchanger effectiveness, etc.). In Figure 140, the PM controls were reported for a representative winter day, March 23rd, still considering the TLT strategy. The PM reduces its power output as a function of the outlet water temperature from the SHW, $T_{out,SHW}$, thanks to a proportional controller: when this temperature is lower than 65°C, the PM works at maximum power. On the other hand, when it is higher than 72°C, the PM turns off and when the temperature goes from 65 to 72°C, the PM operates in part-load conditions. In this way, the temperature at the inlet of the cogenerator, $T_{ret,cog}$, is stably close to 70°C.

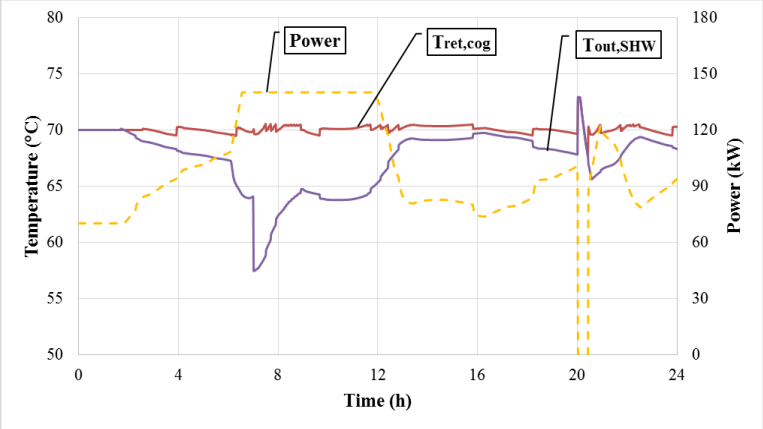

Figure 140. PM controls.

Operation strategies proposal: MPTLT and ELT

Two additional operation strategies were analysed in this subsection, namely: Maximum Power Thermal Load Tracking mode, which is a TLT mode but for the PM that works always at maximum power without PM partialization (switching only on and off alternately), and Electric Load Tracking mode, the PM follows the electric demand and the electric power provided by the PM is always less or equal to the electric demand,

With the MPTLT strategy, the energetic production increases. In fact, the CCHP can provide an additional amount of 60 MWh/year of electric energy with respect to the one produced in TLT strategy. Similarly, the increases in thermal and cooling energies were respectively 25 and 2 MWh/year. By this new strategy, the electric efficiency increases from 35.1% to 36.5%, due to the fact that the small reduction in efficiency typical of part-load operation can be avoided. On the other hand, either the gross thermal efficiency (which refers to all the thermal energy produced) or the net one (which refers only to the useful thermal energy), decreases of about 2%, achieving 53.9% and 53.4%, respectively. In the Figure 141, it is depicted, for November 18th, the PM working in the TLT and MPTLT strategies.

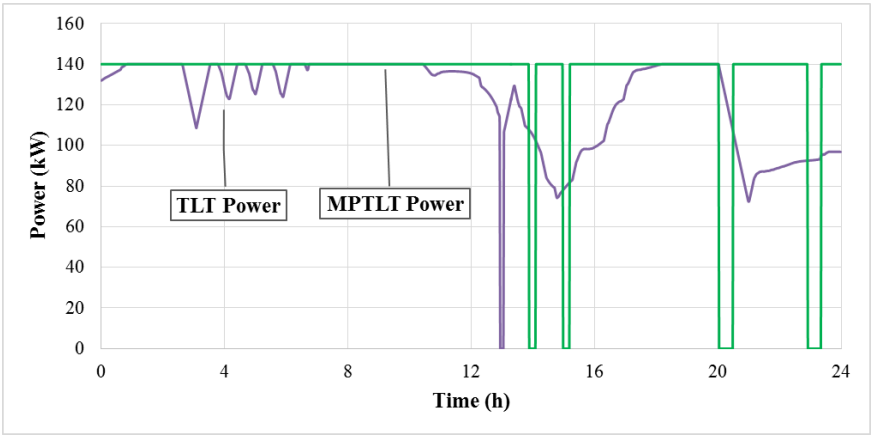

Figure 141. TLT and MPTLT strategies.

In MPTLT case, PM works always at maximum power but the number of its On/Off increases, affecting operating life and maintenance cost, that, in any case, from an economic point of view, lead a higher convenience of this strategy (Table 46).

In the ELT strategy, because of the constant electric load, which is always higher than the CCHP production, the PM never stops working. Anyway, this strategy was possible only by using a suitable dissipative heat exchanger to reject the excess heat. A PID controller regulates the heat dissipation. Figure 142, related to the day November 18th, clearly shows that, when the electricity demand is lower than the maximum electric power (140 kW), the PM partializes to follow the load; when the request exceeds the maximum electric output, the PM works at 100% of the power, and the uncovered electric rate by the production is purchased from the grid.

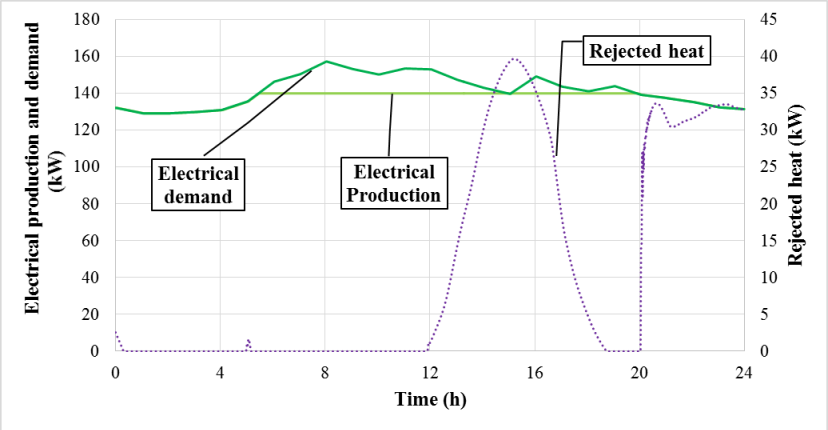

Figure 142. Electric load tracking mode strategy.

By the ELT strategy, the PM can provide 400 MWh/year of electric energy more than the TLT strategy, additional 500 MWh/year and 30 MWh/year of thermal and cooling energy, respectively. However, there is a certain dissipation of thermal energy equal to 490 MWh/year (causing a dramatic reduction of the net thermal efficiency) and the primary energy consumption increases more than 50%. The main energetic/economic parameters of the new strategy proposals are shown in the Table 45 and Table 46.

Table 45. Yearly energy results.

Strategy	TLT	MPTLT	ELT	Unit
$E_{el,\ cog}$	808	869	1203	MWh/year
$E_{ch,\ ACH}$	156	158	184	
$E_{c,\ ACH}$	350	361	435	
$E_{th,\ ACH}$	192	202	250	
$E_{th,\ ExJ}$	479	481	672	
$E_{th,\ JW}$	1261	1285	1794	
$E_{th,\ HEW}$	995	996	996	
$E_{th,\ SHW}$	393	459	459	

In spite of the heat dissipation, ELT strategy is the best solution from the energetic production and economic point of view, providing 1203, 1794 and 184 MWh/year of electric, thermal energy and cooling energy, respectively, with a *SPB* of only 4 years. Anyway, it is the worst solution from an energetic point of view, having the lowest *PES* value, equal to 14%.

Table 46. Yearly economic and energy results.

Control strategy					
Description	**Parameter**	**TLT**	**MPTLT**	**ELT**	**Unit**
Global efficiency	η_{glob}	0.899	0.903	0.756	-
Operation equivalent hours	H_{eq}	5768	6209	8594	hours
Cogenerator required energy	E_{fuel}	2301	2386	3318	MWh/year
Yearly electricity	$E_{el,cog}$	808	869	1203	
Useful thermal energy	$E_{th,useful}$	1250	1272	1291	
Primary energy saving	PES	23	24	14	%
Effective coefficient	C_{eff}	1	1	1	-
Total Fuel consumption	$V_{NG,tot}$	279992	288011	393886	Sm^3/year
Tax free volume fuel consumption	$V_{NG,taxfree}$	177652	191245	264710	
Energy savings certificates	ESC	11800	12800	11300	€/year
Economic saving for cooling	S_{Cool}	7285	7344	8569	
Economic saving for heating and SHW	$S_{Heat}+S_{SHW}$	64691	64995	66935	
Economic saving for electricity	S_{el}	109821	117511	166438	
Total economic saving	S_{tot}	182480	190880	241941	
Electric operating cost	$C_{op,el}$	10094	10886	15040	
Fuel cost	C_{fuel}	91511	93973	128459	
System cost	$C_{el,system}$	1147	1147	1147	
Maintenance cost	Ma	12113	14343	18048	
Total cost	ΔC_{tot}	104770	109463	147654	
Simple Pay Back	SPB	4.4	4.2	4.0	years

Optimizations

In the previous analysis, between the three different control strategies, from an economic point of view, the ELT strategy provided the best results. For this reason, an optimization procedure for finding out the values of the most important design parameters was carried out, in order to optimize furthermore this strategy. This was performed by the TRNEdit tool of TRSNSYS and computer Design of Experiment (DoE) [240]. By such technique, the set of synthesis/design parameters for optimizing the energetic, environmental and economic performances was detected. The DoE is widely adopted for commercial and academic purposes in order to maximize (or minimize) a selected objective function. In particular, this methodology allows one to: (i) analyse the effects of the main design parameters on the considered objective function; (ii) create an analytic model of the selected objective function in relation to the system design variables; (iii) plot the optimum response surface, i.e., the graphical depiction of the assessed analytic function and (iv) perform an optimization procedure aiming at determining the optimal values of the design variables. The optimization procedure was achieved by computer simulations carried out by TRNEdit, another important tool of the TRNSYS, which allows one to design a pre-optimized system, achieving significant energetic and economic savings with respect to the conventional approach based on standard energetic and economic feasibility analyses. In DoE approach, a full factorial design was used in order to improve results accuracy, suffering the only disadvantage of longer computational times. Therefore, the number of system design variables and the corresponding levels were selected in order to achieve reasonable computation times. For the optimization procedure, the following four design variables were selected: (i) the PM nominal capacity; (ii) the ACH nominal capacity; (iii) the TKH volume; (iv) the TKC volume. For all the considered variables, the number of levels was set equal to 4 and the corresponding levels were reported in Table 47.

Table 47. Optimizing variables and corresponding levels.

Variable	Unit	Level 1	Level 2	Level 3	Level 4
PM size multiplier	(-)	0.5	1	1.42	1.7
ACH size multiplier	(-)	0.6	1	1.1	1.5
TKH volume	m^3	5	6	7	8
TKC volume	m^3	2	3	4	5

For such operating conditions, 256 different simulations, referred to a whole year with a time-step of 0.04 h, were conducted in TRNEdit. The resulting computational time was close to 1 hour for simulation. Therefore, the overall optimization can be completed in about 10 days of continuous calculations, but by splitting the iterations in six different groups of processors, the result can be obtained within few days. For each possible combination of the considered design variables, the *SPB* and *PES* objective functions were selected. Through these different simulations, it is possible to observe the main effects of the selected variables on the system performance, optimizing the CCHP system and obtain the results in different plots.

DoE: Main Effects and Interaction Plots

By the main effect plots (factorial plots) the mean value of the selected objective functions for each level of the considered design variable and the influence of each design parameter variation on the objective functions were obtained. Figure 143 shows the main effect plots for *SPB* and *PES* objective functions. It is worth noting that these plots (and all the subsequent ones) show the combinations of factors/levels as discussed before. However, whatever combination of design factors and related levels must provide the same amount of thermal, cooling and electricity to the user. Therefore, for all the combinations, it must be checked that no significant variations of the energy supplied to the user are achieved. In case, a combination returns a lower amount of one of the energy vectors, this must be mandatory discarded. The results of this check showed that energy supply is almost constant for all the combinations, except for all the ones including an ACH size ratio equal to 0.60. In this case, in fact, the sum ACH and electric chiller capacities is lower than user demand in several hours of the year, determining a lower amount of cooling energy supplied to the user. Therefore, all the combinations including ACH size ratio of 0.60, although mathematically possible, must be discarded. Figure 143 (above) shows a minimum for the *SPB* (equal to 3.9 years) which is obtained by selecting the PM and ACH capacities used in the discussion of the results presented before. The analysis also suggests using a 5 m^3 hot tank and a 2 m^3 cold tank. However, it is clearly shown that the most significant parameters for the *SPB* variation are the PM size and the ACH size. In fact, despite the higher cost of a bigger engine, the *SPBs* with the size ratio equal to 1 and 1.42 are lower than the one with the size equal to 0.5. In fact, when the size ratio is 0.50, the PM is not able to provide the energy demand, increasing the auxiliary systems production. This is also true for the ACH size. However, in case of higher ACH capacities, its higher capital costs dominate the savings due to the additional cooling energy production.

Conversely, tanks volumes do not significantly affect the costs. Therefore, in this case the objective function must better face with system stability than with economic parameters. Therefore, it is suggested to select the volumes, which allow the system to be more stable, as the ones selected in the basic case study discussed before. Figure 143 (below), instead, shows that the *PES* is inversely proportional to the ACH capacity. In fact, the maximum *PES* value is equal to 20.6%, obtained

selecting an PM size ratio equal to 0.5. Conversely, ACH capacity and the tanks volumes do not significantly affect the *PES* values.

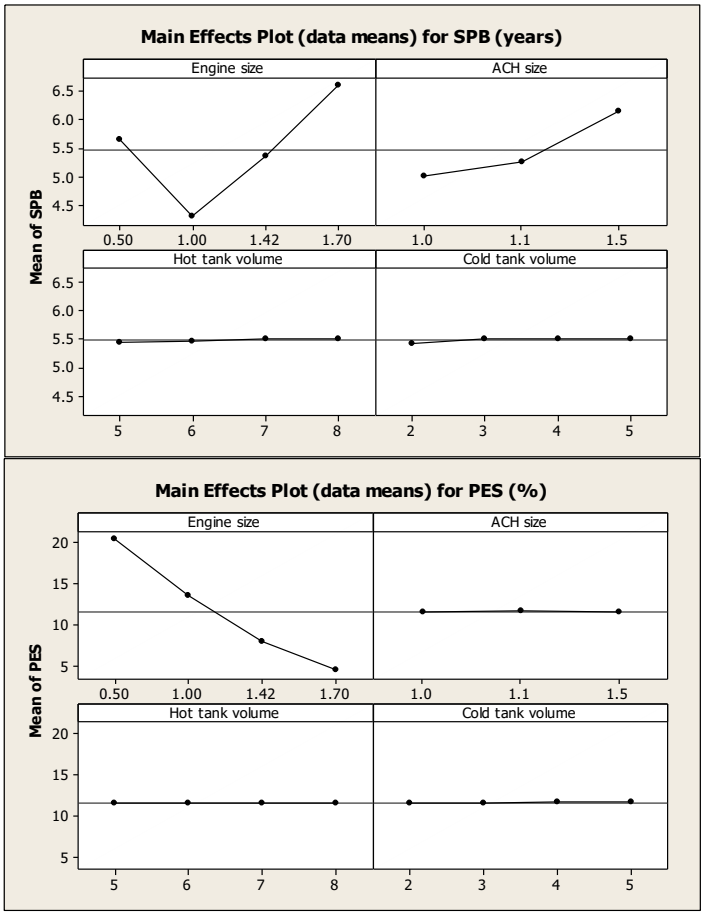

Figure 143. Main effects plots for SPB (above) and for PES (below).

By the interaction plots (factorial plots) showed in the Figure 144, two factors per time were compared, unlike the previous plots in which only one factor was analysed per time to find out the best *SPB* and *PES* values. These plots once again show the results achieved by from the previous analysis. In fact, the best *SPB* value is obtained with the engine and ACH capacity ratio equal to 1, hot tank volume equal to 5 m^3 and cold tank volume equal to 2 m^3. The best *PES* value, instead, is obtained with the engine capacity ratio equal to 0.5, the ACH capacity ratio equal to 1, hot tank volume equal to 6 m^3 and the cold tank volume equal to 2 m^3.

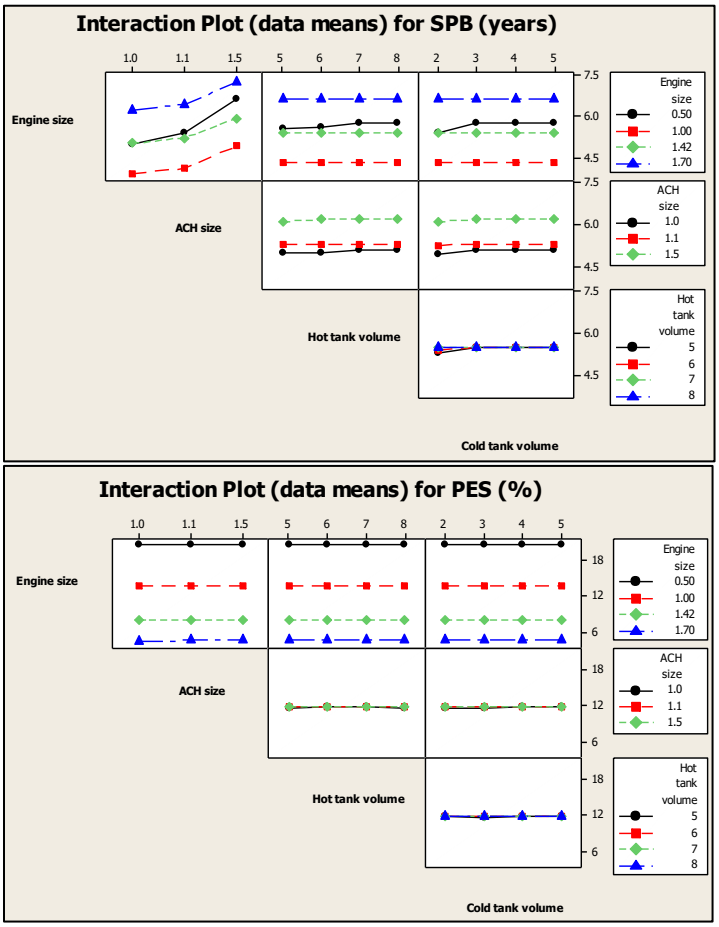

Figure 144. Interaction plots for SPB (above) and for PES (below).

DoE: Contour Plots of the Optimal Response Surface

In Figure 145, the contour plots of the optimal response surface are displayed for *SPB* and *PES*, holding constant the extra factors.

Each figure includes six subplots, showing all the possible combinations among the four considered design values. Each subplot refers to the product between two independent variables under consideration. So, for each plot two design variables were considered at the same time, whereas all the remaining variables were kept constant at fixed values. Such values are reported on the right side of each figure. By observing the *SPB* plots, it is possible to note that system performance is dramatically sensitive to engine and ACH capacity selection. In fact, the subplot showing the highest variation in *SPB* is the upper left one, reporting the combination of those two capacities. The influence of such parameters scarcely depends on the variation of the other ones. In fact, the remaining subplots show almost vertical lines. In particular, a single colour subplot (bottom right) shows that tank volumes negligibly affect system economic performance.

By observing the *PES* plots, it is possible to note that system performance is dramatically sensitive only to the engine capacity selection. In fact, the main variations occur when the engine capacity ratio is involved and the influence of this parameter scarcely depends on the variation of the other ones, presenting the remaining subplots almost vertical lines. A single colour subplot (all in the bottom) shows that ACH capacity and tank volumes negligibly affect system economic performance. In summary, all the results shown by the analysis of the response surface show the same general trends obtained by the main effects plots. However, the analysis of the response

surface is also useful to detect the optimal configuration for all the combinations of the design parameters.

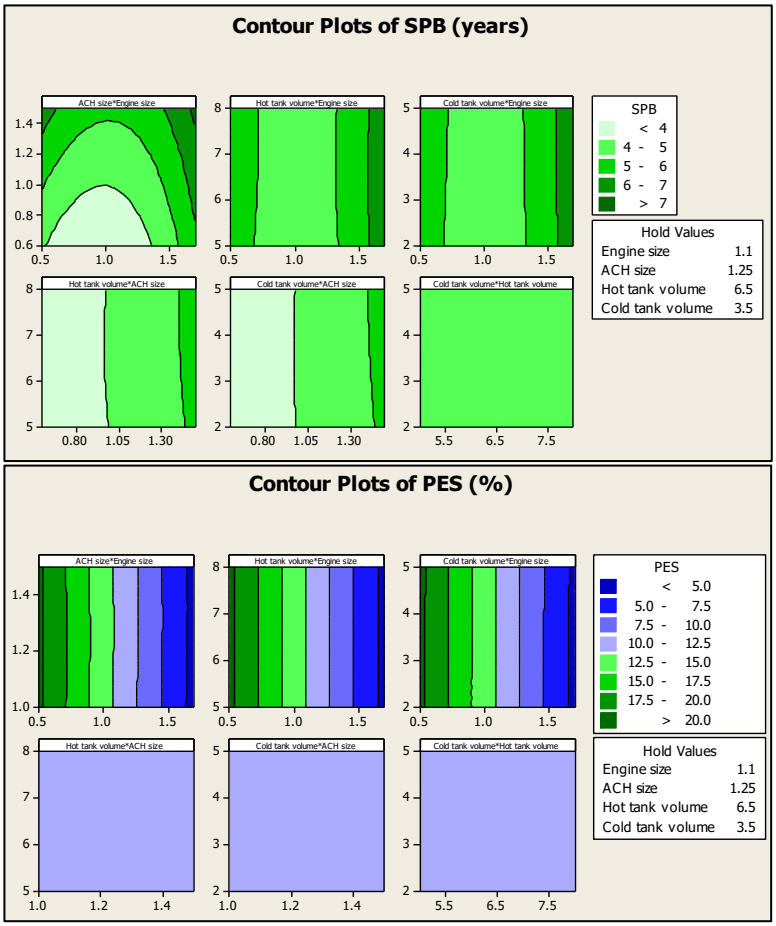

Figure 145. Contour plots of SPB (above) and PES (below), middle settings.

In Table 48, the final optimal solutions for the *SPB* and *PES* objective functions are shown. In this analysis, the minimum ACH capacity was set at 1.00 in order to avoid unfeasible solutions, as discussed before.

Table 48. Optimal values for the objective functions of optimization analysis and comparison with initial values.

Design parameters	Optimal *SPB* value	Optimal *PES* value	Initial value	Unit
Engine size	1	0.5	1	(-)
ACH size	1	1	1	(-)
Hot tank volume	5	6	6	m^3
Cold tank volume	2	2	3	m^3

CONCLUSION

In this thesis, several dynamic models simulating the performances of the polygeneration systems for buildings were in detail presented. By adopting a method based on dynamic simulations, able to predict the real time-dependent operation of the systems investigated, the optimization and the improvement of their performance were potentially achieved. From these analysis, in order to contribute to the diffusion of the polygeneration systems, as plants potentially suitable at reducing the CO_2 emissions and the energy consumption in the buildings sector, useful guidelines related to the design as well as the operation of such systems were also provided.

With this aim in mind, two macro-groups of polygeneration systems were taken into account:

1. polygeneration systems supplied by the solar energy;
2. polygeneration systems supplied by natural gas.

In particular, for the first group the Building Integrated PhotoVoltaic Thermal collectors (BIPVT) were investigated by means of energy, exergy, environmental and economic analyses for residential, offices and fitness center applications. The polygeneration is due to the simultaneous production of the space heating and cooling (solar heating and cooling technology), domestic hot water and electricity, using only the solar radiation converted by the BIPVT collectors.

For the second group, the waste-heat recovery of a reciprocating engine for the production of electricity was used for space heating, cooling and domestic hot water purposes for factory and hospital applications. The energy, economic and environmental performances of this typology of plant were in detail evaluated, as well as the plant optimization to determine the optimal values of the design variables and the optimal operation control strategy from energy and economic point of view.

In the followings, the main findings of the analyses carried out in this thesis, for the polygeneration systems supplied by the solar energy, can be generally resumed:

- These plants showed fairly different *SPB* periods (from 4 to 20 years), remarkable *PESs* (from 59 to 89%) and avoided CO_2 emissions (from 76 to 90%) for all the investigated building-plant system layouts and weather zones;
- The unwanted summer overheating effects of the BIPVT collectors on the space and heating consumption of the analysed buildings are averagely lower than the helpful winter ones, but this depends highly on the investigated weather location;
- The adoption of the electricity storage system leads to a reduction of the electricity required from grid, that is economically advantageous by considering the different selling/purchasing cost of electricity. Anyway, small capacities of the electricity energy storages are recommended due to their current high capital cost;
- The solar cooling technology (by the adsorption chiller system) is recommended mainly for the simultaneity of the solar energy availability and cooling energy demand;

- In the present market framework, a suitable public funding strategy should be necessary for enhancing the economic profitability of BIPVT (and in general solar systems) technology and for promoting its mass-market commercialization.

The main results obtained from the analysis of the natural gas polygeneration systems presented in this thesis are as follows:

- The achieved *SPB* periods for all the applications, plant configurations and control strategies investigated were enough similar and low, ranging from 3.8 and 4.4 years. The *PESs* range between 14% to 24%;

- The development of a dynamic simulation tool for these plants is highly recommended before the final design and the installation of the system, in order to select the optimal size of the engine to be installed in a real case;

- The profitability of the combined cooling, heating and power plants is dramatically affected by the kind of supporting policy and by the selection of the control strategy, depending dramatically on the present energy market scenario, which currently dramatically penalizes systems which sold too much excess electricity to the grid;

- The *PES* index introduced by the Directive 2004/08/EC can overestimate the efficiency of such systems, since also those with poor energy performance could be legally classified as “High-Efficiency Cogeneration”. Therefore, a revision of the current public subsidy policy is suggested.

LIST OF PUBLICATIONS

Journal papers

1. Buonomano, A., Calise, F., Dentice d'Accadia, M., Vicidomini, M. A hybrid renewable system based on wind and solar energy coupled with an electrical storage: Dynamic simulation and economic assessment. Energy. 2018.

2. Buonomano, A., Calise, F., Palombo, A., Vicidomini, M. Transient analysis, exergy and thermo-economic modelling of façade integrated photovoltaic/thermal solar collectors. Renewable Energy. 2017.

3. Calise, F., Dentice d'Accadia, M., Libertini, L., Quiriti, E., Vicidomini, M. A novel tool for thermoeconomic analysis and optimization of trigeneration systems: A case study for a hospital building in Italy. Energy. Volume 126, 2017, Pages 64-87.

4. Buonomano, A., Calise, F., Palombo, A., Vicidomini, M. Adsorption chiller operation by recovering low-temperature heat from building integrated photovoltaic thermal collectors: Modelling and simulation. Energy Conversion and Management. Volume 149, 1 October 2017, Pages 1019-1036.

5. Calise, F., Dentice d'Accadia, M., Libertini, L., Quiriti, E., Vanoli, R., Vicidomini, M. Optimal operating strategies of combined cooling, heating and power systems: A case study for an engine manufacturing facility. Energy Conversion and Management. Volume 149, 1 October 2017, Pages 1066-1084.

6. Calise, F., Libertini, L., Vicidomini, M. Design and optimization of a novel solar cooling system for combined cycle power plants. Journal of Cleaner Production. Volume 161, 10 September 2017, Pages 1385-1403.

7. Buonomano, A., Calise, F., Vicidomini, M. A novel prototype of a small-scale solar power plant: Dynamic simulation and thermoeconomic analysis. American Journal of Engineering and Applied Sciences. Volume 9, Issue 4, 2016, Pages 770-788.

8. Buonomano, A., Calise, F., Vicidomini, M. A dynamic model of an innovative high-temperature solar heating and cooling system. Thermal Science. Volume 20, Issue 4, 2016, Pages 1121-113.

9. Buonomano, A., Calise, F. Palombo, A., Vicidomini, M. BIPVT systems for residential applications: An energy and economic analysis for European climates. Applied Energy. Volume 184, 15 December 2016, Pages 1411-1431.

10. Buonomano, A., Calise, F., Vicidomini, M. Design, simulation and experimental investigation of a solar system based on PV panels and PVT collectors. Energies. Volume 9, Issue 7, July 2016, Article number 497.

11. Calise, F., Dentice d'Accadia, M., Libertini, L., Quiriti, E., Vicidomini, M. Dynamic simulation and optimum operation strategy of a trigeneration system serving a hospital. American Journal of Engineering and Applied Sciences. Volume 9, Issue 4, 2016, Pages 854-867.

12. Calise, F., Libertini, L., Vicidomini, M. Exergetic analysis of a novel solar cooling system for combined cycle power plants. Entropy. Volume 18, Issue 10, 2016, Article number 356.

13. Buonomano, A., Calise, F., Dentice d'Accadia, M., Vanoli, R., Vicidomini, M. Simulation and experimental analysis of a demonstrative solar heating and cooling plant installed in Naples (Italy). American Journal of Engineering and Applied Sciences. Volume 9, Issue 4, 2016, Pages 798-813.

14. Calise, F., Dentice d'Accadia, M., Vicidomini, M., Ferruzzi, G., Vanoli, L. Design and dynamic simulation of a combined system integration concentrating photovoltaic/Thermal solar collectors and organic rankine cycle. American Journal of Engineering and Applied Sciences. Volume 8, Issue 1, 17 April 2015, Pages 100-118.

15. Calise, F., Dentice d'Accadia, M., Vicidomini, M., Scarpellino, M. Design and simulation of a prototype of a small-scale solar CHP system based on evacuated flat-plate solar collectors and Organic Rankine Cycle. Energy Conversion and Management. Volume 90, 15 January 2015, Pages 347-363.

16. Buonomano, A., Calise, F., Palombo, A., Vicidomini, M. Energy and economic analysis of geothermal-solar trigeneration systems: A case study for a hotel building in Ischia. Applied Energy. Volume 138, January 05, 2015, Pages 224-241.

17. Buonomano, A., Calise, F., Dentice d'Accadia, M., Palombo, A., Vicidomini, M. Hybrid solid oxide fuel cells-gas turbine systems for combined heat and power: A review. Applied Energy. Volume 156, October 05, 2015, Pages 32-85.

18. Buonomano A., Montanaro U., Palombo A., Vicidomini M. NZEBs in Mediterranean climates: Energy design and optimization for a non-residential building. ENERGY PROCEDIA, vol. 82, p. 458-464, (2015).

19. Calise, F. Dentice d'Accadia, M., Piacentino, A., Vicidomini, M. Thermoeconomic optimization of a renewable polygeneration system serving a small isolated community. Energies. Volume 8, Issue 2, 2015, Pages 995-1024.

Conference papers

SDEWES 2017 – 12nd Conference on sustainable development on energy, water and environmental systems,4th to 9th of October 2017, at Dubrovnik (Croatia).

1. Calise, F., Dentice d'Accadia, M., Libertini, L., Quiriti, E., Vicidomini, M. Dynamic simulation of an integrated solar combined cycle power plant.

2. Calise, F., Libertini, L., Quiriti, E., Vicidomini, M. Dynamic simulation and thermoeconomic optimization of a novel solar cooling system for three-pressure combined cycle power plants.

3. Buonomano, A., Calise, F., Dentice d'Accadia, M., Vicidomini, M. Dynamic simulation of electric energy storage for polygeneration system using wind and solar energy.

BIRES 2017 - First International Conference on Building Integrated Renewable Energy Systems. 6th to 9th of March 2017, at Dublin, (Ireland).

4. Buonomano A., Calise F., Palombo A., Vicidomini M. Exergetic and energy-economic analysis of a building integrated photovoltaic and thermal system.

Conference: SDEWES 2016 - 11th Conference on sustainable development on energy, water and environmental systems, 4th to 9th of September 2016, at Lisbon (Portugal).

5. Buonomano, A., Calise, F., Forzano, F., Palombo, A., Vicidomini, M. Dynamic simulations of an adsorption chiller using low-temperature heat from Building Integrated PhotoVoltaic and Thermal system.

6. Buonomano, A., Calise, F., Forzano, F., Palombo, A., Vicidomini, M. Solar heating and cooling systems for residential applications: a comparison among different system layouts and technologies.

7. Calise, F., Libertini, L., Vicidomini, M. Dynamic simulation and thermoeconomic analysis of a novel solar cooling system for combined cycle power plants.

8. Calise, F., Dentice d'Accadia, M., Libertini, L., Vanoli, R., Vicidomini, M. Analysis of the optimal operation of trigeneration systems using dynamic simulations.

Conference: SDEWES 2015 - 10th Conference on sustainable development on energy, water and environmental systems, 27th of September to 2nd of October, at Dubrovnik (Croatia).

9. Calise F., Buonomano A., Dentice d'Accadia M., Palombo A., Vicidomini M. Building integration of solar thermal systems: a thermo-economic analysis.

70th Conference of the Italian Thermal Machines Engineering Association, ATI 2015; Technische Universiteit Eindhoven, 9th to 11th of September, at Rome (Italy).

10. Buonomano, A., Montanaro, U., Palombo, A., Vicidomini, M. NZEBs in Mediterranean climates: Energy design and optimization for a non-residential building. Energy Procedia. Volume 82, 2015, Pages 458-464.

6th European Fuel Cell Conference and Exhibition - EFC, 16th to 18th of December 2015, at Naples (Italy).

11. Buonomano, A., Calise, F., Dentice D'Accadia, M., Palombo, A., Vicidomini, M. A Review of Hybrid Power Plants Including Solid Oxide Fuel Cells And Gas Turbine Systems.

Proceedings of COST Action TU 1205 Symposium, 21st July 2015, at Guimarães. (Portugal).

12. Buonomano A., Montanaro U., Palombo A., Vicidomini M. BISTS technologies for NZEBs: a case study for a non-residential building in Mediterranean climate.

EURO-ELECS, 21st to 23rd of July 2015, at Guimarães (Portugal).

13. Buonomano Annamaria, Montanaro Umberto, Palombo Adolfo, Vicidomini Maria. Energy saving technologies for a non-residential NZEB in Mediterranean climate. Codice 11588/609682

La gestione energetica del patrimonio edilizio pubblico: Strategie ed esperienze, 17th of October, at Bologna (Italy).

14. Buonomano Annamaria, Calise Francesco, Ferruzzi Gabriele, Palombo Adolfo, Vicidomini Maria. Riqualificazione energetica di un complesso ospedaliero: il caso studio relativo al policlinico Federico II di Napoli. Codice 11588/563652.

NOMENCLATURE

a	*discount rate, %*
A	*area, m^2*
AF	*annuity factor, years*
c	*specific heat, J/(kg K)*
C	*cost, €*
COP	*Coefficient Of Performance, adim*
E	*energy, kWh or kWh/year*
Eff_T	*temperature efficiency modifier, $°C^{-1}$*
Eff_G	*radiation efficiency modifier, m^2/W*
EER	*Energy Efficiency Ratio, adim*
ESC	*energy savings certificates, €/toe*
ex	*specific exergy, kWh/kg*
$\dot{E}x$	*exergy flow, kW*
Ex	*exergy, kWh or kWh/year*
G	*solar irradiance, kW/m^2*
h	*specific enthalpy, kJ/kg*
H	*operating hours, h*
HDD	*Heating Degree Day, Kd*
j/c	*specific cost-price, €/kWh or €/Sm^3*
J	*component capital cost, €*
LCV	*natural gas lower calorific value, kWh/Sm^3*
$\dot{m}$	*flow rate, kg/h*
Ma	*maintenance, €/year*
NPV	*net present value, €*
p	*pressure, Pa*
$\dot{P}$	*electric power, kW*
P	*electric energy, kWh or kWh/year*
PE	*primary energy, kWh or kWh/year*
PES	*primary energy saving, adim*
PI	*profit index, adim*
$\dot{Q}$	*thermal energy flow rate, kW*
Q	*thernal energy, kWh or kWh/year*
s	*specific entropy, kJ/(kg K)*
SoC	*state of charge, Ah*
SP	*selling price, €/toe*
SPB	*simple pay back, years*
T	*temperature, °C or K*
U	*heat transfer coefficient, $kW/(m^2\ °K)$*
V	*Volume, m^3*

Greek symbols

α	*azimuth, °*
ΔC	*operating costs savings, €/year*
ΔT	*temperature difference, °C*
d	*efficiency defect,-*
ε	*long wave emissivity, adim*
□	*conductivity, W/mK*
η	*efficiency, adim*
ρ	*density, kg/m^3*
$ρ_s$	*solar reflectance, adim*
θ	*time, h*
v	*specific volume, m3/kg*
ξ	*control function, adim*

Subscripts and superscripts

a/amb	*ambient*
ACH	*absorption chiller*
ADS	*adsorption chiller*
AC	*after cooler*
Alm	*Almeria*
aux	*auxiliary*
BB	*backup boiler*
BC	*backup chiller*
cell	*photovoltaic cell*
c/cool	*cooling*
CB	*condensation boiler*
CCHP	*combined cooling, heating and power*
ch	*chilled*
CHP	*combined heat and power*
chw	*chilled water*
COG	*cogenerator*
CT	*cooling tower*
CTK	*cold tank*
cw	*cooling water*
d	*destruction*
D	*diverter*
dem	*demand*
DHW	*domestic hot water*
DL	*design load*
eff	*effective*
el	*electric*
ELT	*electric load tracking*
eq	*equivalent*
EX	*exchange*
exh	*exhaust*

ExJ	*Exhaust gases-Jacket water exchanger*
ext	*external*
ExJw	*heat exchanger exhaust gases – jacket water*
f	*dimensionless design factor*
F	*thermal energy recovered fraction*
glob	*global*
FC	*fan coils*
h/heat	*heating*
H	*from the heat source*
HE	*heat exchanger*
HEC	*high efficiency cogeneration unit*
HEW	*heat exchanger winter*
hot	*hot source*
HP	*heat pump*
HTK	*hot tank*
HVAC	*heating, ventilation, and air conditioning*
hw	*hot water*
HwDHW	*heat exchanger heating water – domestic hot water*
i	*i-th time step of the simulation.*
I	*inverter/intercooler*
ICE	*internal combustion reciprocating engine*
in	*input/inlet*
int	*internal*
IRR	*internal rate of return*
JW	Jacket water/heating Water exchanger
JwHw	*heat exchanger jacket water – heating water*
L	*load*
LAB	*lead-acid battery*
m	*mechanical*
M	*mixer*
Mil	*Milan*
min	*minimum*
MPTLT	*maximum power thermal load tracking*
N	*nominal*
Nap	*Naples*
NG/ng	*natural gas*
NZEB	*net zero energy buildings*
OC	*oil engine*
OFF	*office zone*
op	*operating*
ORC	*organic rankine cycles*
o/out	*output/outlet*
P	*Pump*
ph	*physical*
PLR	*part load ratio*
PM	*prime mover*
PMD	*prime mover dissipator*
PROD	*production zone*
PS	*proposed system*
pump	*referred to pump*
PV	*PhotoVoltaic*
PVT	*PVT solar collectors*
R	*regulator*
rated	*at nominal conditions*
ref	*reference*
req	*required*
ret	*return*
RF	*radiant floor*
RS	*reference system*
SC	*solar collectors*
set	*set by the controller*
SHW	*sanitary hot water*
taxfree	*without taxes*
t/th	*thermal*
thd	*thermodynamic*
TK	*storage tank*
TKC	*cold storage tank*
TKH	*hot storage tank*
TLT	*thermal load tracking*
tot	*total*
y	*year*
z	*zone*

BIBLIOGRAPHY

1. *https://www.iea.org/publications/freepublications/publication/WorldEnergyBalances2017Overview.pdf.*
2. *https://www.iea.org/weo2017/.*
3. *https://www.iea.org/etp/tracking2017/buildings/.*
4. *http://www.iea.org/Textbase/npsum/building2013SUM.pdf.*
5. *https://globalabc.org/uploads/media/default/0001/01/0d6a71a346ea7e6841b1b29c77eba6d6ae986103.pdf.*
6. *https://www.iea.org/etp/tracking2017/lightingappliancesandequipment/.*
7. *http://www.iea.org/publications/freepublications/publication/Energy_Efficiency_2017.pdf.*
8. *https://www.iea.org/etp/tracking2017/buildingenvelopes/.*
9. da Graça Carvalho, M., *EU energy and climate change strategy.* Energy, 2012. **40**(1): p. 19-22.
10. Desideri, U., et al., *Design of a multipurpose "zero energy consumption" building according to European Directive 2010/31/EU: Architectural and technical plants solutions.* Energy, 2013. **58**: p. 157-167.
11. COST Action TU1205 (BISTS), *Overview of BISTS state of the art, models and applications.* 2015.
12. SHC, I.-. *Towards Net Zero Energy Solar Buildings.* 2015. **Task 40 (EBC Annex 52) - Net Zero Energy Solar Buildings SHC Position Paper**.
13. Kalogirou, S., Y. Tripanagnostopoulos, and M. Souliotis, *Performance of solar systems employing collectors with colored absorber.* Energy and Buildings, 2005. **37**(8): p. 824-835.
14. Duffie, J.A. and W.A. Beckman, *Solar Engineering of Thermal Processes. 3rd Edition: Wiley, J.* 2008.
15. Shirazi, A., et al., *A systematic parametric study and feasibility assessment of solar-assisted single-effect, double-effect, and triple-effect absorption chillers for heating and cooling applications.* Energy Conversion and Management, 2016. **114**: p. 258-277.
16. Calise, F., et al., *A novel solar-assisted heat pump driven by photovoltaic/thermal collectors: Dynamic simulation and thermoeconomic optimization.* Energy, 2016. **95**: p. 346-366.
17. Calise, F., et al., *Desiccant-based AHU interacting with a CPVT collector: Simulation of energy and environmental performance.* Solar Energy, 2014. **103**: p. 574-594.
18. Sarbu, I. and C. Sebarchievici, *Review of solar refrigeration and cooling systems.* Energy and Buildings, 2013. **67**(0): p. 286-297.
19. Florides, G.A., et al., *Modelling, simulation and warming impact assessment of a domestic-size absorption solar cooling system.* Applied Thermal Engineering, 2002. **22**(12): p. 1313-1325.
20. Vasilescu, C. and C. Infante Ferreira, *Solar driven double-effect absorption cycles for sub-zero temperatures.* International Journal of Refrigeration, 2014. **39**(0): p. 86-94.
21. Zhang, X., Zhao, Xudong, Smith, Stefan, Xu, Jihuan, Yu, Xiaotong, *Review of R&D progress and practical application of the solar photovoltaic/thermal (PV/T) technologies* Renewable and Sustainable Energy Reviews, 2011. **16**(1): p. 599-617.
22. Ghafoor, A. and A. Munir, *Worldwide overview of solar thermal cooling technologies.* Renewable and Sustainable Energy Reviews, 2015. **43**: p. 763-774.

23. Best, R. and W. Rivera, *A review of thermal cooling systems.* Applied Thermal Engineering, 2015. **75**: p. 1162-1175.
24. Shan, F., et al., *Performance evaluations and applications of photovoltaic–thermal collectors and systems.* Renewable and Sustainable Energy Reviews, 2014. **33**(0): p. 467-483.
25. Buonomano, A., et al., *Energy and economic analysis of geothermal–solar trigeneration systems: A case study for a hotel building in Ischia.* Applied Energy, 2015. **138**: p. 224-241.
26. Buker, M.S., B. Mempouo, and S.B. Riffat, *Experimental investigation of a building integrated photovoltaic/thermal roof collector combined with a liquid desiccant enhanced indirect evaporative cooling system.* Energy Conversion and Management, 2015. **101**: p. 239-254.
27. Kalogirou, S.A. and G.A. Florides, *Solar Space Heating and Cooling Systems☆*, in *Reference Module in Earth Systems and Environmental Sciences*. 2016, Elsevier.
28. Hailu, G., P. Dash, and A.S. Fung, *Performance Evaluation of an Air Source Heat Pump Coupled with a Building-Integrated Photovoltaic/Thermal (BIPV/T) System under Cold Climatic Conditions.* Energy Procedia, 2015. **78**: p. 1913-1918.
29. Buonomano, A., et al., *BIPVT systems for residential applications: An energy and economic analysis for European climates.* Applied Energy, 2016. **184**: p. 1411-1431.
30. Corbin, C.D. and Z.J. Zhai, *Experimental and numerical investigation on thermal and electrical performance of a building integrated photovoltaic–thermal collector system.* Energy and Buildings, 2010. **42**(1): p. 76-82.
31. Chow, T.T., *A review on photovoltaic/thermal hybrid solar technology* Applied Energy, 2010. **87**(2): p. 365-379.
32. Memari, A.M., et al., *Building Integrated Photovoltaic Systems for Single Family Dwellings: Innovation Concepts.* Open Journal of Civil Engineering, 2014. **4**: p. 102-119.
33. Energy, U.S.D.o., O.o.E.E.a.R. Energy, and B.T. Office, *Research & Development Needs for Building-Integrated Solar Technologies.* energy.gov/sites/prod/files/2014/02/f7/BIST_TechnicalReport_January2014_0.pdf, 2014.
34. Lamnatou, C., et al., *Modelling and simulation of Building-Integrated solar thermal systems: Behaviour of the coupled building/system configuration.* Renewable and Sustainable Energy Reviews, 2015. **48**: p. 178-191.
35. Lamnatou, C., et al., *Modelling and simulation of Building-Integrated solar thermal systems: Behaviour of the system.* Renewable and Sustainable Energy Reviews, 2015. **45**(0): p. 36-51.
36. Buker, M.S., B. Mempouo, and S.B. Riffat, *Performance evaluation and techno-economic analysis of a novel building integrated PV/T roof collector: An experimental validation.* Energy and Buildings, 2014. **76**(0): p. 164-175.
37. Zogou, O. and H. Stapountzis, *Flow and heat transfer inside a PV/T collector for building application.* Applied Energy, 2012. **91**(1).
38. Koyunbaba, B.K., Z. Yilmaz, and K. Ulgen, *An approach for energy modeling of a building integrated photovoltaic (BIPV) Trombe wall system.* Energy and Buildings, 2013: p. 680–688.
39. Diarce, G., et al., *A comparative study of the CFD modeling of a ventilated active façade including phase change materials.* Applied Energy, 2014. **126**: p. 307–317.

40. Athienitis, A.K., et al., *A prototype photovoltaic/thermal system integrated with transpired collector.* Solar Energy, 2011: p. 139–153.
41. Aelenei, L., et al., *Thermal Performance of a Hybrid BIPV-PCM: Modeling, Design and Experimental Investigation.* Energy Procedia, 2014. **48**(Supplement C): p. 474-483.
42. Jouhara, H., et al., *The performance of a novel flat heat pipe based thermal and PV/T (photovoltaic and thermal systems) solar collector that can be used as an energy-active building envelope material.* Energy, 2015.
43. D'Orazio, M., C. Di Perna, and E. Di Giuseppe, *Experimental operating cell temperature assessment of BIPV with different installation configurations on roofs under Mediterranean climate.* Renewable Energy, 2014. **68**: p. 378-396.
44. Chow, T.T., et al., *Computer modeling and experimental validation of a building-integrated photovoltaic and water heating system.* Applied Thermal Engineering, 2008.
45. Kaiser, A.S., et al., *Experimental study of cooling BIPV modules by forced convection in the air channel.* Applied Energy, 2014. **135**: p. 88–97.
46. Krauter, S., et al., *Combined photovoltaic and solar thermal systems for facade integration and building insulation.* Solar Energy, 1999: p. 239-248.
47. H.M. Yin, D.J.Y., G. Kelly, J. Garant, *Design and performance of a novel building integrated PV/thermal system for energy efficiency of buildings.* Solar Energy, 2013. **87**: p. 184–195.
48. Yang, T. and A.K. Athienitis, *Experimental investigation of a two-inlet air-based building integrated photovoltaic/thermal (BIPV/T) system.* Applied Energy, 2015. **159**: p. 70-79.
49. Ibrahim, A., et al., *Efficiencies and improvement potential of building integrated photovoltaic thermal (BIPVT) system.* Energy Conversion and Management, 2014. **77**: p. 527-534.
50. Shukla, A.K., K. Sudhakar, and P. Baredar, *Exergetic analysis of building integrated semitransparent photovoltaic module in clear sky condition at Bhopal India.* Case Studies in Thermal Engineering, 2016. **8**: p. 142-151.
51. Peng, J., et al., *Investigation on the annual thermal performance of a photovoltaic wall mounted on a multi-layer façade.* Applied Energy, 2013. **112**: p. 646–656.
52. Gaur, A. and G.N. Tiwari, *Analytical expressions for temperature dependent electrical efficiencies of thin film BIOPVT systems.* Applied Energy, 2015. **146**: p. 442–452.
53. Vats, K. and G.N. Tiwari, *Energy and exergy analysis of a building integrated semitransparent photovoltaic thermal (BISPVT) system.* Applied Energy, 2012. **96**: p. 409–416.
54. Vats, K. and G.N. Tiwari, *Performance evaluation of a building integrated semitransparent photovoltaic thermal system for roof and façade.* Energy and Buildings, 2012. **45**: p. 211-218.
55. Agrawal, B. and G.N. Tiwari, *Optimizing the energy and exergy of building integrated photovoltaic thermal (BIPVT) systems under cold climatic conditions.* Applied Energy, 2010. **87**(2): p. 417–426.
56. Li, S., et al., *System identification and model-predictive control of office buildings with integrated photovoltaic-thermal collectors, radiant floor heating and active thermal storage.* Solar Energy, 2015. **113**: p. 139-157.

57. Kim, J.-H. and J.-T. Kim, *A Simulation Study of Air-Type Building-Integrated Photovoltaic-Thermal System.* Energy Procedia, 2012. **30**(Supplement C): p. 1016-1024.
58. Shahsavar, A., et al., *Energy saving in buildings by using the exhaust and ventilation air for cooling of photovoltaic panels.* Energy and Buildings, 2011. **43**(9): p. 2219-2226.
59. Davidsson, H., B. Perers, and B. Karlsson, *Performance of a multifunctional PV/T hybrid solar window.* Solar Energy, 2010. **84**(3): p. 365-372.
60. Fong, K.F., C.K. Lee, and T.T. Chow, *Comparative study of solar cooling systems with building-integrated solar collectors for use in sub-tropical regions like Hong Kong.* Applied Energy, 2012. **90**(1): p. 189-195.
61. Corbin, C.D. and Z. Z.J., *Experimental and numerical investigation on thermal and electrical performance of a building integrated photovoltaic–thermal collector system.* Energy and Buildings, 2010: p. 76–82.
62. Hazami, M., et al., *Energetic and exergetic performances analysis of a PV/T (photovoltaic thermal) solar system tested and simulated under to Tunisian (North Africa) climatic conditions.* Energy, 2016. **107**: p. 78-94.
63. Jahromi, S.N., A. Vadiee, and M. Yaghoubi, *Exergy and Economic Evaluation of a Commercially Available PV/T Collector for Different Climates in Iran.* Energy Procedia, 2015. **75**: p. 444-456.
64. Chow, T.T., et al., *Energy and exergy analysis of photovoltaic–thermal collector with and without glass cover.* Applied Energy, 2009. **86**(3): p. 310-316.
65. Shukla, A.K., K. Sudhakar, and P. Baredar, *Exergetic assessment of BIPV module using parametric and photonic energy methods: A review.* Energy and Buildings, 2016. **119**: p. 62-73.
66. Gupta, N., A. Tiwari, and G.N. Tiwari, *Exergy analysis of building integrated semitransparent photovoltaic thermal (BiSPVT) system.* Engineering Science and Technology, an International Journal, 2017. **20**(1): p. 41-50.
67. Vats, K., V. Tomar, and G.N. Tiwari, *Effect of packing factor on the performance of a building integrated semitransparent photovoltaic thermal (BISPVT) system with air duct.* Energy and Buildings, 2012. **53**: p. 159-165.
68. Akyuz, E., et al., *A novel approach for estimation of photovoltaic exergy efficiency.* Energy, 2012. **44**(1): p. 1059-1066.
69. Dubey, S., S.C. Solanki, and A. Tiwari, *Energy and exergy analysis of PV/T air collectors connected in series.* Energy and Buildings, 2009. **41**(8): p. 863-870.
70. Agrawal, B. and G.N. Tiwari, *Life cycle cost assessment of building integrated photovoltaic thermal (BIPVT) systems.* Energy and Buildings, 2010. **42**(9): p. 1472-1481.
71. Agrawal, B. and G.N. Tiwari, *Optimizing the energy and exergy of building integrated photovoltaic thermal (BIPVT) systems under cold climatic conditions.* Applied Energy, 2010. **87**(2): p. 417-426.
72. Wu, S.-Y., et al., *A heat pipe photovoltaic/thermal (PV/T) hybrid system and its performance evaluation.* Energy and Buildings, 2011. **43**(12): p. 3558-3567.
73. Buker, M.S., B. Mempouo, and S.B. Riffat, *Performance evaluation and techno-economic analysis of a novel building integrated PV/T roof collector: An experimental validation.* Energy and Buildings, 2014. **76**: p. 164-175.

74. Sohel, M.I., et al., *A dynamic model for air-based photovoltaic thermal systems working under real operating conditions.* Applied Energy, 2014. **132**: p. 216-225.
75. Agency, I.-I.E., ed. *World Energy Outlook 2013*. 2013.
76. Calise, F., M. Dentice d'Accadia, and A. Piacentino, *A novel solar trigeneration system integrating PVT (photovoltaic/thermal collectors) and SW (seawater) desalination: Dynamic simulation and economic assessment.* Energy, 2014. **67**: p. 129-148.
77. Calise, F., et al., *A novel renewable polygeneration system for a small Mediterranean volcanic island for the combined production of energy and water: Dynamic simulation and economic assessment.* Applied Energy, 2014. **135**: p. 675-693.
78. Calise, F., M.D. d'Accadia, and L. Vanoli, *Design and dynamic simulation of a novel solar trigeneration system based on hybrid photovoltaic/thermal collectors (PVT).* Energy Conversion and Management, 2012. **60**: p. 214-225.
79. Soutullo, S., et al., *Energy performance assessment of a polygeneration plant in different weather conditions through simulation tools.* Energy and Buildings, 2016. **124**: p. 7-18.
80. Khojasteh Salkuyeh, Y. and T.A. Adams, *Integrated petroleum coke and natural gas polygeneration process with zero carbon emissions.* Energy, 2015. **91**: p. 479-490.
81. Jana, K. and S. De, *Polygeneration using agricultural waste: Thermodynamic and economic feasibility study.* Renewable Energy, 2015. **74**: p. 648-660.
82. Bai, Z., et al., *A polygeneration system for the methanol production and the power generation with the solar–biomass thermal gasification.* Energy Conversion and Management, 2015. **102**: p. 190-201.
83. Wang, Z., et al., *Proposal and assessment of a new CCHP system integrating gas turbine and heat-driven cooling/power cogeneration.* Energy Conversion and Management, 2017. **144**: p. 1-9.
84. De Kam, M.J., R. Vance Morey, and D.G. Tiffany, *Biomass Integrated Gasification Combined Cycle for heat and power at ethanol plants.* Energy Conversion and Management, 2009. **50**(7): p. 1682-1690.
85. Maraver, D., J. Uche, and J. Royo, *Assessment of high temperature organic Rankine cycle engine for polygeneration with MED desalination: A preliminary approach.* Energy Conversion and Management, 2012. **53**(1): p. 108-117.
86. Chen, Y., W. Han, and H. Jin, *Investigation of an ammonia-water combined power and cooling system driven by the jacket water and exhaust gas heat of an internal combustion engine.* International Journal of Refrigeration, 2017. **82**: p. 174-188.
87. Lin, H., et al., *Techno-economic evaluation of coal-based polygeneration systems of synthetic fuel and power with CO2 recovery.* Energy Conversion and Management, 2011. **52**(1): p. 274-283.
88. Calise, F., et al., *A novel hybrid polygeneration system supplying energy and desalinated water by renewable sources in Pantelleria Island.* Energy, 2017.
89. Calise, F., et al., *Optimal operating strategies of combined cooling, heating and power systems: A case study for an engine manufacturing facility.* Energy Conversion and Management, 2017. **149**: p. 1066-1084.

90. Sibilio, S., et al., *Building-integrated trigeneration system: Energy, environmental and economic dynamic performance assessment for Italian residential applications.* Renewable and Sustainable Energy Reviews, 2017. **68, Part 2**: p. 920-933.
91. Kumar, S., et al., *Current status and future projections of LNG demand and supplies: A global prospective.* Energy Policy, 2011. **39**(7): p. 4097-4104.
92. Li, Y., et al., *Thermodynamic analysis of a coal-based polygeneration system with partial gasification.* Energy, 2014. **72**: p. 201-214.
93. Fan, J., et al., *Thermodynamic evaluation of chemical looping combustion for combined cooling heating and power production driven by coal.* Energy Conversion and Management, 2017. **135**: p. 200-211.
94. Bose, A., et al., *Co-production of power and urea from coal with CO2 capture: performance assessment.* Clean Techn Environ Policy, 2015: p. 1271-1280.
95. Li, Z., et al., *Simulation and exergoeconomic analysis of a dual-gas sourced polygeneration process with integrated methanol/DME/DMC catalytic synthesis.* Computers & Chemical Engineering, 2011. **35**(9): p. 1857-1862.
96. Gao, P., et al., *Thermodynamic performance assessment of CCHP system driven by different composition gas.* Applied Energy, 2014. **136**: p. 599-610.
97. Li, M., et al., *Optimal design and operation strategy for integrated evaluation of CCHP (combined cooling heating and power) system.* Energy, 2016. **99**: p. 202-220.
98. Gao, L., et al., *Proposal of a natural gas-based polygeneration system for power and methanol production.* Energy, 2008. **33**(2): p. 206-212.
99. Zabihian, F. and A. Fung, *A Review on Modeling of Hybrid Solid Oxide Fuel Cell Systems.* International Journal of Engineering, 2009. **3**(2): p. 85--119.
100. Duic, N., et al., *Sustainable development of energy, water and environment systems.* Applied Energy, 2013. **101**: p. 3-5.
101. Bentsen, N.S., C. Felby, and B.J. Thorsen, *Agricultural residue production and potentials for energy and materials services.* Progress in Energy and Combustion Science, 2014. **40**: p. 59-73.
102. Jana, K. and S. De, *Sustainable polygeneration design and assessment through combined thermodynamic, economic and environmental analysis.* Energy, 2015. **91**: p. 540-555.
103. Jana, K. and S. De, *Techno-economic evaluation of a polygeneration using agricultural residue – A case study for an Indian district.* Bioresource Technology, 2015. **181**: p. 163-173.
104. Jana, K. and S. De, *Environmental impact of biomass based polygeneration - A case study through life cycle assessment.* Bioresour Technol, 2017: p. 256-265.
105. Huang, Y., et al., *Performance analysis of biofuel fired trigeneration systems with energy storage for remote households.* Applied Energy, 2017. **186, Part 3**: p. 530-538.
106. Cormos, C.-C., *Biomass direct chemical looping for hydrogen and power co-production: Process configuration, simulation, thermal integration and techno-economic assessment.* Fuel Processing Technology, 2015. **137**(Supplement C): p. 16-23.
107. Hernández, B., E. León, and M. Martín, *Bio-waste selection and blending for the optimal production of power and fuels via anaerobic digestion.* Chemical Engineering Research and Design, 2017. **121**(Supplement C): p. 163-172.

108. Al-Sulaiman, F.A., I. Dincer, and F. Hamdullahpur, *Exergy modeling of a new solar driven trigeneration system.* Solar Energy, 2011. **85**(9): p. 2228-2243.
109. Calise, F., A. Palombo, and L. Vanoli, *Design and dynamic simulation of a novel polygeneration system fed by vegetable oil and by solar energy.* Energy Conversion and Management, 2012. **60**: p. 204-213.
110. Karellas, S. and K. Braimakis, *Energy–exergy analysis and economic investigation of a cogeneration and trigeneration ORC–VCC hybrid system utilizing biomass fuel and solar power.* Energy Conversion and Management, 2016. **107**: p. 103-113.
111. Wang, J. and Y. Yang, *Energy, exergy and environmental analysis of a hybrid combined cooling heating and power system utilizing biomass and solar energy.* Energy Conversion and Management, 2016. **124**: p. 566-577.
112. Sahoo, U., et al., *Development of an innovative polygeneration process in hybrid solar-biomass system for combined power, cooling and desalination.* Applied Thermal Engineering, 2017. **120**: p. 560-567.
113. Calise, F., et al., *A novel solar-geothermal trigeneration system integrating water desalination: Design, dynamic simulation and economic assessment.* Energy, 2016. **115, Part 3**: p. 1533-1547.
114. Calise, F., et al., *Exergetic and exergoeconomic analysis of a novel hybrid solar–geothermal polygeneration system producing energy and water.* Energy Conversion and Management, 2016. **115**: p. 200-220.
115. Bicer, Y. and I. Dincer, *Analysis and performance evaluation of a renewable energy based multigeneration system.* Energy, 2016. **94**: p. 623-632.
116. Tempesti, D., G. Manfrida, and D. Fiaschi, *Thermodynamic analysis of two micro CHP systems operating with geothermal and solar energy.* Applied Energy, 2012. **97**: p. 609-617.
117. Ondeck, A.D., T.F. Edgar, and M. Baldea, *Optimal operation of a residential district-level combined photovoltaic/natural gas power and cooling system.* Applied Energy, 2015. **156**: p. 593-606.
118. Chicco, G. and P. Mancarella, *Distributed multi-generation: A comprehensive view.* Renewable and Sustainable Energy Reviews, 2009. **13**(3): p. 535-551.
119. Bizzarri, G. and G.L. Morini, *New technologies for an effective energy retrofit of hospitals.* Applied Thermal Engineering, 2006. **26**(2): p. 161-169.
120. Basrawi, F., T. Yamada, and S.y. Obara, *Economic and environmental based operation strategies of a hybrid photovoltaic–microgas turbine trigeneration system.* Applied Energy, 2014. **121**: p. 174-183.
121. Buonomano, A., et al., *A novel renewable polygeneration system for hospital buildings: Design, simulation and thermo-economic optimization.* Applied Thermal Engineering, 2014. **67**(1–2): p. 43-60.
122. Arsalis, A., A.N. Alexandrou, and G.E. Georghiou, *Thermoeconomic Modeling and Parametric Study of a Photovoltaic-Assisted 1MWe Combined Cooling, Heating, and Power System.* Energies, 2016. **9**: p. 663.
123. Calise, F., *Thermoeconomic analysis and optimization of high efficiency solar heating and cooling systems for different Italian school buildings and climates.* Energy and Buildings, 2010. **42**(7): p. 992-1003.

124. Angrisani, G., C. Roselli, and M. Sasso, *Distributed microtrigeneration systems.* Progress in Energy and Combustion Science, 2012. **38**(4): p. 502-521.
125. Ziher, D. and A. Poredos, *Economics of a trigeneration system in a hospital.* Applied Thermal Engineering, 2006. **26**(7): p. 680-687.
126. Ghaebi, H., et al., *Energy, exergy and thermoeconomic analysis of a combined cooling, heating and power (CCHP) system with gas turbine prime mover.* International Journal of Energy Research, 2010. **35**(8): p. 697-709.
127. Khaliq, A. and R. Kumar, *Thermodynamic performance assessment of gas turbine trigeneration system for combined heat cold and power production.* Journal of Engineering for Gas Turbines and Power, 2008. **130**(2).
128. Carles Bruno, J., A. Valero, and A. Coronas, *Performance analysis of combined microgas turbines and gas fired water/LiBr absorption chillers with post-combustion.* Applied Thermal Engineering, 2005. **25**(1): p. 87-99.
129. Bruno, J.C., L. Massagués, and A. Coronas. *Power quality and air emission tests in a microgas turbine cogeneration plant*. in *Proceedings of the International Conference on Renewable Energy and Power Quality (ICREPQ'03)*. 2003. Vigo, Spain.
130. Ge, Y.T., et al., *Performance evaluation of a tri-generation system with simulation and experiment.* Applied Energy, 2009. **86**(11): p. 2317-2326.
131. Medrano, M., et al., *Theoretical analysis of a novel integrated energy system formed by a microturbine and an exhaust fired single-double effect absorption chiller.* International Journal of Thermodynamics, 2006. **9**: p. 29-36.
132. Chen, Q., et al., *The exergy and energy level analysis of a combined cooling, heating and power system driven by a small scale gas turbine at off design condition.* Applied Thermal Engineering, 2014. **66**(1): p. 590-602.
133. Huicochea, A., et al., *Thermodynamic analysis of a trigeneration system consisting of a micro gas turbine and a double effect absorption chiller.* Applied Thermal Engineering, 2011. **31**(16): p. 3347-3353.
134. Rahman, M. and A. Malmquist, *Modeling and Simulation of an Externally Fired Micro-Gas Turbine for Standalone Polygeneration Application.* Journal of Engineering for Gas Turbines and Power, 2016. **138**(11).
135. Yilmazoglu, M.Z., *Effects of the selection of heat transfer fluid and condenser type on the performance of a solar thermal power plant with technoeconomic approach.* Energy Conversion and Management, 2016. **111**: p. 271-278.
136. Elsafi, A.M., *Exergy and exergoeconomic analysis of sustainable direct steam generation solar power plants.* Energy Conversion and Management, 2015. **103**: p. 338-347.
137. Sarr, J.-A.R. and F. Mathieu-Potvin, *Increasing thermal efficiency of Rankine cycles by using refrigeration cycles: A theoretical analysis.* Energy Conversion and Management, 2016. **121**: p. 358-379.
138. Serra, L.M., et al., *Polygeneration and efficient use of natural resources.* Energy, 2009. **34**(5): p. 575-586.
139. Starfelt, F., et al., *Performance evaluation of adding ethanol production into an existing combined heat and power plant.* Bioresource Technology, 2010. **101**(2): p. 613-618.
140. Cormos, C.-C., *Renewable hydrogen production concepts from bioethanol reforming with carbon capture.* International Journal of Hydrogen Energy, 2014. **39**(11): p. 5597-5606.

141. Dai, Y., J. Wang, and L. Gao, *Exergy analysis, parametric analysis and optimization for a novel combined power and ejector refrigeration cycle.* Applied Thermal Engineering, 2009. **29**(10): p. 1983-1990.
142. Pan, M., et al., *Application of optimal design methodologies in retrofitting natural gas combined cycle power plants with CO2 capture.* Applied Energy, 2016. **161**: p. 695-706.
143. Ahmadi, P., M.A. Rosen, and I. Dincer, *Greenhouse gas emission and exergo-environmental analyses of a trigeneration energy system.* International Journal of Greenhouse Gas Control, 2011. **5**(6): p. 1540-1549.
144. Zhu, L., et al., *Polygeneration of hydrogen and power based on coal gasification integrated with a dual chemical looping process: Thermodynamic investigation.* Computers & Chemical Engineering, 2016. **84**: p. 302-312.
145. Calise, F., et al., *Thermoeconomic analysis and off-design performance of an organic Rankine cycle powered by medium-temperature heat sources.* Solar Energy, 2014. **103**: p. 595-609.
146. Vélez, F., et al., *A technical, economical and market review of organic Rankine cycles for the conversion of low-grade heat for power generation.* Renewable and Sustainable Energy Reviews, 2012. **16**(6): p. 4175-4189.
147. Calise, F., et al., *Design and simulation of a prototype of a small-scale solar CHP system based on evacuated flat-plate solar collectors and Organic Rankine Cycle.* Energy Conversion and Management, 2015. **90**: p. 347-363.
148. Patel, B., et al., *Thermo-economic analysis of a novel organic Rankine cycle integrated cascaded vapor compression–absorption system.* Journal of Cleaner Production, 2017. **154**: p. 26-40.
149. Uris, M., J.I. Linares, and E. Arenas, *Feasibility assessment of an Organic Rankine Cycle (ORC) cogeneration plant (CHP/CCHP) fueled by biomass for a district network in mainland Spain.* Energy, 2017. **133**: p. 969-985.
150. Ahmadi, P., I. Dincer, and M.A. Rosen, *Exergo-environmental analysis of an integrated organic Rankine cycle for trigeneration.* Energy Conversion and Management, 2012. **64**: p. 447-453.
151. Ji, J., et al., *Simulation Study of an ORC System Driven by the Waste Heat Recovered from a Trigeneration System.* Energy Procedia, 2017. **105**: p. 5040-5047.
152. Sharaf, M.A., A.S. Nafey, and L. García-Rodríguez, *Exergy and thermo-economic analyses of a combined solar organic cycle with multi effect distillation (MED) desalination process.* Desalination, 2011. **272**(1–3): p. 135-147.
153. Bae, C. and J. Kim, *Alternative fuels for internal combustion engines.* Proceedings of the Combustion Institute, 2017. **36**(3): p. 3389-3413.
154. Wu, D.W. and R.Z. Wang, *Combined cooling, heating and power: A review.* Progress in Energy and Combustion Science, 2006. **32**(5): p. 459-495.
155. Hossain, A.K., et al., *Omnigen: Providing electricity, food preparation, cold storage and pure water using a variety of local fuels.* Renewable Energy, 2013. **49**: p. 197-202.
156. Taymaz, I., *An experimental study of energy balance in low heat rejection diesel engine.* Energy, 2006. **31**(2): p. 364-371.

157. Wu, J.Y., et al., *Experimental and simulative investigation of a micro-CCHP (micro combined cooling, heating and power) system with thermal management controller.* Energy, 2014. **68**: p. 444-453.
158. Míguez, J.L., et al., *Feasibility of a new domestic CHP trigeneration with heat pump: I. Design and development.* Applied Thermal Engineering, 2004. **24**(10): p. 1409-1419.
159. Porteiro, J., et al., *Feasibility of a new domestic CHP trigeneration with heat pump: II. Availability analysis.* Applied Thermal Engineering, 2004. **24**(10): p. 1421-1429.
160. Maidment, G.G., et al., *Application of combined heat-and-power and absorption cooling in a supermarket.* Applied Energy, 1999. **63**(3): p. 169-190.
161. Rosato, A., et al., *Energy, Environmental and Economic Effects of Electric Vehicle Charging on the Performance of a Residential Building-integrated Micro-trigeneration System.* Energy Procedia, 2017. **111**: p. 699-709.
162. Rey, G., et al., *Development of an ICE-Based Micro-CHP System Based on a Stirling Engine; Methodology for a Comparative Study of its Performance and Sensitivity Analysis in Recreational Sailing Boats in Different European Climates.* Energies, 2016. **9**: p. 239.
163. Sonar, D., S.L. Soni, and D. Sharma, *Micro-trigeneration for energy sustainability: Technologies, tools and trends.* Applied Thermal Engineering, 2014. **71**(2): p. 790-796.
164. Onovwiona, H.I. and V.I. Ugursal, *Residential cogeneration systems: review of the current technology.* Renewable and Sustainable Energy Reviews, 2006. **10**(5): p. 389-431.
165. Calise, F., *Design of a hybrid polygeneration system with solar collectors and a Solid Oxide Fuel Cell: Dynamic simulation and economic assessment.* International Journal of Hydrogen Energy, 2011. **36**(10): p. 6128-6150.
166. Calise, F., G. Ferruzzi, and L. Vanoli, *Transient simulation of polygeneration systems based on PEM fuel cells and solar heating and cooling technologies.* Energy, 2012. **41**(1): p. 18-30.
167. Calise, F., et al., *Polygeneration system based on PEMFC, CPVT and electrolyzer: Dynamic simulation and energetic and economic analysis.* Applied Energy, 2017. **192**: p. 530-542.
168. Kyriakarakos, G., et al., *Polygeneration microgrids: A viable solution in remote areas for supplying power, potable water and hydrogen as transportation fuel.* Applied Energy, 2011. **88**(12): p. 4517-4526.
169. Samavati, M., R. Raza, and B. Zhu, *Design of a 5-kW advanced fuel cell polygeneration system.* Wiley Interdisciplinary Reviews: Energy and Environment, 2012. **1**(2): p. 173-180.
170. Becker, W.L., et al., *Design and technoeconomic performance analysis of a 1MW solid oxide fuel cell polygeneration system for combined production of heat, hydrogen, and power.* Journal of Power Sources, 2012. **200**: p. 34-44.
171. Ranjbar, F., et al., *Energy and exergy assessments of a novel trigeneration system based on a solid oxide fuel cell.* Energy Conversion and Management, 2014. **87**: p. 318-327.
172. Chitsaz, A., A.S. Mehr, and S.M.S. Mahmoudi, *Exergoeconomic analysis of a trigeneration system driven by a solid oxide fuel cell.* Energy Conversion and Management, 2015. **106**: p. 921-931.
173. Kronenberg, G., *Cogeneration with the LT-MED desalination process.* Desalination, 1997. **208**: p. 287-294.

174. Eveloy, V., P. Rodgers, and L. Qiu, *Performance investigation of a power, heating and seawater desalination poly-generation scheme in an off-shore oil field.* Energy, 2016. **98**: p. 26-39.
175. Mata-Torres, C., et al., *Solar polygeneration for electricity production and desalination: Case studies in Venezuela and northern Chile.* Renewable Energy, 2017. **101**: p. 387-398.
176. Mohan, G., et al., *A novel solar thermal polygeneration system for sustainable production of cooling, clean water and domestic hot water in United Arab Emirates: Dynamic simulation and economic evaluation.* Applied Energy, 2016. **167**: p. 173-188.
177. Lythcke-Jørgensen, C., et al., *Optimization of a flexible multi-generation system based on wood chip gasification and methanol production.* Applied Energy, 2017. **192**: p. 337-359.
178. Adams, T.A. and P.I. Barton, *Combining coal gasification and natural gas reforming for efficient polygeneration.* Fuel Processing Technology, 2011. **92**(3): p. 639-655.
179. Djuric Ilic, D., E. Dotzauer, and L. Trygg, *District heating and ethanol production through polygeneration in Stockholm.* Applied Energy, 2012. **91**(1): p. 214-221.
180. Tzimas, E., et al., *The design of carbon capture IGCC-based plants with hydrogen co-production.* Energy Procedia, 2009. **1**(1): p. 591-598.
181. Farhat, K. and S. Reichelstein, *Economic value of flexible hydrogen-based polygeneration energy systems.* Applied Energy, 2016. **164**: p. 857-870.
182. Consonni, S. and F. Viganò, *Decarbonized hydrogen and electricity from natural gas.* International Journal of Hydrogen Energy, 2005. **30**(7): p. 701-718.
183. Adams, T.A. and P.I. Barton, *High-efficiency power production from natural gas with carbon capture.* Journal of Power Sources, 2010. **195**(7): p. 1971-1983.
184. Adams, T.A. and P.I. Barton, *High-efficiency power production from coal with carbon capture.* AIChe, 2010.
185. Chiesa, P., et al., *Co-production of hydrogen, electricity, and CO2 from coal with commercially ready technology. Part A: Performance and emissions.* International Journal of Hydrogen Energy, 2005. **30**: p. 747-767.
186. Kreutz, T., et al., *Co-production of hydrogen, electricity and CO2 from coal with commercially ready technology. Part B: Economic analysis.* International Journal of Hydrogen Energy, 2005. **30**(7): p. 769-784.
187. Ozturk, M. and I. Dincer, *Thermodynamic assessment of an integrated solar power tower and coal gasification system for multi-generation purposes.* Energy Conversion and Management, 2013. **76**(Supplement C): p. 1061-1072.
188. Zhang, Y., et al., *Pre-feasibility of building cooling heating and power system with thermal energy storage considering energy supply–demand mismatch.* Applied Energy, 2016. **167**: p. 125-134.
189. Rosato, A., S. Sibilio, and G. Ciampi, *Dynamic performance assessment of a building-integrated cogeneration system for an Italian residential application.* Energy and Buildings, 2013. **64**: p. 343-358.
190. Ren, H. and W. Gao, *Economic and environmental evaluation of micro CHP systems with different operating modes for residential buildings in Japan.* Energy and Buildings, 2010. **42**(6): p. 853-861.

191. Klein, S.A., et al., *Solar Energy Laboratory, TRNSYS. A transient system simulation program.* University of Wisconsin, Madison, 2006.
192. Buonomano, A., et al., *A novel renewable polygeneration system for hospital buildings: Design, simulation and thermo-economic optimization.* Applied Thermal Engineering, 2014. **67**(1-2): p. 43-60.
193. Buonomano, A., F. Calise, and G. Ferruzzi, *Thermoeconomic analysis of storage systems for solar heating andcooling systems: A comparison between variable-volume and fixed-volume tanks.* Energy, 2013. **59**: p. 600-616.
194. Buratti, C., et al., *Unsteady simulation of energy performance and thermal comfort in non-residential buildings.* Building and Environment, 2013. **59**(0): p. 482-491.
195. Duffie, J.A. and W.A. Beckman, *Solar Engineering of Thermal Processes, 4th Edition - Chapter 6*. 2013: Wiley.
196. Chao-Yang, H. and H. Chiou-Jye, *A study of photovoltaic thermal (PV/T) hybrid system with computer modeling.* International Journal of Smart Grid and Clean Energy, 2014. **3**: p. 75-79.
197. Murray, M.C., et al. *Live Energy Trnsys -Trnsys Simulation within Google Sketchup*. in *Eleventh International IBPSA Conference*. 2009. Glasgow, Scotland July 27-30.
198. Buonomano, A., et al., *Dynamic energy performance analysis: Case study for energy efficiency retrofits of hospital buildings.* Energy, 2014. **78**: p. 555-572.
199. Voit, P., T. Lechner, and M.T. Schuler. *Common EC validation procedure for dynamic building simulation programs - application with TRNSYS*. in *Conference of international simulation societies*. 1994. Zürich.
200. Aschaber, J., M. Hiller, and R. Weber. *Trnsys17: New features of the multizone building model*. in *Eleventh International IBPSA Conference*. 2009 Glasgow, Scotland July 27-30.
201. IEA, I.E.A.-. *SHC Task 34/ ECBCS Annex 43 Project C-Testing and Validation of Building Energy Simulation Tools-Empirical Validations of Shading/Daylighting/Load Interactions in Building Energy Simulation Tools*. 2007, ecbcs.org/docs/Annex_43_Task34-Empirical_Validation - website visited on February 2016.
202. Zweifel, G. *A simple chiller model for hourly time step applications*. in *IBPSA 2009 - International Building Performance Simulation Association 2009*. 2009.
203. Calise, F., M. Dentice d'Accadia, and A. Piacentino, *A novel solar trigeneration system integrating PVT (photovoltaic/thermal collectors) and SW (seawater) desalination: Dynamic simulation and economic assessment.* Energy, 2014. **67**: p. 129–148.
204. IEA, I.E.A.-. *SHC Task 41. Solar Energy and Architecture*. 2012, task41.iea-shc.org/data/sites/1/publications/Task41-Highlights-2012.pdf - website visited on February 2016.
205. Buonomano, A., F. Calise, and A. Palombo, *Buildings dynamic simulation: Water loop heat pump systems analysis for European climates.* Applied Energy, 2012. **91**(1): p. 222-234.
206. Rohitkumar, P., et al., *Cell (module) temperature regulated performance of a building integrated photovoltaic system in tropical conditions.* Renewable Energy, 2014. **72**: p. 140–148.
207. Huang, Y.-C., et al., *Development of building integrated photovoltaic (BIPV) system with PV ceramic tile and its application for building façade.* Energy Procedia, 2014. **61**: p. 1874 – 1878.

208. Buonomano, A., et al., *Adsorption chiller operation by recovering low-temperature heat from building integrated photovoltaic thermal collectors: Modelling and simulation.* Energy Conversion and Management, 2017. **149**: p. 1019-1036.
209. Kim, D.S. and C.A. Infante Ferreira, *Solar refrigeration options – a state-of-the-art review.* International Journal of Refrigeration, 2008. **31**(1): p. 3-15.
210. Calise, F., L. Libertini, and M. Vicidomini, *Dynamic simulation and thermoeconomic analysis of a novel solar cooling system for combined cycle power plants.*, in *11th Conference on Sustainable Development of Energy, Water and Environment Systems – SDEWES Conference*. 2016: Lisbon.
211. Dufo-López, R., J.M. Lujano-Rojas, and J.L. Bernal-Agustín, *Comparison of different lead–acid battery lifetime prediction models for use in simulation of stand-alone photovoltaic systems.* Applied Energy, 2014. **115**: p. 242-253.
212. de Oliveira e Silva, G. and P. Hendrick, *Lead–acid batteries coupled with photovoltaics for increased electricity self-sufficiency in households.* Applied Energy, 2016. **178**: p. 856-867.
213. Bazilian, M., et al., *Re-considering the economics of photovoltaic power.* Renewable Energy, 2013. **53**: p. 329-338.
214. Dusonchet, L. and E. Telaretti, *Comparative economic analysis of support policies for solar PV in the most representative EU countries.* Renewable and Sustainable Energy Reviews, 2015. **42**: p. 986-998.
215. Ramírez, F.J., et al., *Combining feed-in tariffs and net-metering schemes to balance development in adoption of photovoltaic energy: Comparative economic assessment and policy implications for European countries.* Energy Policy, 2017. **102**: p. 440-452.
216. Italian Republic, *Decree of the president of the Italian Republic 412/93*. 1993: Italy.
217. Marino, C., F. Minichiello, and W. Bahnfleth, *The influence of surface finishes on the energy demand of HVAC systems for existing buildings.* Energy and Buildings, 2015. **95**: p. 70-79.
218. Fudholi, A., et al., *Performance analysis of photovoltaic thermal (PVT) water collectors.* Energy Conversion and Management, 2014. **78**: p. 641-651.
219. Buonomano, A., F. Calise, and M. Vicidomini, *Design, Simulation and Experimental Investigation of a Solar System Based on PV Panels and PVT Collectors.* Energies, 2016. **9**(7): p. 497.
220. Myat, A., et al., *Experimental investigation on the optimal performance of Zeolite–water adsorption chiller.* Applied Energy, 2013. **102**: p. 582-590.
221. Qian, S., et al., *Cyclic steady state performance of adsorption chiller with low regeneration temperature zeolite.* Energy, 2013. **60**: p. 517-526.
222. Hong, S.W., et al., *Optimization of a fin-tube type adsorption chiller by design of experiment.* International Journal of Refrigeration, 2015. **49**: p. 49-56.
223. Buonomano, A., et al., *Transient analysis, exergy and thermo-economic modelling of façade integrated photovoltaic/thermal solar collectors.* Renewable Energy, 2017.
224. Li, R., Y. Dai, and R. Wang, *Experimental investigation and simulation analysis of the thermal performance of a balcony wall integrated solar water heating unit.* Renewable Energy, 2015. **75**: p. 115-122.

225. Calise, F., A. Palombo, and L. Vanoli, *A finite-volume model of a parabolic trough photovoltaic/thermal collector: Energetic and exergetic analyses.* Energy, 2012. **46**(1): p. 283-294.
226. Rosen, M.A. and I. Dincer, *Effect of varying dead-state properties on energy and exergy analyses of thermal systems.* International Journal of Thermal Sciences, 2004. **43**(2): p. 121-133.
227. Kotas, T.J., *The exergy method of thermal plant analysis*, ed. K.P. Co. 1995.
228. Torío, H., A. Angelotti, and D. Schmidt, *Exergy analysis of renewable energy-based climatisation systems for buildings: A critical view.* Energy and Buildings, 2009. **41**(3): p. 248-271.
229. Ajam, H., S. Farahat, and F. Saehaddi, *Exergetic Optimization of Solar Air Heaters and Comparison with Energy Analysis.* International Jouurnal of Thermodynamics, 2005. **8**(4): p. 183-190.
230. Calise, F., et al., *Simulation and exergy analysis of a hybrid Solid Oxide Fuel Cell (SOFC)-Gas Turbine System.* Energy, 2006. **31**(15): p. 3278-3299.
231. Calise, F., A. Palombo, and L. Vanoli, *Design and partial load exergy analysis of hybrid SOFC-GT power plant.* Journal of Power Sources, 2006. **158**(1): p. 225-244.
232. Calise, F., M. Dentice d'Accadia, and G. Restuccia, *Simulation of a tubular solid oxide fuel cell through finite volume analysis: Effects of the radiative heat transfer and exergy analysis.* International Journal of Hydrogen Energy, 2007. **32**(17): p. 4575-4590.
233. Fujisawa, T. and T. Tani, *Annual exergy evaluation on photovoltaic-thermal hybrid collector.* Solar Energy Materials and Solar Cells, 1997. **47**(1): p. 135-148.
234. ASHRAE, *Handbook of fundamentals. American Society of Heating, Refrigerating and Air-Conditioning Engineers*. 2001, Atlanta.
235. *http://ahi-carrier.at/wp-content/uploads/2012/pdf/industrial/16lj.pdf.*
236. *http://www.viessmann.de/content/dam/vi-brands/DE/Produkte/Kraft-Waerme-Kopplung/Blockheizkraftwerke/Vitobloc_200_EM-363-401-530/Technische_Beschreibung_BHKW_Vitobloc_200_EM-401_EM-363.pdf/_jcr_content/renditions/original.media_file.download_attachment.file/Technische_Beschreibung_BHKW_Vitobloc_200_EM-401_EM-363.pdf.*
237. Calise, F., A. Palombo, and L. Vanoli, *Maximization of primary energy savings of solar heating and cooling systems by transient simulations and computer design of experiments.* Applied Energy, 2010. **87**(2): p. 524-540.
238. Calise, F., et al., *A novel tool for thermoeconomic analysis and optimization of trigeneration systems: A case study for a hospital building in Italy.* Energy, 2017. **126**(Supplement C): p. 64-87.
239. Calise, F., et al., *Dynamic Simulation and Optimum Operation Strategy of a Trigeneration System Serving a Hospital.* American Journal of Engineering and Applied Sciences, 2016.
240. Calise, F., et al., *Thermoeconomic optimization of a renewable polygeneration system serving a small isolated community.* Energies, 2015. **8**(2): p. 995-1024.